Dissertation

SUBMITTED TO THE

Combined Faculty of Mathematics, Engineering and Natural Sciences
of Heidelberg University, Germany

FOR THE DEGREE OF

Doctor of Natural Sciences

Put forward by

Helena Xiayi, Ren 任夏怡

Born in: Barcelona, Spain

Oral examination: July 10$^{\text{th}}$, 2025

University of Heidelberg
Department of Physics and Astronomy

Very-High-Energy and Ultra-High-Energy Gamma-ray Emission from the Galactic Centre

Referee: **Prof. Dr. James A. Hinton**
Max Planck Institute for Nuclear Physics
Referee: **Prof. Dr. Simon C. O. Glover**
ZAH, Institut für Theoretische Astrophysik
Supervisors: **Prof. Dr. James Hinton, Prof. Dr. Simon Glover, Dr. Julia Djuvsland**

Abstract

The Galactic Centre is a unique and complex astrophysical region, characterised by dense molecular gas, bright point-like sources in very high energies, and a potential PeVatron cosmic-ray accelerator. It is also a key target for indirect dark matter searches, due its high dark matter density and its proximity. However, the region's complexity, along with challenges posed by line-of-sight superposition of gas and dust emissions, complicates efforts to isolate γ-ray sources and study cosmic-ray propagation.

This thesis presents a comprehensive study of the Galactic Centre environment using multi-wavelength data, focusing on the distribution of gas and dust and the analysis of γ-rays. A refined decomposition of the interstellar medium is achieved through employing a new method in decomposing molecular and atomic line emission, from HI and several CO isotopologue data. By distinguishing the gas in the central molecular zone and the Galactic disk as well as incorporating atomic and molecular contributions, a more accurate description of the gas distribution is derived. This improved gas template allows for a more realistic estimate of cosmic-ray energy density across the Galactic Centre.

The dust thermal emission is fitted using single- and two-component modified Planck functions. A clear deviation from linearity has been observed for the dust opacity as a function of the hydrogen column density, indicating that a simple correlation between dust emission and gas column density is not sufficient.

The second part of the thesis includes γ-ray data from the H.E.S.S. telescopes, an array of imaging atmospheric Cherenkov telescopes. A novel background rejection technique, ABRIR, is developed and implemented within the H.E.S.S. analysis software. ABRIR uses time-based image cleaning and muon tagging to improve signal extraction from high-energy γ-ray data. Its performance is validated through a detailed comparison of Galactic Centre observations with and without the method, showing enhanced source significance and reduced spectral uncertainties.

Finally, the thesis explores the future observational potential of the Southern Wide-field Gamma-ray Observatory (SWGO), a ground-based water Cherenkov detector. Currently under development, SWGO will be the first large-scale water Cherenkov detector in the southern hemisphere. Using updated instrument response functions and simulated observations of the Galactic Centre, the expected performance of various array and tank configurations is assessed. SWGO's sensitivity to WIMP dark matter annihilation is also evaluated.

In summary, this thesis contributes with a new description of the gas and dust in the Galactic Centre, an improved background rejection method for H.E.S.S., and prospect estimates for the Galactic Centre observation with SWGO, to the field of Galactic Centre studies at very-high and ultra-high energies.

Zusammenfassung

Das Galaktische Zentrum ist eine einzigartige und komplexe astrophysikalische Region, die durch dichtes molekulares Gas, helle punktförmige Quellen bei sehr hoher Energie und einen potenziellen PeVatron-Beschleuniger für kosmische Strahlung gekennzeichnet ist. Aufgrund der hohen erwarteten Dichter Dunkler Materie und ihres geringen Abstands ist sie auch ein wichtiges Ziel für die indirekte Suche nach dunkler Materie. Die Komplexität der Region sowie die Herausforderungen, die sich aus Überlagerungen entlang der Sichtlinien und den begrenzten Beobachtungsmöglichkeiten von Gas- und Staubemissionen ergeben, erschweren jedoch die Isolierung von γ-Strahlenquellen und die Untersuchung der der Ausbreitung kosmischer Strahlung.

In dieser Arbeit wird eine umfassende Studie des galaktischen Zentrums unter Verwendung von Daten unterschiedlicher Wellenlängen vorgestellt, die sich auf die Verteilung von Gas und Staub und die Analyse der γ-Strahlung konzentriert. Eine verbesserte Beschreibung des interstellaren Mediums wird durch eine neue Methode zur Zerlegung der molekularen und atomaren Linienemission anhand von HI und verschiedenen CO-Isotopologendaten erreicht. Dabei wird das Gas in der galaktischen Scheibe getrennt vom Gas der zentralen Molek ü lzone betrachtet, was unter Beachtung der atomaren und molekularen Beitrge geschieht. Somit wird eine verbesserte Beschreibung der Gasverteilung erreicht, welche es ermglicht eine realistischere Schtzung der Energiedichte der kosmischen Strahlung im gesamten galaktischen Zentrum zu berechnen.

Die thermische Emission des Staubes wird mit ein- und zweikomponentigen modifizierten Planck-Funktionen gefittet. Für die durch Staub verursachte Opazitt als Funktion der Wasserstoffsäulendichte wurde eine deutliche Nicht-Linearität beobachtet, was darauf hinweist, dass eine einfache Korrelation zwischen Emission des Staubes und Gassäulendichte nicht ausreicht.

Der zweite Teil der Arbeit umfasst γ-ray-Daten des H.E.S.S.-Teleskope, einem Array von abbildenden atmosphärischen Cherenkov-Teleskopen. Eine neuartige Technik zur Unterdrückung des Untergrunds, ABRIR, wurde entwickelt und in die Software zur Analyse von H.E.S.S. integriert. ABRIR verwendet zeitbasierte Bildreinigung und Myonen-Tagging, um die Signalextraktion aus hochenergetischen γ-Strahlen-Daten zu verbessern. Die Leistungsfähigkeit des Verfahrens wird durch einen detaillierten Vergleich von Beobachtungen des galaktischen Zentrums mit und ohne ABRIR validiert, der eine verbesserte Signifikanz der Quellen und geringere spektrale Unsicherheiten zeigt.

Schließlich wird in dieser Arbeit das künftige Beobachtungspotenzial des Southern Wide-field Gamma-ray Observatory (SWGO), eines Wasser-Tscherenkov-Detektor Arrays, untersucht. SWGO, das sich derzeit in der Entwicklung befindet, wird der erste großflächige Wasser-Tscherenkov-Detektor auf der südlichen Hemisphäre sein. Anhand von aktualisierten nstrumentenresponsefunktionen und simulierten Beobachtungen des galaktischen Zentrums wird die erwartete Leistung verschiedener Array- und Tankkonfigurationen bewertet. Zudem wird die Sensititvitt von SWGO f ü r WIMP-Annihilationen dunkler Materie ausgewertet.

Zusammenfassend lässt sich sagen, dass diese Arbeit mit einer neuen Beschreibung des Gases und des Staubs im galaktischen Zentrums, einer verbesserten Methode zur Unterdrückung des Untergrunds für H.E.S.S. und Abschtzungen f ü r die Beobachtung des galaktischen Zentrums mit SWGO, einen Beitrag zur Erforschung des galaktischen Zentrums bei sehr hohen und ultrahohen Energien leistet.

List of Abbreviations

Sgr A* Sagittarius A*

AGN Active Galactic Nuclei

APEX Atacama Pathfinder Experiment

ATCA Australia Telescope Compact Array

CC Central Cavity

CL Confidence Level

CMB Cosmic Microwave Background

CMZ Central Molecular Zone

CNR Circumnuclear Ring

CR Cosmic ray

CTAO Cherenkov Telescope Array Observatory

DAQ Data Acquisition

DM Dark Matter

DSA Diffusive Shock Acceleration

EAS Extensive Air Shower

EBL Extragalactic Background Light

EM Electromagnetic

EVF Extended Velocity Features

FF Filling factor

FIR Far-Infrared

FoV Field of View

GC Galactic Centre

GMC Giant Molecular Cloud

GoF ImPACT Goodness of Fit

GRB Gamma-Ray Burst

HE High Energy

HFI High Frequency Instrument

Hi-GAL *Herschel* infrared Galactic Plane Survey

IACT Imaging Atmospheric Cherenkov Telescope

IR Infrared

IRAS Infrared Astronomical Satellite

IRF Instrument Response Function

IRF Instrument Response Function

LAT Large Area Telescope

MBB Modified Black-Body

MC Monte Carlo

MHD Magnetohydrodynamic

MIR Mid-Infrared

NRO Nobeyama Radio Observatory

NSB Night Sky Background

NSC Nuclear Star Cluster

NSD Nuclear Stellar Disk

p.e. Photoelectrons

PeVatron PeV accelerator

PMT Photomultiplier

PWN Pulsar Wind Nebula

RMS Root Mean Square

SED Spectral Energy Distribution

SMBH Supermassive Black Hole

SNR Supernova Remnant

SUSY Supersymmetric

SVC Support Vector Classifier

UHE Ultra High Energy

UV Ultraviolet

VHE Very High Energy

WCD Water Cherenkov Detector

WIMP Weakly Interacting Massive Particle

Contents

Preface

The work presented in this Thesis is a result of collaboration work from many people. Here I highlight my personal contributions to each of the projects:

Chapter 3 and Ren et al. [173]:

- I performed the data analysis of the molecular line emission data cubes from the Nobeyama Radio Observatory (NRO) and the Atacama Pathfinder EXperiment (APEX)-SEDIGISM survey. While the line decomposition algorithm was provided by Quentin Remy, I carried out the downsampling of each of the CO maps, applied baseline corrections to the emission profiles, and conducted the detection and fitting of the individual emission lines.
- I compared the brightness temperature of ^{13}CO to ^{12}CO, as well as C^{18}O to ^{13}CO, across different velocity ranges. Through this analysis, I identified a clear change in the $T^{10}_{^{13}\mathrm{CO}}$ versus $T^{10}_{^{12}\mathrm{CO}}$ relation at lower velocities. Following extensive discussions with the co-authors, we decided to incorporate the $T^{10}_{^{12}\mathrm{CO}}/T^{10}_{^{13}\mathrm{CO}}$ ratio into the foreground gas separation procedure. This approach successfully separated most of the Galactic disk emission from that of the central molecular zone, using clustering methods processed by S. Ravikularaman.
- I processed the dust thermal emission data from the Herschel Hi-GAL survey, APEX, and Planck HFI for the Galactic Centre region. This involved reprojection of the maps to a common geometry and correction for CO contamination in three of the HFI maps. I then fitted both single- and two-component Modified Black-body functions, initially using all the maps, and in a subsequent step, excluding the HFI maps due to their coarser angular resolution.

Chapter 6 and Olivera-Nieto et al. [151]:

- With the help from L. Olivera-Nieto, I produced the H.E.S.S. performance in rejecting background events for the "hybrid" case, which was included in the appendix of the publication [151].
- I presented the performance of the Algorithm for Background Rejection using Image Residuals (ABRIR), along with the ongoing improvements at that time, at the 7th Heidelberg International Symposium on High-Energy Gamma-Ray Astronomy. I also summarised the work in the corresponding conference proceedings [172].
- I integrated the ABRIR algorithm for background rejection into the H.E.S.S. Analysis Package (HAP), writing it in `C` language, with the help of L. Olivera-Nieto for providing the original source code, and V. Marandon for understanding the logic flow in HAP. I run the test on simulated γ-rays, background events, and on crab observations. Then, I also applied ABRIR to a subset of Galactic Center data, and compared the result of the analysis with and without ABRIR algorithm.

Chapter 7:

- I simulated the Galactic Centre region as observed by SWGO using `Gammapy` and the instrument response functions (IRFs) corresponding to each of the candidate configurations developed during SWGO's Research & Development phase. While a tutorial script for simulating sources was provided by L. Olivera-Nieto, I adapted and extended it for the specific case of the Galactic Centre sources. For each IRF update, I performed hundreds of simulations per configuration to evaluate their performance.
- With the help of J. Djuvsland, I conducted the study about the dark matter sensitivity for SWGO, again with considering all the candidate configurations. For each IRF update, I computed the expected upper limits on the velocity-weighted annihilation cross section, repeating the calculations hundreds of times for each configuration, dark matter annihilation channel, and dark matter mass. These results contributed to the design selection process during the SWGO development phase.
- I contributed to two conferences with results from this work. The first was a poster presentation at the 38th International Cosmic Ray Conference (July 2023), and the second was a contributed talk at the 8th Heidelberg International Symposium on High-Energy Gamma-Ray Astronomy (September 2024), where I presented the outcomes of the simulation studies [171, 174].

Chapter 1

Introduction

This dissertation focuses on the central ∼200 pc of the Milky Way. At the heart of this region lies Sagittarius A* (Sgr A*), a supermassive black hole. Its existence was recently reaffirmed by the Event Horizon Telescope Collaboration, which captured the first image of its shadow. In the inner 200 pc, many complex gas structures exist, including the central molecular zone (CMZ), a collection of massive molecular clouds. This region, primarily composed of dense molecular gas, exhibits extreme physical conditions, including elevated density, temperature, turbulence, pressure, and metallicity, when compared to local molecular clouds.

The Galactic Centre (GC) region is also the most promising region for the observation of dark matter (DM) annihilation signal, because of the expected high DM density. DM composes around 85% of the matter in the Universe. One of the most popular candidates of DM is the weakly interacting massive particles (WIMPs), which are non-baryonic particles interacting only gravitationally and through weak forces with standard model particles. The complexity of the GC region is discussed in detail in **Chapter 2**.

From the perspective of very-high-energy (VHE) astronomy, γ-ray emission from the GC is primarily attributed to the interaction of accelerated cosmic rays with the interstellar medium, including both gas and radiation fields. On the other hand, WIMPs can also self-annihilate in dense regions, producing TeV γ-rays. **Chapter 4** gives an introduction to the γ-ray production mechanisms, their detection methods, and also gives a review about particle acceleration. Diffuse γ-ray emission is observed throughout the Galactic plane, forming a complex foreground and background against which point-like and extended γ-ray sources must be identified. This, combined with the large number of overlapping sources within the GC region, makes it one of the most intricate and challenging regions to study in the Galaxy. The following paragraphs provide a brief overview of the observational techniques used for detecting γ-rays and a historical review of the GC observations.

VHE γ-rays can be detected using both space-based and ground-based observatories. Satellite telescopes are capable of directly detecting the primary γ-ray flux via pair production, typically covering an energy range from a few tens of MeV up to several hundred GeV. On the ground, however, the Earth's atmosphere absorbs the primary γ-rays. These photons interact with atmospheric particles via pair production, initiating a cascade of secondary particles known as an extensive air shower (EAS). As the secondary particles travel through the atmosphere at velocities exceeding the speed of light in the medium, they emit short flashes of blue light, referred to as Cherenkov radiation, which can be detected by ground-based telescopes.

Two main techniques have been developed for ground-based γ-ray detection, both based on the observation of Cherenkov radiation emitted by secondary particles in particle showers. The first technique employs Imaging Atmospheric Cherenkov Telescopes (IACTs), which consist of highly sensitive and fast-response cameras mounted on large reflective mirror dishes. The second technique uses Water Cherenkov Detector (WCD)

arrays, which are composed of large tanks filled with purified water and instrumented with photon detectors installed at the bottom.

Existing IACTs are optimised for detecting γ-rays in the energy range of a few tens of GeV up to a few tens of TeV, whereas WCDs are sensitive to higher-energy photons, from several TeV to several hundreds of TeV. A detailed discussion of the advantages and limitations of both techniques is provided in **Chapter 4**. Importantly, the two methods are highly complementary: WCDs offer wide field-of-view coverage and operate nearly continuously, making them ideal for monitoring the VHE sky, while IACTs provide superior angular resolution, essential for high-precision morphological studies.

One of the earliest detections of VHE γ-ray emission from the GC was reported by EGRET onboard the Compton Gamma-Ray Observatory (CGRO) [129], within the 100 MeV to GeV energy range. EGRET identified a central source spatially coincident with the GC, with a brightness approximately 13 times that of the Crab pulsar. However, the observed diffuse emission did not correlate with the distribution of CO-traced molecular gas.

Subsequently, compelling evidence for particle acceleration in the GC region emerged from the discovery of the large-scale Fermi bubbles by the Large Area Telescope onboard *Fermi* satellite (*Fermi*-LAT) [4, 198]. These structures extend up to 10 kpc above and below the Galactic plane. While the origin of the particles energising these giant outflows remains unclear, the processes responsible must be located within the central few hundred parsecs of the GC, motivating continued investigation of this complex region.

In the early 2000s, several IACTs detected VHE γ-ray emission from the direction of the GC. CANGAROO-II [208] reported a sub-TeV γ-ray excess at energies above 250 GeV, with a flux approximately one order of magnitude lower than that of the Crab pulsar at 1 TeV, and spatially consistent with the earlier EGRET detection. However, their measured spectrum is very steep, contradicting all observations made later. The High Energy Stereoscopic System (H.E.S.S.) subsequently reported the detection of VHE γ-ray emission from the direction of Sgr A* [10, 12].

In a 2016 analysis using an expanded dataset of approximately 250 hours, H.E.S.S. investigated both the central source and the surrounding diffuse Galactic ridge emission. The study provided strong evidence that a candidate PeV accelerator (PeVatron) is located in the region. The γ-ray emission was separated into two components: one associated with the central point source, spatially coincident with Sgr A*, and another corresponding to the more extended CMZ. Notably, while the central source spectrum exhibits a cutoff at high energies, the CMZ emission shows no such feature, extending up to at least 100 TeV. This observation suggests the presence of ultra-high-energy (UHE) particles, likely accelerated to PeV energies near the GC, which then propagated through the dense molecular environment and interacted with the interstellar gas to produce VHE γ-rays.

The ground-based IACTs mentioned above are located in the Southern Hemisphere, which provides optimal visibility of the GC region. Nonetheless, several Northern Hemisphere observatories also reported tentative detections of γ-ray emission from the GC region in the early 2000s. The Whipple 10 m telescope [116] observed a possible TeV γ-ray signal from the direction of the GC, based on 26 hours of data, with a reported significance of 3.7σ. The measured flux corresponded to approximately 40% of the Crab Nebula flux at 2.7 TeV. Slightly later in 2006, the MAGIC telescope [17] also reported an excess in the direction of Sgr A*, consistent with the results from H.E.S.S.. However, due to the limited exposure of around 24 hours and the use of only a single 17-m dish at the time, the statistical significance of the detection remained low.

So far, H.E.S.S. has provided the most detailed study of the GC region at VHE [88, 89]. In [88], the CR density distribution in the Galactic ridge was estimated as a function of distance from the GC, and the resulting profile was best fitted with a $1/r$ dependence. In [89], the GC γ-ray emission was decomposed into several components. After subtracting the two brightest point sources, the central source and the composite supernova remnant G0.9+0.1, the remaining diffuse emission was modelled using a CS line-emission template, which traces the densest regions of molecular gas in the CMZ. Additionally, two more components were empirically introduced: a central component and a large-scale component, both required to adequately fit the data.

The limitations of the models presented in [89] were primarily due to the absence of a foreground/background gas template and the restricted molecular gas template available for the CMZ. In this dissertation, we aim to construct a gas column density template for the GC region, with introducing the separation of the Galactic disk gas from the CMZ. The contribution from Galactic disk gas could account for up to ∼50% of the total gas mass. Moreover, in the absence of disk gas, atomic gas alone could contribute as much as ∼30%. These contributions were examined in our CMZ Paper I [173], where we reported a new gas column density distribution, with including HI and several CO isotopologue line emission data. These findings will be discussed in detail in **Chapter 3**.

In addition, a three-dimensional gas distribution would enable a more accurate determination of the CR density across the region. The methodology used to derive the 3D gas structure in the CMZ will be presented in a forthcoming publication (CMZ Paper II), and is also described in this dissertation in **Chapter 3**.

A reanalysis of the GC region with H.E.S.S. is now opportune, not only due to the availability of an improved gas density template, but also because of several significant advancements since the previous H.E.S.S. publications [88, 89]. One major improvement is the inclusion of data from CT5, the largest telescope in the H.E.S.S. array, which enhances hadron background rejection. Additionally, the H.E.S.S. analysis chain has undergone important updates: new Monte Carlo γ-ray simulations have been introduced, along with improved calibration and time-based cleaning techniques for low-level image processing. At the high-level analysis stage, the workflow has been migrated to a more modern and flexible framework, Gammapy. This transition also allows for a more sophisticated approach to background estimation, using a template-based method in three dimensions, including energy as an additional axis [135].

Chapter 5 introduces the H.E.S.S. telescope array and provides an overview of the data analysis workflow, which includes the H.E.S.S. Analysis Package (HAP) for low-level processing and the use of the more modern `Gammapy` software for high-level analysis. In this chapter, the future future Southern Wide-field Gamma-ray Observatory (SWGO) is also introduced, as well as, the various unit WCD and array layout configurations studied to test its expected performance.

Chapter 6 presents the conventional γ/hadron separation techniques, followed by the development of a new background rejection method, known as ABRIR. This new method takes advantage of CT5 images, where Cherenkov light from muons can be detected. Muons are more prevalent in hadron-induced air showers than in electromagnetic ones, particularly at energies above 1 TeV. Thus, the presence of muon light serves as a powerful veto to discriminate hadron-like events. ABRIR leverages time-based image cleaning to identify isolated clusters of pixels in the CT5 images that are characteristic of muon signatures. The performance of the ABRIR method, specifically as applied to observations of the GC region, will be presented and evaluated.

Lastly, in **Chapter 7**, the expected performance of SWGO for observations of the GC

region is investigated. This includes simulations based on updated instrument response functions (IRFs) for a variety of candidate detector designs and array configurations. In the second part of this Chapter, SWGO sensitivity to DM annihilation signals is simulated. Sensitivity estimates are derived through likelihood-based hypothesis testing, comparing configurations across different DM masses and annihilation channels. These studies contributed to the configuration evaluation process undertaken during the SWGO R&D phase.

A summary of the PhD work is given in **Chapter 8**, together with an outlook for future plans for the study of the GC region in the highest energy ranges.

Chapter 2

The Galactic Centre Environment

The 'Milky Way', '*Via Lactea*' in Latin, or '*Silver River (银河)*' in Chinese, beautifully names our galaxy, describing its shape as we see it in the sky. Figure 2.1 is a picture of the night sky at the site of H.E.S.S. telescopes, in Namibia [100], where part of the Milky Way can be seen. It extends to 26.8 ± 1.1 kpc in diameter [84], but the Dark Matter component could extend further [54]. It is estimated to have of the order of 10^{11} stars, most of them in the Galactic disk. The shape of the galaxy is a barred spiral galaxy, with a diameter of ∼25 kpc, and the height of the Galactic disk is ∼300 pc. The Sun is located in one of the spiral arms in the disk, the Local arm, at ∼ 8.1 kpc from the centre. See, for example, [43] and [187] for an overview of the Milky Way and its evolution and structure.

The *Galactic Centre* (GC) is an extremely complex region composed of many kinds of astronomical sources, such as the supermassive black hole Sagittarius A* (Sgr A*), massive stars, supernova remnants, stellar clusters, and giant molecular clouds, where the gas is very dense and turbulent. In this chapter, general properties of the central few hundred pc of the Milky Way are described, followed by the characteristics of the gas in the *central molecular zone* (CMZ), a complex of giant molecular clouds extending up to ∼200 pc in the GC region.

This chapter gives a general description of the GC region, explaining each of the known astronomical components, in Section 2.1. Section 2.2 focuses on the CMZ, the physical properties of the gas in it, and the gas geometry. Section 2.3 describes the expected dark matter content in the GC region. Finally, Section 2.4 gives the multiwavelength observations of the GC. A summary and connection to the next chapter is given in Section 2.5.

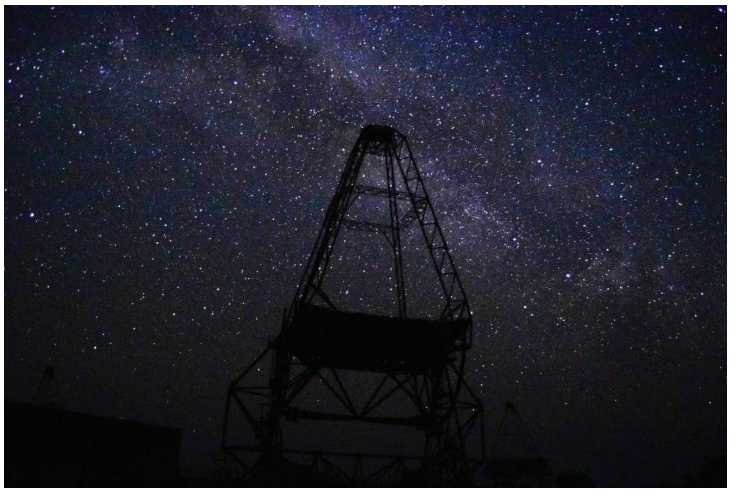

Figure 2.1: Photograph of the night sky at H.E.S.S. site, Namibia, where the Milky Way is seen as a bright white path on the sky. Credits: Helena Ren.

2.1 General view

The central region of galaxies has always been a very interesting region for astronomers, since galaxy formation and dynamics can be studied from the observation of these regions. The GC of the Milky Way is the nearest galactic nucleus that we can observe, and it can be considered as our "local" laboratory. However, it is very hard to understand the real geometry and structure of the GC region, not only due to our location in the Galactic disk, but also because of the severe interstellar extinction along the line of sight, and the strongly non-circular motion of the interstellar gas observed.

Let's start describing the GC from the centre towards the CMZ. At the very centre of the Milky Way, there is a *supermassive black hole* (SMBH), called Sagittarius A* (Sgr A*). This central source was originally identified in radio wavelength as a compact non-thermal source [76]. The mass of this SMBH is $M \sim 3.4 \times 10^6$ M$_\odot$ and has been measured through the Kepler motion of neighbouring stars over more than 10 years [182]. The first ever picture of the central SMBH has been reported recently by the Event Horizon Collaboration [69] (see Figure 2.2). A small accretion disk was observed by [140], at ∼0.01 pc, primarily composed of 10^4 K gas. Stars orbiting around the SMBH in the inner region of about 0.04 pc are called the *S-stars*.

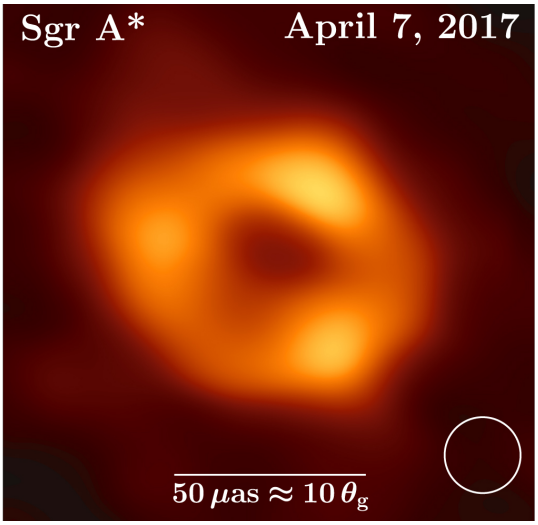

Figure 2.2: Event Horizon Telescope image of the SMBH Sgr A*. The diameter of the ring is $\sim 51.8 \pm 2.3$ μas, approximately 10 times the angular gravitational radius θ_g. Figure from [69].

A massive star cluster is in the central parsec in close vicinity of Sgr A*, called the *nuclear star cluster* (NSC), with a total mass of $\sim 10^6$ M$_\odot$ and extending to several parsecs [181]. NSCs have been observed in most other galaxies, too, and they are the densest known star clusters in the universe. It has also been observed that the NSC of the Milky Way has a stellar cusp at 0.22±0.04 pc [180]. The NSC has over a million stars, most of them are old giants with masses up to 10^4 M$_\odot$. Several massive stars are orbiting within 0.5 pc in a clockwise stellar disk as seen from Earth, known as the *nuclear stellar disk* (NSD) [124, 218]. These massive young stars are collectively called the *Young Nuclear Cluster*, which has an inner cutoff at ∼0.04 pc.

The *circumnuclear disk*, or more appropriately the *Circumnuclear ring* (CNR), is a dense ring of molecular gas with an inner radius of 1.5 pc and extending up to 7 pc at

negative galactic longitudes [87, 148]. It is orbiting in projection in a counterclockwise direction. The molecular gas in the CNR has been measured to have high kinematic temperatures of $T_k \sim 200 - 300$ K, possibly heated by shocks [35]. The estimated hydrogen number density in the CNR is between 10^4–10^6 cm^{-3}.

The CNR has a relatively evacuated *central cavity* (CC) with a radius of around 1–2 pc. This region contains ∼hundreds of $M_\odot$ of neutral, partially ionized, ionized, and molecular gas [44]. The CC is referred to as the *ionized cavity* or *Sgr A West* H_{II} region sometimes in the literature. Three filamentary structures were observed inside the CC, known as the *mini-spiral*: the Eastern, Northern, and Western Arms [see for example 207, 221, and references therein]. An image of the mini-spiral is shown in Figure 2.3. These filaments contain tens of $M_\odot$ of ionized gas and warm dust [71]. Additionally, a schematic plot of the inner 2 pc of the GC region is illustrated in Figure 2.4, adapted from [193].

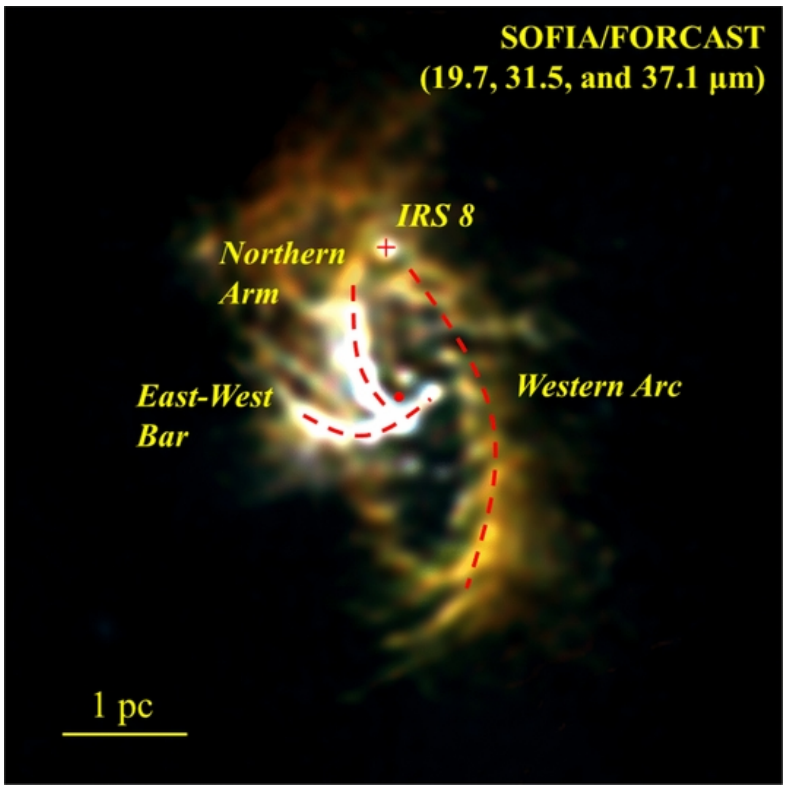

Figure 2.3: SOFIA observation of the mini-spiral. Figure adopted from [118].

In projection, at ∼2.1 pc away from Sgr A*, a nonthermal radio shell of ∼10 pc scale called *Sgr A East* was observed [61] with elongated shape. It is most probably a supernova remnant (SNR), and its western side overlaps with the Sgr A West H_{II} region or the CC, where the Western Arm seems to merge smoothly into the shell. The SNR is in turn surrounded by a ∼20 pc diameter radio halo, composed of warm ionized gas and relativistic particles.

A belt of molecular clouds, stretching over ∼30 pc around Sgr A East is found. The brightest among these clouds are the M−0.02−0.07 (or 50 km s^{-1}) and M−0.13−0.08 (or 20 km s^{-1}) giant molecular clouds (GMCs), located east and south of Sgr A East, respectively. Both GMCs have a similar dimension scale of ∼15 pc, and a few 10^5 $M_\odot$ of hydrogen mass. However, their position in the line of sight is still controversial, and evidences that these clouds are interacting with the SNR Sgr A East and the mini-spiral

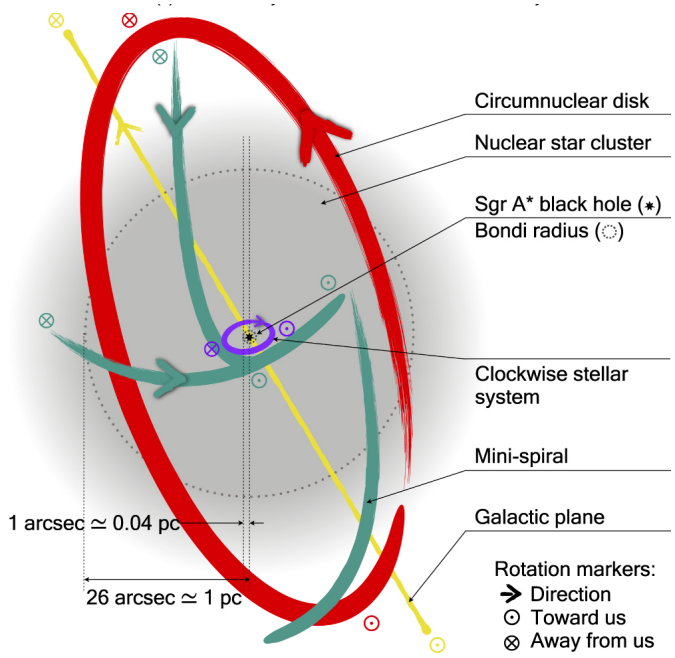

Figure 2.4: Schematic drawing of the inner 2 pc of the GC in the plane of the sky. A description of each of the elements in this plot can be found in the text. Figure adapted from [193].

were suggested by several authors [as is summarised by 71, 95].

Further away from the centre, at around ∼180 pc, the gas tends to concentrate in the so-called CMZ. This structure has an asymmetric torus shape, extending in projection to ∼250 pc at positive longitudes and ∼150 pc at negative longitudes. The total mass in the CMZ is estimated to be $2-6\times10^7$ $M_\odot$ [72], corresponding to $3-10\%$ of the total molecular mass in the galaxy (6.5×10^8 $M_\odot$ [176]). Inside the CMZ, two young massive stellar clusters can be found: the Arches and Quintuplet, both formed $\lesssim 5$ Myr ago.

The atomic gas in the entire region extends up to ∼1.5 kpc, confined in a tilted layer, and it is referred to as the *H_I Galactic bulge disk*. The Galactic bulge can be defined as the central around 3 kpc of the Milky Way, this radius corresponds roughly to the inner boundary of the Galactic disk. Between ∼1.5 kpc and ∼3 kpc, the interstellar region is largely devoid of gas. Inflow of gas from the Galactic disk toward the CMZ is in the shape of two main dust lanes, closely parallel with the major axis of the Galactic bar. Similar structures can be clearly seen in the face-on spiral galaxies, however, due to our viewing angle, the identification of dust lanes in the Milky Way is more challenging. A schematic plot of the CMZ and the dust lanes is shown in Figure 2.7.

2.2 The Central Molecular Zone

Now let's focus on the CMZ. It has been extensively studied and observed at multiple wavelengths. However, there is no clear picture of its three-dimensional structure so far. The CMZ is composed mainly of molecular hydrogen, which is the most abundant molecule in the universe [194]. Yet, H_2 is very difficult to detect, due to its symmetric

molecular shape [90, 213]. Hence, emission from other abundant molecules is used to trace the molecular gas. The molecular emission lines of the gas are related to the H_2 column density by a conversion factor.

H_2 molecules can be formed by recombination of hydrogen atoms on the surface of interstellar dust grains [213]. They can be photo-dissociated rapidly by UV radiation or by collisional dissociation. So, H_2 can only survive in dark interiors of the interstellar clouds, shielded from UV photons, where it is cold enough to avoid collisions. Therefore, in the more diffuse regions, a larger fraction of atomic hydrogen is expected.

Consequently, our understanding of the CMZ today is based on the measurement of different observables, like observations of the atomic hydrogen 21 cm line emission [130], emission lines of molecular species [see for example 109, 179, 217] and dust thermal emission in the infrared [see for example 136]. At high energies, γ-ray measurements were provided by *Fermi*-LAT [52] and H.E.S.S. [88, 89].

The CMZ has a torus shape with an average radius of 180 pc, therefore, it is sometimes also referred to as the *180-pc molecular ring*. The torus is slightly twisted, which in projection has a $\infty-$shape on the sky, visible in sub-millimeter dust emission. This can be seen, for example, in the image provided by the Herschel Telescope, a Space Observatory sensitive to the far infrared wavebands 55–672 μm (see Figure 2.5).

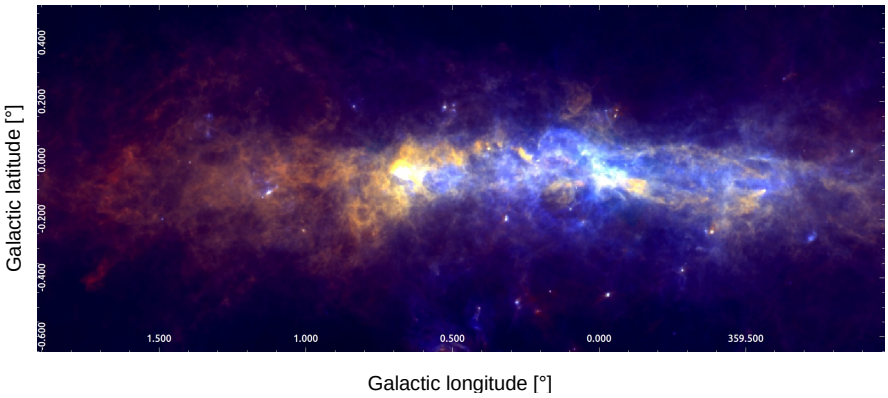

Figure 2.5: Herschel view of the inner 3° of the Milky Way. In red is the 250 µm band, green is the 160 µm band, and blue is the 70 µm band. We can clearly notice the twisted ring shape of the CMZ.

The CMZ is not an isolated structure, instead, gas constantly inflows from the Galactic disk. The dynamical landscape of the inflow can be studied via the spectroscopic emission of molecules, such as carbon monoxide CO. Molecules can emit photons due to rotational transitions between different quantum levels. The CO emission depicted in Figure 2.6 shows the distribution of molecular gas structures in the longitude-latitude $(l-b)$ space and in the longitude-velocity $(l-v)$ space.

With the help of the velocity information, many overlapping structures in the $(l-b)$ space can be separated in the $(l-v)$ space. In Figure 2.6, horizontal dotted black lines in the $(l-v)$ space are the spiral arms in the Galactic disk. The parallelogram shape marked in a dashed red line indicates the emission from the CMZ. The dust lanes are formed by gas inflow, and can be identified in the $(l-v)$ space indicated by the dashed black lines, and tagged as the Near dust lane, the Far dust lane, and Secondary dust lanes. Another phenomenon related to the inflow is the extended velocity features (EVF). These are also indicated in thicker dashed lines as vertical structures. EVFs are possibly due to the collision between the inflow gas with either the gas in the CMZ or gas originally from the other dust lane that has been 'overshot' the CMZ. The most prominent of the EVFs is the structure located at $\approx 5.4°$, also known as Bania's Clump 2 [22].

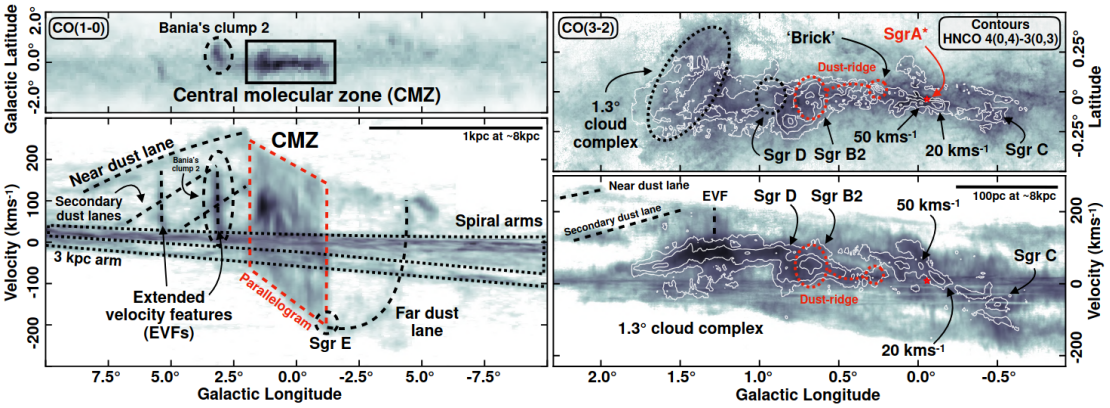

Figure 2.6: $(l-b)$ and $(l-v)$ space plots of the CO molecular line emissions. The different components (Spiral arms, dust lanes, EVFs, and GMCs in the CMZ) from the line of sight of the GC can be further identified in the velocity space. Figure adopted from [95].

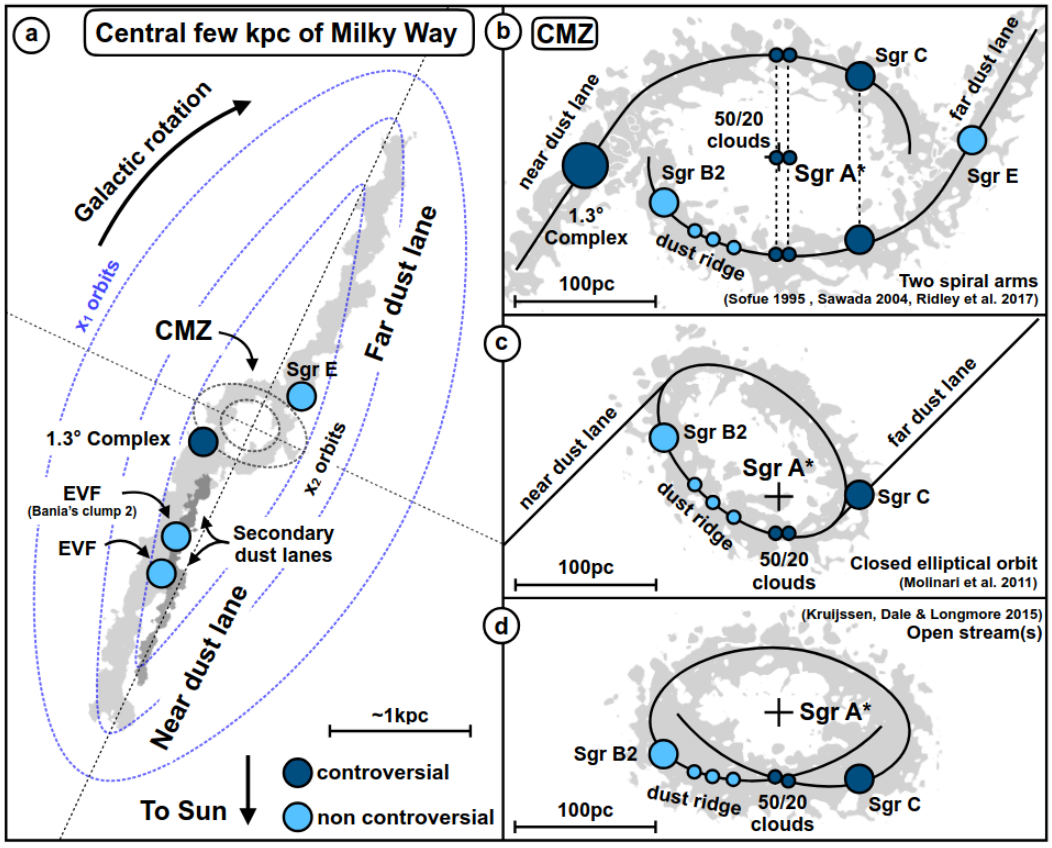

Figure 2.7: Left: Face-on schematic view of the central few kpc of the GC. The dust lanes are oriented in parallel with the Galactic bar major axis, while the major axis of the CMZ is perpendicular to it. The x_1 and x_2 orbits are the two families of stable orbits for gas rotation under a bar potential. The possible location of some of the gas structures is indicated, such as the EVFs and the Sgr E cloud. The 1.3° Complex cloud has a more controversial location, therefore indicated by a darker blue colour. Right: three different models for the geometry of the CMZ. Figure adopted from [95].

The origin of the CMZ is basically the inflow driven by the Galactic bar. Its size and distribution, as well as the evolution of the molecular clouds, are controlled by the

gravitational potential of the bar and other components in the GC: the potential of the central SMBH Sgr A*, the NSC, and NSD. Gas flow in the barred potential follows ballistic orbits, mainly in two families of stable closed orbits, x_1 and x_2, as shown in the left panel of Figure 2.7. x_1 orbits are highly elongated in the direction of the bar major axis, whereas x_2 orbits are mildly elongated in the direction perpendicular to the bar major axis. x_2 orbits exist only when the potential possesses an inner Lindblad resonance [20, 46]. Hydrodynamical simulations show that the gas in the outer parts of the bar follows roughly the x_1 orbits, while dissipation processes drift the gas inwards along a sequence of x_1 orbits. The x_1 orbits become more elongated when closer to the center, until they self-intersect. The gas then transitions onto x_2 orbits through large-scale shocks, which correspond to the dust lanes.

2.2.1 Properties of the central molecular zone

Several properties of the CMZ were observed and computed by a long list of authors [see for example 95, and references therein]. Here is a brief summary of our current knowledge.

(a) The extension of the CMZ in longitude ranges between $-1.0^\circ \lesssim l \lesssim 1.7^\circ$ and it has a radius of $R \simeq 100 - 200$ pc.

(b) Some of the most prominent GMCs in the CMZ, from negative to positive longitudes are: the 1.3° cloud complex, Sgr D, the "dust ridge" clouds which includes Sgr B2, G0.253+0.016 (or "the Brick"), Sgr A clouds (the 50 km s^{-1} and 20 km s^{-1} clouds) and Sgr C (see Figure 2.6 for the location of these GMCs in the $(l-b)$ and $(l-v)$ spaces). Some authors suggest that the 1.3° cloud complex is not in the CMZ ring, but located at the end of the near dust lane, where it merges with the CMZ.

(c) The gas density has been estimated to be much higher in the CMZ than in local clouds. Typical column densities estimated from dust thermal emission is $\sim 10^{23}$ cm^{-2}, peaking at $> 10^{24}$ cm^{-2} towards Sgr B2. Measurements using molecular line emissions are compatible with dust measurements, and the typical volume densities in clouds are between $\sim 10^3 - 10^4$ cm^{-3}.

(d) The cloud dust temperatures in the CMZ range from ∼20 to 25 K, according to single black body component Planck fit estimations. The lowest temperatures are associated with the densest cores. The dust opacity index β ranges between 1.8−2.4, being steeper than in local clouds.

(e) The gas temperature, on the other hand, was measured to be higher $T_{\rm gas} \sim 30 - 100$ K, using molecular line tracers. Thus, the gas and the dust in the CMZ clouds are not thermally coupled. The reasons for such high temperatures, the heating of the gas, and the decoupling are still unknown and under study.

(f) The highest velocities observed in the molecular gas emission in the CMZ are of the order of $|v| \sim 250$ km s^{-1}, as can be seen in Figure 2.6. The velocity dispersion (line width of the molecular emission) is well above the measurements in the Galactic disk, which indicates a higher level of turbulence. Possible drivers of the turbulence are the gas inflow from the bar, acoustic instabilities, gravitational instabilities, and stellar feedback.

(g) A higher CR ionization rate has been observed, in the range of $0.2 - 2 \times 10^{-14}$ s^{-1}, which is about 10−100 times the CR ionization rate in local clouds [108, 119, 146]. The origin of CRs remains debated, with possible contributors being the high supernova rate, the central NSC, and Sgr $A^{\star}$, the massive stellar clusters Arches and Quintuplet, and H_{II} regions.

(h) The chemical composition of the CMZ is highly influenced by the high CR ionization, high density, dust temperature, strong shocks, and bright X-ray emission. The molecular chemistry is so rich that even in low-density regions, new molecules are being discovered. Some of the molecules commonly used for tracing star-forming regions or shocks are not useful in the CMZ since they do not correlate with dust observations, and some are basically spread over all dense molecular regions.

(i) The star formation rate in the CMZ is $\sim 0.07 M_{\odot}$ yr^{-1}, and therefore much lower than in the Galactic disk. Whether it is a quasi-continuous star formation or if it was higher or lower in the past is under debate.

(j) Finally, the study of the magnetic field strength and shape in the CMZ has recently started. Measurements of the bright non-thermal filaments and large-scale B-field were published by [97]. While, details about the magnetic field on small scales can be found in [153].

In this work, we estimate the total gas mass in the CMZ using CO isotopologues and H_I emission, to take into account both the molecular and the atomic gas mass, respectively. We then further compare the results from the atomic and molecular gas emission to the dust thermal emission to study the dust opacities. A detailed explanation is given in our recently published paper [173], and also in the next chapter.

2.2.2 Geometry of the central molecular zone

The three-dimensional geometry of the CMZ is currently not well understood, and many different models have been considered for simulation purposes [as is explained in 95]. The three right panels in Figure 2.7 show the 3D structure models and list the authors who suggested/used them. In the first interpretation, the gas in the CMZ is organized into two spiral arms, and within this model, there are different options for the location of the individual GMCs. The second interpretation proposes that the gas is in an elliptical ring with the gas streams located at the near and far sides of the ellipse. The third model distributes the gas in a ballistic open orbit with a *prezel*-shape. The latter, however, does not give an explanation about how the dust lanes and other structures connect to the CMZ.

An attempt to determine the 3D distribution of the CMZ using the $(l - b - v)$ space and the absorption of OH molecule emission compared to CO emission lines was proposed by [179]. Later [217] followed their method, with more recent data from the Southern Parkes Large-Area survey in Hydroxyl (SPLASH) with improved sensitivity to four OH ground-state transitions. The advantage of this method is its independence of a dynamical model of the CMZ. Both studies confirmed a bar-like structure in the CMZ. [217] obtained a 3D map of the molecular gas, in six slices in latitude $b = (-0.375°, -0.25°, -0.125°, 0°, 0.125°, 0.25°)$, and the spatial resolution in longitude is 15.4 arcmin. The sparse resolution of the 3D gas map, however, cannot resolve most of the clouds and structures in the CMZ.

2.3 Dark matter component of the Galactic Centre

The concept of "Dark Matter" (DM) emerged in the 1930s when Fritz Zwicky observed that galaxies in the Coma cluster moved too fast to be held together by their visible mass, suggesting the presence of unseen matter [222]. Vera Rubin's work in the 1970s further solidified this idea by confirming similar phenomena in spiral galaxies [178]. It is now widely believed that $\sim 85\%$ of the total content of matter in the universe is made of DM.

The GC is the closest target to detect a DM signal, which benefits its detections since higher fluxes are expected compared to extragalactic measurements. It is expected to contain a large amount of DM, as modelled by DM density distribution profiles, such as the Einasto [195] and NFW [141] profiles.

2.3.1 Thermal relic density of cold dark matter particles

In the early universe, all the particles composing it were in thermal contact with each other, and the particle properties were evolving with time [26]. As the universe expanded, the number density of particles, n, decreased, and the thermal contact was no longer maintained. This also reduced the interaction rate $\Gamma = n\sigma v$, where v is the particle velocity and σ is its cross section. The particle annihilation became inefficient for scales below the Hubble parameter (which has dimensions of 1/time), and this epoch is called the "freeze-out", since the particles were decoupled. Such particles maintained their abundance, freezing to the relic density. For particles with different masses, the decoupling time also differed because of the distinct interaction processes.

The relic of the cold (non-relativistic) DM particles can be approximated as

$$\Omega h^2 \sim \frac{3 \times 10^{-27} \mathrm{cm}^3 \mathrm{s}^{-1}}{\langle \sigma v \rangle}, \tag{2.1}$$

where $\langle \sigma v \rangle$ is the thermally averaged velocity weighted annihilation cross section, or the thermal relic cross section.

A recent measurement by the Planck Collaboration of the relic density for cold DM is $\Omega h^2 = 0.120 \pm 0.001$ [161], which gives a thermal relic cross section $\langle \sigma v \rangle \sim 3 \times 10^{-26}\ \mathrm{cm}^3 \mathrm{s}^{-1}$.

2.3.2 DM candidate particles

Measurements show that DM particles are non-baryonic, electromagnetically neutral, color neutral, and massive, exhibiting gravitational interactions. One of the most compelling candidates meeting all these criteria is the class of Weakly Interacting Massive Particles (WIMPs), which are comprised in several extensions of the Standard Model of particle physics. These particles interact primarily through gravity and possibly through other forces not included in the Standard Model, with interaction strengths comparable to or weaker than the weak nuclear force. WIMPs are further motivated within the framework of supersymmetric (SUSY) extensions of the Standard Model, where they naturally arise as stable, weakly interacting relics.

In SUSY models [144], each particle has a supersymmetric partner, differing by a half-integer spin. The R-parity ensures the stability of the lightest supersymmetric

particle (LSP), making it a viable WIMP dark matter candidate. The LSP is often the lightest neutralino, a mixture between fermionic partners of the neutral Higgs boson and neutral electroweak gauge bosons. An alternative to SUSY-based WIMPs are Kaluza-Klein particles, arising in extra-dimensional theories [110]. These particles, stabilized by KK-parity, have the same spin as their Standard Model counterparts. The lightest KK particle serves as a viable non-SUSY dark matter candidate.

Some of the other non-WIMP candidates are the axion-like particles [62], sterile neutrinos (a good candidate for warm DM) [132], and primordial black holes [113].

2.3.3 Indirect search of DM at the GC

The indirect searches for DM look for the products of the DM annihilation or decay in space. Products of such annihilation or decay of DM particle, χ, can produce γ-ray photons, neutrinos, hadrons, leptons, or electroweak bosons. In the framework of the γ-ray astrophysics, we are interested in the annihilation or decay of χ into γ-rays.

The amount of DM signal scales with the DM density of the region of interest. Models of the Galactic DM density profile can be divided into two classes: cuspy and cored density profiles. In the former category, the two well-known profiles are the Einasto profile [195] and the NFW profile [141]. The Einasto profile can be parameterized as:

$$\rho_{\mathrm{Ein}} = \rho_{\mathrm{s}} \exp\left(\left[-\frac{2}{\alpha}\left(\left(\frac{r}{r_{\mathrm{s}}}\right)^{\alpha} - 1\right)\right]\right). \tag{2.2}$$

While the NFW profile can be written as:

$$\rho_{\mathrm{NFW}} = \rho_{\mathrm{s}}\left(\frac{r}{r_{\mathrm{s}}}\left(1 + \frac{r}{r_{\mathrm{s}}}\right)^{2}\right)^{-1}. \tag{2.3}$$

In these two equations, ρ_{s} is the critical density at the position of the Sun, r is the distance from the GC, r_{s} is the scale radius for the slope change in the profile, and α is the Einasto index. Cored DM profiles are used for less massive galaxies, and the main models are the Burkert [37] and the isothermal [30] profiles.

Figure 2.8 shows the DM density distribution for distances close to the GC. Cuspy profiles are three to four orders of magnitude higher than the cored profiles at the center of the Galaxy. Therefore, we expect a large amount of DM particles at the GC, providing a promising DM annihilation or decay signals in the form of γ-ray excess above the expected emission. However, due to the complexity of the γ-ray emitters in this region, modelling the "background" sources (in this case, we consider all γ-ray sources other than DM as background) is a complex work. Many of the previous studies were masking the Galactic plane, to avoid contamination from astrophysical γ-ray source [see for example 1]. In our approach, we aim to investigate the potential of DM signal studies at the GC region without masking the plane through modelling each of the known γ-ray sources. For than, more sophisticated gas mass distribution in the CMZ also contributes to reducing the astrophysical background while analysing the possible DM signal. Research on the DM detectability with the future telescope SWGO is given in Chapter 7.

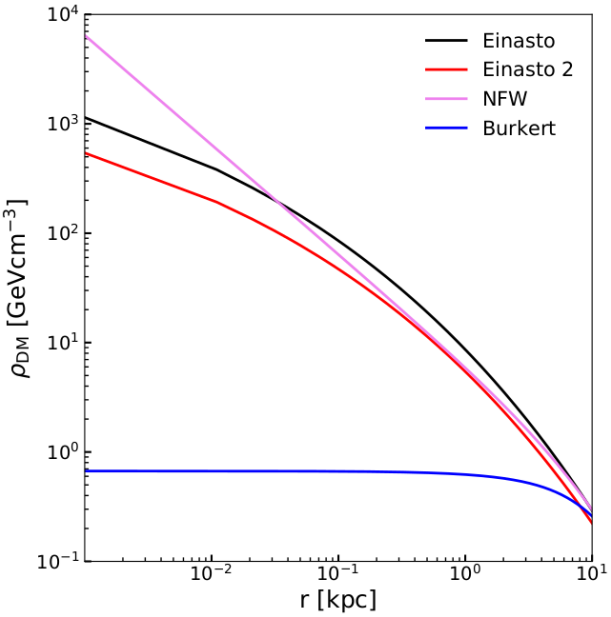

Figure 2.8: DM density distribution in the GC for two examples of the Einasto profile, NFW, and Burkert profiles. Figure adopted from [138].

2.4 Multiwavelength detection of the Galactic Centre

Due to the dust absorption, the GC region is obscured at near-IR, visible, and UV wavelengths. Thus, observations of the GC are done in the radio to middle IR bands, and in the X-ray to γ-ray bands.

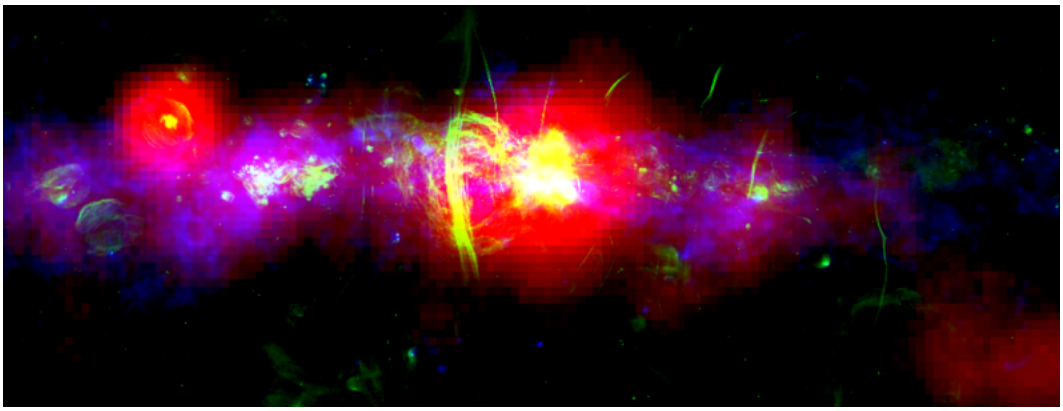

Figure 2.9: Composite image of the GC. In red is the H.E.S.S. γ-ray emission, in green is the Meerkat radio map at 1.28 GHz, and in blue is the Herschel dust emission at 250 µm. Figure from [45].

2.4.1 Radio

The radio picture of the GC taken by Meerkat is shown in Figure 2.9 in green colour. Prominent emission around Sgr A* can be seen, as well as many filamentary structures and other bright cores and shells. These radio photons can be emitted by very-high-energy electrons traveling in the interstellar medium, via synchrotron losses [see Chapter 4].

Thus, the radio band can reveal some of the most energetic regions, despite being the lowest energy band in the electromagnetic spectrum. Indeed, the filamentary shapes are believed to indicate the direction of the magnetic field, and accelerated electrons follow these lines to escape the GC while emitting synchrotron photons. These filaments are therefore referred to as non-thermal filaments.

In the radio band, we also have the molecular line emissions, which can trace the molecular hydrogen column density. Tracers such as CO, CS, HCN, etc, are commonly used molecules to estimate the molecular content in the CMZ, since the H_2 cannot be directly observed.

2.4.2 Infrared

In the infrared band, the dust thermal emission can be detected. Dust emission is separated into mid-infrared (MIR) and far-infrared (FIR). The Herschel FIR dust emission reveals a ∞-shape of the CMZ, as is illustrated in Figure 2.9 in blue colour. Dust emission is thought to be proportional to the total gas mass via the so-called dust-to-gas factor. Emissions at different wavelengths are dominated by dust at different temperatures. FIR radiation is basically emitted by cold and dense dust, located at the core of the dense gas regions. At shorter wavelengths, in the MIR band, emission is dominated by dust at higher temperatures, thus revealing regions of the dust being heated by energetic radiation from stars or other astrophysical processes.

The dust spectrum can be modelled as a black body emitter using the Planck function. However, the distribution of different components of dust in dust temperature is unknown along the line of sight. Thus, simple assumptions must be made such as considering the dust distribution to be dominated by a single temperature component [see for example 159], or more sophisticated approaches use two dust temperature components to describe the dust emission [first proposed by 168].

2.4.3 X-rays

Photons by thermal bremsstrahlung emission inside SNR shells, and synchrotron emission of accelerated electrons (see Section 4.2.1) can be produced in this energy range. Bright emitters in X-rays at the GC are Sgr A* and the immediate surrounding, the Quintuplet and the Arches star clusters, and hundreds of unknown point-like sources that are probably associated with black holes, neutron stars, or binaries. Furthermore, outflow emission from the Northern and the Southern sides of the GC has been observed in X-rays, with the XMM-Newton satellite [163]. These outflows were named the *X-ray Chimney*, and are shown in the XMM-Newton image in Figure 2.10. The elongated shapes of the X-ray structures appear to connect the GC to the Fermi bubbles, thus, relevant energy and mass could be transferred from the GC to the Fermi bubbles via the X-ray chimneys. More extended structures were detected by ROSAT and eROSITA, named as the eROSITA bubbles [see Figure 1 in 164]. These giant X-ray shells seem to spread above and below the Galactic plane. The Northern side of the structure reaches latitudes up to 75°, with an angular width of $\approx 20°$. The connection between the X-ray bubbles and the γ-ray bubbles is still uncertain.

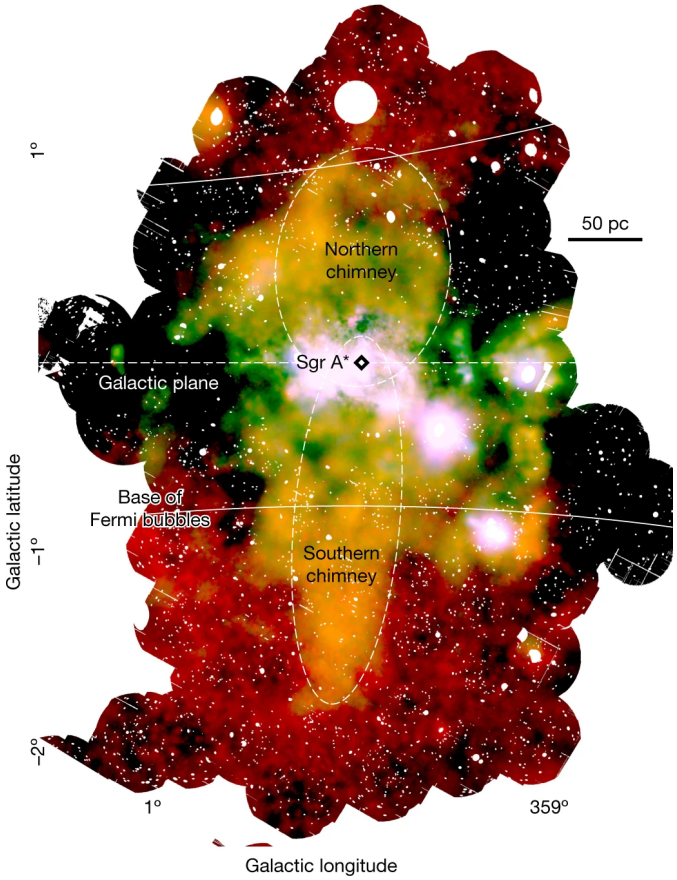

Figure 2.10: XMM-Newton X-ray image of the GC region. In red is the $1.5 - 2.6$ keV band, in green the $2.35 - 2.56$ keV band, and in blue the $2.7 - 2.97$ keV band. The horizontal dashed line indicates the Galactic plane, while the solid lines illustrate the base of the Fermi bubbles. Northern and Southern chimneys are indicated by elliptical dashed lines. Figure adopted from [163].

2.4.4 Gamma-rays

At high energies, the emission of γ-rays indicates important particle acceleration activity happening in the GC. Detailed γ-ray production mechanisms are described in Chapter 4.

GeV γ-ray measurements were provided by *Fermi*-LAT [52], which detected an excess in the GC region. This GeV γ-ray excess was initially thought to be of DM origin [83, 104], however [23, 120] suggested the unresolved γ-ray point sources and, in particular, the millisecond pulsars, to explain the observed excess. *Fermi*-LAT also discovered the amazing Fermi Bubbles [199]. These γ-ray bubbles extend up to 50° above and below the Galactic plane, as can be seen in Figure 2.11.

H.E.S.S. published its observations of the GC region at TeV energies [11, 88, 89], and possible DM interpretations of the γ-ray excess were also investigated [12, 139, 175]. In Figure 2.9, the H.E.S.S. view of the GC is illustrated in red colour.

The γ-ray emission from the CMZ is of hadronic origin (also described in Chapter 4), and can be assumed to be proportional to the CR energy density and the gas mass in the region. [88] estimated the CR energy density in relevant regions in the CMZ (see the regions indicated by the black lines in Figure 2.12), using the CS molecular emission, given by [206], as tracer of the molecular gas mass. The CR energy distribution as a function of the distance to the GC has then been estimated to be in good agreement with the 1/r profile [see Figure 3 in 88]. The 1/r profile corresponds to a constant accelerator

at the GC continuously ejecting relativistic particles to the CMZ. Moreover, the highly energetic spectrum of the CMZ, without energy cutoff beyond 10 TeV, led the authors to claim that the GC is accelerating particles to the PeV band (such energetic accelerators are called PeVatrons).

Additionally, a more detailed analysis of the VHE γ-ray diffuse emission was reported in [89]. Figure 2.13 shows the significance map of the GC (top panel). After subtracting the main point-like sources HESS J1745-290 (in spatial coincidence with Sgr A*) and SNR G0.9+0.1, the γ-ray emission associated with gas in the CMZ can be better illustrated (bottom panel of Figure 2.13). A few more components were fitted to the residual of the γ-ray map, including a large-scale emission and a central Gaussian component. As a result of the sophisticated modelling of the diffuse emission, a detection of the "Arc source" HESS J1746-285 was reported, in spatial coincidence with the bright radio arc extending from the GC to the south of the plane (see the Meerkat radio image in Figure 2.9 in green colour).

The MAGIC Collaboration measured a CR energy density distribution consistent with the H.E.S.S. 1/r profile [127], and more recently, the presence of a PeVatron at the GC is further confirmed by the HAWC observations [15].

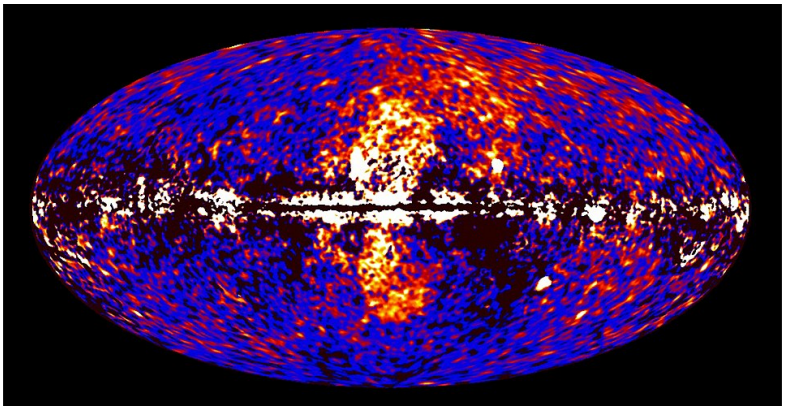

Figure 2.11: Fermi bubbles. *Fermi*-LAT residual all-sky map where the excess shows two dumbbell-shaped structures south and north of the Galactic Plane. Credits: NASA.

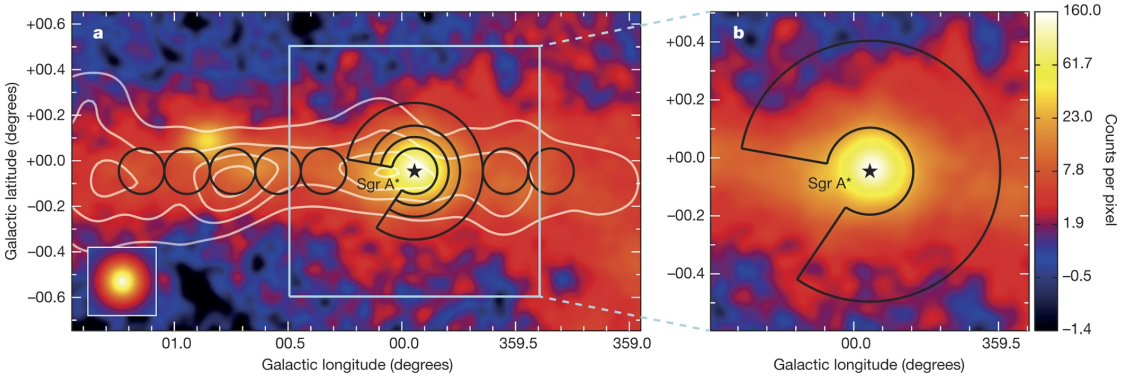

Figure 2.12: H.E.S.S. image of the GC. Left: The black lines indicate the regions used to calculate the CR energy densities in the CMZ. The gas density distribution as traced by the CS molecule is outlined by the white contour lines. Right: Zoomed view of the inner ∼70 pc region, and the outlined region used to extract the spectrum of the diffuse emission close to Sgr A*. Figure from [88].

Regarding the DM component, H.E.S.S. found no significant γ-ray excess in the region

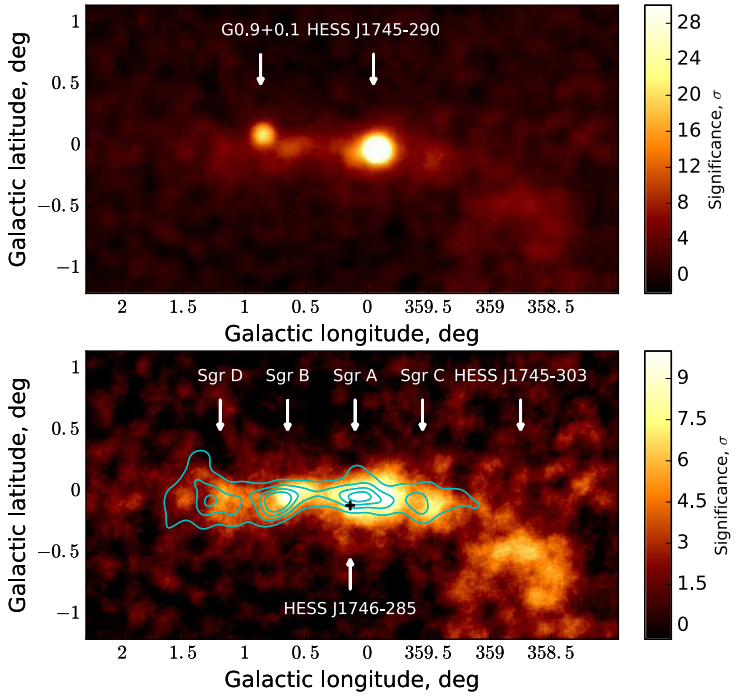

Figure 2.13: H.E.S.S. observation of the GC. Top: the γ-ray significance map. Bottom: The residual γ-ray significance map after subtracting the point-like sources HESS J1745-290 and G0.9+0.1. The cyan contour is the CS molecule emission. Figure taken from [89].

$10^\circ \times 10^\circ$ around the GC, with masking known γ-ray sources in the Galactic plane. Strong constraints on the thermal annihilation cross section $\langle \sigma v \rangle$ were obtained for Einasto and NFW profiles. For the former, the limit reached $\langle \sigma v \rangle$ values of 3.7×10^{-26} cm^{3}s^{-1} for 1.5 TeV DM mass, in the W^+W^- annihilation channel, and 1.2×10^{-26} cm^{3}s^{-1} for 0.7 TeV DM mass in the $\tau^+\tau^-$ annihilation channel.

2.5 Summary

In this chapter, the GC region and its components have been introduced. The CMZ, composed by GMCs, has a radius of $\sim 100 - 200$ pc. The main GMCs that can be identified in the $(l - b)$ and $(l - v)$ spaces are the 1.3° cloud complex, Sgr D, Sgr B2, G0.253+0.016, Sgr A clouds (the 50 km s^{-1} and 20 km s^{-1} clouds) and Sgr C. Some of the properties of the CMZ are the higher gas density, temperature, and turbulence, compared to the gas in the disk. Higher star formation rate, metallicity, and magnetic field strength are also observed in the CMZ. The 3D geometry of the CMZ is, however, still uncertain, mostly due to the highly non-circular motion of the gas and the harsh interstellar extinction in the line of sight.

The GC region is also the best location for indirect detection of DM via measuring the γ-ray emission produced by relic DM annihilation and decay processes. However, no strong hints of a DM signal have been detected by current γ-ray instruments. We present in Chapter 7 a future ground-based particle detector, SWGO, which is complementary to CTAO, and together they are the most promising instruments to detect a DM signal in the GC region. In particular, our approach does not mask the GC where most of the DM density is located, instead, we model the astrophysical γ-ray sources together with the DM component.

A brief description of the multiwavelength observations of the GC region has been given. In particular, at the VHE γ-ray band, one can notice that the γ-ray emission links the gas mass and the CR energy distribution studies. However, uncertainties arise from both sides. On the one hand, gas distribution in the CMZ is highly non-trivial, and many unknowns are in play, like, for example, the conversion factors of molecular line emission and dust emission to hydrogen masses (for more details see Chapter 3). On the other hand, there is no consensus on the CR acceleration sites in the GC, and thus, CR transport models around the GC are vastly speculative. As a consequence, many free parameters exist in the research of the gas and CR properties towards the GC, and, while studying these properties, one should consider a limited parameter space while keeping in mind the constraints of the assumptions.

In the next chapter, the estimation of the gas mass in the CMZ using CO, HI, and dust emission is explored. This approach is extensively described in our publication [173]. Here, I focus more on the procedure to prepare the gas and dust data, since I was involved in most parts of the data preparation. The issues encountered during the data analysis and the way to solve these problems are also given in more detail.

Chapter 3

Gas and dust distribution in the CMZ

So far, we have outlined the broader picture of the GC region, describing the various astronomical objects and structures near Sgr A*, as well as, the different components identified through multiwavelength observations, including the expected DM density distribution in the GC. However, this picture remains incomplete, and many open questions persist. Focusing on the gas distribution in the CMZ, one may ask: What is the three-dimensional distribution of the GMCs? What are their masses? What is the ratio of atomic to molecular gas in the CMZ? And is the atomic component truly negligible?

Studying the gas distribution in the CMZ is not only essential for determining its star formation rate [see the overview by 95], but also plays a crucial role in estimating the CR energy density in the GC region, which is closely linked to particle acceleration processes. A detailed understanding of the gas structures provides key insights into the density of CRs in the CMZ, assuming that the γ-ray emission comes from hadronic processes.

The CMZ is predominantly composed of molecular hydrogen, H_2, a molecule that is very difficult to detect due to its low molecular rotational-vibrational transition probability [189, 213]. As a result, other molecular species are commonly used to trace the molecular gas. These range from various CO isotopologues, which are sensitive to a broad range of gas densities, to molecules like HCN and CS that trace the densest regions, along with many others. In this work, we focus on CO and its different isotopes and transition lines, as they provide extensive coverage across a wide range of molecular gas densities [see 133, and references therein].

The CO emission is commonly converted into H_2 column density using the CO-to-H_2 conversion factor, $X_{\rm CO}$. However, this estimation is subject to several uncertainties and unknowns. The effectiveness of CO as a molecular gas tracer is questionable at both low and high density extremes. At low densities, near the atomic-to-molecular hydrogen transition, CO surveys often lack the sensitivity to detect faint emission. At high densities, within dense cores, CO emission tends to saturate due to optical thickness. To address this, we employ three different isotopologues (^{12}CO, ^{13}CO, and C^{18}O) and two rotational transition lines ($J = 1 \rightarrow 0$ and $J = 2 \rightarrow 1$), which together extend the accessible density range. In fact, most of the cloud mass is traced by ^{12}CO, since most of its mass is in the envelope, which has low to intermediate column densities [147], while rarer isotopes, which are less optically thick, reach higher densities.

The $X_{\rm CO}$ factor varies depending on the intrinsic gas properties in different environments, such as the temperature, density, and metallicity, so that it can vary from cloud to cloud and within a cloud, and it also varies depending on the resolved observation scale. Here we consider the simulations provided by [82], who gave $X_{\rm CO}$ as a function of metallicity, resolved scale, and integrated line brightness of CO line emission. In their work, only environments at 2, 4 and 8 kpc from the Galaxy are simulated, thus in order to apply their results to the GC region, where the level of turbulence is much higher, a correction following the behaviour seen in the work of [28] has been adopted.

The amount of gas in the atomic phase is typically estimated using the HI 21 cm

line emission. However, in the central region of the Galaxy, this emission is affected by HI self-absorption, which can lead to underestimations of the true column density. To correct this, we propose a method to estimate the intrinsic HI emission using information from neighbouring pixels that are unaffected by HI self-absorption.

Due to our line-of-sight perspective towards the CMZ, both atomic and molecular gas observations contain emission from the CMZ itself as well as from the Galactic disk. Separating these components has been made possible by analysing the line-of-sight velocity, velocity dispersion, and line density in the CO emission. This separation was performed using a clustering algorithm applied to the ^{12}CO emission lines. The resulting clustering mask is then applied to other CO isotopologues and to the HI emission.

Another approach to tracing the total gas column density involves measuring the dust optical depth through thermal dust emission observations in the submillimetre range. However, estimating the total gas content from dust emission is not straightforward, and several other questions arise: how does the dust-to-gas mass ratio vary with spatial scale, and by how much? Is the dust well mixed with the gas? How does the dust temperature vary along the line of sight? And how does the dust grain evolution in different environments affect the estimation of dust mass? In this chapter, the dust emission has been modelled as a combination of two black-body components at various temperatures. The warmer dust component is typically more diffuse, and the colder dust component is expected to be denser, located at the cores. We then compute the dust opacity using results derived from CO isotopologue emission to investigate how it varies with gas column density.

Estimates of the CR energy density from γ-ray observations are closely tied to the estimation of gas column density. As mentioned in section 2.4.4, H.E.S.S. measured an integrated γ-ray luminosity and used a two-dimensional gas template, based on CS, CO, and HCN to derive the CR energy density [88, 89]. The 2D gas distributions represent a line-of-sight integration, tracing the hydrogen column density within the densest cores of the CMZ. The resulting 1/r CR profile is therefore a 2D projection of the underlying three-dimensional CR distribution around the GC. Whether this profile holds in 3D can only be tested with a 3D gas mass distribution. To this end, in the following, the total gas mass in the CMZ is clustered into 30 molecular clouds. These structures will be the subject of future work, in which their line-of-sight distances will be estimated to enable a fully three-dimensional analysis.

This chapter is structured as follows. In Section 3.1 we describe our estimation of the molecular and atomic gas column densities in the CMZ, including the corrections applied to both datasets, the analysis procedure, and the separation of the CMZ and disk components. Section 3.2 outlines the method used to determine the dust distribution and its comparison with the gas column densities, estimated in Section 3.1. Section 3.3 presents a new estimate of the CR energy density in the 2-dimensional projection, based on the H.E.S.S. γ-ray observations published in [88]. Section 3.4.1 describes the clustering of molecular gas into GMCs, using clustering techniques, as a preparatory step towards reconstructing the three-dimensional gas distribution in future work. Finally, Section 3.5 presents a summary of this chapter.

A thorough report of most of the work described in this Chapter has been published in our CMZ Paper I [173]. The clustering part of the project was carried out in collaboration with Sruthiranjani Ravikularaman (see her Thesis [167]), and will be presented in a forthcoming CMZ Paper II.

3.1 Gas mass estimation using Hi and CO line emission

The neutral gas in the interstellar medium (ISM) is present in atomic and molecular phases. The dense molecular cores are surrounded by structures of an atomic gas envelope. The atomic phase can be traced by the HI 21cm line emission, while the molecular hydrogen can be traced by molecules like carbon monoxide CO. Both phases of the gas must be considered to correctly determine the total gas mass.

Atomic phase: $N_{\mathbf{HI}}$

The neutral hydrogen atom in its ground state has two hyperfine levels, due to the spin of the electron. When the electron spin flips from being parallel to the proton spin to the antiparallel state, the atom emits a photon at a frequency of 1.4 GHz, or equivalently, 21 cm in wavelength.

The measured brightness temperature, $T_{\rm B}$, as a function of the longitude, latitude, and velocity (Doppler shift of the emission), is related to the spin temperature, $T_{\rm S}$, and the optical depth, τ of the line. $T_{\rm S}$ is the excitation energy of the hyperfine levels. The relation can be written as [191]:

$$T_{\rm B} = (T_{\rm S} - T_{\rm C})(1 - e^{-\tau}), \tag{3.1}$$

where $T_{\rm C}$ is the background continuum emission, including the Galactic background and the cosmic microwave background (CMB).
To convert the observed $T_{\rm B}$ to column density of atomic hydrogen, $N_{\rm HI}$, we use:

$$N_{\rm HI}(l,b) = X_{\rm HI} T_{\rm S} \int \tau {\rm d}v = -X_{\rm HI} T_{\rm S} \int \ln\left(1 - \frac{T_{\rm B}(l,b,v)}{T_{\rm S}}\right) {\rm d}v, \tag{3.2}$$

with $X_{\rm HI} = 1.82 \times 10^{18}$ cm^{-2}(K km s^{-1})$^{-1}$ the conversion factor.

Molecular phase: $N_{\rm H_2}$

In the molecular phase of the ISM, H_2 is by far the most abundant molecule, exceeding others by several orders of magnitude. However, it is extremely difficult to detect due to its highly symmetric molecular structure, consisting of two identical atoms [90, 213]. As a result, the H_2 molecule has no dipole moment, rendering its ro-vibrational transitions forbidden. Only weak quadrupole transitions are allowed, but these have low spontaneous emission coefficients. Although electronic transitions in H_2 can produce ultraviolet (UV) radiation, this emission is often absorbed by dust in the CMZ. Furthermore, most of H_2 is likely hidden within dense, cold, and well-shielded regions, where excitation conditions are too low for detection and UV emission is strongly attenuated by extinction.

There are three main approaches to mitigate this challenge and probe the H_2 gas: molecular line spectroscopy of a proxy molecule, dust emission and extinction measurements, and diffuse γ-ray emission resulting from interactions between cosmic rays and the H_2 gas. In this section, we describe the methodology used to trace molecular hydrogen using CO as a proxy.

CO is the second-most abundant molecule in the Galaxy [152], and thus the most widely used tracer for H_2. Its emission arises from rotational transitions, which are easily excited under typical molecular cloud conditions. The excitation temperature of $J = 1 \rightarrow 0$ line is around 5 K, and its critical density for collisional excitation is $\sim 10^3$ cm^{-3} in the optically thin limit [188]. In fact, CO is so abundant in the molecular

clouds that photons emitted by molecules are rapidly absorbed by other CO, keeping these molecules excited. This phenomenon is known as optical trapping. This effect is so important that the ^{12}CO$(1-0)$ line can be detected even in regions with densities below 10^2cm^{-3} [188]. Furthermore, the lower-energy transitions of CO emit at frequencies that can be detected on the ground. This makes CO the preferred tracer for many studies ([see 155, and references therein]). However, ^{12}CO$(1-0)$ traces only a limited range of densities. At low density, CO is more easily photodissociated by the interstellar radiation field than H_2, while at high densities the line emission becomes optically thick and saturates.

To extend the range of traced gas densities, we consider other isotopologues of CO and higher rotational transition $J = 2 \rightarrow 1$. The ^{13}CO and C^{18}O isotopologues are significantly less abundant than ^{12}CO. [123] modelled the ^{13}CO$(1-0)$ and C^{18}O$(1-0)$ transition lines and estimated their critical densities at 25 K to be 8×10^2cm^{-3}. These isotopologues therefore trace denser regions than ^{12}CO$(1-0)$. Additionally, the higher rotational transition is less populated than $J = 1 \rightarrow 0$, and is consequently less optically thick.

The H_2 column density can be estimated from CO line emission with the following relation:

$$N_{H_2} = X_{CO} W_{CO}, \tag{3.3}$$

where X_{CO} is the CO-to-H_2 conversion factor, and W_{CO} is the integrated brightness temperature:

$$W_{CO} = \int T_B(v) \mathrm{d}v. \tag{3.4}$$

3.1.1 Gas tracer datasets

The list of the atomic and molecular line emission data used is provided in Table 3.1. The analysed region spans from $-0.8°$ to $1.4°$ in galactic longitude and from $-0.3°$ to $0.3°$ in galactic latitude, constrained by the coverage of the high-resolution CO survey employed. The line emission datasets are structured as data cubes, providing three-dimensional information across longitude l, latitude b, and velocity v. For each position in longitude and latitude values, the line emission profile corresponds to the brightness temperature, T_B, in each velocity channel. The measured brightness represents the intensity of the emission in temperature units under the Rayleigh-Jeans approximation.

All maps used in this work are downsampled to a common angular resolution of $0.02°$. This bin size is slightly larger than the minimum resolved scaled probed by the simulations that we use to model the evolution of X_{CO}. Moreover, given that these maps are employed in the context of γ-ray astronomy, this resolution is sufficient, since current γ-ray instruments provide coarser angular resolutions.

We use the HI 21 cm emission line from the Galactic Center survey data conducted with the Australia Telescope Compact Array (ATCA) and the Parkes Radio Telescope [130].

For molecular gas, we use three different CO isotopologues – ^{12}CO, ^{13}CO and C^{18}O– and two rotational transitions – $J = 1 \rightarrow 0$ and $J = 2 \rightarrow 1$ –, hereafter noted $(1-0)$ and $(2-1)$, respectively. The ^{12}CO$(1-0)$ and ^{13}CO$(1-0)$ lines are from the 45m telescope at the Nobeyama Radio Observatory (NRO)[1] [203], and the ^{13}CO$(2-1)$ and

[1]Public data can be found at NRO official webpage.

Table 3.1: Atomic and molecular data used in this study.

Tracer	Frequency [GHz]	v_{LSR} range [km s^{-1}]	v_{LSR} resolution: effective (channel) [km s^{-1}]	Angular resolution: beam size (pixel) [°]	Sensitivity (rms noise) [K]	Instrument
HI	1.4	$-309:349$	1 (0.82)	0.0403 (0.0097)	0.7 – 2	ATCA
^{12}CO(J = 1 − 0)	115.27	$-220:220$	1.3 (2)	0.0043 (0.0021)	1	45m NRO-BEARS
^{13}CO(J = 1 − 0)	110.20	$-220:220$	1.3 (2)	0.0043 (0.0021)	0.2	45m NRO-FOREST
^{13}CO(J = 2 − 1)	220.40	$-200:200$	0.25 (0.25)	0.0083 (0.0026)	0.8 – 1	APEX
C^{18}O(J = 2 − 1)	219.56	$-200:200$	0.25 (0.25)	0.0083 (0.0026)	0.8 – 1	APEX

C^{18}O(2 − 1) lines are taken from the SEDIGISM survey conducted with the Atacama Pathfinder Experiment (APEX) 12m submillimetre telescope[2] [184].

The velocity-integrated brightness temperatures, $W_{\mathrm{H_I}}$, for HI 21 cm emission is illustrated in Figure 3.1, while W_{CO}, for the CO isotopologues are shown in top panel of Figures 3.2, 3.3, 3.4, 3.5 and 3.6. Initially, we also considered the C^{18}O(1−0) emission line map from NRO. However, as shown in Figure 3.4, this dataset exhibits several anomalous regions (over-bright stripes and patches), like for example at $l \sim -0.75°, b \sim 0.18°$, that could not be corrected through baseline correction (see in the next section). Consequently, this dataset was excluded from our analysis.

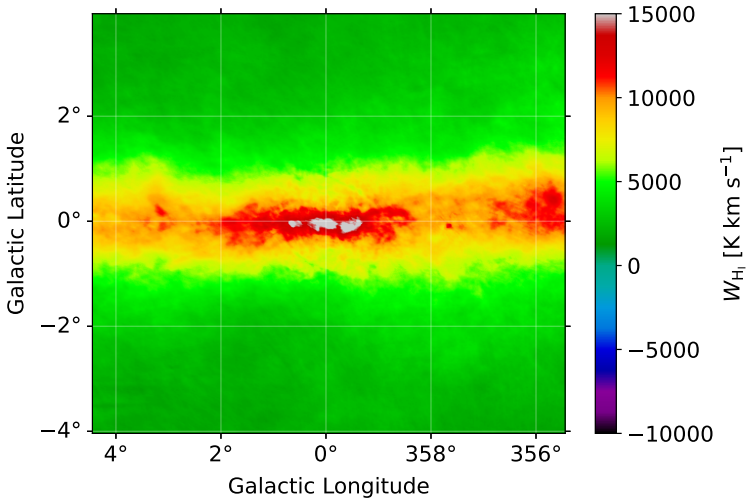

Figure 3.1: Integrated brightness temperature map of HI 21 cm line emission from ATCA, after the absorption correction.

[2]Public data can be found at SEDIGISM official webpage.

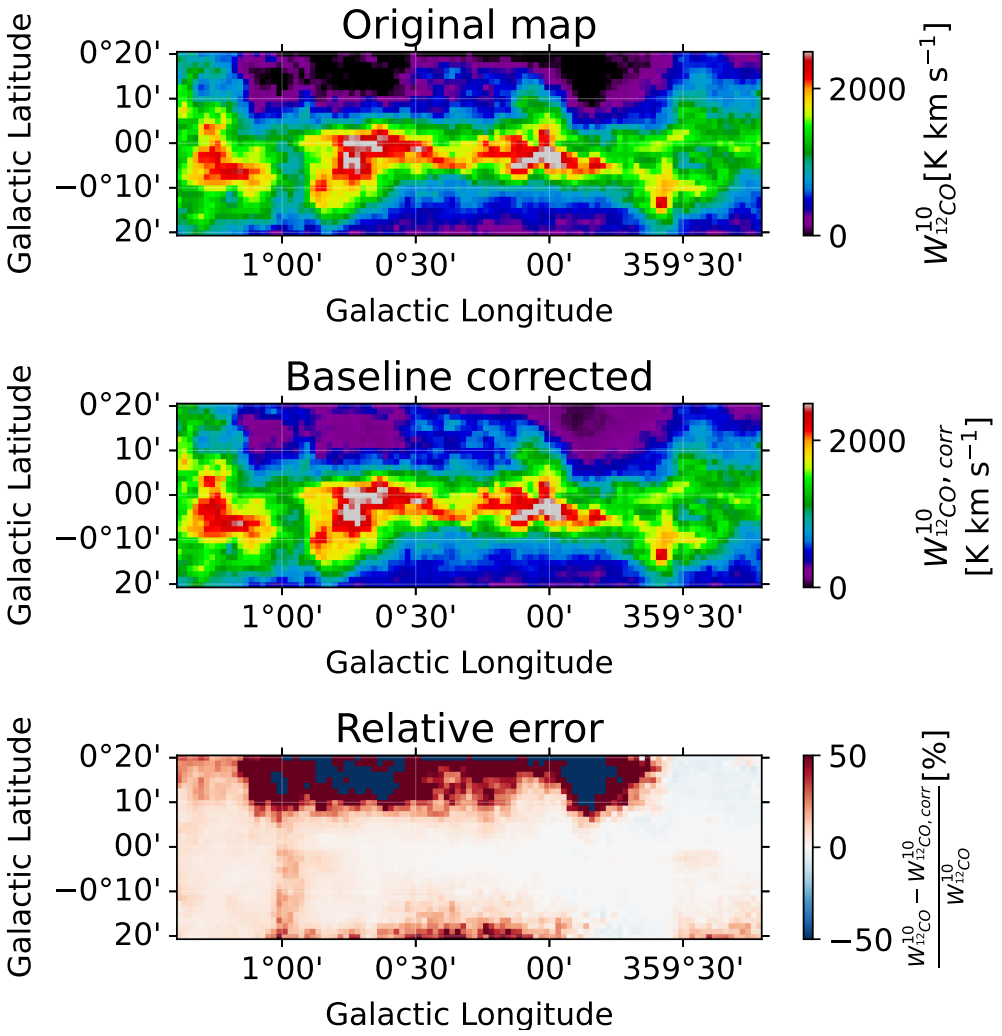

Figure 3.2: $^{12}\mathrm{CO}(1-0)$ maps. Top: original integrated brightness temperature map from NRO, downsampled to the angular resolution of 0.021°. Middle: baseline corrected integrated brightness temperature maps. Bottom: relative error comparing the map before and after baseline correction.

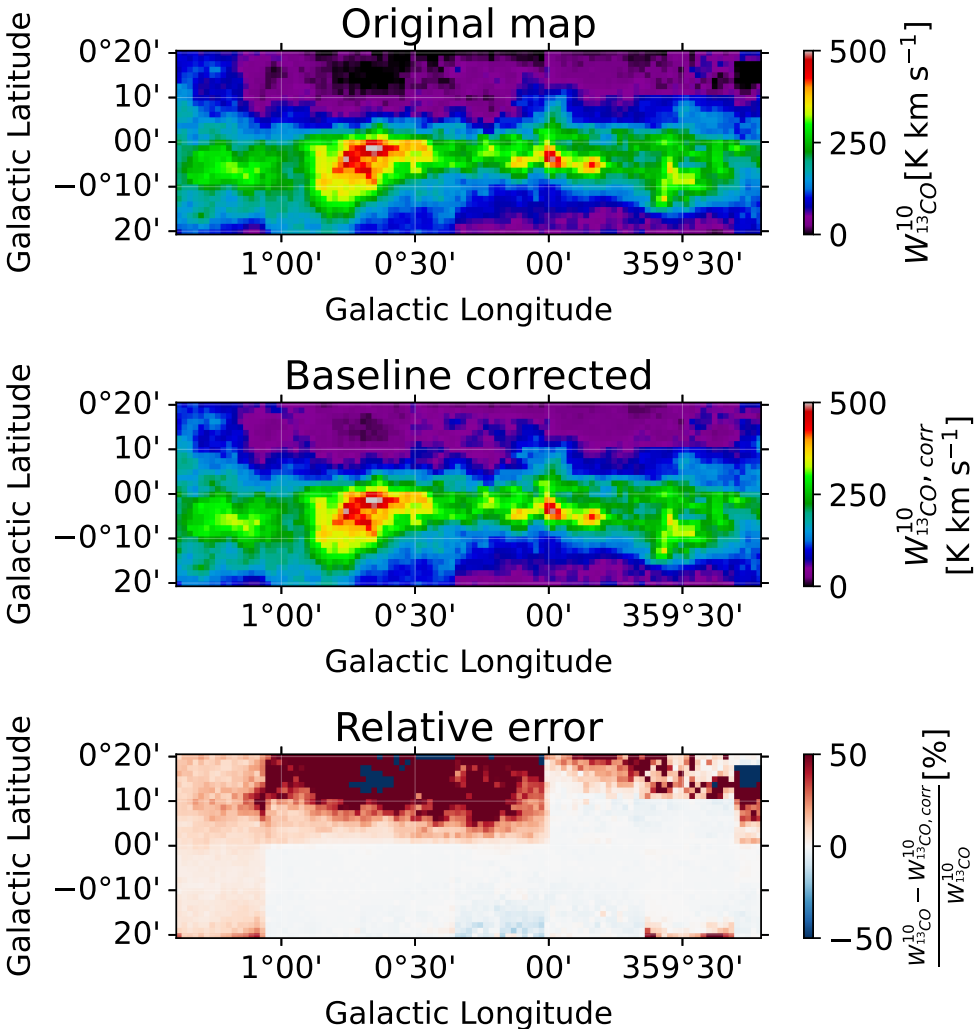

Figure 3.3: $^{13}\mathrm{CO}(1-0)$ maps. Same description as Figure 3.2.

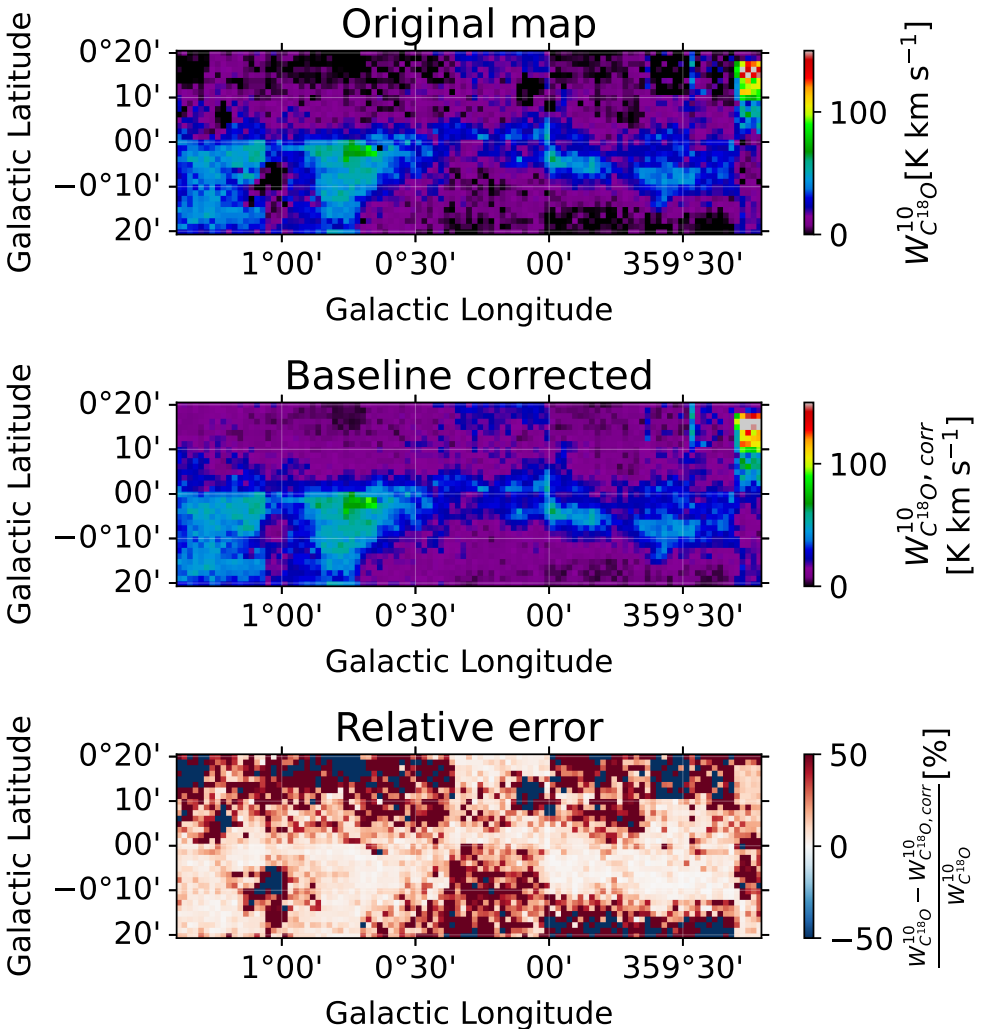

Figure 3.4: $C^{18}O(1-0)$ maps. Same description as Figure 3.2.

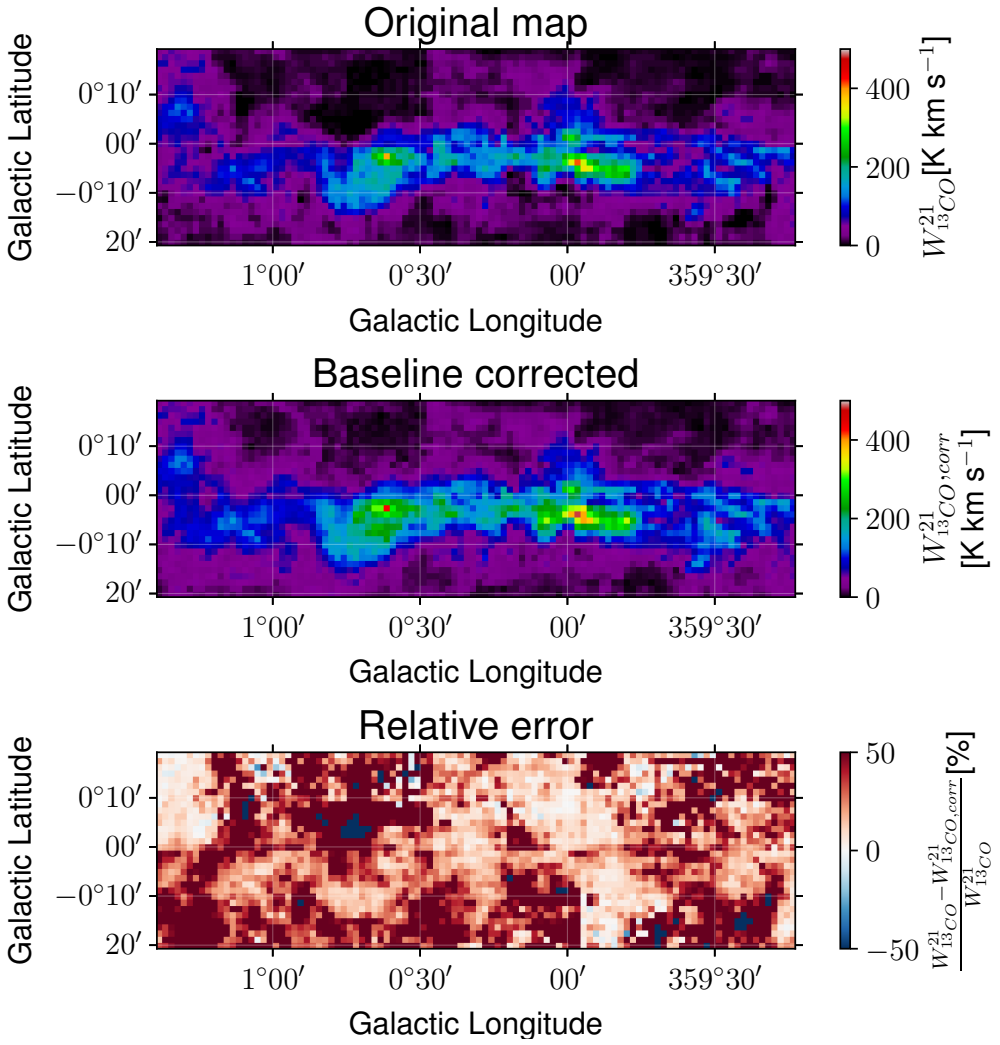

Figure 3.5: $^{13}\mathrm{CO}(2-1)$ maps. Top: original integrated brightness temperature map from APEX-SEDIGISM, downsampled to the angular resolution of 0.021°, and velocity resolution downsampled to 0.5 km s^{-1}. Middle: baseline corrected integrated brightness temperature maps. Bottom: relative error comparing the map before and after baseline correction.

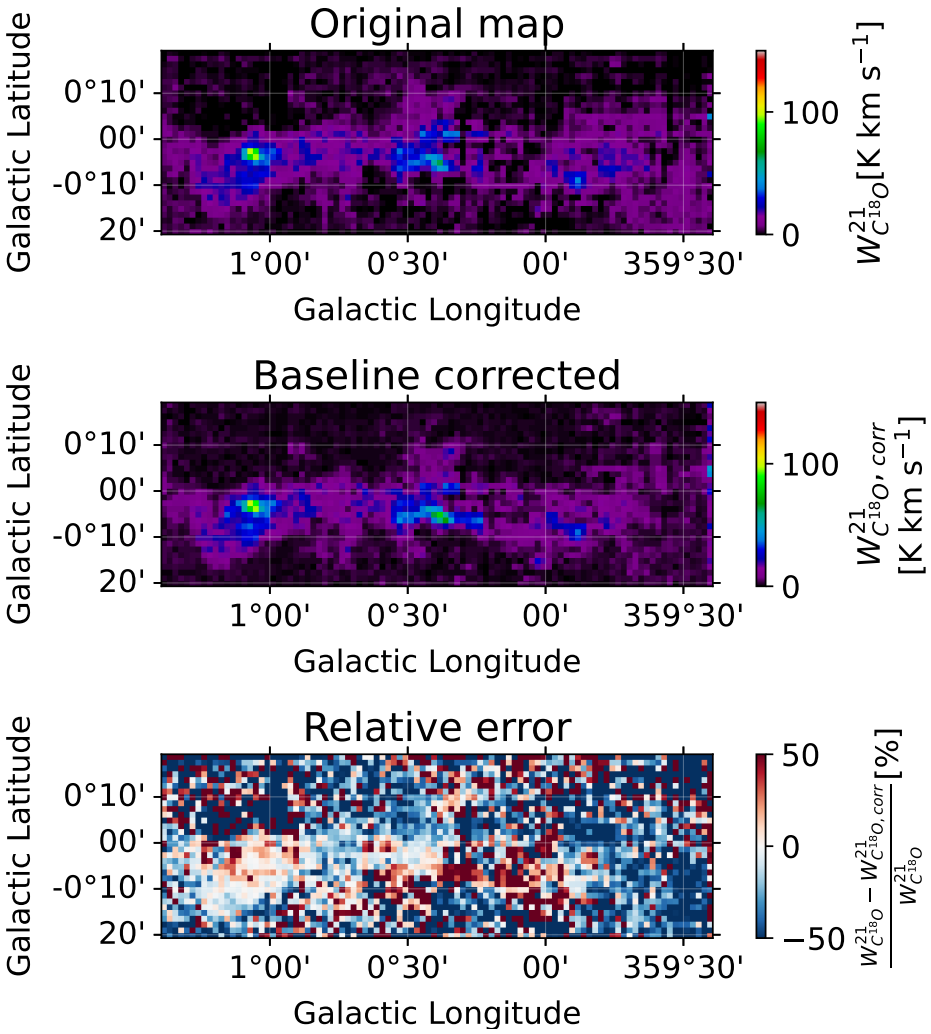

Figure 3.6: $C^{18}O(2-1)$ maps. Same description as Figure 3.5.

3.1.2 Data preparation

Some corrections and processing of the publicly available raw data maps are necessary in order to enable reliable estimates of the gas mass and dust opacity.

Hi absorption correction

Due to the strong absorption observed in the HI 21 cm emission line towards the direction of GC, a correction has to be applied (details can be found in CMZ paper I [173]). This correction involves reconstructing the affected pixels by estimating a plausible signal based on information from neighbouring pixels that are not significantly impacted by self-absorption.

CO baseline correction

On the other hand, the CO emission line profiles in the public datasets provided by the 45m NRO and the APEX observatories are found to be systematically shifted from zero toward negative values across broad velocity ranges along several lines of sight. To correct this deviation, we recalculated and applied a new baseline.

We compute a new baseline for each velocity channel as a running mean in a 60 km s^{-1} window. The corresponding number of velocity bins for each dataset is listed in Table 3.2. Regions with significant signal, larger than a certain threshold brightness temperature, $T_{\rm Th}$, are clipped to zero while computing the running mean. $T_{\rm Th}$ is defined as

$$T_{\rm Th} = {\rm STD}[T_{\rm B} < {\rm MAD}(T_{\rm B}) + {\rm MED}(T_{\rm B})], \tag{3.5}$$

where STD is the standard deviation, MAD is the standard median absolute deviation and MED is the median.

An example of a line profile with the applied baseline correction is shown in the top panel of Figure 3.7, where the running mean used for the correction is indicated by the thick green line. This profile corresponds to the line of sight marked by the black cross in the middle and bottom panels, which display the velocity-integrated CO line emission before and after the baseline correction, respectively.

By comparing the middle and bottom panels of Figure 3.7, it becomes evident that the integrated intensity is, on average, higher after the baseline correction. Additionally, a greater number of gas structures become visible, while the zero-filled rectangular artefacts are effectively removed. This improvement is particularly noticeable in the vicinity of Sgr B2 cloud (around $l = 0.7°, b = 0°$) and in the fainter regions located to the north and south of Sgr B2.

See the velocity-integrated $T_{\rm B}$ maps for ^{12}CO, ^{13}CO, and C^{18}O before and after the baseline correction for the NRO datasets in Figures 3.2 and 3.3, and for the SEDIGISM survey in Figures 3.5 and 3.6. This correction strongly attenuates the distinct sensitivity across different patches, likely associated with different observation phases. As a result, the baseline correction improves their average sensitivity.

3.1.3 Line profile decomposition

We separate each emission line in the $T_{\rm B}$ profile, for each longitude and latitude, following the method described in [162, 170]. The procedure consists of two main steps: line detection and line fitting. Figure 3.8 illustrates this process for the same line of sight shown in Figure 3.7.

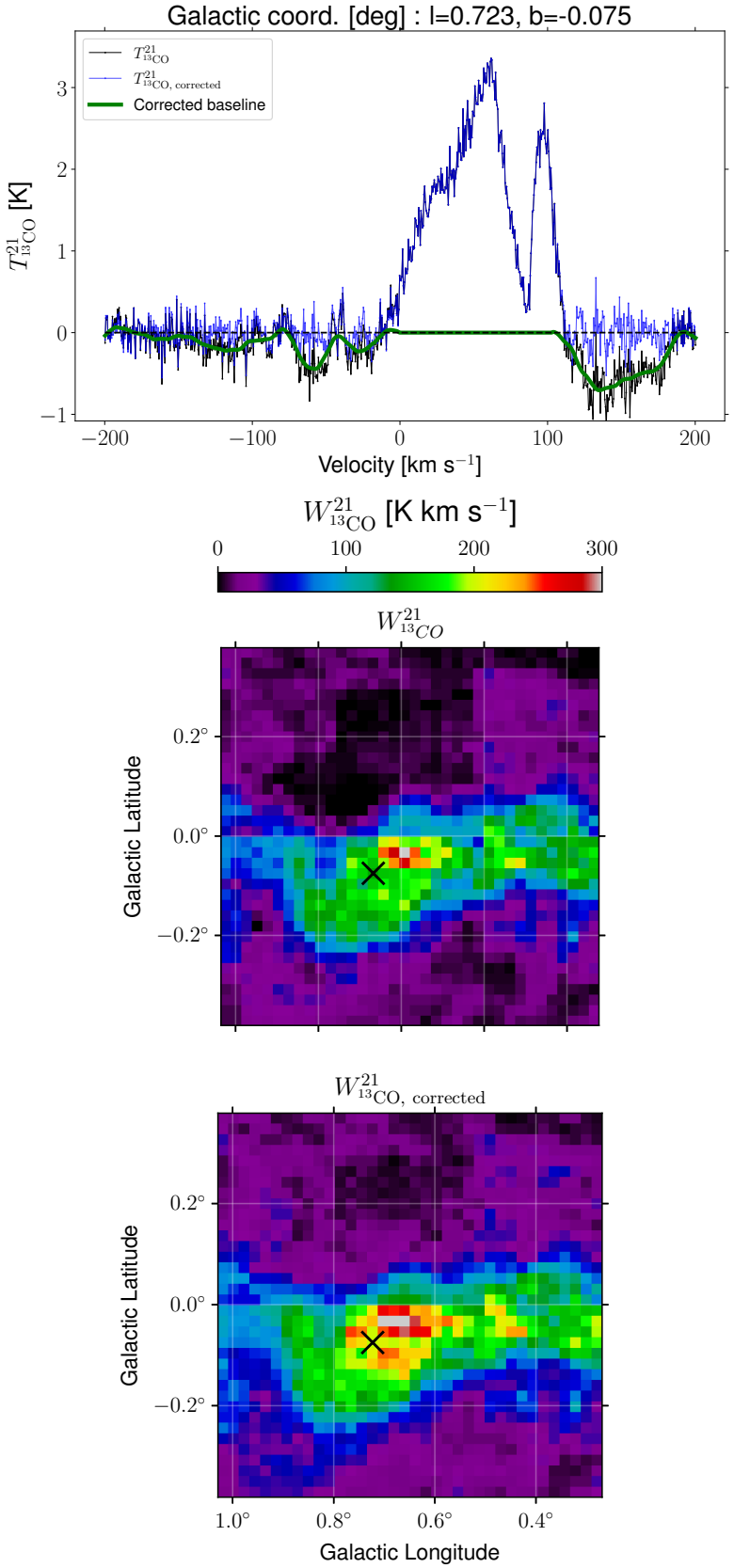

Figure 3.7: Top: Profile of the brightness temperature profile (black) for the line of sight indicated by the black cross in the middle and bottom panels, the running mean (green) and the corrected brightness temperature (blue). Middle: Original integrated brightness temperature of $^{13}\mathrm{CO}(2-1)$ from APEX. Bottom: Integrated brightness temperature of $^{13}\mathrm{CO}(2-1)$ after the baseline corection.

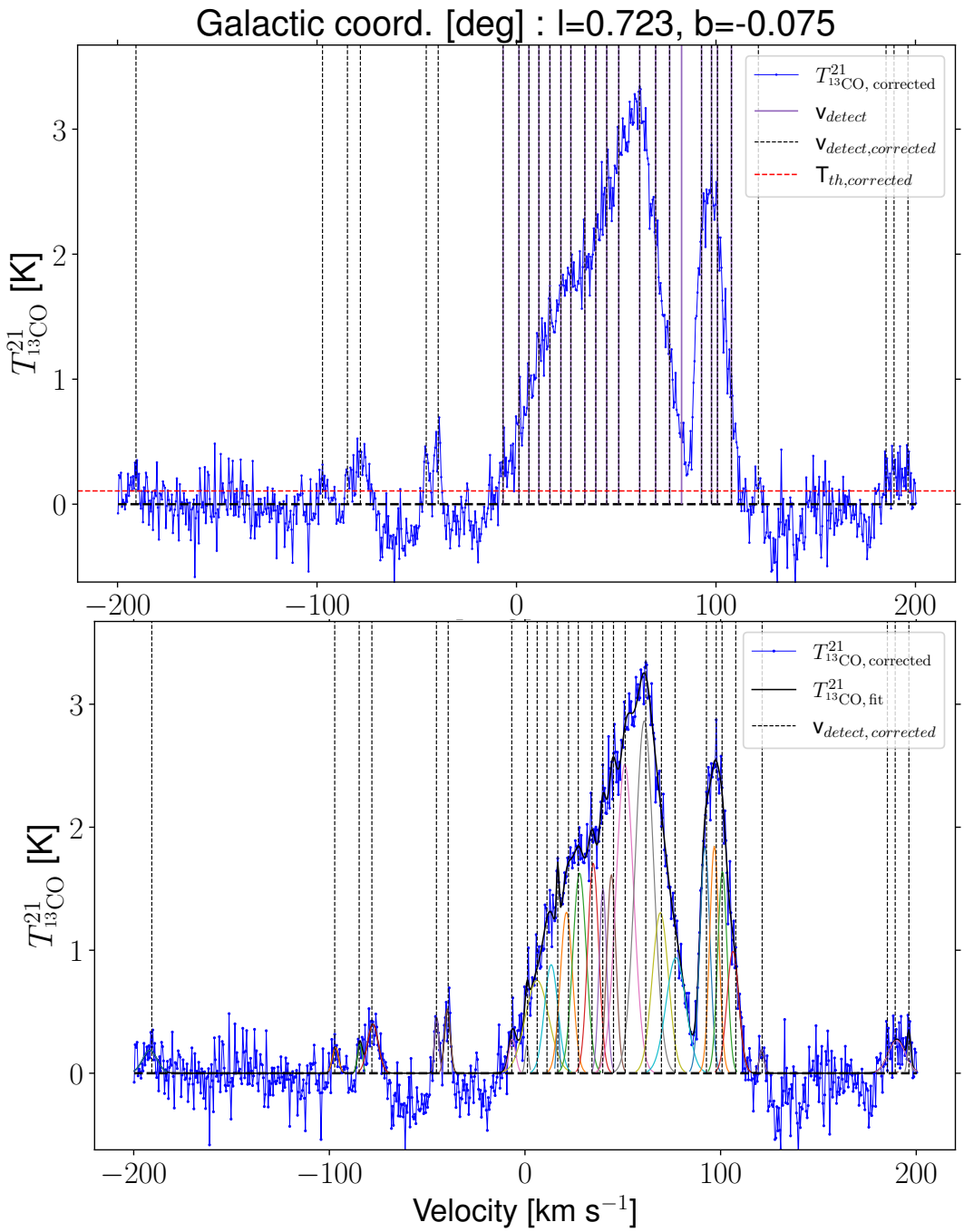

Figure 3.8: Line profile decomposition for the indicated line of sight. Top: Detected lines in the original profile (solid purple) and in the baseline corrected profile (dashed black). Bottom: Detected lines and fitted profiles as pseudo-Voigt functions in various colors. One can notice several 'new' lines that can be detected and fitted after applying the baseline correction.

Line detection is performed by identifying velocities at which local minima appear in the second derivative of the brightness temperature profile. These minima correspond to local maxima or inflection points in T_{B}, indicating the presence of emission lines. To reduce fluctuations due to noise, the second derivative is computed after applying Gaussian smoothing to the T_{B} profile. Detected lines are required to (1) exceed the

threshold $T_{\rm Th}$ (as defined in eq. 3.5, applied to the baseline-corrected profile), and (2) exhibit a local minimum in the second derivative within a minimum velocity separation, which ensures a sufficient distinction between adjacent lines. The Gaussian smoothing width, $\sigma_{\rm Gauss}$, and the line separation, Δv, for each dataset are indicated in Table 3.2.

Table 3.2: List of parameters used for baseline correction and line detection. In parentheses, the corresponding number of velocity bins, dv.

Tracer	Running mean width [km s^{-1}]	Gaussian smoothening width σ_{Gauss} [km s^{-1}]	Line separation Δv [km s^{-1}]	Line detection threshold σ_{Thr}
HI	-	0.82 (1dv)	3.3 (4dv)	2
^{12}CO$(1-0)$	60 (30dv)	0.6 (0.3dv)	4.0 (2dv)	1
^{13}CO$(1-0)$	60 (30dv)	0.6 (0.3dv)	4.0 (2dv)	1
^{13}CO$(2-1)$	60 (120dv)	1.5 (3dv)	6.0 (6dv)	2
C^{18}O$(2-1)$	60 (120dv)	1.5 (3dv)	6.0 (6dv)	2

In the second step to fit the lines, each detected line is then modelled as a pseudo-Voigt function:

$$pV = \eta L + (1-\eta)G, \tag{3.6}$$

where $0 < \eta < 1$ is the form factor, G and L are a Gaussian and a Lorentzian distribution, respectively:

$$G = h\exp\left\{\left(\frac{v-v_0}{\sigma}\right)^2\right\} \quad \text{and} \quad L = \frac{h}{\left(1+\left(\frac{v-v_0}{\sigma}\right)^2\right)}, \tag{3.7}$$

where h is the height of the line, σ its width and v_0 its central velocity. See the example fitted pseudo-Voigt functions in the bottom panel of Figure 3.8. v_0 is constrained into the range $[\mathrm{v}_* - \mathrm{dv}; \mathrm{v}_* + \mathrm{dv}]$ with dv being the velocity resolution of the survey, and v_* the velocity of the line obtained previously in the detection step. To reduce the statistical fluctuations in the SEDIGISM data, which has the finest velocity resolution, we downsampled the ^{13}CO$(2-1)$ and C^{18}O$(2-1)$ profiles to a velocity resolution of $\mathrm{dv} = 0.5$ km s^{-1}.

The sum of all detected line components is fitted to reproduce the observed $T_{\rm B}$ profile. For each detected line, the best-fit parameters η, h, σ, and v_0 are determined using a χ^2 minimization method. To preserve the observed photometry, the residuals between the observed and fitted spectra in each velocity channel are redistributed among the fitted lines proportionally to their intensity in that channel. Finally, the integrated intensity, $W_{\rm CO}$, for each line is calculated by integrating the corresponding pseudo-Voigt function over the entire velocity range.

More detailed descriptions of this method can be found in Chapter 2 of [169] and in [170].

The line component decomposition is performed independently for each gas emission data, including HI and the CO isotopologues. The different lines separated in velocity can be associated with different structures at various distances, i.e., in the CMZ or in the foreground or background. This allows us not only to identify molecular clouds within the CMZ but also to distinguish and separate gas components outside the CMZ. This separation is feasible because gas in the Galactic disk generally has different properties than the gas in the CMZ. These aspects will be discussed in detail in the following section.

3.1.4 Disk component separation

Due to our viewing angle, the emission observed along the line of sight toward the CMZ inevitably includes contributions from the Galactic disk, both in the foreground (disk gas between the CMZ and the observer) and the background (disk gas located behind the CMZ). To disentangle these components, we exploit the distinct physical and kinematic properties of gas in the CMZ compared to those in the Galactic disk.

While exploring the T_B of $^{13}CO(1-0)$ versus $^{12}CO(1-0)$ across different velocity ranges, distinct behaviours are observed. As shown in Figure 3.9, the relationship between $T^{10}_{^{12}CO}$ and $T^{10}_{^{13}CO}$ becomes noticeably steeper within the velocity range ~ -70 and ~ 10 km s^{-1}, compared to velocities outside this interval. As explained in Chapter 2, gas in the CMZ is moving at much higher absolute velocity compared to the gas in the disk. In contrast, most foreground gas is located in the Local Arm, which rotates at approximately the same angular velocity as the Sun, resulting in relative velocities closer to zero.

This suggests that the $^{12}CO(1-0)$ line becomes more saturated in the disk than in the CMZ. The higher level of turbulence in the CMZ likely reduces the optical depth of the $^{12}CO(1-0)$ lines, thereby increasing its maximal T_B. Since the ^{13}CO emission lines are intrinsically less optically thick, they are less susceptible to this saturation effect. This behaviour can be exploited to distinguish between disk and CMZ components. Accordingly, we compute the ratio $T_{^{12}CO}/T_{^{13}CO}$ for each velocity-integrated brightness measurement.

Two additional parameters can be used to distinguish the disk from the CMZ. For any given line of sight, the number of emission lines, N_{lin}, tends to be higher in the disk than in the CMZ, whereas the average line width $\bar{\sigma}_v$ is typically larger in the CMZ. This is consistent with the higher levels of turbulence and shear present in the CMZ, which lead to greater velocity dispersion both within individual clouds and between neighbouring clouds, compared to the Galactic disk.

The separation of disk contamination from the CMZ has been carried out using clustering methods, and was performed mostly by Sruthiranjani Ravikularaman (explained extensively in her Thesis [167]). A wide range of clustering algorithms exists, each relying on different strategies. In our case, since the number of clusters is known in advance (CMZ and disk), we employ the `AgglomerativeClustering`[3] algorithm. This method performs a hierarchical clustering using a bottom-up approach, where each line starts in its own cluster, and they are successively merged until the requested number of clusters is obtained. Given the large number of emission lines, we use the `InductiveClustering`[4] method to reduce computational cost. In this approach, clustering is first performed on a small subset of the data, which is then used to train a classifier that is subsequently applied to the remaining data. Both algorithms are available in the `scikit-learn` Python library [66].

The parameter space for clustering consists of N_{lin}, $\bar{\sigma}_v$ and the brightness temperature ratio $T_{^{12}CO}/T_{^{13}CO}$. For each longitude and velocity value, we calculate the sum of $N_{lin,^{12}CO}$, as well as the average values of $T_{^{12}CO}/T_{^{13}CO}$ and $\bar{\sigma}_{v,^{12}CO}$ over the latitude range covered by our map. The resulting parameter maps as functions of (l, v) are shown in Figure 3.10.

To implement the separation, `AgglomerativeClustering` was applied on 20% of the emission lines, randomly selected from the dataset. The clustering result is used to train

[3] https://scikit-learn.org/stable/modules/generated/sklearn.cluster.AgglomerativeClustering.html
[4] https://scikit-learn.org/stable/auto_examples/cluster/plot_inductive_clustering.html

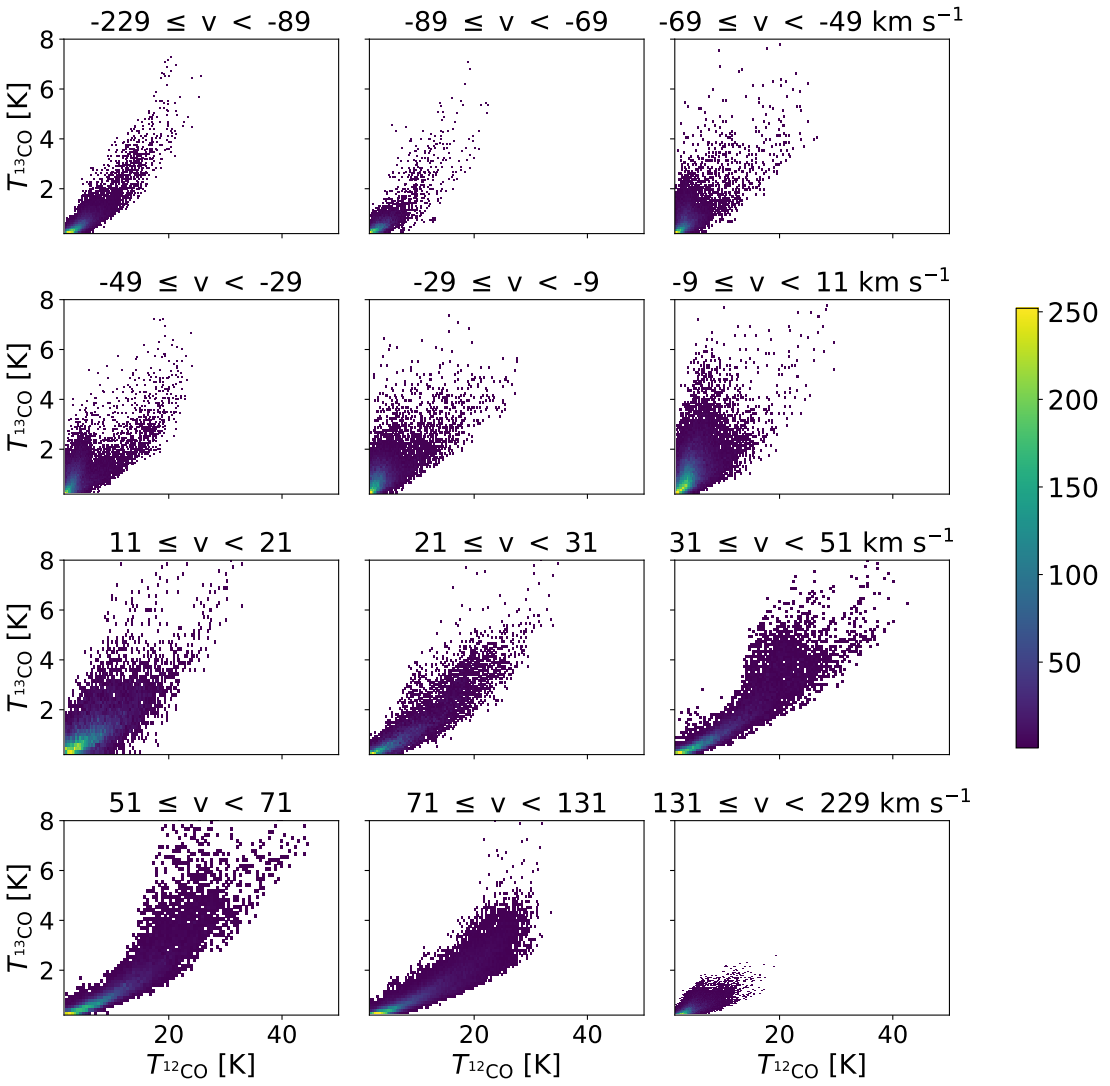

Figure 3.9: $T^{10}_{^{13}\mathrm{CO}}$ vs $T^{10}_{^{12}\mathrm{CO}}$ two-dimensional histogram for various velocity ranges. We can notice how the histogram changes its shape at different velocities. In particular, for the velocity range between ~ -70 and ~ 10 km s^{-1}, the slope is much steeper.

a support vector classifier (SVC)[5]. This trained classifier is subsequently applied to the full dataset, producing a Boolean mask in longitude and velocity space. The result of the clustering into two groups – the CMZ and the disk –, in the parameter space used for classification, as shown in Figure 3.11. The clustering is performed on ^{12}CO$(1-0)$ data, and the resulting classification is then applied as a mask to the other datasets. Finally, the velocity and W_{CO} thresholds are enforced to reassign lines between the CMZ and disk components where necessary.

To minimise contamination from foreground and background disk emission being misidentified as CMZ gas, two further conditions are imposed: (i) the upper limit of the ± 80 km s^{-1} for the line velocity, and (ii) upper limits of 100 and 5 K km s^{-1} on the integrated intensity of ^{12}CO$(1-0)$ and ^{13}CO$(2-1)$, respectively. The thresholds in (ii) are empirically determined from the distribution of the integrated intensities in regions

[5] https://scikit-learn.org/stable/modules/generated/sklearn.svm.SVC.html, with probability = True, gamma = 1, C = 100

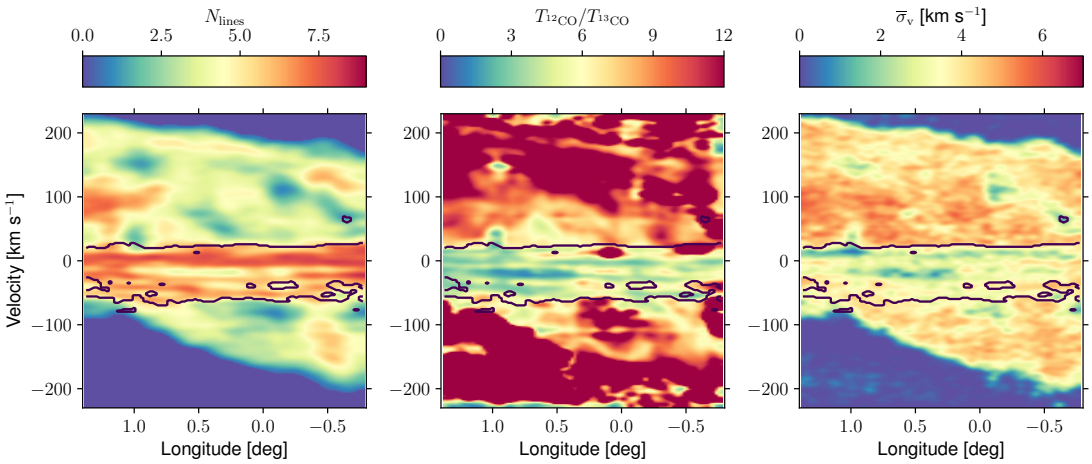

Figure 3.10: Parameter maps involved in the disk component separation. From left to right: longitude-velocity diagrams of the number of ^{12}CO emission lines, the brightness temperature ratio $T_{^{12}\rm CO}/T_{^{13}\rm CO}$, and the ^{12}CO line width. The overlaid contours delineate the two components identified via hierarchical clustering, using these three parameter maps as input. Pixels outside the contour are associated with the CMZ, while those inside are attributed to the disk, provided they also satisfy the additional criteria described in the text (see Sect. 3.1.4). Figure from our CMZ paper I [173].

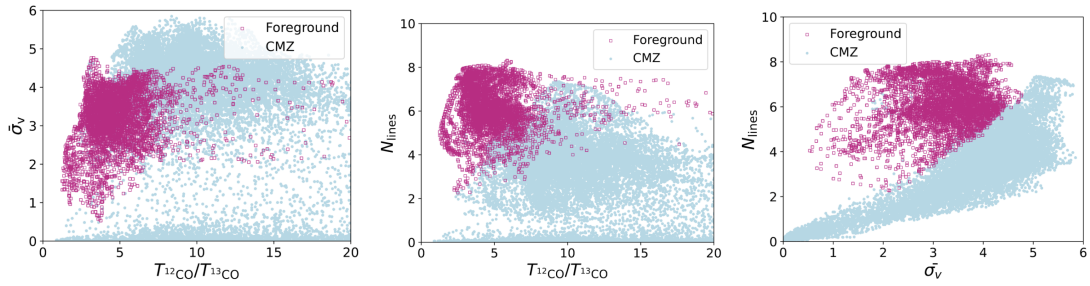

Figure 3.11: Galactic disk and CMZ separation using `AgglomerativeClustering`, based on the parameters $T_{^{12}\rm CO}/T_{^{13}\rm CO}$, $N_{\rm lin}$, and $\bar{\sigma}_v$. Figure adapted from [167].

outside the CMZ.

3.1.5 Hydrogen column density estimation

Atomic phase: $N_{\rm HI}$

Equation 3.2 is used to estimate the HI column density from HI brightness temperature, following continuum subtraction [130] and after applying the HI absorption correction described in section 3.1.2. A spin temperature of $T_{\rm S} = 146.2 \pm 16.1$ K is adopted, based on measurements by [191] for the region towards the GC. This value is, however, not specific to the CMZ, since the CMZ is not well-resolved in the HI data. $N_{\rm HI}$ is computed separately for the CMZ and disk components.

The resulting HI column density, $N_{\rm HI}$ maps are shown in the first panel of Figure 3.16.

Molecular phase: $N_{\rm H_2}$

The H_2 column density is calculated using the relation given in Equation 3.3.

Although typical values found for the $X_{\rm CO}$ factor at Galactic scale are around $2{\times}10^{20}$ cm^{-2} K^{-1} km^{-1} s, [51] showed that this value overestimates the gas mass in the CMZ by a factor of 10. In fact, the $X_{\rm CO}$ factor varies both within individual clouds and across the Galaxy, depending on a range of environmental parameters. Accurately estimating $N_{\rm H_2}$, therefore, requires accounting for these variations. The dependence of $X_{\rm CO}$ factor on various physical conditions has been explored through three-dimensional magnetohydrodynamic (MHD) simulations of Galactic disks [81, 82, 105]. In this work, the results from [82] is adopted, which provides an explicit prescription for the evolution of $X_{\rm CO}$ as a function of metallicity Z (in units of $Z_\odot$), resolved scale, r, and integrated intensity of each line decomposed in velocity, $W_{\rm CO,\,i}$, as:

$$X^{10}_{^{12}{\rm CO,\,i}} = f(W^{10}_{^{12}{\rm CO,\,i}}) W^{10}_{^{12}{\rm CO}}, i^{0.19\log(r)} Z^{-0.8} r^{-0.25}, \tag{3.8}$$

$$X^{21}_{^{12}{\rm CO,\,i}} = g(W^{21}_{^{12}{\rm CO,\,i}}) W^{21}_{^{12}{\rm CO,i}}{}^{0.34\log(r)} Z^{-0.5} r^{-0.41}, \tag{3.9}$$

where the subscript i indicates that the value corresponds to individual lines, while the superscripts 10 and 21 of $W_{\rm CO,\,i}$ indicate the transition lines $(1-0)$ and $(2-1)$, respectively. f and g are derived from the mean values given by the simulation (see yellow points in Figures 10 and 15 of [82] for ^{12}CO$(1-0)$ and ^{12}CO$(2-1)$, respectively). The reference values for f and g in their figures were computed for $Z=1$ and $r=2$ pc, so we correct them for the resolved scale and metallicity as:

$$f = \frac{X^{10}_{^{12}{\rm CO,\,i,\,figure}}(W^{10}_{^{12}{\rm CO,\,i}}, Z=1, r=2\,{\rm pc})}{(W^{10}_{^{12}{\rm CO,\,i}}{}^{0.19\log(2)} 2^{-0.25})}, \tag{3.10}$$

with similar correction for g.

Due to the higher turbulence levels in the CMZ, we introduce an additional correction to the relationship presented in Equation 3.8. Turbulence in the CMZ results in larger velocity dispersions, which in turn reduce the optical thickness of the CO lines compared to gas in the disk. The simulation by [28] incorporates a virial parameter, defined as the ratio of kinematic to gravitational potential energies, to account for varying turbulence levels. Variations in the virial parameter predominantly affect the shape of the $X_{\rm CO}$ curve at high $W_{\rm CO}$ values, after the minimum in $X_{\rm CO}$ (see the dotted lines in Figure 3.12), while the average trend at low $W_{\rm CO}$ the remains largely unaffected. To account for this effect in our analysis, we introduce an empirical correction in the form of a power-law modification to Equation 3.8:

$$X^{10}_{^{12}{\rm CO,\,i}} = f(W^{10}_{^{12}{\rm CO,\,i}}) \left(\frac{W^{10}_{^{12}{\rm CO,\,i}}}{W^{10}_{^{12}{\rm CO,\,i,\,Xmin}}}\right)^{\eta} W^{10}_{^{12}{\rm CO,\,i}}{}^{0.19\log(r)} Z^{-0.8} r^{-0.25}. \tag{3.11}$$

with $W^{10}_{^{12}{\rm CO,\,i,\,Xmin}}$ the $W_{\rm CO}$ value where there is a minimum in $X_{\rm CO}$.

The comparison of $X_{\rm CO}$ predictions before and after the power-law correction is illustrated in Figure 3.12.

Note that Equations 3.8 and 3.9 provide the $X_{\rm CO}$ evolution only as a function of integrated line emissions of ^{12}CO$(1-0)$ and ^{12}CO$(2-1)$, while we have ^{13}CO$(1-0)$, ^{13}CO$(2-1)$, and C^{18}O$(2-1)$ observations. Therefore, we must determine the average line ratio $\overline{R}_{1312}$ between ^{12}CO$(1-0)$ and ^{13}CO$(1-0)$ isotopologues. We assume that this scaling factor applies similarly to both transition lines. This assumption is supported by the study of [65] in Orion clouds, where $\overline{R}_{1312}$ is similar for both transitions, and close to the value we find toward the GC. Hence, we have:

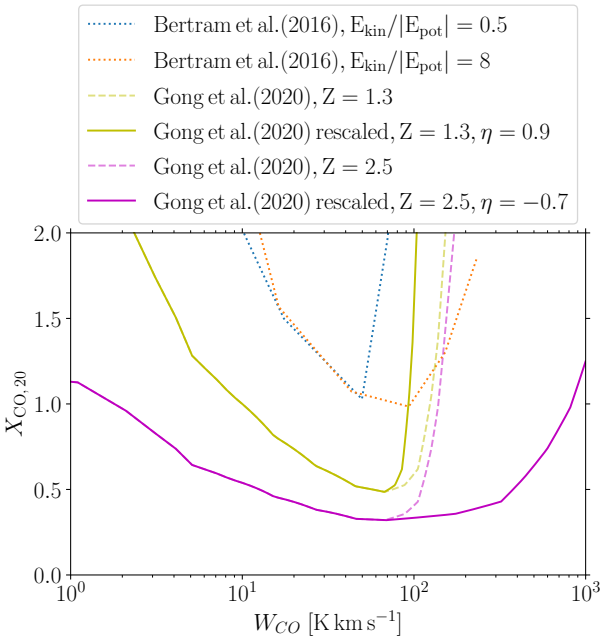

Figure 3.12: $X_{\rm CO}$ correction to account for the turbulence level in the CMZ. Mean trend for the $X_{\rm CO}$ factor evolution as a function of $W_{\rm CO}$, as predicted by simulations, is shown by curves adapted from Figure 6 of [28] and Figure 10 of [82]. The influence of turbulence is incorporated in [28] by varying the ratio of kinetic to gravitational potential energies, represented by the dotted curves. The dashed curves correspond to the reference functions from [82], denoted $f(W^{10}_{^{12}{\rm CO,\,i}})$ in Equation 3.8. A power-law correction with index η can be applied to this curve to mimic the effect of the turbulence, as introduced in Eq. 3.11. Figure from our CMZ paper I [173].

$$\overline{R}_{1312} = \mathrm{median}(\mathrm{W}^{10}_{^{13}{\rm CO,\,i}}/\mathrm{W}^{10}_{^{12}{\rm CO,\,i}}), \tag{3.12}$$

$$W^{21}_{^{12}{\rm CO,\,i}} = W^{21}_{^{13}{\rm CO,\,i}}/\overline{R}_{1312}. \tag{3.13}$$

In the top panel of Figure 3.13, the two-dimensional histogram shows the correlation between $W^{10}_{^{13}{\rm CO,\,i}}$ and $W^{10}_{^{12}{\rm CO,\,i}}$, which are found to be well-correlated, with a Pearson correlation coefficient of 94%. We derive a median conversion factor between the two isotopologues over the full $W_{\rm CO}$ range of $\overline{R}_{1312} = 0.14^{+0.04}_{-0.03}$, where positive and negative uncertainties correspond to the 84 and the 16 percentile, respectively. This value remains compatible with the mean value 0.12 ± 0.01 reported by [203], based on the same dataset, even after applying our baseline correction.

The strong correlation observed between ^{12}CO$(1-0)$ and ^{13}CO$(1-0)$, except toward the cores of Sgr B2 and Sgr A, suggests that the optical thickness of the lines is rather low along most lines of sight toward the CMZ. This conclusion is supported by several earlier studies. [51] demonstrated that the optical depth in the CMZ is significantly lower ($\tau \lesssim 2$ for $W_{^{12}{\rm CO}}/\ W_{^{C18}{\rm O}} > 60$) than in the Galactic disk ($\tau \geq 10$), except in a few dense cores such as Sgr B2. Similarly, [67] reported lower optical depths for ^{12}CO$(1-0)$ in the GC compared to the disk, and proposed two explanations: (i) even at comparable densities, higher temperatures in the CMZ excite more molecules into higher-J states, thereby reducing the optical depth of lower-J transitions; and (ii) larger velocity dispersions in the CMZ further decrease optical depth due to line broadening.

In contrast to ^{12}CO$(1-0)$, the ^{13}CO$(1-0)$ transition does not saturate in the simulations by [28], and the corresponding $X_{\rm CO}$ factor remains nearly constant at large

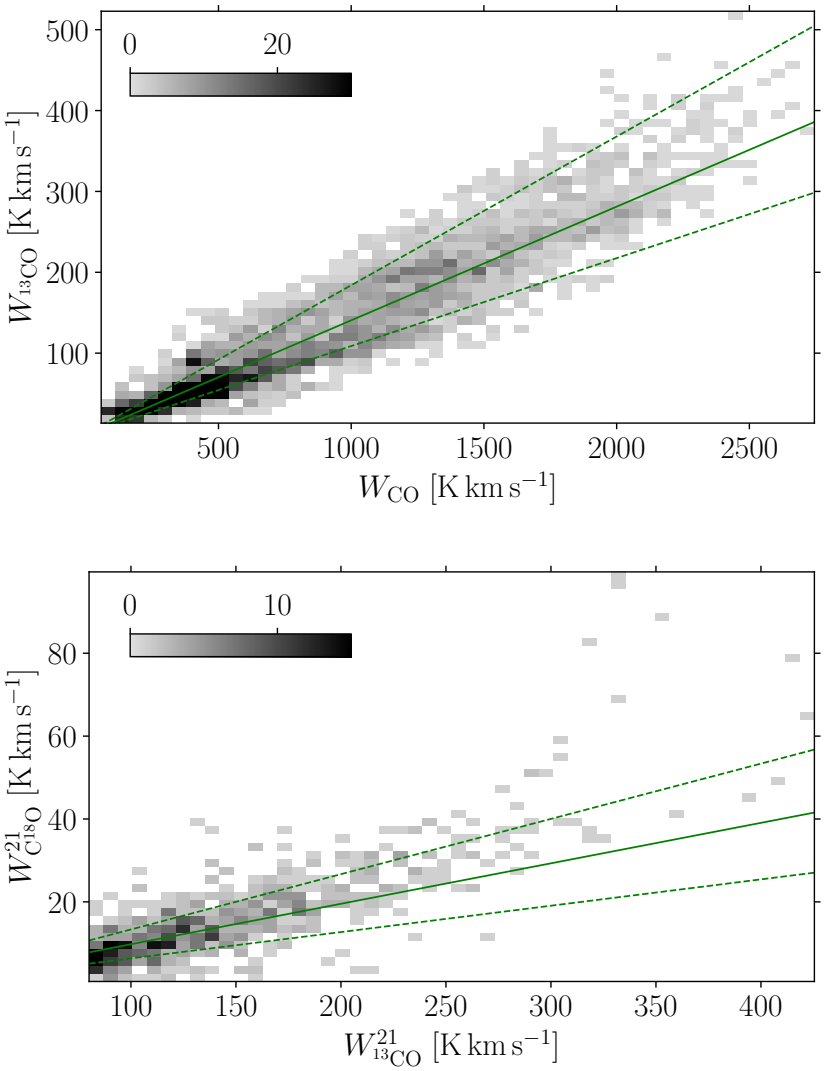

Figure 3.13: Two-dimensional histograms of the integrated line intensities, $W_{\mathrm{CO,i}}$. Top: $W_{^{13}\mathrm{CO}}$ versus $W_{^{12}\mathrm{CO}}$ for the $(1-0)$ transition. Bottom: $W_{\mathrm{C^{18}O}}$ versus $W_{^{13}\mathrm{CO}}$ for the $(2-1)$ transition. The green full lines in both panels correspond to a linear relation for which the slope is the median W_{CO} ratio, and dashed lines give 1σ errors from the 16 and 84 percentiles. Figure from our CMZ paper I [173].

W_{CO} with minimal impact from turbulence. Therefore, the η parameter is not introduced for rarer isotopologues.

The correlation between $^{13}\mathrm{CO}(2-1)$ and $\mathrm{C^{18}O}(2-1)$ is also examined, as shown in the bottom panel of Figure 3.13. Saturation of the $^{13}\mathrm{CO}(2-1)$ line is observed only in the densest cores, such as Sgr B2 and Sgr A, where a deviation from linearity appears. To account for this, we apply a saturation correction following the approach of Yan et al. [217] (see their Figure 3). The corrected $W^{21}_{^{13}\mathrm{CO,i}}$ is obtained by scaling $W^{21}_{\mathrm{C^{18}O,i}}$ using the ratio between $^{13}\mathrm{CO}(2-1)$ and $\mathrm{C^{18}O}(2-1)$ measured in the unsaturated regime, specifically in the range 80 $<W^{21}_{^{13}\mathrm{CO,i}} <$ 200 K km s^{-1}. This ratio, denoted $\overline{R}_{1813}$ is defined analogously to $\overline{R}_{1312}$ in Equation 3.12:

$$\overline{R}_{1813} = \mathrm{median}(\mathrm{W}^{21}_{\mathrm{C^{18}O,i}}/\mathrm{W}^{21}_{^{13}\mathrm{CO,i}}). \tag{3.14}$$

For saturated lines, $W^{21}_{^{13}\mathrm{CO}} > 200$ K km s^{-1}, the following scaling is applied:

$$W^{21}_{^{13}\mathrm{CO,\,i}} = W^{21}_{\mathrm{C}^{18}\mathrm{O,\,i}} / \overline{R}_{1813}. \tag{3.15}$$

The correlation between $^{13}\mathrm{CO}(2-1)$ and $\mathrm{C}^{18}\mathrm{O}(2-1)$ is found to be 77%, reflecting deviations from linearity at both high and low W_{CO} values. At large W_{CO}, the $^{13}\mathrm{CO}(2-1)$ line saturates in the densest cores, while at low W_{CO}, there is not enough sensitivity, especially to detect $\mathrm{C}^{18}\mathrm{O}$ emission. In the intermediate range, $80 < W^{21}_{^{13}\mathrm{CO,\,i}} < 200$ K km s^{-1}, a median scaling factor of $\overline{R}_{1813} = 0.10^{+0.04}_{-0.03}$ is obtained.

With this approach, we can estimate $N_{\mathrm{H_2}}$ using $W^{10}_{^{12}\mathrm{CO,\,i}}$ and $W^{21}_{^{13}\mathrm{CO,\,i}}$ separately, such that:

$$N_{\mathrm{H_2}}(l,b) = \sum_{i}^{\mathrm{n_{lines}}} X^{10}_{^{12}\mathrm{CO,i}}(W^{10}_{^{12}\mathrm{CO,i}}, Z, r, \eta)\, W^{10}_{^{12}\mathrm{CO,i}}(l,b), \tag{3.16}$$

$$N_{\mathrm{H_2}}(l,b) = \sum_{i}^{\mathrm{n_{lines}}} X^{21}_{^{12}\mathrm{CO,i}}(W^{21}_{^{12}\mathrm{CO,i}}, Z, r)\, W^{21}_{^{12}\mathrm{CO,i}}(l,b). \tag{3.17}$$

In order to match the $N_{\mathrm{H_2}}$ values obtained from $^{12}\mathrm{CO}(1-0)$ lines with the ones obtained from $^{13}\mathrm{CO}(2-1)$ lines, we fit the parameters Z and η by minimising the difference between the two $N_{\mathrm{H_2}}$ estimates using a least-squares approach. Thanks to the prior separation of CMZ and disk components, the fitting can be performed independently for each region.

Table 3.3: X_{CO} best-fit parameters for the estimate of $N_{\mathrm{H_2}}$.

Component	r(pc)$^{(a)}$	$Z(Z_\odot)$	η
CMZ$^{(b)}$	2.8	2.5	-0.71 ± 0.01
CMZ	2.8	1.92 ± 0.02	-1 ± 0.1
Disk	0.8 ± 0.1	1.3 ± 0.1	0.9 ± 0.1

(a) r is computed assuming a distance to GC of 8.18 kpc for the CMZ, and an average resolved scale is obtained from the fit for the Galactic disk.
(b) Fit with fixed Z.

The best-fit parameters are listed in Table 3.3. Given the angular resolution of 0.02°, the resolved physical scales are computed assuming a distance to GC of 8.18 kpc [86] for the CMZ, resulting in $r = 2.8$ pc. For the Galactic disk, a mean distance of $\overline{d}_{\mathrm{disk}} = 2.3 \pm 0.4$ kpc is fitted, yielding an average resolved scale of $r_{\mathrm{disk}} = 0.8 \pm 0.1$ pc. Note that we are considering mean values for the disk component for simplicity. Consequently, the fitted parameters for the disk should be treated as nuisance parameters, provided for completeness rather than for physical interpretation. We expect this approximation to have a limited impact, as the disk contribution is significantly lower compared to that of the CMZ, and most of the disk gas toward the CMZ originates from its inner regions, which are denser. Therefore, the average values are dominated by disk gas within a relatively narrow range of distances and physical properties.

For the CMZ, two different models are fitted: a first one fixing the metallicity to $Z_{\mathrm{CMZ}} = 2.5$ (corresponding to $\sim +0.4$ dex), a value close to the higher mean value reported in the literature [58]; and second by allowing both Z and η to vary freely. In the first case, we obtain $\eta_{\mathrm{CMZ}} = -0.71 \pm 0.01$, which is consistent with expectations for the CMZ. Indeed, negative values of η correspond to an increased level of turbulence,

as anticipated in this region. In the second case, where both parameters are free, we find $Z_{\rm CMZ} = 1.92 \pm 0.02$ ($\sim +0.3$ dex) and $\eta_{\rm CMZ} = -1 \pm 0.1$. While these values are still physically plausible, the degeneracy between Z and η leads to a reduced quality of the fit, particularly at high $N_{\rm H_2}$. Therefore, in the following, we adopt the results from the fit with fixed metallicity, which are also the values used in Figure 3.12.

For the disk component, the best-fit mean values are $\overline{Z}_{\rm disk} = 1.3 \pm 0.1$ and $\overline{\eta}_{\rm disk} = 0.9 \pm 0.1$. These values are consistent with expectations, exhibiting lower metallicity and a positive η parameter, indicative of reduced turbulence, in comparison to the CMZ.

The systematic uncertainties associated with the fitting procedure are estimated as fractional values of the predicted $N_{\rm H_2}$, adjusted such that the reduced χ^2 reaches unity. For ^{13}CO$(2-1)$, this results in an uncertainty of 10%, while for ^{12}CO$(1-0)$, the uncertainty is 33%, likely due to the greater degree of line saturation.

In contrast, the statistical uncertainties of Z and η are only a few percent, significantly smaller than the systematic in $N_{\rm H_2}$. This discrepancy may be attributed to variations in the isotopic line ratios, whose observed dispersions are of a similar magnitude.

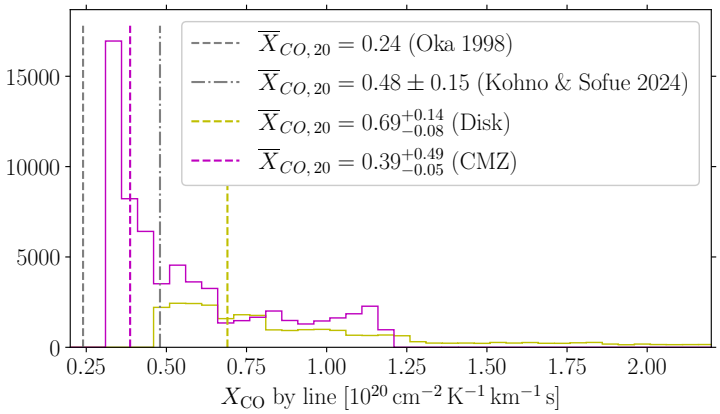

Figure 3.14: $X_{\rm CO}$ distribution derived for each fitted line. The grey dashed and dashed-dotted lines correspond to the average values reported by [147] and [115], respectively. The magenta and yellow lines are the median values of $X_{\rm CO}$ maps for the CMZ and disk components. Figure from our CMZ paper I [173].

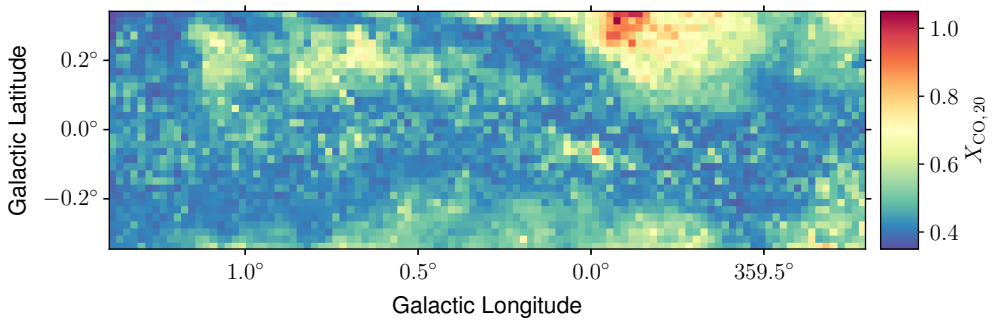

Figure 3.15: Map of $X_{\rm CO,20}$, the CO-to-H_2 conversion factor in units of 10^{20} cm^{-2}K^{-1}km^{-1}s, computed as the weighted average $X_{\rm CO}$ for each pixel across the velocity range. Figure from our CMZ paper I [173].

The resulting $X_{\rm CO}$ values are presented in Figure 3.14, which shows a histogram of the fitted $X_{\rm CO}$ values per each detected line, separated by component. The corresponding map of the $W_{\rm CO}$-weighted average of $X_{\rm CO}$ value, computed over all detected lines, is

displayed in Figure 3.15.

For the CMZ, the $X_{\rm CO}$ values for individual lines range between $(0.32 - 1.37) \times 10^{20}$ cm^{-2} K^{-1} km^{-1} s. The $X_{\rm CO}$ distribution is highly asymmetric and strongly skewed towards the lower bound, , as most of the detected lines have $W_{\rm CO}$ values between a few tens and a few hundreds of K km s^{-1}, where the $\rm X_{CO}(W_{CO})$ profile is nearly flat around its minimum (see Figure. 3.12). The median value of $X_{\rm CO}$, obtained after integrating over velocity and averaging across the entire map, is $\overline{\rm X}_{\rm CO}^{\rm CMZ} = 0.39 \times 10^{20}$ cm^{-2} K^{-1} km^{-1} s. This value is compatible with those reported in the literature, which typically fall within the range $(0.2 - 0.7) \times 10^{20}$ cm^{-2} K^{-1} km^{-1} s [see Table 3 of 115, and references therein].

For the disk, the $X_{\rm CO}$ distribution is also asymmetric but much significantly flatter, in a wider range $(0.49 - 2.87) \times 10^{20}$ cm^{-2} K^{-1} km^{-1} s. The median value in this case is 0.69×10^{20} cm^{-2} K^{-1} km^{-1} s. This value is notably lower than the usually reported Galactic average value ($\sim 2\times 10^{20}$ cm^{-2} K^{-1} km^{-1} s), which is expected given that our analysis is limited to a relatively small region towards the GC. Anyway this value should not be over-interpreted given the simplified assumptions adopted in the $X_{\rm CO}$ evolution model for the disk component.

Hydrogen column density maps

The final $N_{\rm H_2}$ column density map is derived by averaging the two independent estimates obtained from Equation 3.16 and 3.17, which use the ^{12}CO$(1-0)$ and ^{13}CO$(2-1)$ line emissions, respectively. The results are show in Figure 3.16, where the hydrogen column density maps for the atomic and molecular phases are displayed (first and second panels), along with the total gas column density maps for the entire region (third panel), the disk component (forth panel), and the CMZ component (fifth panel).

The relative uncertainty of the two $N_{\rm H_2}$ estimates, with respect to their average, is shown in Figure 3.17, where the larger of the two uncertainties is retained for each pixel. Figure 3.18 illustrates the relative difference between the two estimates as a function of their mean, in a two-dimensional histogram. On average, the ^{13}CO$(2-1)$-based approach yields values approximately 5% higher, with a dispersion of about 30%, as indicated by the solid and dashed lines in Figure 3.18.

It can also be observed that the relative uncertainty increases at lower $N_{\rm H_2}$ and becomes increasingly asymmetric. This behaviour can be attributed to the limitations of the $X_{\rm CO}$ ($W_{\rm CO}$) relations derived from simulations, which may not fully capture the variation in $X_{\rm CO}$ for the two tracers near their sensitivity thresholds, where the uncertainties in $W_{\rm CO}$ also become significant. However, for the CMZ, uncertainties at such low column densities are not the dominant source of error. Instead, the absolute uncertainty is driven by higher column density regions, particularly where $N_{\rm H_2} > 4.9 \times 10^{22}$ cm^{-2}.

Another result is the maps of the molecular hydrogen fraction, f_{H_2}, and the fraction of the disk contamination, f_{disk}, in the total hydrogen column density, which are presented in Figure 3.19. Contribution of the atomic gas toward the GC is ∼15-30%. When the disk contamination is removed, this fraction decreases to about ∼5-15% within the CMZ clouds, still a non-negligible contribution.

Just 0.2° away from the CMZ, the disk component becomes dominant, and in these regions the atomic gas fraction rises to 50-70%. This highlights the importance of accounting for both the atomic gas phase and the disk component when analysing γ-ray emission from the direction of the CMZ. The diffuse Galactic γ-ray emission largely originates from the interaction of CRs with all phases of gas in the ISM. Therefore, even in dense regions such as the CMZ clouds, the contribution from atomic gas and disk

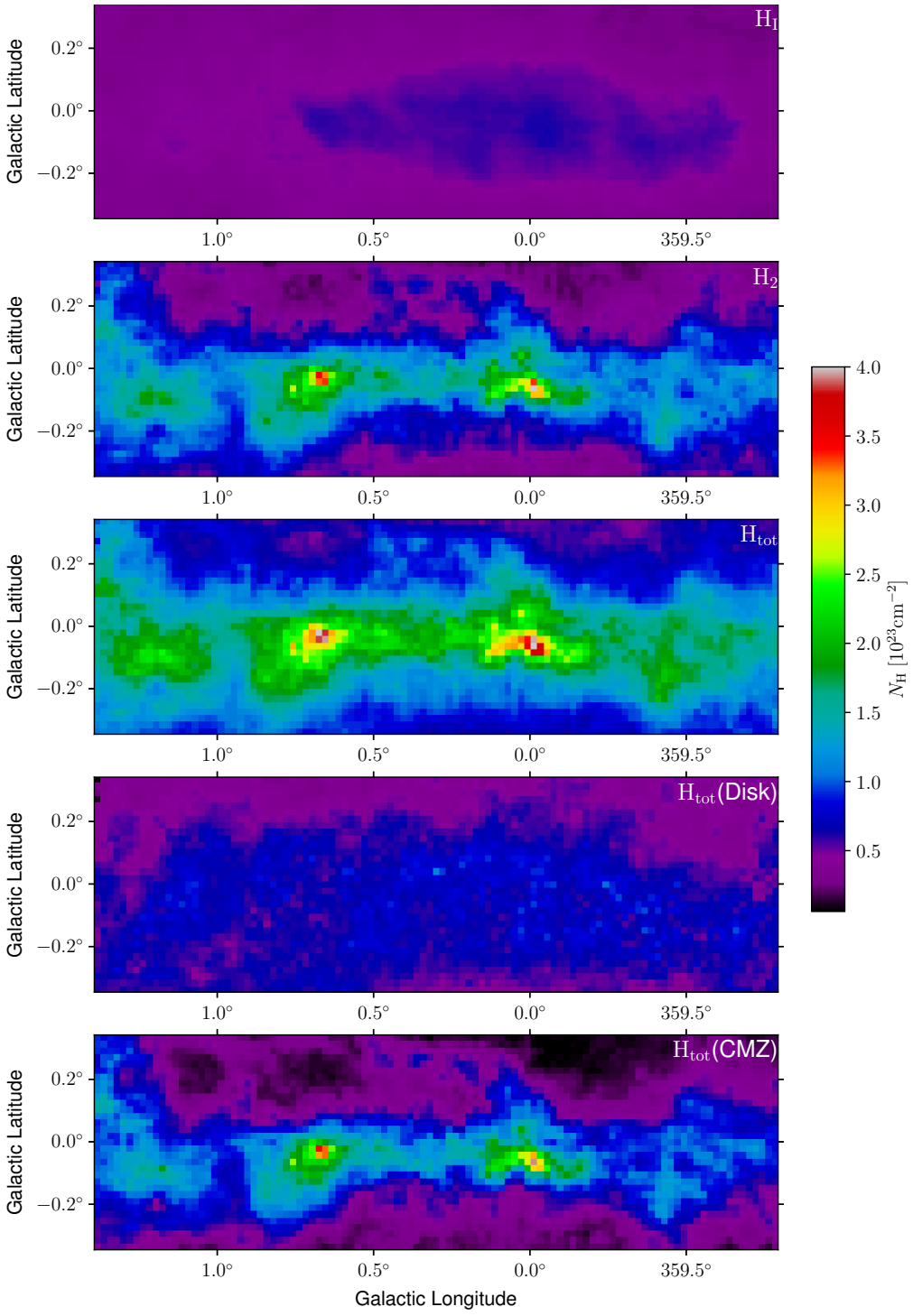

Figure 3.16: Hydrogen column density for the different phases and components. From top to bottom: HI, H_2, H_{tot} = HI + H_2, total H_2 in the disk component, and total H_2 in the CMZ component. Figure from our CMZ paper I [173].

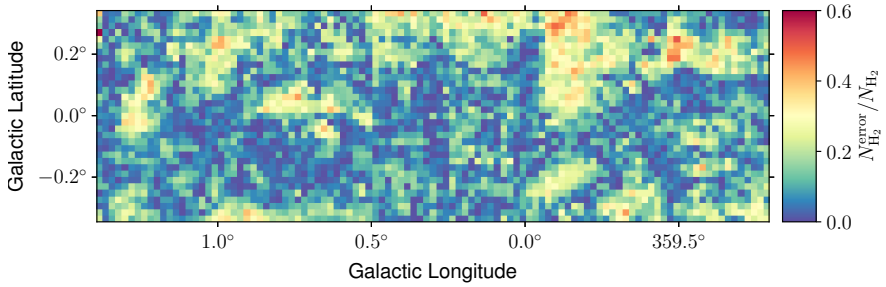

Figure 3.17: Relative uncertainty with respect to the average N_{H_2} estimate, for the two estimates using $^{12}CO(1-0)$ and $^{13}CO(2-1)$. The relative uncertainty is taken as the maximal deviation among the two CO isotopes considered. Figure from our CMZ paper I [173].

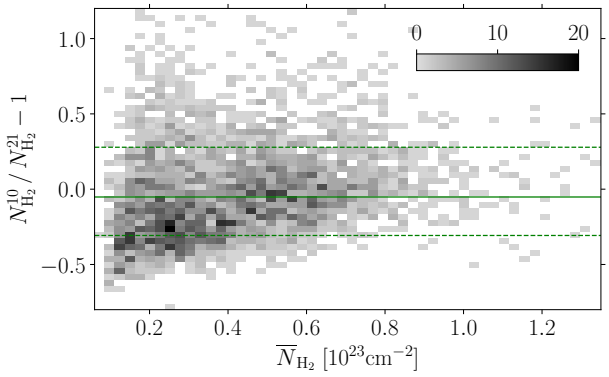

Figure 3.18: Relative uncertainty on the N_{H_2} estimate from $^{12}CO(1-0)$ and $^{13}CO(2-1)$ as a function of the average estimate. Figure from our CMZ paper I [173].

components should not be neglected.

3.1.6 Mass estimates

The total hydrogen column density is the sum of the atomic and the molecular column densities:

$$N_{\rm H} = N_{\rm HI} + N_{\rm H_2}. \tag{3.18}$$

The total gas mass is then computed as

$$M = \mu\, m_{\rm H}\, d^2 \sum_{\rm pixels} N_{\rm H}\, {\rm d}\Omega, \tag{3.19}$$

with d the distance to the observer, $\mathrm{d}\Omega$ the solid angle, $m_{\rm H}$ the atomic mass, and $\mu = 1.4$ the mean molecular weight [same as in 192].

The resulting atomic, molecular, and total gas masses, integrated over the full field of view, are reported in Table 3.4, where values for the CMZ and disk components are also listed separately. For this comparison, the disk is assumed to lie at the same distance as the CMZ, to evaluate the potential bias in total mass estimates if the two components are not separated. We find the total gas mass in the CMZ to be $2.3^{+0.3}_{-0.3} \times 10^7$ M$_\odot$ with the atomic gas contributing only ∼10%. In the absence of component separation, the total gas mass would increase to $4.4^{+0.3}_{-0.7} \times 10^7$ M$_\odot$, with the atomic gas contribution rising to ∼30%.

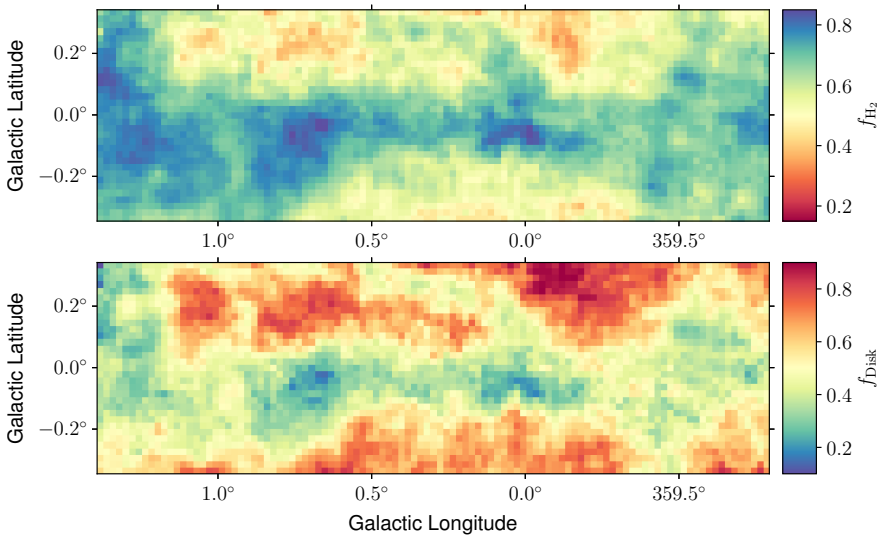

Figure 3.19: Top: map of the fraction of H_2 in the total hydrogen column density. Bottom: map of the fraction of disk component in the total hydrogen column density. Figures from our CMZ paper I [173].

Table 3.4: Gas mass per phase and component in solar masses toward the GC within $-0.8° < l < 1.4°$ and $|b| < 0.3°$.

	HI [a]	H_2 [b]	H_{tot}
Disk[c]	$1.2^{+0.0}_{-0.3} \times 10^7$	$8.9^{+1.8}_{-1.8} \times 10^6$	$2.1^{+0.2}_{-0.5} \times 10^7$
CMZ	$2.7^{+0.0}_{-0.6} \times 10^6$	$2.0^{+0.3}_{-0.3} \times 10^7$	$2.3^{+0.3}_{-0.3} \times 10^7$
Total[c]	$1.4^{+0.0}_{-0.3} \times 10^7$	$2.9^{+0.3}_{-0.3} \times 10^7$	$4.4^{+0.3}_{-0.7} \times 10^7$

[a] The lower uncertainty corresponds to a milder HI absorption correction.
[b] Positive/negative errors correspond to the min/max deviation from the average N_{H_2} estimate between the two CO isotopes considered.
[c] The mass in the disk is only computed considering the distance of the CMZ in order to evaluate the bias on the total mass estimate that would be introduced by the absence of component separation.

Our result is similar to those reported by Sofue [192] who found a total gas mass of 2.8×10^7 $M_\odot$ and a CMZ gas mass of 2.3×10^7 $M_\odot$. The small differences in the CMZ gas mass may be attributed to the slightly different region definition of the analysed field of view and the use of a constant X_{CO} factor in their analysis. A larger discrepancy arises in the atomic gas mass, where our estimate is approximately three times higher than theirs. This can be explained by differences in methodology: Sofue [192] derived a minimal mass assuming optically thin emission, whereas our approach, which uses a fixed spin temperature, yields a mass about 1.6 times larger. Furthermore, the correction for HI self-absorption in the GC allows recovery of approximately 1.7 times more mass, further contributing to the difference.

3.2 Dust in the CMZ

Several studies use thermal dust emission as the tracer of the total gas column density. In this work, we quantify the variations of the dust opacity and discuss how it relates to the evolution of dust properties in different environments. This is crucial to determine in which limit the dust can be used as a reliable gas.

3.2.1 Dust Datasets

The dust submillimetre emission maps used in this study are listed in Table 3.5. Three different datasets are explored: (i) the *Herschel* infrared Galactic Plane Survey (Hi-GAL)[6], which includes the measurements from two instruments *Herschel* PACS and SPIRE, and covers five wavebands at 70, 100, 250, 350 and 500 µm [137]; (ii) the Atacama Pathfinder EXperiment (APEX) [7] data at 870 µ*m* and corrected using *Planck* data [49]; and (iii) the *Planck* High Frequency Instrument (HFI)[8] data at 100, 143, 217, 353, 545, 857 GHz.

Table 3.5: Dust thermal emission datasets used in this study.

Wavelength [µm]	Angular resolution beam size (pixel) [°]	Sensitivity (rms noise) [mJy/beam]	Instrument
70, 160	0.0023, 0.0033 (beam/2.66)	Fig 3 of Ref.	Herschel-PACS
250, 350, 500	0.005, 0.0067, 0.0096 (beam/3)	Fig 3 of Ref.	Herschel-SPIRE
870	0.0053 (0.0017)	70 – 90	APEX + *Planck*
350, 550, 850, 1382, 2096, 2998	0.070–0.162 (0.029)	Table 12 of Ref.	*Planck*-HFI

Some data reduction steps were necessary before performing dust emission fitting using the Planck function. For the Hi-GAL and APEX-*Planck* datasets, only minimal preparation was required. This included reorienting the maps from equatorial coordinates to galactic coordinates, interpolating over missing pixels, and downsampling to lower angular resolution as for the HI and CO line emission maps.

For the *Planck*-HFI datasets, an additional correction was needed, as the 100, 217, and 353 GHz bands are significantly contaminated by CO molecular emission. These bands are affected by the CO rotational transitions at $J = (1 \rightarrow 0)$ (115 GHz), $J = (2 \rightarrow 1)$ (230 GHz), and $J = (3 \rightarrow 2)$ (345 GHz), respectively. To correct for this contamination, we followed the procedure outlined in Section 3.4 of [131]. The *Planck*-HFI PR3-2018 data is used, as it provides available CMB-subtracted dust emission maps along with dedicated CO correction maps.

Before subtracting the CO contribution from the *Planck* intensity maps, appropriate unit conversions must be applied. The *Planck* maps are provided in native units of $K_{\rm CMB}$, while the CO emission map is given in units of $K_{\rm RJ}$ km s^{-1} for $J = (1 \rightarrow 0)$ transition line emission. To convert the CO emission into $K_{\rm CMB}$, we assume the simplification that the observed emission arises entirely from the ^{13}CO isotope. The Planck-observed CO intensity in units of $K_{\rm CMB}$ is then derived using the following scaling:

$$I^{\rm NM}_{{\rm CO},\,\nu} = I_{\rm CO} F^{\rm NM}_{{\rm CO},\,\nu} R^{\rm NM}, \tag{3.20}$$

[6] Public data available at *Herschel* Science Archive
[7] Public data available at ATCA official webpage.
[8] Public data available at Planck Legacy Archive.

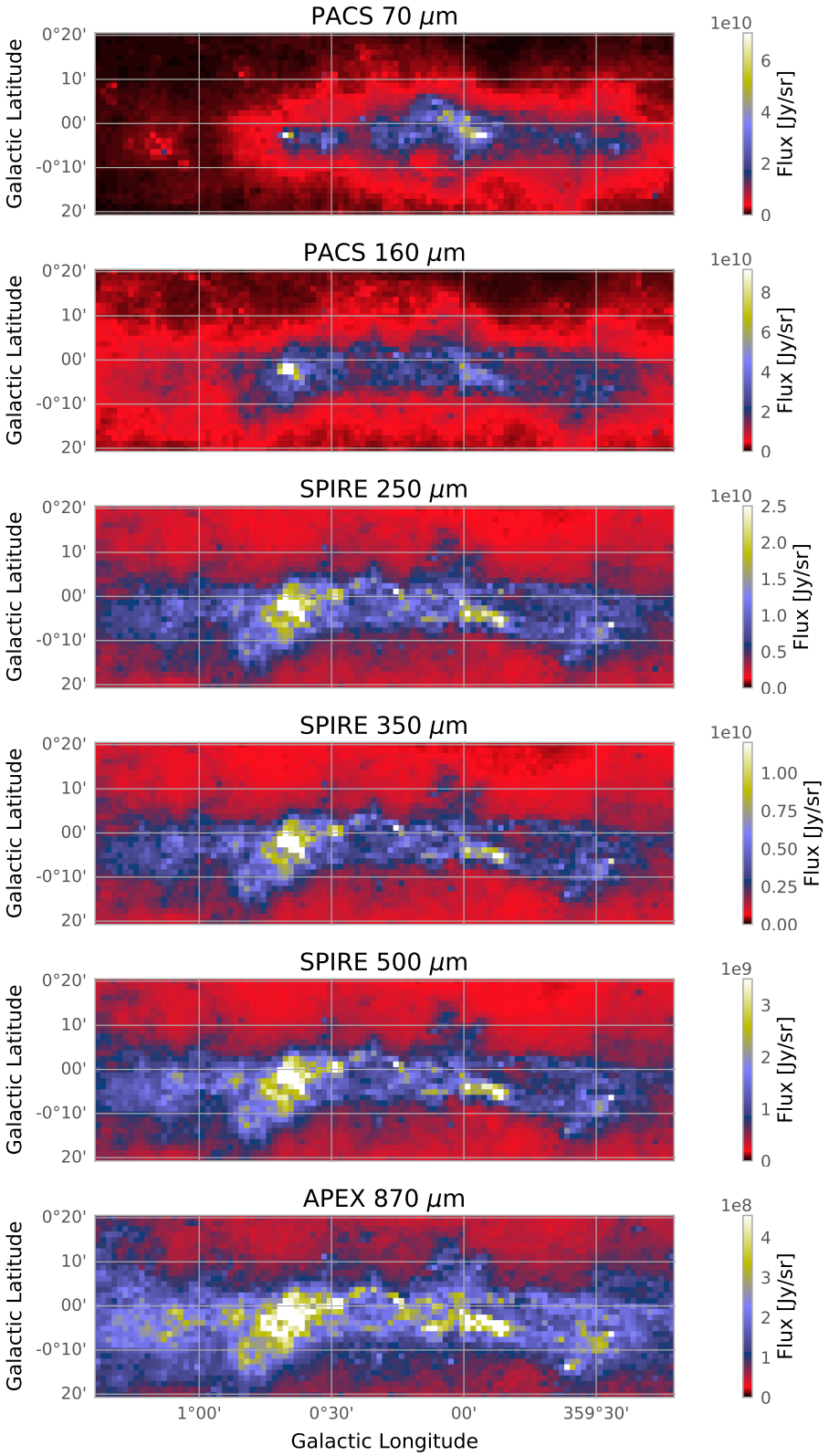

Figure 3.20: Herschel and APEX dust thermal emission maps. The maps are downsampled to the same angular resolution as the CO line emission maps ($\sim$0.02°), and cut out to the same field of view.

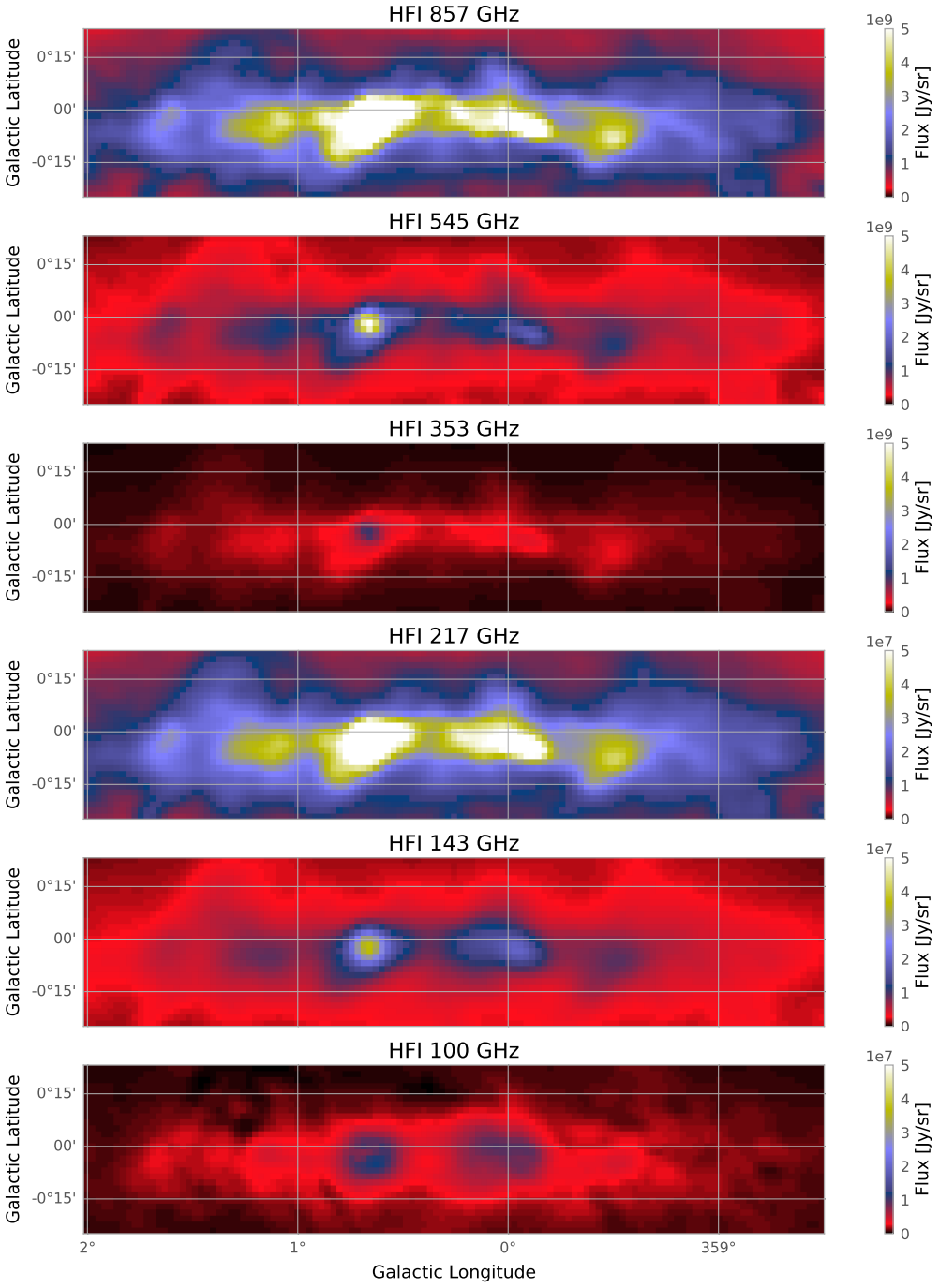

Figure 3.21: *Planck*-HFI dust thermal emission maps. The maps have a slightly sparser angular resolution than the target 0.02°, thus the original angular resolution is maintained. For the Planck fit, HFI maps are used only for the two-component model (see Section 3.2.2), and only in the first step to determine the spectral index β_2 parameter. In this step, all other dust maps are downsampled to the resolution of the HFI maps. In the next step, we recover the angular resolution of the CO maps, and fit again the two-component model using only the Herschel and APEX data points.

where NM indicates the transition $J = (N \rightarrow M)$ and $F^{\rm NM}_{{\rm CO},\nu}$ is the unit conversion factor, which for each transition is $F^{10}_{{\rm CO},\nu} = 1.478 \times 10^{-5} K_{\rm CMB}/(K_{\rm CRJ}{\rm kms}^{-1})$, $F^{21}_{{\rm CO},\nu} = 4.585 \times 10^{-5} K_{\rm CMB}/(K_{\rm CRJ}{\rm kms}^{-1})$, and $F^{32}_{{\rm CO},\nu} = 1.751 \times 10^{-4} K_{\rm CMB}/(K_{\rm CRJ}{\rm kms}^{-1})$, respectively. $R^{\rm NM}$ is the line ratio of the transition $J = (N \rightarrow M)$ relative to the $J = (1 \rightarrow 0)$. Hence $R^{10} = 1$, values for the other two transitions $R^{21} = 0.595$ and $R^{21} = 0.297$ are adopted from [160].

The reduced dust thermal emission maps are illustrated in Figures 3.20 and 3.21.

3.2.2 Modelling the dust emission

In the optically thin limit, the spectral energy distribution of the emission from dust grains can be modelled as a modified black-body (MBB) at temperature T, with the Planck function, $B_\nu(T)$, as:

$$I_\nu = \tau_\nu B_\nu(T), \tag{3.21}$$

where I_ν is the dust specific intensity and τ_ν is the optical depth.

The distribution of the dust temperature along the line of sight is inherently complex. Consequently, most studies adopt the simplifying assumption that the integrated dust emission along a given line of sight can be modelled as originating from a single-component dust mixture with an average temperature. This approach allows the use of single MBB models. For instance, [159] employed a single MBB model to fit the four available photometric bands (353, 545, and 857 GHz from the *Planck* mission and 100 μm from the Infrared Astronomical Satellite (IRAS)). While this method provides a practical approximation, it may overlook variations in dust temperature and composition along the line of sight, particularly in dense or thermally complex regions such as the CMZ.

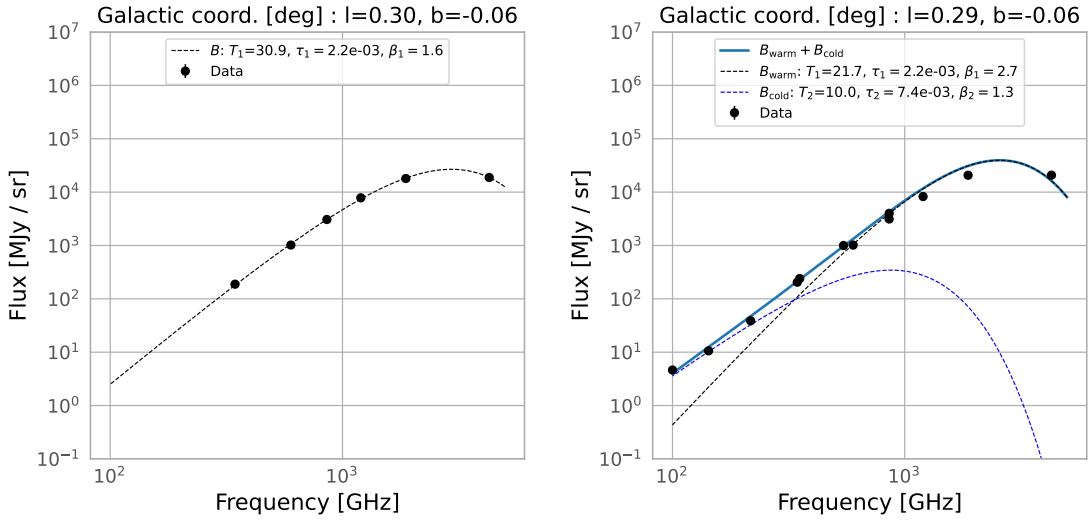

Figure 3.22: Dust thermal emission model fitting. Left: Single-component MBB model fitting, with only Herschel and APEX data points. Right: Two-component MBB model fitting using the Herschel, APEX, and HFI datasets.

The optical depth τ_ν is usually expressed as a power-law $\tau_\nu = \tau_{\nu_0}(\nu/\nu_0)^\beta$, where β is the power-law index and ν_0 is the reference frequency at which τ_{ν_0} is measured. The

single MBB can then be parametrized as:

$$I_\nu = \tau_{\nu_0} \left(\frac{\nu}{\nu_0} \right)^\beta B_\nu(T). \tag{3.22}$$

On the other hand, two-component dust models have been proposed as a more accurate representation of dust emission. [168] fitted COBE/FIRAS observations using single and two-component MBB models, and demonstrated that the two-component approach provided a significantly better fit. This model assumes that the dust emission arises from two distinct dust populations, each characterised by different temperatures and dust emissivity spectral indices β.

A few years later, [73] applied a two-component MBB model to FIRAS data to extrapolate the dust emission at 100 μm and CMB radiation, noting that single MBB models failed to reproduce the FIRAS/DIRBE spectrum accurately across both the Wien and Rayleigh-Jeans regimes. More recently, [131] adopted the model of [73] to fit the *Planck*-HFI and joint *Planck*/DIRBE maps over the 100–3000 GHz range. This approach resulted in improved predictive accuracy, particularly in the 100–217 GHz bands.

This work aims to investigate how the use of single and two-component models impacts the estimation of dust optical depth and, consequently, the derived gas mass. The two-component MBB model is expressed as the sum of the emission from warm and cold dust components:

$$I_\nu = \tau_{\nu_0}^{\rm warm} \left(\frac{\nu}{\nu_0} \right)^{\beta_{\rm warm}} B_\nu(T_{\rm warm}) + \tau_{\nu_0}^{\rm cold} \left(\frac{\nu}{\nu_0} \right)^{\beta_{\rm cold}} B_\nu(T_{\rm cold}). \tag{3.23}$$

We adopt the same reference frequency as in [159] $\nu_0 = 353$ GHz, to facilitate comparison of the results. Following the approach of Meisner and Finkbeiner [131], a spatially fixed $\beta_{\rm warm}$ is assumed, and with the best-fit value of 2.7 as reported by [73]. The free parameters in the two-component model are therefore: $T_{\rm warm}$, $\tau_{\nu_0}^{\rm warm}$, $\beta_{\rm cold}$, $T_{\rm cold}$ and $\tau_{\nu_0}^{\rm cold}$. These parameters are fitted to the data using a χ^2 minimisation method.

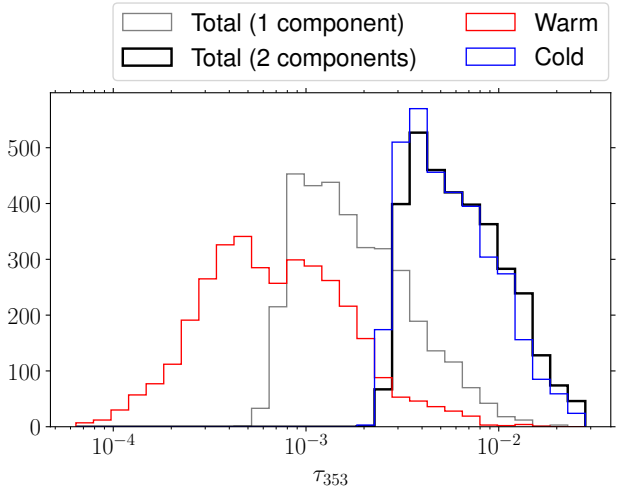

Figure 3.23: Dust optical depth histograms. The grey line corresponds to the result obtained by fitting a single-component MBB model, and the others to the fit result for the two-component MBB model. Figure from our CMZ paper I [173].

Single and two-component MBB models are fitted over the same field of view as the gas maps (i.e., $-0.8° < l < 1.4°$ and $|b| < 0.3°$). For the two-component MBB model,

the fitting is performed in two steps. First, the complete set of 12 wavebands listed in Table 3.5 is considered, including Herschel, APEX, and HFI datasets. An example of the two-component MBB fit with the 12 data points for a given line of sight is shown in the right panel of Figure 3.22.

Due to the coarser resolution of the *Planck*-HFI data, which is worse than our target angular resolution of $\sim 0.02°$, we perform a second step in the two-component MBB fitting, excluding the *Planck*-HFI bands. In this second step, only six data points per line of sight are used, corresponding to observations from the PACS, SPIRE, and APEX instruments. We interpolate the result for the parameters $\beta_{\rm cold}$, $T_{\rm warm}$, and $T_{\rm cold}$ obtained from the previous step to the angular resolution of $\sim 0.02°$. Then, we refit the optical depths $\tau_{\nu_0}^{\rm warm}$ and $\tau_{\rm cold}$ for both warm and cold dust components, respectively.

The single-component MBB model is also fitted with only the PACS, SPIRE, and APEX dust data. The left panel of Figure 3.22 shows the single-component fitting for an example line of sight.

In Figure 3.23, the optical depth distribution for single and two-component MBB models is shown, including separate distributions for the warm and cold dust components. The black solid line corresponds to the total optical depth for the two-component model, where the weighting is given by the integral of the Planck function for each component.

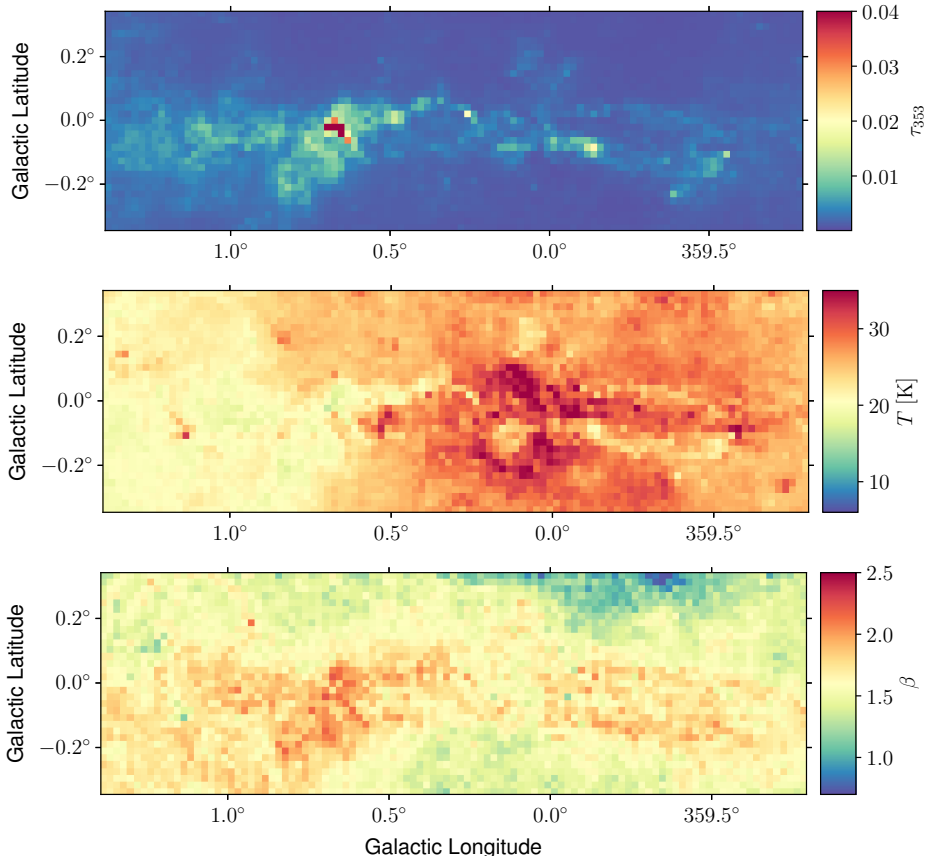

Figure 3.24: Parameter maps obtained by fitting the dust thermal emission using a single-component MBB model. Figure from our CMZ paper I [173].

The result for the fitted parameters using the two-component MBB model is shown in the maps shown in Figure 3.25, while those from the single-component MBB model are displayed in Figure 3.24.

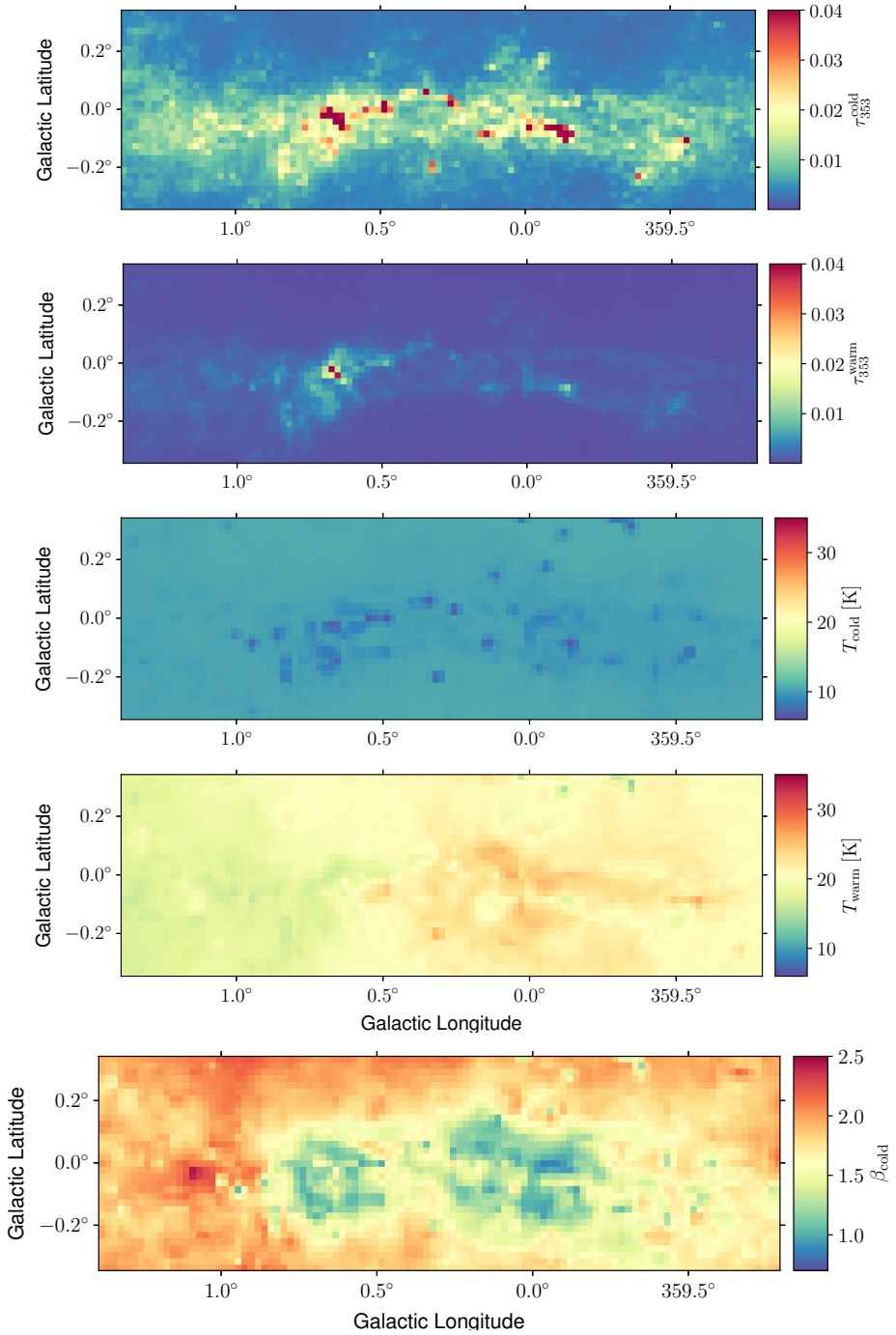

Figure 3.25: Parameter maps obtained by fitting the dust thermal emission using a two-component MBB model. Figure from our CMZ paper I [173].

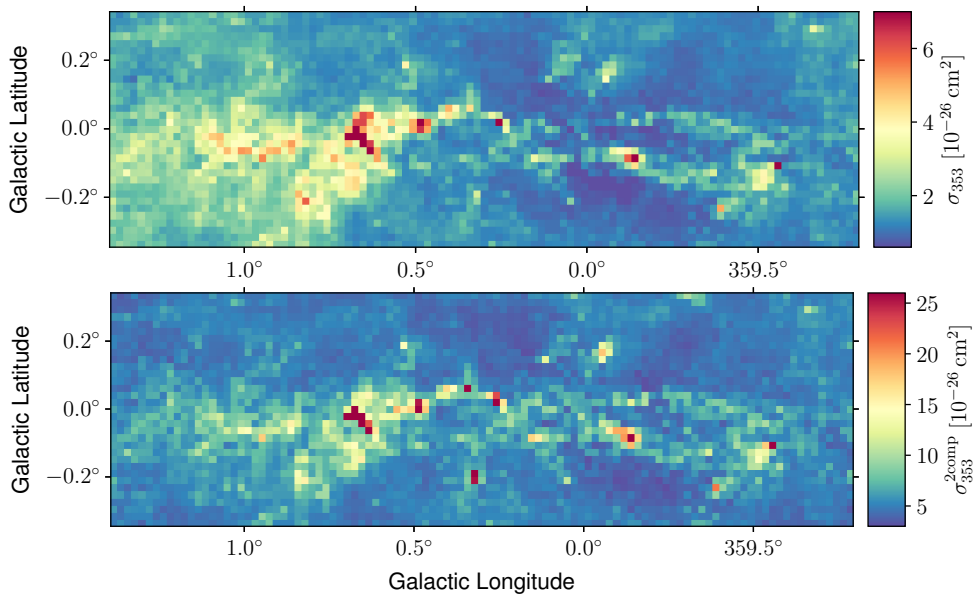

Figure 3.26: Dust opacity maps at 353 GHz, $\sigma_{353} = \tau_{353}/N_{\mathrm{H}}$. Top: Dust opacity derived from the single-component fit. Bottom: Total dust opacity derived from the two-component fit. In both cases, N_{H} is the total hydrogen column density shown in the third panel of Fig. 3.16. Figure from our CMZ paper I [173].

3.2.3 Dust opacity variations

We can express the optical depth as a function of the dust mass, M_{dust}, and gas column density, N_{H}, as:

$$\tau_\nu = \kappa_\nu M_{\mathrm{dust}} \tag{3.24}$$

$$\tau_\nu = \sigma_\nu N_{\mathrm{H}}, \tag{3.25}$$

where κ_ν is the dust emissivity cross section per unit mass, $\sigma_\nu = \kappa_\nu r_{\mathrm{dg}} \mu m_{\mathrm{H}}$ is the dust opacity, r_{dg} is the dust-to-gas mass ratio, and $\mu = 1.4$ is the mean molecular weight.

We can first compare the opacities at 353 GHz derived from the single and two-component dust models, as illustrated in the top and bottom panels of Figure 3.26, respectively. The opacity values obtained from the two-component MBB model are systematically higher by a factor of 2 to 12 compared to those from the single-component dust model.

We also compare our two-component model results with the one obtained by [131], converting our values from τ_{353} to τ_{545}, and interpolating them to their angular resolution of 6.1 arcmin. Our derived opacities are within a factor $0.85 - 2.3$ of their results, which were obtained assuming models with fewer free parameters. This highlights the significant impact that the underlying assumptions in the dust emission modelling can have on the resulting opacity estimates.

We also compare our single-component results to values reported in the literature. The average opacity in the HI dominated regions (which closely correspond to the region dominated by the disk component) is $1.36 \pm 0.28\ 10^{-26}$ cm^2. This is consistent with values reported for atomic gas in local clouds (see Table 2 of [162] and [170]). Significantly higher opacities, up to a factor of 9 larger, are observed in the dense molecular clouds such as Sgr B2 and Sgr C. A similar trend is seen in dense regions of local clouds, although the enhancement at the Galactic Centre is much more pronounced.

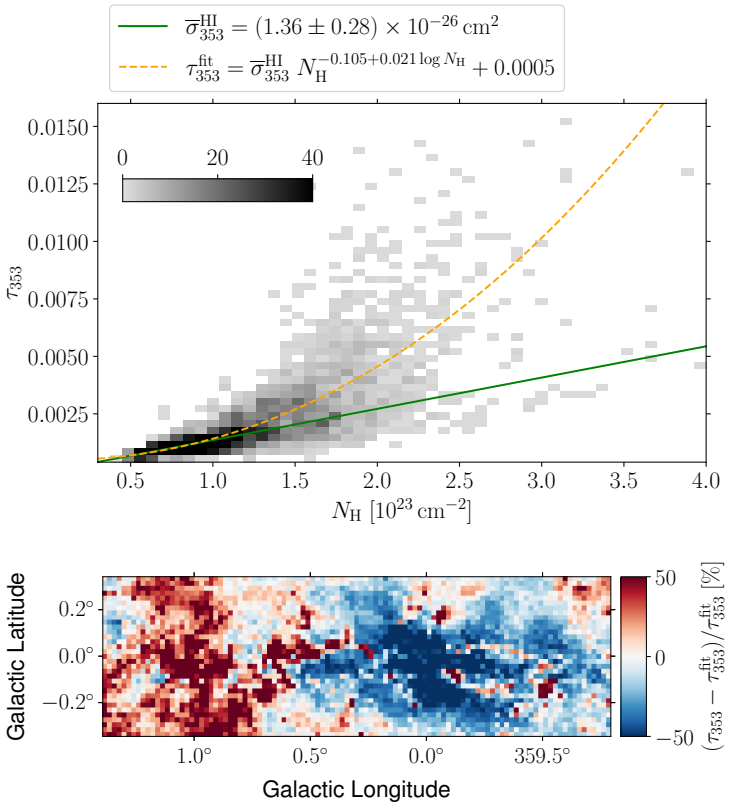

Figure 3.27: Top: Dust optical depth as a function of $N_{\rm H}$. The solid green line represents a linear relation, where the slope corresponds to the mean opacity in regions dominated by atomic gas ($f_{H_2} < 0.5$). The dashed orange curve shows the best-fit τ_{353} as a function of $N_{\rm H}$ with a log-parabola model. Bottom: Relative error on the fit. Figure from our CMZ paper I [173].

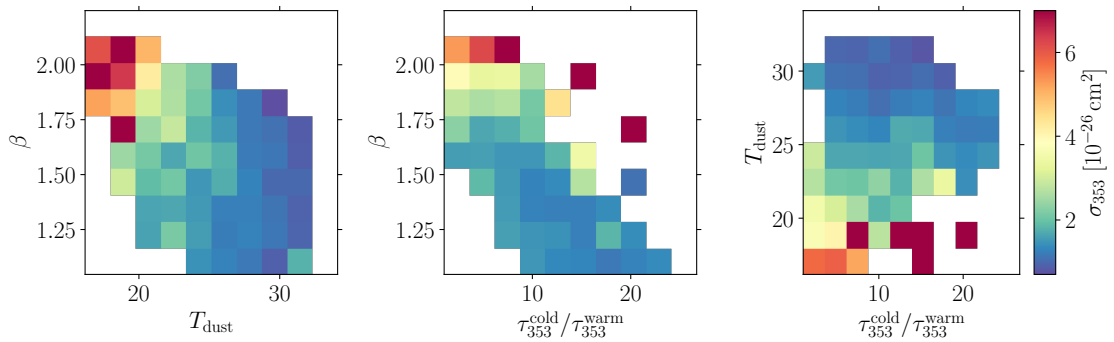

Figure 3.28: 2D histograms of the dust opacity as a function of dust spectral index β, dust temperature $T_{\rm dust}$ (single-component), and the cold to warm components ratio in dust optical depth, $\tau^{\rm cold}_{353}/\tau^{\rm warm}_{353}$. Figure from our CMZ paper I [173].

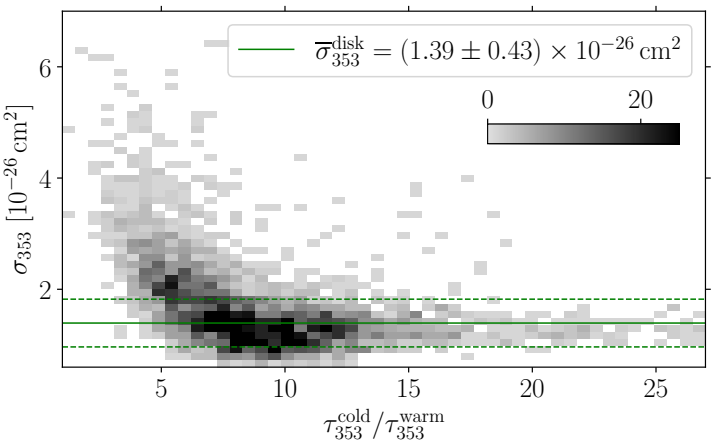

Figure 3.29: Dust opacity versus the cold to warm components ratio in dust optical depth, $\tau_{353}^{\rm cold}/\tau_{353}^{\rm warm}$. The solid green line corresponds to the mean opacity in the regions dominated by the disk gas ($f_{\rm disk} > 0.5$) which mostly correspond to regions dominated by atomic gas. The dashed green lines are the 1σ uncertainty from the 16 and 84 percentiles. Figure from our CMZ paper I [173].

If we plot τ_{353} as a function of $N_{\rm H}$ (see top panel of Figure 3.27), we see that the relation deviates from linearity, indicated by the green solid line. Non-linear relations between dust optical depth and hydrogen column density have been considered in previous studies [92, 149, 177]. We fit a similar non-linear relation to our data, shown by the orange dashed line in the top panel of Figure 3.27. The fitted relation is

$$\tau_{353}^{\rm fit} = \overline{\sigma_{353}^{\rm HI}} N_{\rm H}^{-0.105+0.021 \log N_{\rm H}} + 0.0005. \tag{3.26}$$

However, there is a large dispersion around the fitted relation, and the fit residuals exhibit strong spatial structure. This indicates that accounting for non-linearity alone is insufficient to fully describe the variations in dust opacity as a function of $N_{\rm H}$.

The dependence of dust opacity on β, $T_{\rm dust}$, and the cold-to-warm optical depth ratio is explored in Figure 3.28. One can observe that opacity increases with increasing β and decreasing $T_{\rm dust}$, which is consistent with findings in local clouds [see Figure 18 of 170].

The range of dust opacities in the CMZ is notably broader than that observed in local clouds. As shown in Figure 3.29, the opacity increases with decreasing cold-to-warm dust optical depth ratio. Warm dust is typically associated with more diffuse envelopes, where dust grains are more effectively heated by the interstellar radiation field. An increasing fraction of warm dust correlates not only with a rise in opacity, but also with an increase in β and a decrease in colour temperature, as derived from the single-component model. It is, however, difficult to determine whether this behaviour arises from parameter degeneracies in the fitting procedure or reflects underlying physical processes in the dust grain population or environment.

In fact, several studies have shown that different dust properties lead to variations in their observation. Increase of dust opacity and temperature, and decrease in spectral index in dense ISM regions can be due to coagulation and aggregation processes, as reported by [114]. Whereas, strong influences from size distribution and chemical composition of the dust were described by [220]. The larger values of the opacity observed in the CMZ may also be attributed to the higher levels of turbulence, which can enhance the dust-to-gas mass ratio. For instance, [205] reported evidence of grain-size dependent sorting of the dust, showing that turbulence preferentially concentrates larger grains within dense regions.

These findings highlight the complexity of interpreting dust emission, owing to the uncertain dust composition and varying physical conditions along the line of sight toward the GC. Consequently, estimating gas mass from dust measurements is particularly challenging and subject to significant uncertainties. In particular, any gas mass estimate based on a single, fixed value of dust opacity is likely to be highly unreliable.

3.3 Impact on cosmic-ray energy density estimation

The diffuse γ-ray emission observed in the CMZ is mostly attributed to the interaction of CRs with interstellar gas, producing γ-rays primarily through the decay of neutral pions in proton-proton collisions.

3.3.1 Estimation of the cosmic-ray energy density

Assuming that other sources of diffuse γ-rays are negligible, the CR energy density can be estimated from the γ-ray luminosity L_γ above a threshold energy E_γ, and the gas mass M, using the following relation:

$$w_{\rm CR}(\geq 10E_\gamma) \simeq 0.018 \left(\frac{1.5}{\eta_{\rm N}}\right) \left(\frac{L_\gamma(\geq E_\gamma)}{10^{34}\,{\rm erg/s}}\right) \left(\frac{10^6\,{\rm M}_\odot}{M}\right) {\rm eV/cm^3}, \tag{3.27}$$

where $\eta_{\rm N} = 1.5$ accounts for heavier nuclei in both CRs and the interstellar medium.

Using this relation, H. E. S. S. Collaboration [88] estimated the CR energy densities above 10 TeV across several regions towards the CMZ, which are outlined by solid black lines in Figure 2.12. The mass in each region was computed as a fraction of a fixed total mass, assumed to be $3 \times 10^7\,{\rm M}_\odot$, weighted by the ratio of the integrated intensity in the region to the whole map. They used three different tracers: CS, CO, and HCN lines, and assumed a constant conversion factor. This method ignores the gas at densities below the critical density of the considered tracer and the atomic gas, which contributes increasingly with higher latitudes.

In this work, the CR energy densities are recomputed using our own gas mass estimates, and we found notable discrepancies, particularly in regions with significant disk contributions. The comparison, shown in Figure 3.30, highlights both the differences in gas mass and the impact on the derived CR densities. The largest deviation in mass and CR density is found in the first three regions that include more disk contribution because they extend at higher latitudes.

[88] fitted this $w_{\rm CR}$ distribution with a 1/r profile as a function of the projected distance to the GC, which suggests a continuous injection from a central accelerator. Their analyses implicitly assume that most of the γ-rays are from the CMZ and that the disk contribution is negligible. However, from our study of the gas mass distribution detailed in Section 3.1.6, we found that gas mass in the disk contributes to 25–60% depending on the regions considered. Moreover, increasing CR density or γ-ray emissivity in the Galactic disk up to a factor of three compared to the local value was reported by several studies (see, for example, *Fermi*-LAT measurements [202] and LHAASO measurements [41]). The local value measured by H. E. S. S. Collaboration [88] is $w_{\rm CR,\,local}(\geq 10\,{\rm TeV}) \sim 10^{-3}\,{\rm eV\,cm^{-3}}$, thus a factor of three in the disk would not be negligible, as the CR energy density in several of the regions considered is of the same order of magnitude.

Thanks to the disk component separation (see Section 3.1.4), now we can evaluate the contamination from the disk and fit the CR energy density considering an additional disk

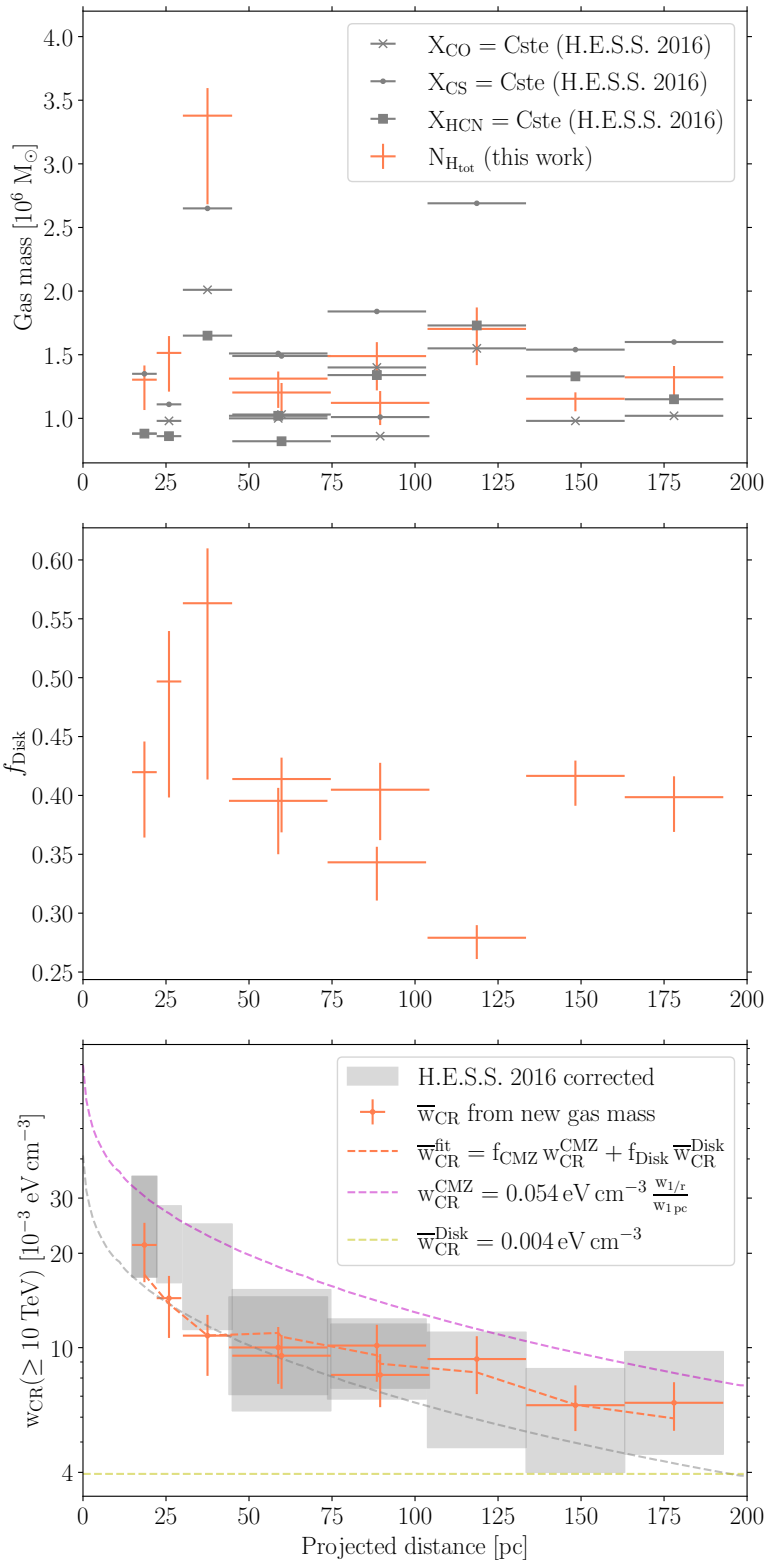

Figure 3.30: Top: Gas mass estimates from [88] in grey and from this work in orange. Middle: Fraction of disk contamination in the total hydrogen column density. Bottom: Average CR density as a function of its projected distance from Sgr A*. The grey line is the 1/r profile in CR energy density integrated provided in their paper as a fit to the data points. The orange error bars are the values derived from our mass estimates. The orange line corresponds to the fit to these points, considering a 1/r profile for the CMZ component (magenta) and a constant for the disk component (yellow). Figure from our CMZ paper I [173].

component:

$$\overline{w}_{\rm CR}^{\rm fit} = f_{\rm CMZ}\, w_{\rm CR}^{CMZ} + f_{\rm Disk}\, \overline{w}_{\rm CR}^{Disk}. \tag{3.28}$$

This relation is fitted using a χ^2 minimisation. $f_{\rm CMZ}$ and $f_{\rm DisK}$ are the fractions of the CMZ and disk components in the total gas column density, respectively. For the CMZ, the CR energy density is modelled using the same 1/r profile as in [88], noted $w_{1/r}$, and only a normalization is fitted. For the Galactic disk, we fit a flat average level of the CR sea, towards the GC direction. The fitted values are $w_{\rm CR}^{\rm CMZ} = (53.9 \pm 10.7) \times 10^{-3}\, w_{1/r}/w_{1\,\rm pc}$ eV cm^{-3} and $\overline{w}_{\rm CR}^{\rm Disk} = (4.0 \pm 3.6) \times 10^{-3}$ eV cm^{-3}.

The two-component model improves the fit by 4.9σ, compared to a single uniform value and by 2.6σ, compared to a $1/r$ profile alone. Including both components results in a CR density in the CMZ that is about twice as high as the previous study. Interestingly, the average value found in the disk is four times the local value, consistent with the enhancement reported in the studies cited above. However, due to the large uncertainty, a broader analysis involving more and larger regions would be needed to further investigate CR densities across the Galactic disk.

As in [88], this fit does not account for the three-dimensional distribution of gas in the CMZ, which limits the interpretation of the $1/r$ profile for the CR density. For that, a more refined study estimating the distance of the individual clouds in the CMZ would be necessary.

3.4 Towards a 3D gas mass distribution

A proper three-dimensional gas mass distribution in the GC is essential for understanding the dynamics of the CMZ and for investigating the processes of CR acceleration in this region. Our approach begins by isolating the individual molecular clouds in the CMZ, with the goal of estimating their distances through γ-ray emission fitting, under the assumption of continuous CR injection into the interstellar medium from sources in the GC. In this section, we present the clustering of the molecular data as a first step towards determining the 3D gas mass distribution.

3.4.1 Clustering CMZ gas into molecular clouds

After removing the Galactic disk component, we retain only the HI, ^{12}CO$(1-0)$, and ^{13}CO$(2-1)$ lines that are potentially associated with the CMZ. These data are then clustered in the (l, b, v) space to identify individual molecular clouds as smaller coherent structures.

For the clustering, we again use the combination of the `AgglomerativeClustering` and `InductiveClustering` methods, which are introduced in section 3.1.4. To reduce computational cost and identify initial seed clusters, a classifier is trained on a subset of the ^{12}CO lines. The `InductiveClustering` method then expands these initial clusters by incorporating the remaining lines. Thanks to consistent labelling, the same classifier can be applied to the ^{12}CO$(1-0)$, ^{13}CO$(2-1)$, and HI lines, allowing us to recover the same clustered structures across all tracers to find the same clustered structures.

This time, the initial subset of lines is not chosen randomly, but selected by identifying locally bright lines, as the goal is to initialise clusters around dense cores. To identify these lines, we define a quantity called the local height, $\overline{h}_{\rm loc}$, which represents the average peak height of a line within its neighbourhood in (l, b, v) space. Further details on how the local height is computed can be found in Section 5.4 of [167].

The lines selected as part of the seed clusters must satisfy the following conditions:

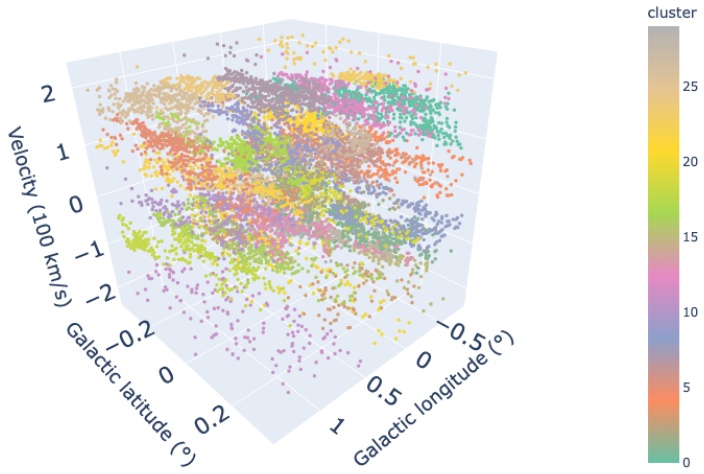

Figure 3.31: Seed clusters obtained by applying `AgglomerativeClustering` on 5% of ^{12}CO$(1-0)$ line which pass the local height criteria described in Equations 3.29 and 3.29. Figure adapted from [167].

$$h_{\rm fit}(l,b,v) \geq X\overline{h}_{\rm loc}(l,b,v) \tag{3.29}$$
$$h_{\rm fit}(l,b,v) \geq Y \tag{3.30}$$

where $h_{\rm fit}$ is the height of the peak derived from the pseudo-Voigt fit. X is a new quantity that defines how bright the line must be compared to the average heights in its neighbourhood; after testing several values, we adopt $X = 2$. And Y is an additional low threshold for the heights, chosen to be $Y = 0.2$, introduced to avoid taking the weak peaks that may arise from noise. For ^{12}CO$(1-0)$, approximately 5% of the total number of lines pass these criteria.

We then apply `AgglomerativeClustering` to the selected lines to identify the seed clusters. The number of clusters is fixed at 30, as this value allows all known clouds to be separated. Figure 3.31 shows the clustering of the selected ^{12}CO lines in (l, b, v) space in the projections (l, b) and (l, v).

Finally, the result with `AgglomerativeClustering` trains the SVC classifier, and the `InductiveClustering` is applied on the rest of the data. Figures 3.32, 3.33, and 3.34 illustrate the projections of the clustering results for ^{12}CO$(1-0)$, ^{13}CO$(2-1)$ and HI lines, respectively.

Figure 3.35 shows the 30 clusters we obtained by using this method. In future work, we will fit each cloud to the γ-ray data. However, some of these clouds may be too faint to be observed in γ-ray data. To address this, we will iteratively merge the faintest clouds with their nearest brighter neighbours in (l, b, v) space, ensuring that each step reduces the number of undetectable structures while preserving spatial and velocity coherence.

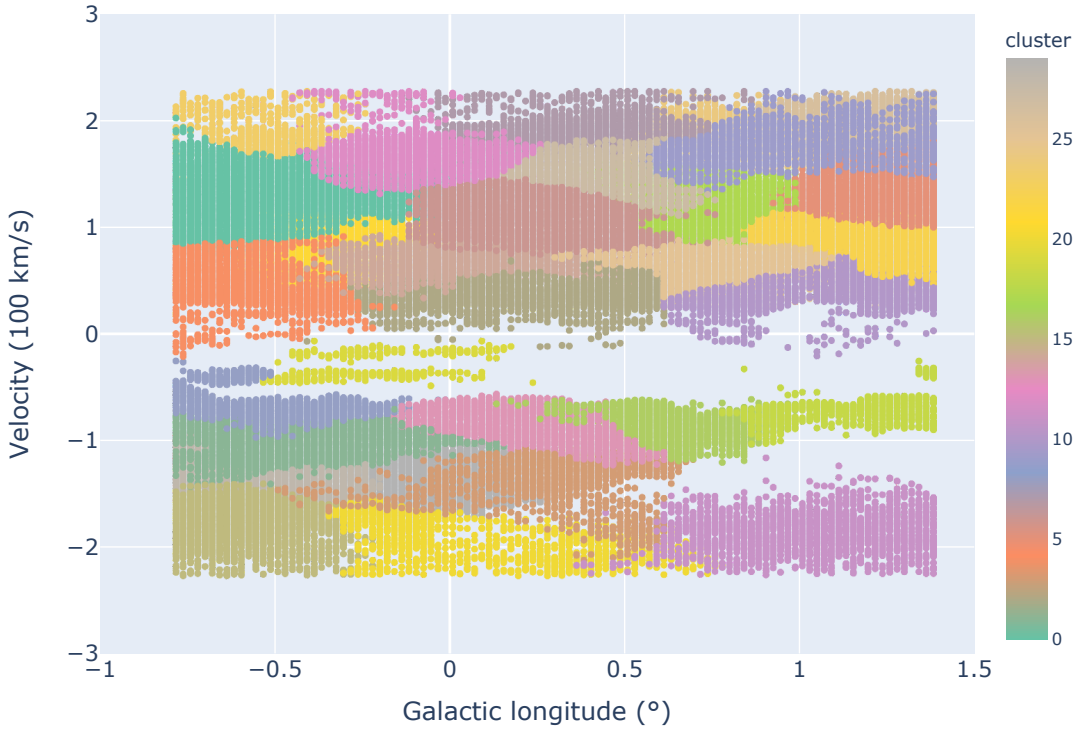

Figure 3.32: $^{12}\mathrm{CO}(1-0)$ clusters obtained by `InductiveClustering`, applied on all lines, projected in (l, v) space. Figure adapted from [167].

3.5 Summary

This chapter presented the estimation of the total hydrogen column density in the CMZ by using atomic and molecular line emission. Atomic hydrogen was traced using HI 21 cm line emission from ATCA, and molecular gas was mapped using CO isotopologue (^{12}CO, ^{13}CO, and C^{18}O) transitions from NRO and APEX. Spectral line decomposition is used to separate emission from the CMZ and the Galactic disk, based on differences in turbulence, velocity dispersion, and line ratios.

The line decomposition and the component separation allow us to derive a X_{CO} value for each line, considering the model from simulations provided by Gong et al. [82]. An empirical power-law correction is added to this model, take account of the effect of the higher level of turbulence in the CMZ following Bertram et al. [28].

Separate gas maps are produced for both the CMZ and the disk components. The CMZ's total gas mass is estimated to be $2.3^{+0.3}_{-0.3} \times 10^7; \mathrm{M}_\odot$, with atomic gas contributing around 10%. If the disk contamination is not removed, the total mass estimate nearly doubles, and the atomic gas fraction rises to 30%, highlighting the importance of separating the two components.

We analysed the dust thermal emission by fitting its flux with both single and two-component MBB models. The relationship between the dust opacity and the total gas mass estimated from HI and CO lines is found to be non-linear. As a result, deriving gas mass from dust emission in the CMZ is unreliable, as the dust-to-gas mass ratio can not be modelled with a simple relation and is affected by significant complexities in the dust

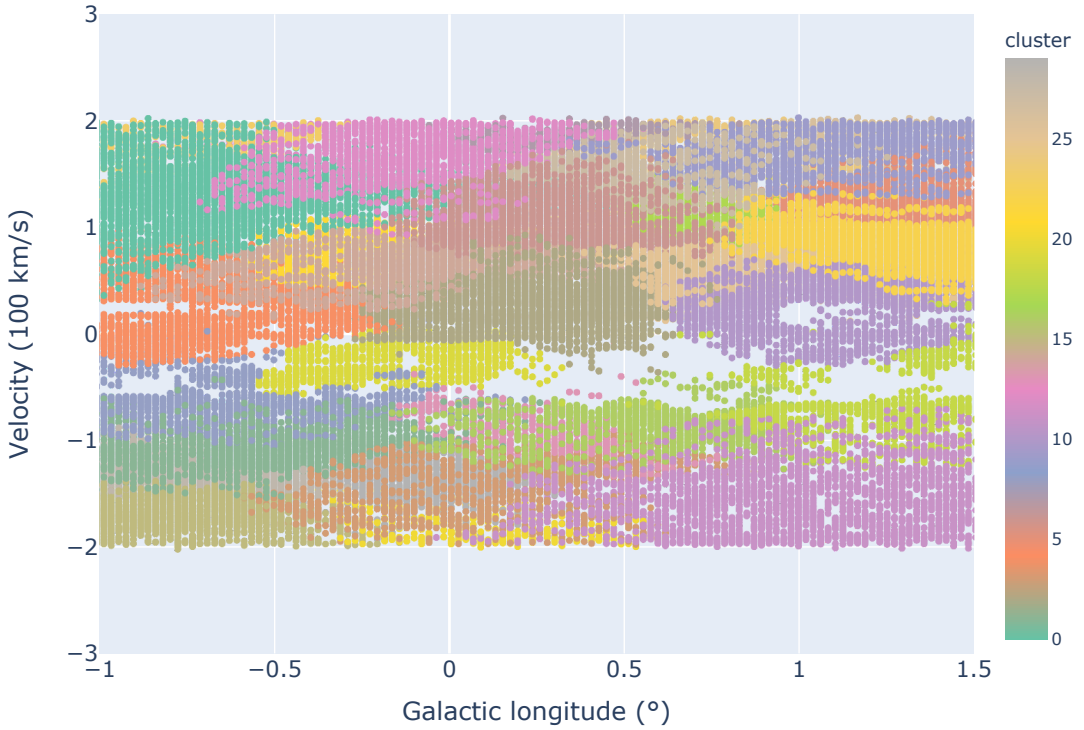

Figure 3.33: $^{13}\mathrm{CO}(1-0)$ clusters obtained by `InductiveClustering`, applied on all lines, projected in (l, v) space. Figure adapted from [167].

modelling, related to the change of dust properties in different environments.

Using the updated gas mass estimates, the CR energy density was recalculated following the method of H. E. S. S. Collaboration [88]. A two-component model, including both CMZ and disk contributions, provided a significantly better fit than a single profile. This model suggests a CR density in the CMZ twice as high as previous estimates, and a disk value four times higher than the local CR density.

Future improvements will require incorporating the three-dimensional structure of gas and CRs in the GC region. As a first step, we have started constructing a 3D gas template by clustering the gas line emission into 30 distinct cloud structures. Estimating the distances of these clouds to the GC will be addressed in future work.

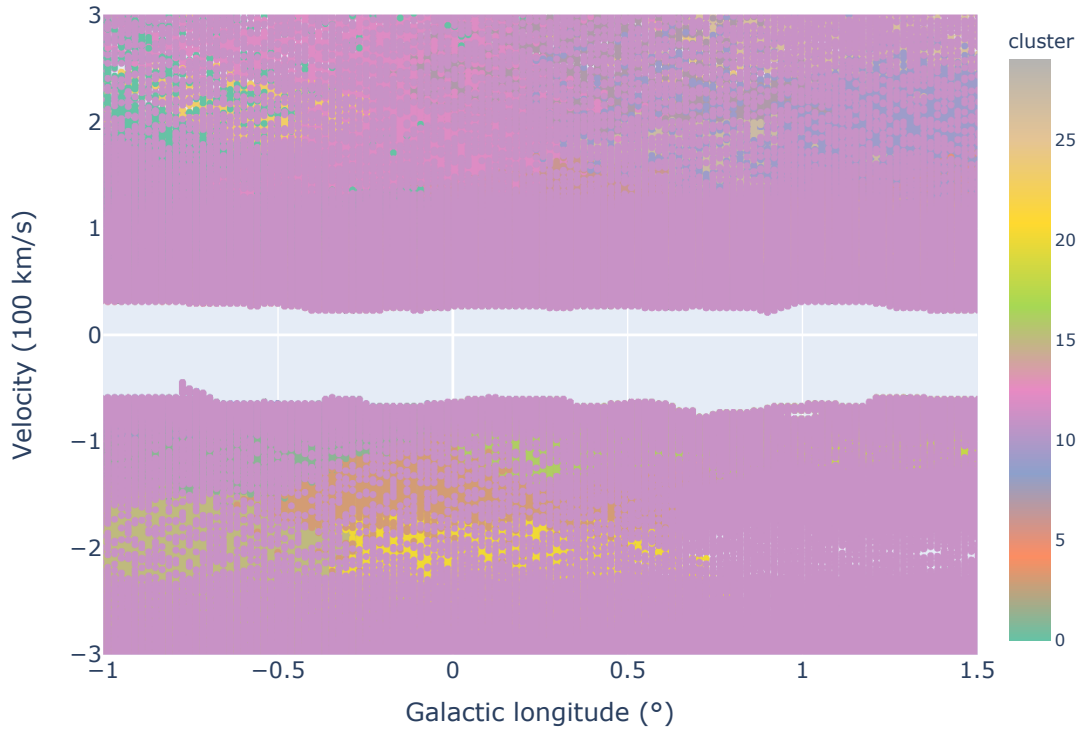

Figure 3.34: HI clusters obtained by `InductiveClustering`, applied on all lines, projected in (l, v) space. Figure adapted from [167].

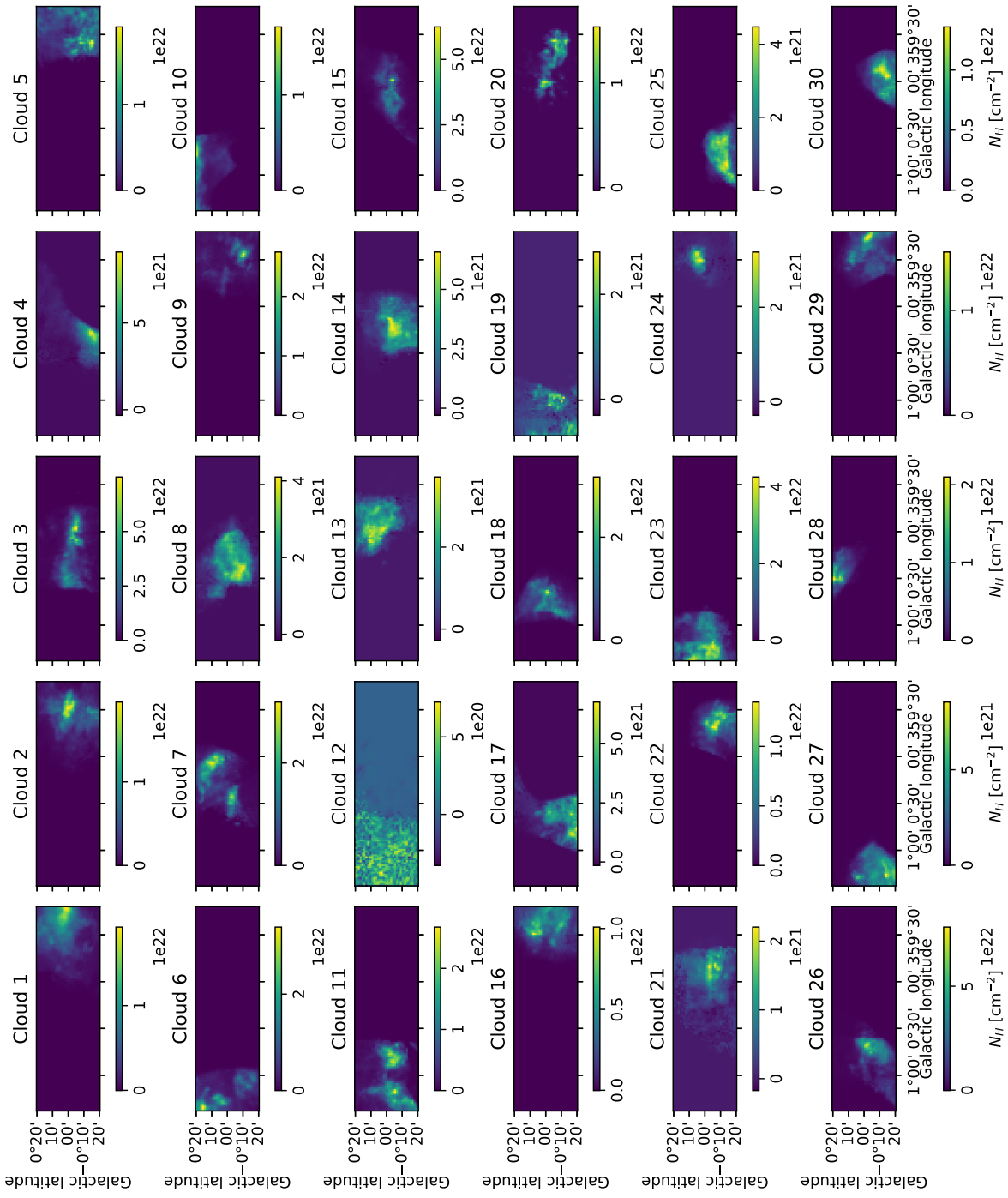

Figure 3.35: Molecular clouds obtained using `AgglomerativeClustering` and `InductiveClustering` algorithms. The maps show the total hydrogen column density computed as explained in Section 3.1.5.

Chapter 4

Gamma-Ray emission and detection

γ-rays are the most energetic photons, spanning the last $\sim$12 orders of magnitude in the electromagnetic spectrum. The distinction between X-rays and γ-rays is not strictly defined by energy, but rather by their origin. X-rays are emitted by electrons outside the atomic nucleus, whereas γ-rays can be produced through nuclear radioactivity, particle annihilation, and processes involving accelerated particles in astrophysical environments.

In astrophysics, we conventionally consider that radiation with energies above 100 keV is γ-rays. These photons can be produced through the interaction of highly accelerated CRs with ambient matter, radiation fields, or magnetic fields. CRs consist of protons, electrons, positrons, neutrons, heavy ions, and other antiparticles. Since most CRs are charged particles, their trajectories are deflected by magnetic fields during propagation, so their arrival directions observed on Earth do not trace back to their origin. As a result, the observed CR spatial distribution appears nearly isotropic. In contrast, photons (and other neutral particles, such as neutrinos) are not deflected by magnetic fields, travel in straight lines from their sources. This makes γ-rays valuable probes for studying particle acceleration processes.

On the other hand, γ-rays can also be produced by the annihilation and decay of DM in the Universe. In particular, WIMP DM particles may decay or annihilate into γ-rays via several different channels. Indirect searches for such signatures in different types of astronomical sources have become an active and widely studied topic in recent years.

This chapter begins with an overview of the photon spectrum in Section 4.1. The γ-ray production mechanisms and the corresponding energy loss processes are discussed in Sections 4.2 and 4.3, respectively. Section 4.4 presents the CR spectrum, along with CR acceleration processes and sources. The production of γ-rays from DM annihilation is covered in Section 4.5. γ-ray detection techniques and data analysis methods are presented in Sections 4.6 and 4.7, respectively. Finally, Section 4.8 summarises this chapter.

4.1 The electromagnetic spectrum

The electromagnetic spectrum ranges from radio waves, which are the least energetic (wavelengths $>$ 1 mm), through infrared (IR, 100 nm to 1 mm), optical (400–700 nm), ultraviolet (UV, 10–400 nm), and X-ray bands (0.01–10 nm), up to γ-rays, which represent the most energetic part of the spectrum (wavelengths $<$ 0.01 nm). Observations across the different wavelengths provide complementary information about astronomical sources and are essential for our understanding of the Universe.

Not all electromagnetic wavelengths can penetrate the Earth's atmosphere, and in particular, γ-rays are mostly blocked by this protective layer. As γ-rays are highly ionising and hazardous to life, the atmosphere plays a crucial role in shielding the surface and enabling life to thrive in the way we know it. The full electromagnetic spectrum, along with the atmospheric transmission windows, is shown in Figure 4.1. The solid blue

line in this figure represents the height at which half of the total incoming radiation is absorbed by the atmosphere.

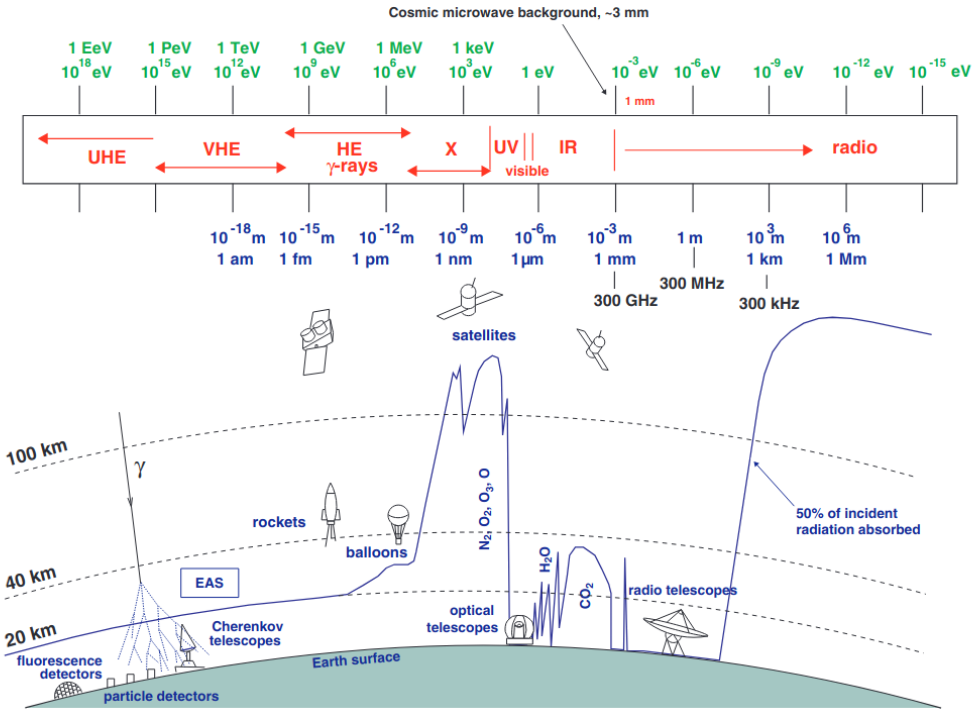

Figure 4.1: Electromagnetic spectrum and atmospheric windows for astronomical observations. For each energy band, typical observation methods are also indicated. Figure from [212].

In the γ-ray regime, energies between 100 keV and 100 GeV are referred to as the High-Energy (HE) range. This band can be observed using satellite-based detectors, as a relatively large number of photons are emitted in the Universe within this range. One example detector is the Large Area Telescope (LAT) onboard *Fermi*, which reconstructs incident γ-rays by measuring the trajectories of electron-positron pairs produced through pair conversion.

Above 100 GeV, the number of photons rapidly decreases, making satellite detection impractical. These energetic γ-rays are further classified into two categories: Very-High-Energy (VHE) range, covering 100 GeV to 100 TeV, and Ultra-High-Energy (UHE) range, above 100 TeV. At these energies, observations can only be performed from the ground. However, as it is mentioned, the atmosphere is opaque to γ-rays, so how can we detect these photons on the ground? Thankfully, γ-rays interact with the particles in the atmosphere upon entry, generating a cascade of interactions that results in a shower of secondary particles, known as an Extensive Air Shower (EAS). These secondary particles travel faster than the speed of light in the atmosphere, emitting Cherenkov radiation in the process. Hence, the atmosphere acts as a calorimeter, and ground-based γ-ray observatories can detect either the Cherenkov light (IACT) or directly the secondary particles (WCD), enabling indirect measurements of the original γ-rays. More details on the principles of Cherenkov light emission and detection are discussed in Section 4.6.

The observed γ-ray emission is the result of non-thermal processes, in which astrophysical sources cannot be modelled as black bodies. These emissions involve accelerated CR particles. The following section describes the main mechanisms responsible for γ-ray production.

4.2 Gamma-ray production mechanisms

Continuum γ-ray emission is primarily produced when highly energetic accelerated particles (hadrons and leptons) interact with ambient matter, radiation, and magnetic fields as they travel in the cosmos. The dominant mechanisms of γ-ray production are listed in Figure 4.2 and example γ-ray spectral energy distributions (SEDs) are given in Figure 4.3 generated with `GAMERA` [1] software. In the following, the different ways of generating γ-rays, by electrons and protons, are presented.

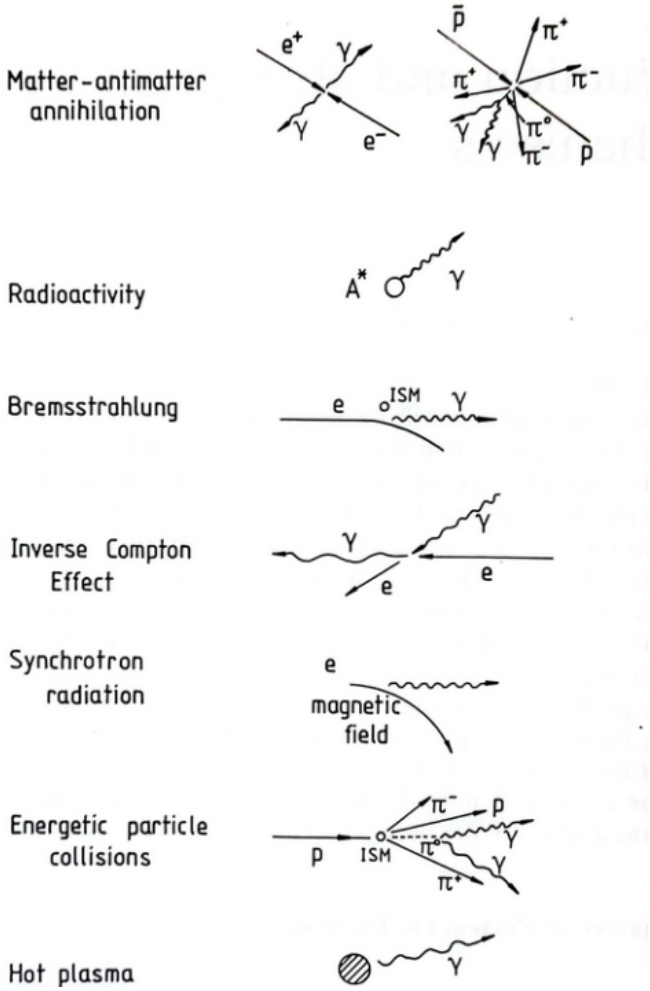

Figure 4.2: γ-ray production mechanisms. Figure from [166].

4.2.1 Electrons

The main processes due to accelerated electrons are:

(a) **Electron-positron annihilation**

An electron-positron pair can annihilate at rest, producing two photons at 511 keV, or in flight mode (free annihilation), producing a continuum energy distribution. The cross section for e^+e^- annihilation under extreme relativistic energies is given by:

[1] GAMERA on Github and the GAMERA document page.

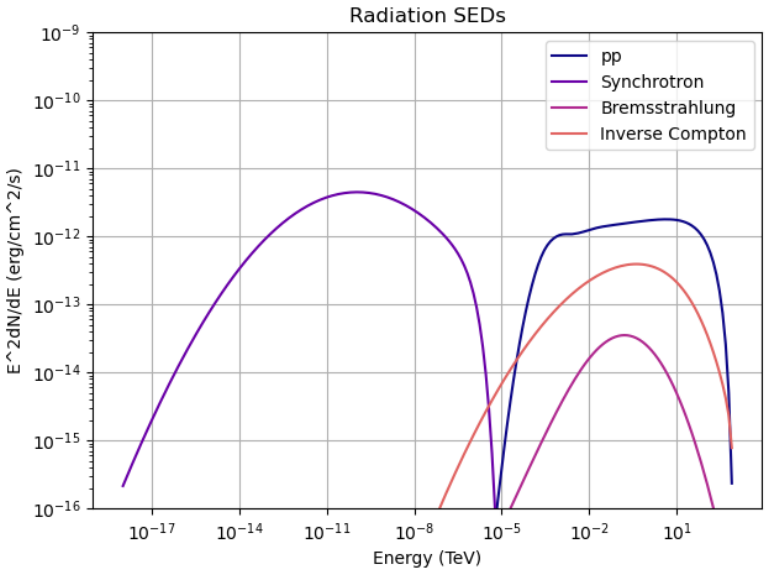

Figure 4.3: Example SED of hadronic and leptonic emissions, produced using `GAMERA`. The original proton spectral index is 2, the initial electron spectral index is 2.3. Ambient gas density is 1 cm^{-3}, and magnetic field strength is 10 μG, the CMB energy density is 1 erg cm^{-3}

$$\sigma_{\mathrm{A}} = \frac{\pi r_{\mathrm{e}}^2}{\gamma_e}[ln(2\gamma_{\mathrm{e}}) - 1], \tag{4.1}$$

where $\gamma_{\mathrm{e}} = E_{\mathrm{e}}/m_{\mathrm{e}}c^2$ is the Lorentz factor of the positron, and r_{e} is the classical radius of the electron. The dominant product of the annihilation is two photons. When the positron energy is high, the photon in the forward direction has almost all the energy, and the other photon has an energy of 0.256 MeV.

In principle, the emitted γ-ray could have as much energy as the high-energy positron, however, the cross section in Equation 4.1 is quite small, meaning that high-energy positrons rather escape from the Galaxy before interacting with the ambient electrons. In fact, for a 100 MeV positron, the cross section would be $\sigma_{\mathrm{A}} = 6 \times 10^{-27}\mathrm{cm}^2$, and its mean free path in the ISM would be $\sim 5 \times 10^{26}\mathrm{cm} \approx 2000 Mpc$ (considering an electron density of $n_{\mathrm{e}} \approx 3 \times 10^{-2}\mathrm{cm}^{-3}$). This corresponds to a mean free life of the positron of 5×10^9 years. Other processes are clearly more important to generate γ-rays at VHE.

(b) **Bremsstrahlung**

Highly energetic photons can be emitted when an electron is deflected by the Coulomb field of a nucleus. The differential cross section of the electron in this case follows:

$$\sigma(E_{\mathrm{e}}, E_\gamma)\mathrm{d}E_\gamma = 4\alpha Z^2 r_{\mathrm{e}}^2 \frac{\mathrm{d}E_\gamma}{E_\gamma} F(E_{\mathrm{e}}, \nu) \tag{4.2}$$

where E_{e} is the electron energy, E_γ is the photon energy, Z is the nucleus charge, α is the fine structure constant, $\nu = E_\gamma/E_{\mathrm{e}}$ is the energy ratio and

$$F(E_{\mathrm{e}}, \nu) = [1 + (1-\nu)^2 - \frac{2}{3}(1-\nu)]\left[\ln\left(\frac{2E_{\mathrm{e}}}{m_{\mathrm{e}}}\frac{(1-\nu)}{\nu}\right) - \frac{1}{2}\right], \tag{4.3}$$

for the case of no screening (bare nucleus) and $E_e \ll 100 m_e c^2 [\nu/(1-\nu)] Z^{-1/3}$, and

$$F(E_e, \nu) = [1 + (1-\nu)^2 - \frac{2}{3}(1-\nu)]\left[\ln\left(183 Z^{-1/3}\right) + \frac{1}{9}(1-\nu)\right], \quad (4.4)$$

for the case of complete screening and $E_e \gg 100 m_e c^2 [\nu/(1-\nu)] Z^{-1/3}$.

Bremsstrahlung loss happens for all charged particles, however, it is dominant only for electrons and positrons, since its radiation rate is inversely proportional to the square of the mass. For electrons, Bremsstrahlung dominates over ionization losses until reaching a critical energy. The electron energy loss rate due to this mechanism is proportional to the electron incident energy:

$$\frac{\mathrm{d}E_e}{\mathrm{d}t} = \frac{c m_p n}{X_0} E_e, \quad (4.5)$$

where c is the speed of light, m_p is the proton mass, n is the number density of the ambient gas, and X_0 is the radiation length, which is defined as the mean distance over which energetic electrons lose all but $1/e$ of their energy.

The cooling time of electrons at speed $v \sim c$ due to Bremsstrahlung is:

$$t_B = \frac{E_e}{-\mathrm{d}E_e/\mathrm{d}t} \approx 4 \times 10^7 \,\mathrm{yr}. \quad (4.6)$$

[196] showed that the Bremsstrahlung γ-ray emissivity from electrons in the ISM is proportional to the electron integral energy spectrum. Thus, the spectral index of the product γ-rays follows the parent electron energy spectrum.

For γ-rays with energies below 100 MeV, this is the most dominant mechanism, being also responsible for the diffuse galactic γ-ray emission at this range of energy, as a result of electrons interacting with the ISM.

(c) **Inverse Compton scattering**

Relativistic electrons can also interact with low-energy ambient photons and elevate the energy of the photon via inverse Compton scattering.

For an electron with Lorentz factor γ_e, the energy loss by the inverse Compton process is given by:

$$-\frac{\mathrm{d}E}{\mathrm{d}t}(\gamma_e) = \frac{3}{4}\sigma_T c \gamma_e^2 U_{rad}, \quad (4.7)$$

where $\sigma_T = 8\pi r_e^2/3 = 6.65 \times 10^{-25} \mathrm{cm}^2$ is the Thompson cross section, and U_{rad} is the radiation energy density.

When the photon energy ϵ or the electron Lorentz factor γ_e is low such that $\gamma_e \epsilon \ll m_e c^2$, the interaction occurs in the Thomson regime. In this case, the scattering is elastic, and the energy of the upscattered photon is given by $E_\gamma \simeq \gamma_e^2 \epsilon$. Whereas above this regime, when the condition $\gamma_e \epsilon \gtrsim m_e c^2$ is met, the interaction enters the Klein-Nishina regime. Here, the scattering becomes inelastic, and the energy of the scattered photon is $E_\gamma \sim \gamma_e m_e c^2$.

The cross section of this process, for each case, is:

$$\sigma_{\rm e} = \sigma_{\rm T}\left(1 - \frac{2\gamma_{\rm e}\epsilon}{m_{\rm e}c^2}\right), \qquad \text{if } \gamma_{\rm e}\epsilon \ll m_{\rm e}c^2 \tag{4.8}$$

corresponding to the Thomson limit, and

$$\sigma_{\rm e} = \frac{3}{8}\sigma_{\rm T}\left(\frac{m_{\rm e}c^2}{\gamma_{\rm e}\epsilon}\right)\left[\ln\left(\frac{2\gamma_{\rm e}\epsilon}{m_{\rm e}c^2}\right) + \frac{1}{2}\right], \qquad \text{if } \gamma_{\rm e}\epsilon \gg m_{\rm e}c^2, \tag{4.9}$$

corresponding to the extreme Klein-Nishina limit. Thus, in the Klein-Nishina regime, IC scattering gets exponentially attenuated, due to a decrease in cross-section.

Interaction of energetic electrons with the CMB is dominant, with mean photon energy $\langle\epsilon\rangle \sim 6 \times 10^{-4}$ eV. The change from the Thomson limit to the Klein-Nishina regime, in this case, happens at around 100 TeV electron energy. The relationship between the mean values of E_γ and ϵ is $\langle E_\gamma\rangle = 4/3\gamma_{\rm e}^2\langle\epsilon\rangle$.

For a power-law distribution of parent electrons,

$$I_{\rm e}(E_{\rm e}) = KE_{\rm e}^{-\Gamma} \tag{4.10}$$

The γ-ray distribution in the Thomson limit follows [196] :

$$q_{\rm c}(E_{\rm e}) \propto KE_\gamma^{-(\Gamma+1)/2}, \tag{4.11}$$

thus, for parent electrons with $\Gamma > 1$, the spectral index of the γ-ray energy spectrum is flatter.

In the case of the Klein-Nishina regime, the γ-ray energy spectrum follows:

$$q_{\rm c}(E_{\rm e}) \propto KE_\gamma^{-(\Gamma+1)}. \tag{4.12}$$

Hence, the transition from Thomson to Klein-Nishina regimes has also a break in the γ-ray energy spectrum, with a softening of the spectral index at higher energies.

(d) **Synchrotron emission**

Also known as the magnetobremsstrahung, Synchrotron radiation is emitted when a charged particle is accelerated while gyrating around magnetic field lines, present in astrophysical environments. Exhaustive studies about this subject can be found in [32, 78]. This mechanism contributes to the production of radio, optical, and X-rays in the universe.

The energy loss for a general charged particle of mass M and charge Ze moving in a magnetic field strength B can be expressed as:

$$-\frac{{\rm d}E}{{\rm d}t} \simeq 2.6\frac{\rm keV}{\rm s}\left(\frac{Zm_{\rm e}}{M}\right)^4\left(\frac{E}{1{\rm keV}}\right)^2\left(\frac{B}{1{\rm G}}\right)^2. \tag{4.13}$$

Thus, synchrotron energy loss is much more important for electrons than for protons.

In the leptonic case, an electron with energy $E_{\rm e}$, moving with a pitch angle θ (angle between its velocity and the magnetic field direction), in a magnetic field with strength B, will lose its energy emitting the following synchrotron power:

$$P_\nu(\gamma_\mathrm{e}) = \frac{\sqrt{3}e^3 B sin(\theta)}{m_\mathrm{e}c^2} F(\nu/\nu_\mathrm{c}), \tag{4.14}$$

where F is defined as $F(x) = x\int_x^\infty K_{5/3}(x')dx'$, where $K_{5/3}$ is the modified Bessel function of order 5/3, ν is the photon frequency and ν_c is the so-called critical frequency, where the function F peaks at:

$$\nu_\mathrm{c} = \frac{3eB}{4\pi m_\mathrm{e}c}\gamma_\mathrm{e}^2 sin(\theta). \tag{4.15}$$

For a power-law distribution of electrons (same as in Equation 5.8), the resulting synchrotron photon number spectrum also follows a power law:

$$G_\mathrm{s} \propto E_\gamma^{-(\Gamma+1)/2}, \tag{4.16}$$

leading to a synchrotron power spectrum:

$$J_\mathrm{s} \propto E_\gamma^{-(\Gamma-1)/2}. \tag{4.17}$$

However, synchrotron radiation is, in general, low in energy, and only in extreme cases can it reach the γ-ray regime, when electrons are accelerated to ultra-relativistic energies and the magnetic field is strong. Therefore, this mechanism is only important as an energy loss process. Nevertheless, these low-energy synchrotron photons can be boosted via Inverse Compton by the same ultra-relativistic electrons that generated the synchrotron photons, leading to the so-called Synchrotron self-Compton process, a purely leptonic mechanism.

4.2.2 Protons

Protons can also generate γ-rays via Bremsstrahlung, Inverse Compton scattering, and Synchrotron emission. However, these mechanisms are very inefficient for protons compared to electrons, due to the much higher mass-to-charge ratio for protons. Instead, protons can directly or indirectly generate pions in inelastic collisions with matter (pp interaction) or radiation ($p\gamma$ interaction). The 'p' stands for protons, however, the same processes can occur for heavier nuclei. Here we only consider protons, since they are the most abundant species.

$p\gamma$ interactions can result into photo-pion production ($\gamma\pi$), photo-pair production (γe) and photo-disintegration for heavier nuclei. In the $\gamma\pi$ production, pions decay intro γ-rays, or $\mathrm{e}^+/\mathrm{e}^-$, while in the case of γe production, a pair of e^+/e^- is created.

Let's focus now on the more relevant pp interaction, which generates in most cases a pion, either charged or neutral:

$$\begin{aligned}
&p + p \rightarrow p + p + \pi^0 \Rightarrow \pi^0 \rightarrow 2\gamma \\
&p + p \rightarrow p + p + \pi^+ \Rightarrow \pi^+ \rightarrow \mu^+ + \nu_\mu \Rightarrow \mu^+ \rightarrow \mathrm{e}^+ + \bar{\nu}_\mu + \nu_\mathrm{e} \\
&p + p \rightarrow p + p + \pi^- \Rightarrow \pi^- \rightarrow \mu^- + \bar{\nu}_\mu \Rightarrow \mu^- \rightarrow \mathrm{e}^- + \nu_\mu + \bar{\nu}_\mathrm{e}
\end{aligned}$$

The final neutral pions naturally decay into γ-rays with a mean lifetime $\gamma_\pi 0.83 \times 10^{-16}$s, where γ_π is the Lorentz factor of the pion. The production of neutral pions π^0 via hadronic interactions, i.e., pp interactions, takes place for protons above a certain threshold energy:

$$E_{\mathrm{p}}^{\mathrm{Th}} = m_{\mathrm{p}} + \frac{m_{\pi^0}}{m_{\mathrm{p}}}\left(2m_{\mathrm{p}} + \frac{m_{\pi^0}}{2}\right) \simeq 1.22\mathrm{GeV} \tag{4.18}$$

which leads to a kinetic energy of the proton $T_{\mathrm{p}}^{\mathrm{Th}} \simeq 280\mathrm{MeV}$.

The relation between the spectral shape of the secondary γ-rays and the spectral shape of the parent protons is currently estimated via analytical approaches. The simple analytical result (Fermi model) gives:

$$q_\gamma(E_\gamma) \propto E_\gamma^{-\frac{4}{3}\Gamma+\frac{1}{3}}, \tag{4.19}$$

which is not far from the complete computation [166].

4.3 Gamma-ray energy loss processes

γ-rays can lose their energy mainly in two ways: γ-matter interactions and γ-γ interactions.

4.3.1 γ-γ interactions

This is the inverse of the electron-positron annihilation process explained in section 4.2.1(a). γ-rays with energies above a certain energy threshold can interact with ambient low-energy photons and produce a pair of electron-positron. The γ-ray is then lost, or "absorbed". The energy threshold is given by:

$$E_\gamma E_{\mathrm{rad}}(1 - cos(\theta)) \geq 2m_{\mathrm{e}}c^2, \tag{4.20}$$

where E_{rad} is the energy of the ambient photon and θ is the angle of the collision.

The differential cross section of pair production is also identical to that of pair annihilation, except for a different phase-space volume. In the relativistic regime, this process is also quite similar to inverse Compton scattering. The large cross section makes this mechanism very important in dense radiation fields, where relevant γ-ray absorption takes place. Thus, a steepening in the detected energy spectrum would be expected for astronomical objects in dense radiation fields. It also becomes important for extragalactic γ-ray due to interaction with the Extragalactic Background Light (EBL) and the CMB photons.

The electron-positron pair created in the absorption of a γ-ray can also produce γ-rays by pair annihilation or Compton scattering. These photons can, in turn, be absorbed if they have sufficient energy, leading to a cascading process. Therefore, the energy of the initial γ-ray is not lost, but transferred to lower energies.

4.3.2 γ-matter interactions

The major γ-matter processes are the photoelectric effect, the Compton effect, and pair production. In Figure 4.4, the relative importance of these mechanisms as a function of the photon energy can be seen. For energies above 0.5 MeV only the Compton effect and pair production would be important. Such processes are also useful mechanisms for detection of γ-rays.

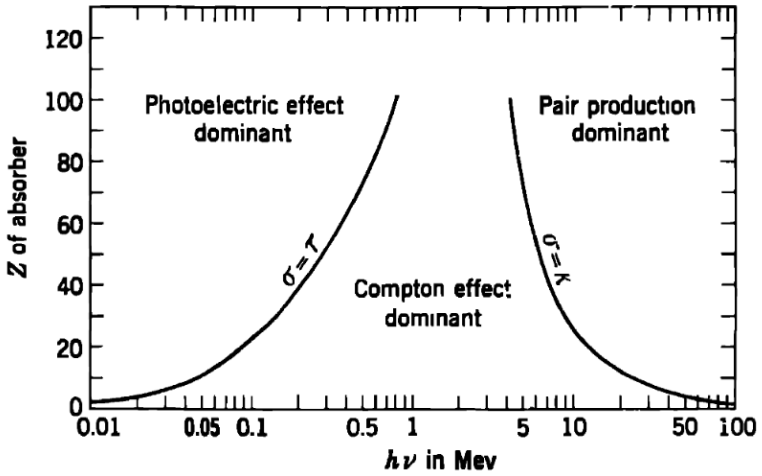

Figure 4.4: The major types of γ-matter interaction and their relative importance as a function of the photon energy. Solid lines indicate the values at which two neighbouring processes have the same importance. Figure from [68]

(a) **Compton scattering**

In the Compton scattering process, a high-energy photon collides with a stationary electron and transfers some of its energy to the electron. This change in energy can be expressed as an increase in wavelength:

$$\frac{\lambda - \lambda'}{\lambda} = \frac{\hbar\omega}{m_e c^2}(1 - cos(\alpha)), \tag{4.21}$$

where λ and λ' are the initial and the scattered wavelength, respectively. $\hbar$ is the reduced Planck constant, ω is the photon's frequency, and α is the angle of scatter.

For the case of highly energetic photons, the Klein-Nishina cross-section applies (see Equation 4.9). This cross-section decreases as E_γ^{-1} at the highest energies, where pair production becomes much more important. Note again that the Compton scattering effect for nuclei can be neglected, since they cause very small scattering compared to electrons, by a factor $\sim (m_e/m_N)^2$.

Compton telescopes like the Imaging Compton Telescope (COMPTEL) [183] on-board the Compton Gamma Ray Observatory (CGRO) were a pioneering detector in the MeV range, which made use of the Compton effect to detect γ-rays in the energy range of 0.8-30 MeV. A future mission, Compton Spectrometer and Imager (COSI) [204] is planned to be launched by NASA in 2026

(b) **Pair production**

Electron-positron pair production can also occur when a high energy photon is in the electric field of neighboring nuclei (or an electron, but it is very rare), and transforms itself into e^+/e^-. The energy threshold for this process is $2m_e c^2$. The γ-ray cannot produce a pair in free space, because momentum and energy cannot be conserved simultaneously. Therefore, the field of the nuclei will take up the balance of momentum.

The analytical cross section for nuclear pair production can only be given for extreme cases, when the atomic screening is negligible and when there is complete screening [166].

The LAT onboard *Fermi* Gamma-ray Space Telescope is an example detector that observes γ-rays via pair production, using a high atomic number converter material. This instrument is sensitive to γ-rays in the range of about 20 MeV to 300 GeV, with a fine angular resolution of 0.15°for photon energies above 10 GeV, and energy resolution <10%.

(c) **Cherenkov radiation**

When a γ-ray interacts with matter, it can produce an electron-positron pair. If these charged particles travel through a dielectric medium at a speed greater than the phase velocity of light in that medium, i.e. $v > \frac{c}{n}$, where n the refraction index, they emit a cone of blue light known as Cherenkov radiation, as illustrated in Figure 4.5. This phenomenon occurs because,the fast-moving charged particle polarises the surrounding atoms in the medium, which then quickly return to their ground state by emitting EM radiation. The resulting wavefronts interfere constructively at a characteristic angle, producing a coherent shockwave of light.

The opening angle of this light cone follows:

$$\cos\theta = \frac{c}{vn}. \tag{4.22}$$

In the Earth's atmosphere, considering standard temperature and pressure, the refraction index is $n = 1.0003$, thus the opening angle is $\theta \simeq 1°$. However, atmospheric pressure varies with altitude, hence, the opening angle also varies accordingly. In water, $n = 1.3$, which leads to $\theta \simeq 40°$.

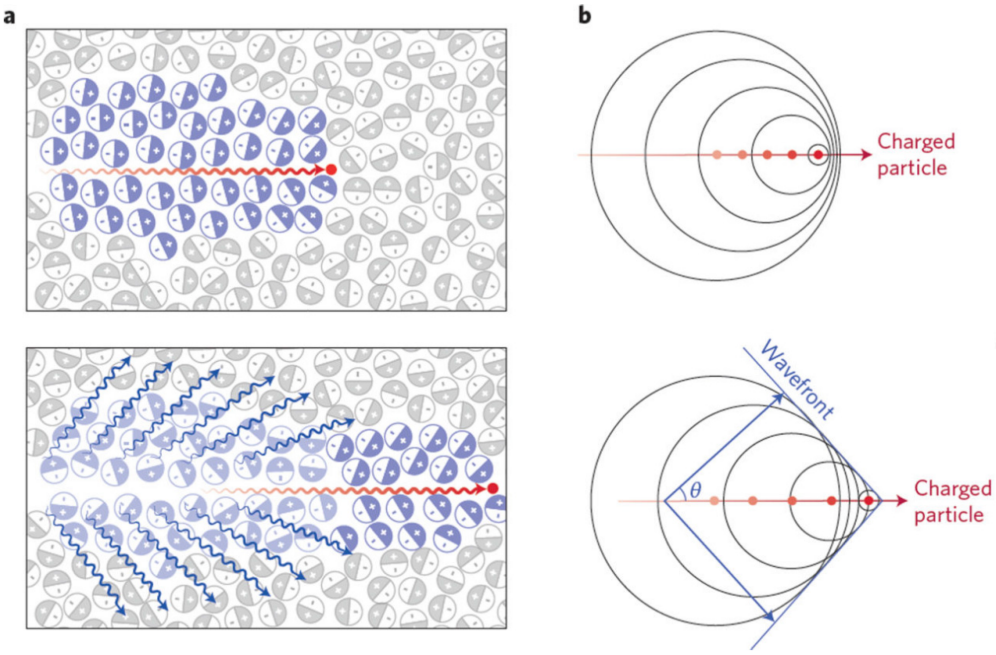

Figure 4.5: Left: Polarization of the dielectric medium by a charged particle, travelling at a speed $v < c/n$ (top) and $v > c/n$ (bottom). Right: Emission from the moving particle in the medium for each case. In the case $v > c/n$, the Cherenkov radiation wavefront is indicated by the blue line, and the opening Cherenkov angle θ. Figure adapted from [185]

The electron-positron pair can further interact with particles in the atmosphere or water, producing a cascade of secondary particles (see Section 4.6.1). The

Cherenkov light produced by all secondary particles overlaps and produces a light pool on the ground of typically ∼120 m in radius.

IACTs, like H.E.S.S., are able to measure the Cherenkov light produced in the atmosphere, while WCDs, like SWGO, can detect the Cherenkov light produced in water. More details about this detectors are given in section 4.6.

4.4 Cosmic Rays

We have reviewed the various mechanisms responsible for producing high-energy γ-rays, which involve accelerated CR particles, both hadrons and leptons. However, the question of where and how these primary CRs are accelerated remains open in the field of high-energy astrophysics, even more than a century after the discovery of CRs by Victor Hess [96].

Let us first examine the all-particle spectral energy distribution of primary CRs, shown in Figure 4.6, where the flux is multiplied by E^2. This spectrum spans an enormous energy range, from 10^8 to 10^{21} GeV, around seven orders of magnitude higher than the maximum energy achievable by the Large Hadron Collider on Earth. The inferred main chemical elements from several instruments are also shown in this figure, together with an estimate of the neutrino flux from IceCube. Some interesting characteristics can be noted from the spectrum:

(a) The *knee* at around 10^6 GeV (1 PeV), where there is a change in spectral index from $\sim E^{-2.7}$, to $\sim E^{-3.1}$.

(b) The *second knee* at around 10^8 GeV, where there is a downward bend.

(c) The *ankle* at around $10^{9.7}$ GeV, where the spectral index turns back to $\sim E^{-2.7}$.

(d) A cutoff at around $10^{10.7}$ GeV, probably because most of the extra-galactic CRs interact with the CMB before arriving to Earth (the Greisen-Zatsepin-Kuzmin limit).

Figure 4.7 is the all-particle CR spectrum with the flux multiplied by E^3. This representation shows more clearly the change of the slopes at the knees and the ankle.

CRs with energy below the knee come from the astrophysical sources in our Galaxy. Beyond the knee, its origin is under debate, some believe that the change in slope is due to propagation effects, while others suggest these CRs have an extragalactic origin. It is commonly believed that, around the ankle and above, extragalactic sources are dominant. Finally, at the highest energies, the high suppression is due to the interaction of long-traveling CRs with the CMB.

The characteristic shape of the CR spectrum and the extremely high energies observed cannot be explained by thermal phenomena, indicating that CRs must be accelerated by non-thermal processes. Measurements of their energy, composition, and the anisotropies in their arrival directions are crucial for studying the origin, acceleration, and propagation of CRs. However, identifying the specific sources accelerating CRs requires observations of other neutral messengers – photons and neutrinos. Unlike charged CRs, these particles are not deflected by magnetic fields and therefore, retain information about their source direction.

The composition of CRs is dominated primarily by hydrogen, which is mostly protons, with smaller contributions from heavier nuclei, electrons, positrons, and other antiparticles.

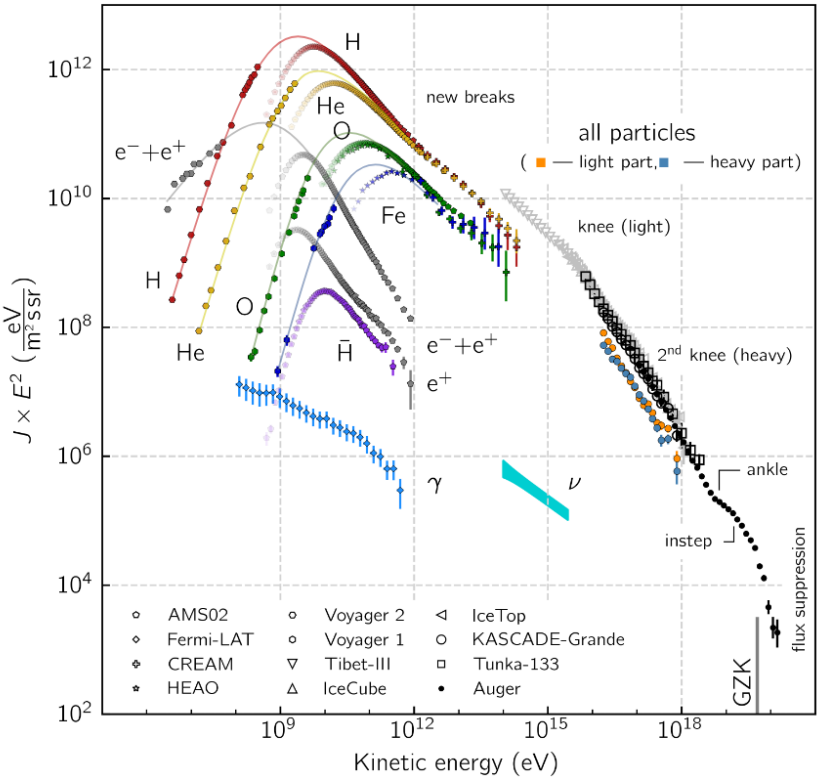

Figure 4.6: All-particle primary CR spectrum, including several chemical species and neutrino measurements. Figure from [31].

In the HE regime, all chemical species exhibit approximately the same spectral index, at least up to the first knee. This suggests that, at these energies, the acceleration and diffusion of CRs are largely independent of their composition.

This section examines the mechanisms that can accelerate CRs to such high energies, as well as the potential astrophysical sources where such acceleration may occur.

4.4.1 How are the cosmic rays accelerated?

The most relevant particle acceleration processes to boost CRs to VHE energies are the Fermi acceleration and the Diffusive Shock Acceleration (DSA).

(a) **The Fermi Mechanism**

Charged particles can be accelerated by electric fields. In regions where the magnetic field is strongly turbulent, a variable electric field can be induced, and thus accelerates CRs, usually in many acceleration cycles.

Fermi proposed in 1949 a mechanism in which charged particles can be accelerated in stochastic collisions. Consider a particle with energy E_1, in the "laboratory" frame, moving with velocity v. When this particle collides with a partially ionized gas cloud (a boundary separating regions of different density) moving at velocity V, an increase of energy can be calculated for each head-on encounter by a double change of reference frame. Head-on collisions lead to energy gain, same as when a tennis ball collides with a racket moving towards it. On the other hand, the energy of the CR can be lost when the cloud is moving away from it. The Fermi acceleration is based on the idea that the charged particle is accelerated after

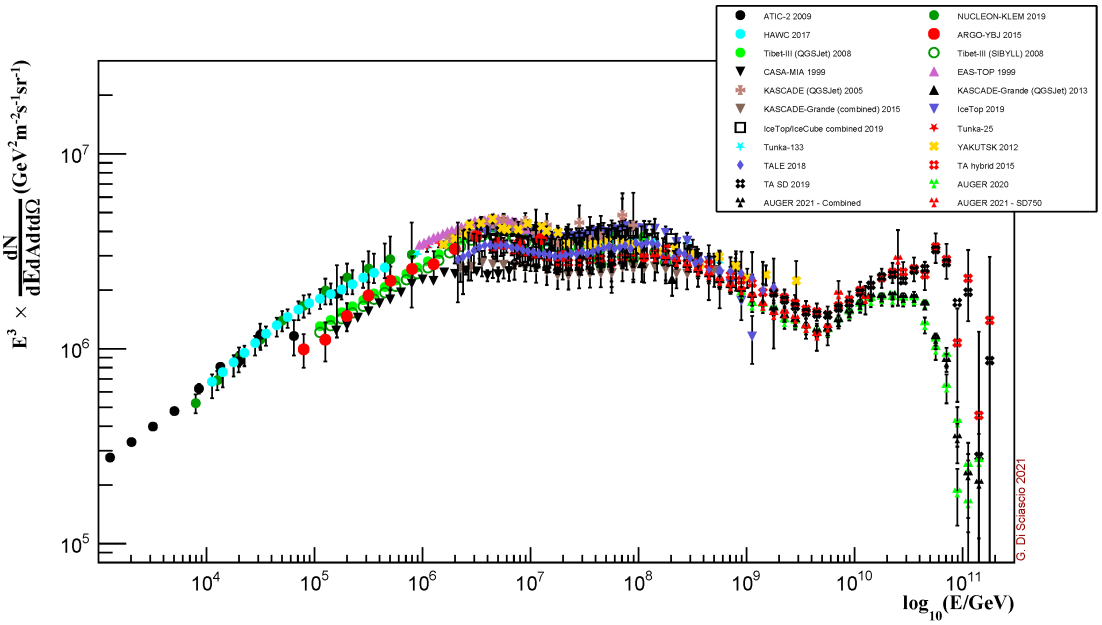

Figure 4.7: All-particle primary CR energy spectrum, with the flux multiplied by E^3. The two knees and the ankle can be better visualized in this format. Figure from [57]

multiple encounters with magnetic clouds, and this will only work if the head-on collisions are more frequent on average. Indeed, for particles traveling at high velocities, it obviously crosses more clouds coming towards it than clouds moving away from it. The average energy gain in this case is

$$\frac{\Delta E}{E} \simeq \frac{4}{3}\left(\frac{V}{c}\right)^2, \tag{4.23}$$

which is indeed positive. This mechanism is known as the second-order Fermi acceleration mechanism, which is not very effective, since the cloud velocities are usually small.

The acceleration time can be defined as

$$t_{\rm acc}(E) = \left(\frac{1}{E}\frac{{\rm d}E}{{\rm d}t}\right)^{-1}. \tag{4.24}$$

In the case of Fermi acceleration and neglecting the time spent by the particle inside the clouds, we obtain:

$$t_{\rm acc} \simeq \frac{3}{4}\frac{L}{c}\beta^{-2}, \tag{4.25}$$

where L is the typical distance between two clouds and $\beta = V/c$.

The number spectrum of the accelerated particles has a power-law shape

$$n(E) \propto t_{\rm acc}\left(\frac{E}{E_1}\right)^{-x} \tag{4.26}$$

where $x = 1 + \frac{t_{\rm acc}}{t_{esc}}$ and t_{esc} is the escape time of the particle, i.e., the average time for the particle to leave the region where magnetic clouds are present. Thus, the

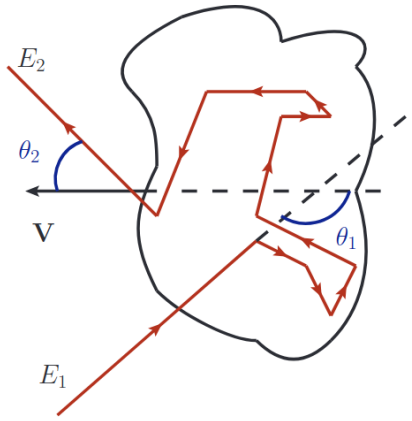

Figure 4.8: Second order Fermi mechanism. A particle with energy E_1 enters a magnetized cloud moving at velocity V with angle θ_1, and is scattered several times. In the cloud rest frame, the particle suffered only a change in direction, whereas in the laboratory rest frame, the particle departs with a change also in velocity. Figure from [142].

shape of the power law depends on the configuration of the acceleration region and the distances between individual clouds. Consequently, the combination of multiple power-law contributions is unlikely to produce a global power law like the one shown in Figure 4.6.

(b) The Diffusive Shock Acceleration

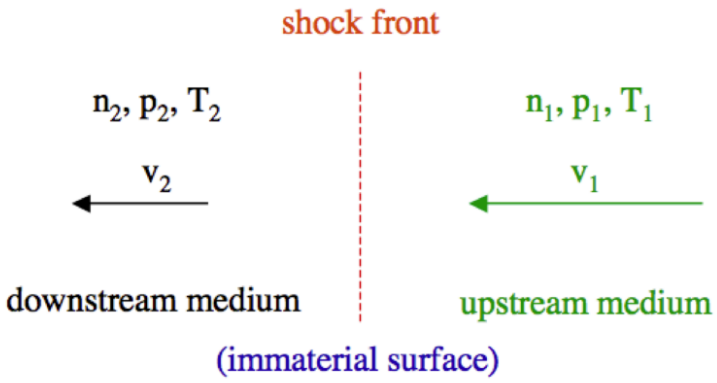

Figure 4.9: Schematic view of a diffusive shock acceleration or first order Fermi mechanism, in the shock rest frame. The upstream (left) is moving towards the shock at velocity v_1, whereas the downstream (right) is moving away from it at velocity v_2.

A more effective acceleration mechanism is the DSA or the first-order Fermi acceleration. In this process, charged particles are accelerated while crossing shock wave fronts, where collisions are head-on only.

The process is depicted in Figure 4.9. The front of the shock wave is an abrupt discontinuity separating two regions with different properties, such as density, temperature, pressure, velocity, and magnetic field. The downstream is the region behind the shock wave front, and the upstream is the gas ahead of it. In the

reference frame of the shock wave front (the dashed line in the sketch), upstream (ahead) is moving towards it with a velocity $V = \mathrm{v}_1$, while the downstream (shocked gas) is leaving it at a velocity $v_\mathrm{d} = \mathrm{v}_2$.

Shocks in astrophysical environments are magnetodynamic shocks, where magnetic fields play an important role, and shocks are typically collisionless.

Particles in the upstream are approximately isotropic in the laboratory reference frame, due to scattering of magnetic fluctuations. The shock advances in this isotropic medium with velocity V, and when particles crosses the shock front, they gains an energy $\Delta E \sim V/c$

After crossing the shock, in the downstream, particles are scattered again to an isotropic distribution. When they cross the front again, this time to the upstream, they see the shock front at the same speed V, leading to the same increase in energy. As a result, every time a particle crosses the shock front, it gains energy. The energy gain after a cycle of upstream–downstream-upstream for a particle moving with velocity $v \approx c$ is

$$\frac{\Delta E}{E} \propto \frac{4}{3}\left(\frac{V - v_\mathrm{d}}{c}\right). \tag{4.27}$$

The number spectrum for DSA is:

$$n(E) \propto \left(\frac{E}{E_1}\right)^{-x}, \tag{4.28}$$

where $x = \frac{r+2}{r-1}$, and $r = V/v_\mathrm{d}$ is the compression ratio. In the case of strong shocks, when the velocity V is much larger than the ambient sound speed v_s, and $r = 4$, the power law index is $x = 2$. This result naturally arises for DSA, in contrast to the Fermi mechanism.

4.4.2 Where are the cosmic rays accelerated?

To accelerate particles to very high energies, certain conditions must be satisfied by the astrophysical source. Hillas [98] established constraints based on the size of the source and its magnetic field strength. CR particles can reach UHE when they are confined within the acceleration region. This means that the Larmor radius of the accelerated particle is smaller than the size of the accelerator. Under this condition, the maximum energy E_max that is achievable for a source of size R and magnetic field B is given by:

$$E_\mathrm{max} = \eta \frac{v}{c} BR, \tag{4.29}$$

where η is the acceleration efficiency. This is known as the "Hillas condition".

Figure 4.10 shows the Hillas diagram, which presents candidate astrophysical sources of CR acceleration as a function of their size and magnetic field strength. The diagram illustrates that potential CR accelerators include neutron stars/magnetars, gamma-ray bursts (GRBs), starburst winds, active galactic nuclei (AGN), and galaxy clusters. Other possible sources are supernova remnants (SNRs), pulsar wind nebulae (PWNe), binary systems, and stellar clusters.

A brief overview of example astrophysical sources capable of accelerating particles to VHE, with particular relevance to the Galactic Centre (GC) region, is provided below.

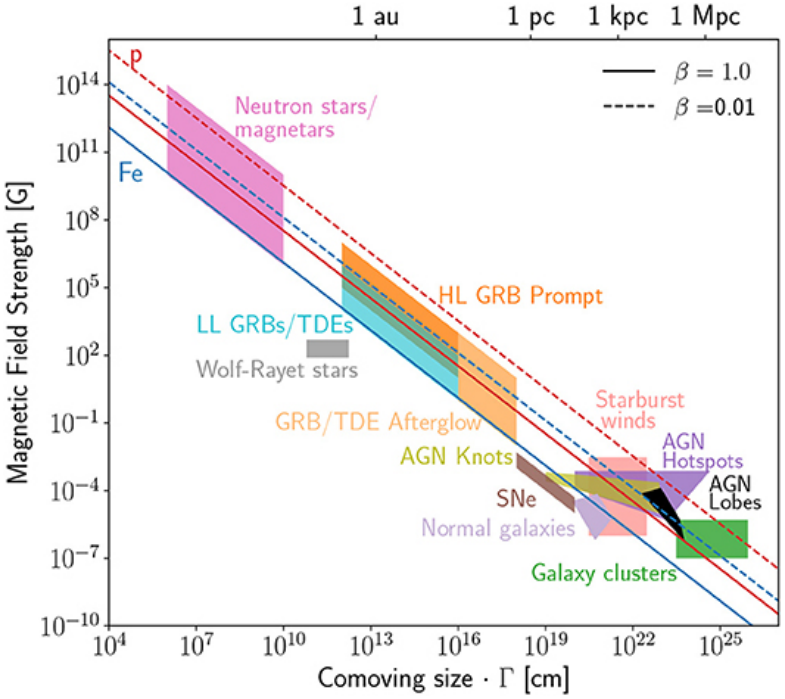

Figure 4.10: Hillas diagram. Potential CR accelerators a displayed as a function of their size R and magnetic field strength B. The solid lines indicate the minimum RB required to accelerate protons and iron nuclei to 10^{20} eV energies for strong shocks, while dashed lines are for less energetic shocks. Figure from [19]

Supernova Remnants

Stars with masses greater than eight solar masses end their life in a supernova explosion. Such an event releases a total energy of $\sim 10^{51}$ erg into the ISM. In the Milky Way, supernovae occur at a rate of about two to three per century. If even a few percent of this energy is transferred to accelerating particles, a supernova could account for the CR spectrum up to the knee.

During the supernova event, supersonic plasma is ejected, compressing and heating the surrounding gas swept up by the shock. The particles are subsequently accelerated through the DSA mechanism. The supersonic flow propagates until it slows down to subsonic speeds and mixes with the ISM. The duration of this process lasts up to $\sim 10^5$ years.

The shock propagation following a supernova explosion occurs in two main phases. The first is the free expansion phase, which lasts a few hundred years and is characterised by an almost constant shock velocity. This is followed by the Sedov-Taylor or adiabatic phase, during which the shock begins to decelerate after sweeping up an amount of ISM gas comparable to the mass of the ejected material [21]. As the forward shock slows down during this phase, a reverse shock forms and propagates inward, towards the center of the SNR. The evolution of the SNR radius in this phase can be approximated as $R(t) \propto t^m$, where m is the expansion parameter [107]. After the expansion phase, $m \approx 1$ by definition, and it gradually decreases in the second phase to $m = 0.4$.

It is now well established that SNRs can accelerate CRs; however, the maximum energy they can reach appears to fall below the knee. This makes it difficult to conclude

whether SNRs are the main source of Galactic CRs. In principle, only young SNRs could accelerate particles up to PeV energies, but no such remnant has been firmly identified so far.

Pulsar Wind Nebula

Pulsars are rapidly rotating magnetized neutron stars with radii of about 10 km and masses comparable to that of the Sun. They possess extremely strong magnetic fields, ranging from around 10^8 G in millisecond pulsars up to 10^{15} G in the case of magnetars.

Some pulsars are surrounded by nebulae, forming the so-called PWNe. An active pulsar can launch a relativistic wind with a total energy of the order of its spin-down luminosity. This pulsar wind consists of both magnetic flux and relativistic electrons and positrons generated in the magnetosphere. The wind eventually terminates at a relativistic shock, known as the termination shock, where particles, primarily leptons that were loaded with the wind, are efficiently accelerated. The energy loss rate of the pulsar is given by:

$$E = L_{\mathrm{s}D} = 4\pi r^2 \Gamma n_{\mathrm{e}} m_{\mathrm{e}} c^3 (1+\sigma), \quad \text{with}\, \sigma = \frac{1}{4\pi\Gamma n_e m_{\mathrm{e}} c^2} \tag{4.30}$$

where $L_{\mathrm{s}D}$ is the spin down luminosity, n_{e} is the electron and positron number density, and Γ is the bulk Lorentz factor of the electron-positron flow.

PWNe are efficient particle accelerators, capable of reaching energies up to the PeV range. This was demonstrated by [125], who recently detected PeV γ-rays from the direction of the Crab Nebula.

Massive Stellar clusters

A recently emerging and very active research topic is the role of massive stellar clusters as CR accelerators. These systems consist of many massive stars grouped together in bound clusters or associations. The massive stars produce powerful stellar winds and eventually explode as supernovae, expelling the surrounding circumstellar gas. This process carves out large cavities around the clusters, forming structures known as superbubbles. This makes massive stellar clusters powerful contributors to the population of Galactic CRs, and provides a promising explanation for the origin of PeV accelerators (PeVatrons) [74].

Only a handful of stellar clusters have been detected in γ-ray observations. These include Westerlund 1, a young massive stellar cluster detected by H.E.S.S. [14] and the detection of > 100 TeV γ-rays from the Cygnus Cocoon reported by LHAASO [40]. The limited number of detected stellar clusters in γ-rays may be explained by two reasons: either only a small fraction of clusters are capable of producing detectable γ-ray emission, or the γ-ray emission of stellar clusters is not being recognised as such.

Peron et al. [156] attempted to correlate the Gaia DR2 stellar clusters to unassociated γ-ray sources, and found a strong correlation with sources detected by *Fermi*-LAT. However, no significant associations were obtained for GeV and TeV sources. This could be due to a lack of target ISM gas for γ-ray production, or simply insufficient observation time.

Nevertheless, massive stars appear to be promising candidates for accelerating CRs up to the knee. Even more than SNR, as their lifetimes are significantly longer, on the order of ~ 1 Myr compared to $\sim 10^4$yr for the SNRs. Furthermore, even if these sources are not individually resolved in γ-rays, they can contribute to diffuse γ-ray emission.

4.5 Dark Matter

4.5.1 Expected gamma-ray flux from the DM annihilation

As introduced in Section 2.3, WIMPs can decay or annihilate into other Standard Model particles, including γ-rays. The rate of γ-ray production from dark matter is usually separated into two terms: one to characterize the astrophysical properties of the source, and another one for the particle physics contribution to the rate.

$$\frac{d\Phi_\gamma}{dE}(E,\Delta\Omega) = \underbrace{\frac{1}{4\pi}\frac{\langle\sigma v\rangle}{m_\chi^2}\sum_i Br_i\frac{dN_i}{dE_\gamma}}_{\text{particle physics}} \times \underbrace{J(\Delta\Omega)}_{\text{astrophysics}}, \tag{4.31}$$

where in the particle physics contribution, m_χ is the DM mass, $\langle\sigma v\rangle$ is the thermally averaged velocity weighted annihilation cross section, dN_i/dE_γ is the spectrum of the annihilation, for a specific channel, i, and Br_i is the branching ratio for that channel which represents the probability for the DM particle to annihilate into that channel.

The astrophysical term is called the J-factor and is defined as:

$$J_{\Delta\Omega} = \int_{\Delta\Omega} \mathrm{d}\Omega \int_{\mathrm{los}} \mathrm{d}l \times \rho^2[r(l)], \tag{4.32}$$

where ρ is the dark matter density distribution (see the different options for ρ in Section 2.3) and it is integrated over the line of sight (los) and inside the observed solid angle $\Delta\Omega$. The number of observable events can be estimated as:

$$S_{ij} = T_{\mathrm{obs}} \int_{\Delta E_j} dE' \int^{\infty} dE\, \frac{d\Phi_\gamma(\Delta\Omega_i, E)}{dE} \times A_{\mathrm{eff}}(E) \times \mathrm{PDF}(E, E'). \tag{4.33}$$

where T_{obs} is the live time of observation, A_{eff} is the detector effective area, $\mathrm{PDF}(E, E')$ takes into account the energy resolution of the observational instrument, and E' is the reconstructed energy.

4.5.2 Other DM candidate sources

Beyond the GC, several other regions are considered promising targets for DM searches. These regions are expected to contain dense DM halos or clumps, potentially producing detectable γ-ray signals. Within the Milky Way, Galactic DM halos are considered potential sources, although smaller predicted DM subhalos may not generate sufficient γ-ray emission. Wide-field observations with *Fermi*-LAT have revealed a population of unidentified sources that could be viable candidates for DM subhalos [111].

Outside the Milky Way, the dwarf galaxies orbiting our Galaxy are among the most DM-dominated candidates known. These systems are especially favourable for DM searches, as they lack star formation and are largely devoid of gas, providing a clean environment for observing potential γ-ray emission from DM annihilation. Further away from the Earth, galaxy clusters are the largest systems dominated by DM, with 80% of their total mass composed of DM. However, they are very far away, resulting in a very low J-factor, making γ-ray signals much harder to detect.

In general, DM searches are most effective in regions with a high DM density that are also nearby, where γ-ray emission from DM annihilation or decay can be distinguished from the astrophysical background. In this context, the GC remains the most promising target due to its proximity and the expected high DM content.

4.6 Detection of gamma-rays

γ-ray astronomy is a rather young field compared to other wavelength domains in astronomy. The first detection of γ-rays occurred in the 1960s, originating from solar eruptions at energies of a few MeV. Because the Earth's atmosphere is opaque to γ-rays, the first dedicated γ-ray instruments were deployed in space. As discussed in section 4.3, several γ-ray energy loss mechanisms are used to detect γ-rays. For instance, missions like COSI and CGRO detect γ-rays by Compton scattering, and *Fermi*-LAT relies on the pair production process.

Yet with increasing energies, γ-rays become increasingly rare. In fact, a detector with an effective area of 1 m^2 would detect roughly one photon from the Crab Nebula in the energy range of 100 MeV to 5 GeV every minute. In contrast, at energies above 1 TeV, it would detect only about seven photons per year. Therefore, larger instruments are required to collect sufficient γ-ray statistics at higher energies. However, such large detectors are extremely difficult to launch into space, and therefore must be deployed on the ground.

Ground-based detectors observe VHE γ-rays via the detection of Cherenkov radiation. These detectors are generally classified into two types: Imaging Atmospheric Cherenkov Telescopes (IACTs), which detect Cherenkov light produced in the atmosphere, and the Water Cherenkov Detectors (WCDs), which measure the Cherenkov light generated by secondary particles passing through water.

In this dissertation, we focus on the ground-based detectors for observing the highest energy range of γ-rays. To understand how the energy and direction of the primary γ-ray can be reconstructed after its interaction with matter, either in the atmosphere or in water, it is essential to first introduce the concept of particle cascades and the development of Extensive Air Showers (EAS).

4.6.1 Extensive Air Shower

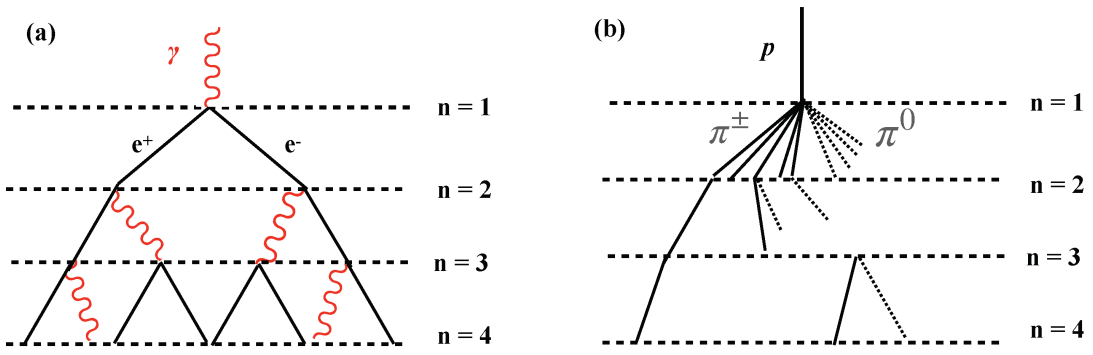

Figure 4.11: Schematic diagram of the EM cascade (left) and the hadronic shower (right). In the hadronic shower, neutral pions π_0 are indicated by dashed lines, which decay and produce electromagnetic showers. Therefore, hadronic cascades produce more chaotic images of the Cherenkov light pool on the ground. Figure from [57].

A schematic picture of electromagnetic (EM) cascade induced by a γ-ray is illustrated in the left panel of Figure 4.11. This shower of secondary particles is known as an Extensive Air Shower (EAS) and is based on two main mechanisms: pair production and Bremsstrahlung by electrons and positrons.

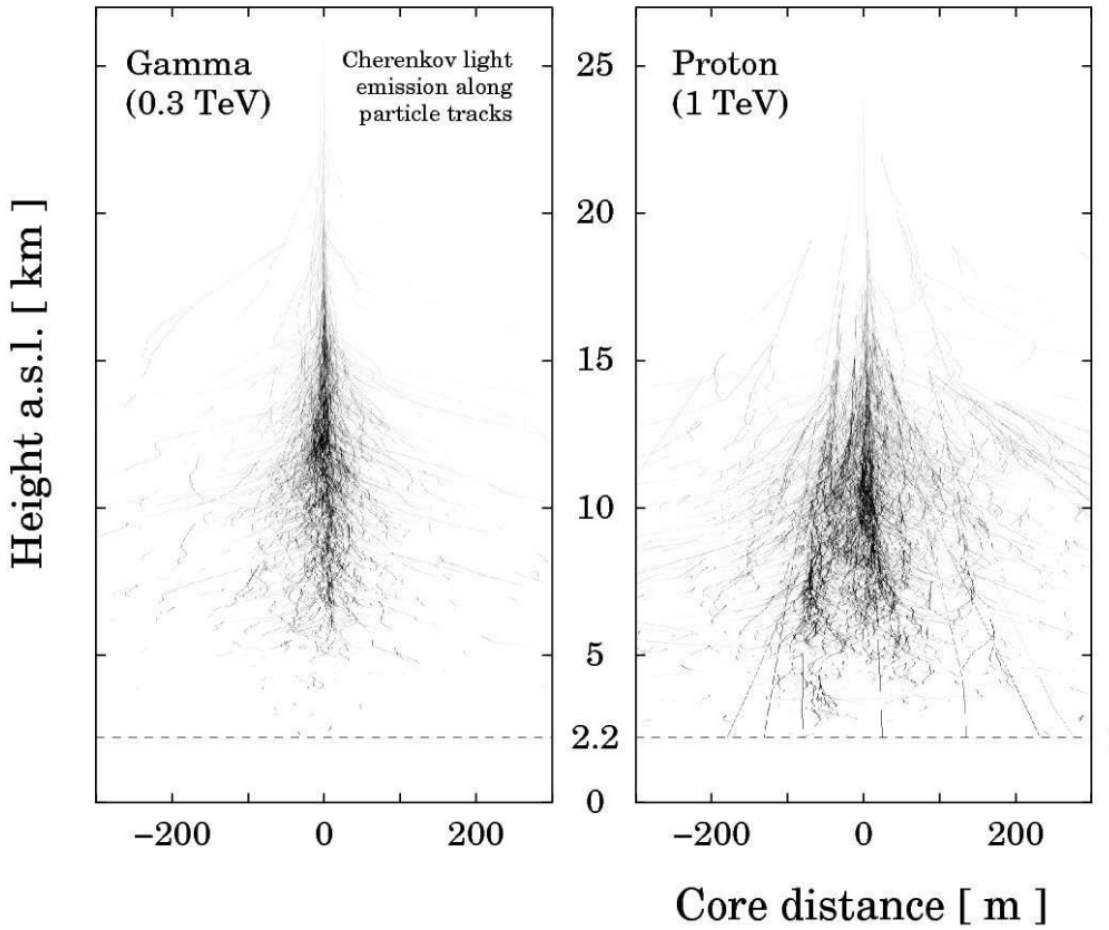

Figure 4.12: Simulations of γ-ray (left) and proton (right) initiated showers using CORSIKA. Figure from [27]

Let's start with the γ-ray entering the atmosphere. The γ-ray can be scattered by the Coulomb field of an atmospheric nucleus and produce an electron-positron pair. These charged particles can, in turn, emit secondary γ-rays via Bremsstrahlung as they pass near other nuclei, which can then generate additional pairs. This cascade process continues, repeating multiple times, until the particle energies fall below the critical energy of 83 MeV (in air), at which point they are quickly attenuated through ionisation losses. As a result, a large shower of secondary particles is formed in the atmosphere, usually consisting of billions of particles.

The high-energy charged particles within the air shower produce Cherenkov light (see section 4.3.2 (c)). Given a typical Cherenkov radiation opening angle in the atmosphere $\theta \sim 1°$, the resulting light pool on the ground at an altitude of $\sim$2 km above sea level is about 120 m.

However, γ-rays are not the only particles capable of initiating EAS, relativistic hadrons and electrons can also generate particle cascades in the atmosphere, each with distinct characteristics. Hadronic showers (shown in right panels of Figures 4.11 and 4.12) are much more frequent compared to γ-ray showers, and they are usually a mixture of hadronic and EM components, making them generally more chaotic and irregular compared to those initiated by γ-rays.

Energetic hadrons mainly produce pions and kaons upon interacting with atmospheric

nuclei, which further generate muons. Those secondary particles energetic enough will continue to collide with other nuclei to produce more pions and kaons (hadronic component). Neutral pions are unstable and eventually decay into two γ-rays, which initiate the EM component of the cascade. Charged pions decay into neutrinos and muons, contributing to the muonic component of the shower. Charged kaons can decay into charged pions or directly into muons and neutrinos. The muonic component carries most of the shower energy and can reach the ground without interacting with other particles.

Electron-initiated showers, on the other hand, closely resemble those produced by γ-rays and are basically indistinguishable from each other when observed with ground-based detectors. However, the electron spectrum is expected to steeply decline at relatively low energy ($\sim$100 GeV), meaning that electrons do not contribute significantly to the overall rate of air showers.

The atmosphere acts as a calorimeter where the energy of the initial particle is deposited. However, only the degraded information at the bottom of the shower can be registered by ground-based instruments. These detectors can observe either the Cherenkov radiation produced in the atmosphere or the charged particles that reach the ground, in the case of sufficiently high-energy particles. The main goal of the ground-based telescopes is to identify the incident particle, whether it is a γ-ray or a hadron, and to determine its energy and direction.

Identifying the primary particle, particularly distinguishing γ-rays from background CR events, is not always straightforward. A dedicated discussion on background rejection techniques is presented in Chapter 5.

The development of an electromagnetic EAS can be characterised by the EM radiation length:

$$X_0 = \left[4\alpha r_e^2 \frac{N_A}{A} Z^2 \ln(183 Z^{-1/3})\right]^{-1} [\text{G cm}^{-2}], \tag{4.34}$$

where $\alpha = 1/137$ is the fine structure constant, r_e is the classical electron radius, N_A is the Avogadro number, and A and Z are the mass and atomic number of the material. This follows the Heitler model, a simplified description, but it gives the basic features of the shower development. In the atmosphere, the radiation length is on average $X_0 = 36.7$ G cm^{-2}, which means that the atmosphere is a thick calorimeter of $\sim$27 radiation lengths.

The energy loss due to Bremsstrahlung as a function of the traversed depth $X = \int_z^\infty \rho(z)\mathrm{d}z$ is then

$$E(t) = E_0 \, exp\left(-\frac{X}{X_0}(1+b)\right), \tag{4.35}$$

where $b = (18 \ln(183 Z^{-1/3}))^{-1} = 0.0122$ in the atmosphere.

Each electron loses half of its energy at a depth of $R = X_0 \ln 2$. We assume that the energy is transferred to a single γ-ray, and that the γ-ray undergoes a pair production after the same depth $R = X_0 \ln 2$. This simple model is schemed in Figure 4.11, where we can see in the left panel for the EM cascade that after a number of depth steps $n = X/R$, the number of particles reaches 2^n. The shower maximum is defined as the depth of the maximum shower development

$$X_{max} = X_0 \ln \frac{E_0}{E_c} \tag{4.36}$$

where E_c is the critical energy in air.

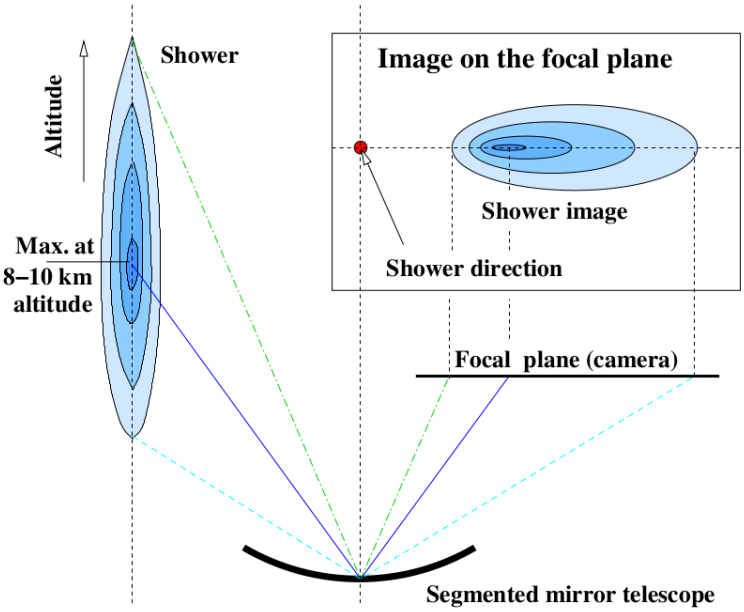

Figure 4.13: Shower imaging by an IACT. The shower image on the telescope mirror has an elliptical shape. Figurre from [211].

For a hydrostatic atmosphere, the pressure and density depend on the altitude, which leads to a depth as a function of the altitude. In this more realistic case, the maximum of shower development for a 1 TeV photon is $z_{\max} \approx 9$ km, from the ground.

4.6.2 Imaging Atmospheric Cherenkov Telescopes

The Imaging Atmospheric Cherenkov Telescopes (IACTs) use large dish mirrors and very fast and sensitive cameras to capture the Cherenkov light produced by the EAS when a VHE γ-rays enter the atmosphere. The effective collection area of a single dish is basically determined by the radius of the Cherenkov light pool, $R_c \simeq 120$ m. The shower duration is typically of the order of nanoseconds. An IACT located in the Cherenkov light pool detects the shower as an ellipse on its camera, as shown in Figure 4.13. The observations are typically conducted in exposures of about 30 minutes, referred to as runs.

Starting from the 1950s, exploration of possibilities to detect γ-rays both from space and from the ground began. The IACT technique was pioneered by the Whipple telescope (formerly known as the Mount Hopkins Observatory), which started operation in 1968, in Arizona, with a 10 m mirror dish [8]. In 1989, after the addition of a 37 pixel camera and improved shower parameterization with Hillas parameters (which lead to better reconstruction and background rejection) [99], they reported the detection of TeV γ-rays from the direction of the Crab Nebula at 9.0σ [214]. This success opened up the field of γ-ray astronomy for imaging telescopes. Another group at the Crimean Astrophysical Observatory also developed a very complex system of Gamma Telescope with 48 (1.2 m) mirrors, equipped with 37 pixel cameras, and was completed in 1989. Unfortunately, due to the political circumstances, this instrument did not receive much support, and the operation ceased in 2002.

Several new projects followed. CANGAROO 3.8m telescope measured the Crab

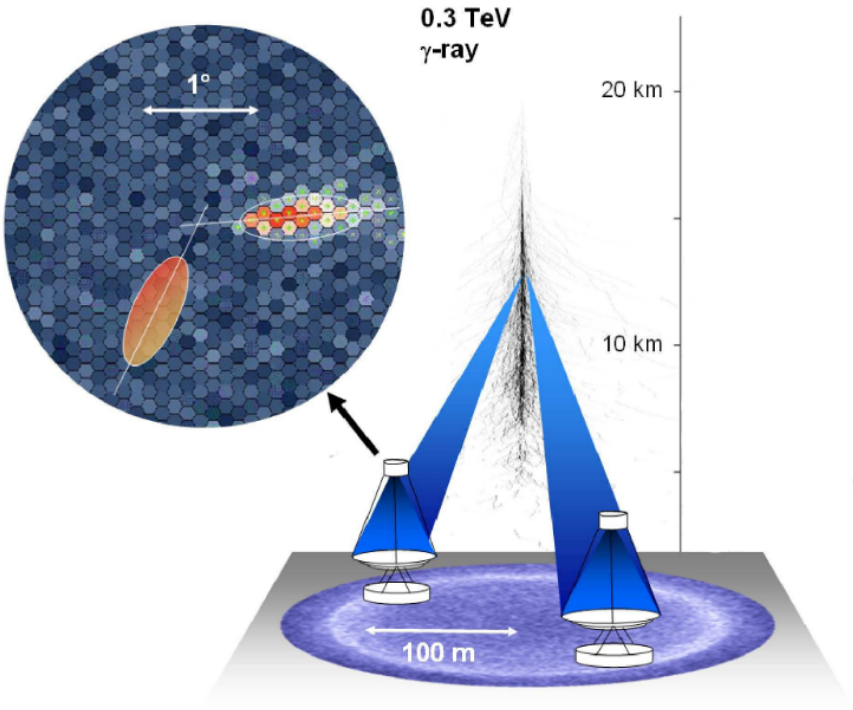

Figure 4.14: Sketch of stereoscopic system of IACTs. The images produced on each telescope is shown. Figure adapted from [101].

spectrum up to 50 TeV and detected γ-rays from the supernova remnant SN 1006 in 1998 [200, 201]. Whereas, HEGRA (the first stereoscopic system) confirmed the detection of the extragalactic source Markarian 421 in 1996 [157], which was also detected by the Whipple telescope in 1992 [165].

A stereoscopic system of IACTs offers improved event reconstruction and background rejection, even by simply requiring coincidence between multiple camera images. Figure 4.14 illustrates the formation of a stereoscopic image on the telescope cameras. The intersection point of the major axes of the recorded images indicates the direction of the primary γ-ray.

The current generation of IACT arrays includes the Very Energetic Radiation Imaging Telescope Array System (VERITAS) in Arizona [34], the Major Atmospheric Gamma Imaging Cherenkov Telescopes (MAGIC) on the Canary Island La Palma [48], and the High Energy Stereoscopic System (H.E.S.S.) in Namibia [102]. These observatories are located at altitudes between 1500 and 2200 m, and are equipped with large mirror dishes ranging from 12 to 28 m in diameter. They are highly sensitive to γ-rays in the energy range from tens of GeV to tens of TeV. H.E.S.S. is currently the only IACT array located in the southern hemisphere, providing optimal conditions for observing the Galactic Centre region.

The future of IACTs lies in the Cherenkov Telescope Array Observatory (CTAO), which is currently under construction. It will consist of two arrays/stations: one in the northern hemisphere and another in the southern hemisphere, each hosting more than ten telescopes. This dual-site configuration will optimise both sky coverage and energy range, ensuring the highest performance ever achieved by an IACT array.

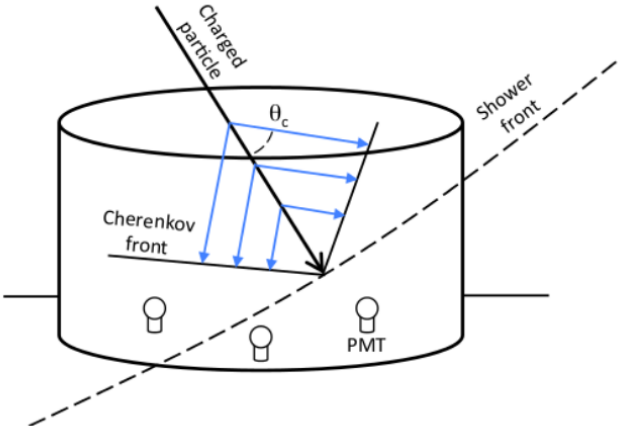

Figure 4.15: Cherenkov radiation in a WCD tank. Photomultipliers (PMTs) are placed at the bottom of the tank to collect the Cherenkov photons. Figure from [91].

4.6.3 Water Cherenkov detectors

This technique uses water as the calorimeter, requiring detectors to be placed at higher altitudes, closer to the shower maximum, to ensure that a sufficient number of secondary particles can be detected. Compared to IACTs, Water Cherenkov detector (WCD) arrays offer lower angular and energy resolution. However, they compensate with a very large field of view (FoV) and, in principle, a 100% duty cycle, allowing them to continuously monitor a large portion of the sky. While, in the case of IACTs, observations can only be performed at night, under good weather conditions, and without excessive moonlight, resulting in approximately 1000 hours of observation time per year. Figure 4.15 displays a sketch of the Cherenkov radiation in a WCD.

The first generation of this type of detector was the Milagro experiment, which consisted of an 8 m deep, light-tight pool of water, with a surface area of 5000 m^2, located at 2630 m altitude in New Mexico. Over six years of operation, Milagro successfully detected a total of six TeV γ-ray sources [190].

A follow-up experiment is the High Altitude Water Cherenkov (HAWC) Experiment, built in Mexico at an altitude of 4100 m, fully functional since 2015 [2, 16]. HAWC consists of two arrays of WCDs. A primary array of 300 densely packed water tanks, each of 5.4 m high and 7.3 m diameter, covers an area of 22000 m^2. This primary array is surrounded by a sparser array of 345 small WCDs. Figure 4.16 shows example shower images for a hadronic (left panel) and an EM shower (right panel) on the HAWC array.

In the eastern side of the globe, the Large High Altitude Air Shower Observatory (LHAASO) started its operation in 2019, at an altitude of 4410 m in Sichuan [39]. LHAASO is a hybrid observatory, with an outer array of scintillators to detect the charged particles in the EAS, an array of underground WCDs, also loght-tight, to collect muons, another array of air shower telescopes of small size mirrors, and three water ponds (WCDA) at the centre to detect water Cherenkov light. The water ponds have depth of 4.5 m and a total size of nearly 300 $\times$ 300 m.

Until now, all WCDs have been placed in the northern hemisphere. A future southern-hemisphere WCD array, currently in the development phase, is the Southern Wide-field Gamma-ray Observatory (SWGO) [106]. It is planned to be built at the Atacama Astronomical Park in Chile, at an altitude of 4770 m. Current designs envision a

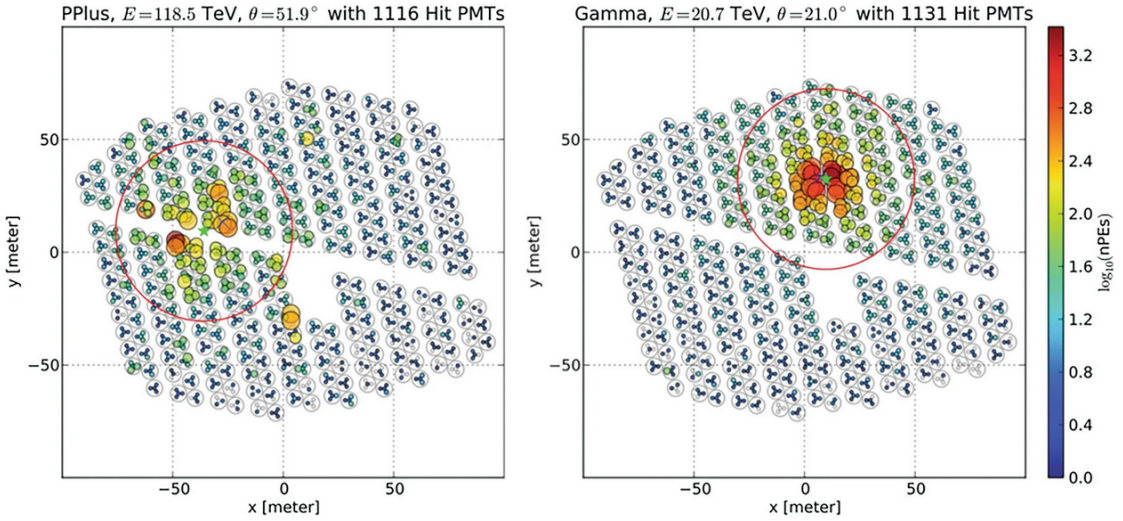

Figure 4.16: Shower images on the HAWC array. Left: hadronic shower. Right: EM shower. The hadronic shower image has energy deposited further away from the core, which enables γ/hadron separation. Figure from [60].

structured array with different filling factors, consisting of large water tanks ∼4 m depth and ∼5m in diameter. Each tank will feature two layers: an upper layer for measuring Cherenkov light of secondary particles from EAS and a lower chamber dedicated to capturing Cherenkov light from muons. SWGO is expected to cover a total area of 1 km^2. A multi km^2 array of bladders in a natural lake is contemplated as a possible extension of SWGO in a later phase, aimed at enhancing the observatory's sensitivity to UHE γ-rays.

4.7 Scheme of gamma-ray data reduction

Figure 4.17 depicts the data levels and data processing steps for IACTs. This scheme is used for CTAO data model [47], but it is also applicable to all γ-ray data. The process begins with the output from the data acquisition (DAQ) system, containing the signal from camera pixels (Data Level 0 or DL0). After calibration of the signal, these signals are converted into pixelated images of the Cherenkov light produced by the air shower (DL1). In the next step (DL2), the image parameters are used to reconstruct the observables of the shower, such as the energy, incoming direction, and the probability that the event is a γ-ray (commonly referred to as gammaness). The selected γ-ray candidate events are recorded in an event list, and the parameterization of the response of the system, or also called as instrument response functions (IRFs), is produced (DL3). Finally, the event list and the IRFs are used in statistical analyses to derive scientific results (DL4). The last step is generally referred to as high-level data analysis

This data processing procedure can also be applied to WCD arrays, with the primary difference being in the format of the raw data. For particle detectors, instead of camera images, the raw data (DL0) consists of the charge deposited by the shower in the detector array and its time evolution. Using this information, reconstruction algorithms estimate the shower parameters (DL1). From this point onward, the subsequent data levels and analysis steps follow the same structure as in the IACT workflow.

With the advent of next-generation γ-ray observatories and the growing demand for open science, there has been a push to standardise the data format used in astronomical

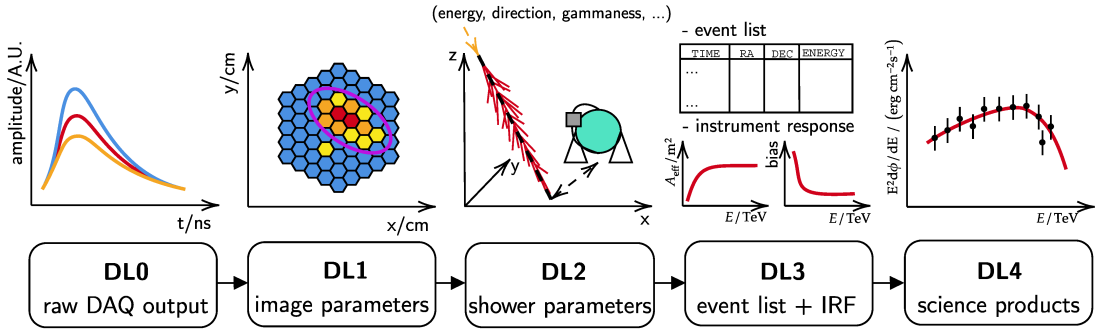

Figure 4.17: Scheme of the γ-ray data processing from raw data to scientific results, for IACTs. Figure from [143].

γ-ray research. This effort led to the creation of the *Data Formats for Gamma-ray Astronomy* or GADF, a documentation specifying the format of the γ-ray high-level data products [143]. GADF primarily focuses on the DL3 data products, and modern high-level analysis tools such as `Gammapy` and `ctoos` are designed to work with this standardised data format.

4.8 Summary

In this chapter, we described the mechanisms responsible for γ-ray production, which can originate from either leptonic or hadronic processes, as well as the various γ-ray energy loss mechanisms that enable their detection from space or ground-based observatories. The CR energy spectrum was introduced, along with the particle acceleration processes and potential astrophysical sources responsible for CR acceleration. Additionally, we discussed the potential γ-ray signatures of DM and presented the promising targets for DM searches, including the GC, dwarf galaxies, and DM halos.

Ground-based γ-ray detection methods can be divided into two main approaches: Imaging Atmospheric Cherenkov Telescopes (IACTs) and Water Cherenkov Detectors (WCDs). IACTs offer superior energy and angular resolution with respect to the WCDs, while the latter provide a much longer duty cycle and a wider field of view. Finally, a brief overview of data reduction and the efforts to standardise γ-ray data formats was presented.

The next chapter will provide a detailed description of the H.E.S.S. and SWGO instruments.

Chapter 5

H.E.S.S. and SWGO, two instruments for gamma-ray detection

Stereoscopic arrays of IACTs have significantly improved the observations of γ-rays compared to single-dish experiments. They enable more precise reconstruction of shower parameters, enhance γ/hadron separation power, and allow for more effective suppression of background light, such as the night sky background (NSB) and local muons [9].

The High Energy Stereoscopic System (H.E.S.S.) is the only stereoscopic IACT array located in the Southern Hemisphere, making it the most suitable instrument for observing the GC region in the GeV to TeV energy range. This chapter introduces the H.E.S.S. experiment, outlining its key characteristics and operational modes. Particular attention is given to methods used for identifying hadronic background showers. This is a crucial task as CR induced showers dominate the recorded events, while the scientific interest lies in detecting EM showers initiated by γ-rays. Thus, effective separation of CR and γ-ray events directly influences the sensitivity and angular resolution of the observational instrument.

Moreover, a new WCD observatory – the Southern Wide-field Gamma-ray Observatory (SWGO) – is currently under development. The observatory will consist of an array of water Cherenkov detectors (WCDs) designed to detect the secondary particles produced in extensive air showers (EAS) initiated by γ-rays (see Figure 5.10). Several detector sizes and array layouts were designed for SWGO in order to test the different technological and design possibilities, which are also included in this chapter.

H.E.S.S. and its characteristics are introduced in Section 5.1. An outline about the H.E.S.S. data analysis procedure, from raw data to the final scientific results, is provided in Section 5.2. Section 5.3 introduces SWGO and Section 5.4 describes the multiple design options that were suggested. A summary of the chapter is then given in Section 5.5.

5.1 The H.E.S.S. telescopes

H.E.S.S. stands for High Energy Stereoscopic System, and is an array of IACTs located in the Namibian region of Khomas Highland, at geographic coordinates 23°16'17"S and 16°30'00"E. The altitude of the plateau is approximately 1800 m above sea level.

H.E.S.S. is currently the only IACT array in operation in the Southern Hemisphere, which makes it the best among this kind of instrument to observe the Galactic plane and, especially, the GC, due to its high elevation angle.

H.E.S.S. is an array of four small IACTs (named CT1-4) with a mirror size of 12 m in diameter, arranged in a square with 120 m sides, and a larger IACT (CT5) at the centre of the square, with a 28 m diameter mirror. CT1-4 began operation in September 2004 (H.E.S.S. I phase) [102], and the central CT5 started collecting data in 2014 (H.E.S.S. II phase) [117]. Later, the camera electronics of the small IACTs were upgraded in 2015-2016, to improve the performance of the array (H.E.S.S. IU phase) [77]. Finally, an

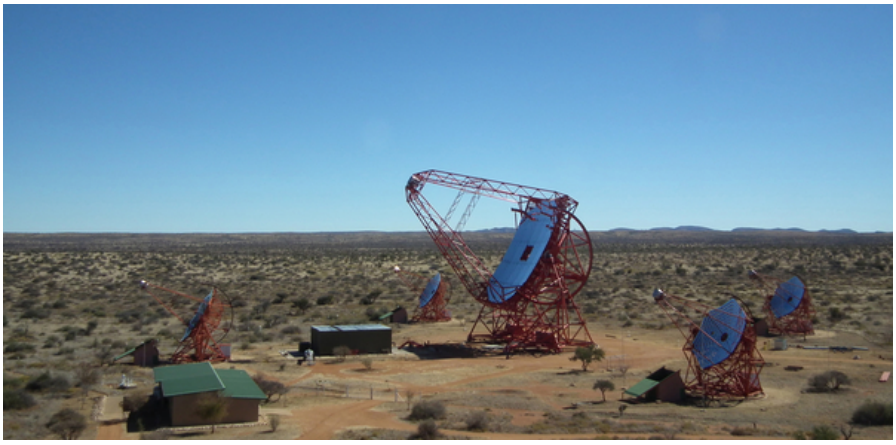

Figure 5.1: H.E.S.S. array of IACTs. The small CT1-4 telescopes are at the corner of the square, while the large CT5 telescope is at the center. Image credit: H.E.S.S. Collaboration.

upgrade of the CT5 camera to FlashCam occurred in 2019 [29]. A picture of the current array can be seen in Figure 5.1.

The mirror of each small telescope is a group of 382 smaller circular mirrors, facets of 60 cm diameter. The mirror facets are arranged in a Davies-Cotton configuration, and the total mirror area is 108 m^2 per telescope. The focal length is 15 m and the d/f ratio is 0.8. The mirror reflectivity is more than 80% in the wavelength range of Cherenkov radiation. The camera, positioned at the focus of the mirror, is equipped with 960 photomultipliers (PMTs) with a FoV of 0.16°each. The total FoV is 5°. The camera is triggered when a coincidence of signal is detected in 3 to 5 pixels in an 8×8 pixel sector. The coincidence trigger can effectively reject uncorrelated signals caused by the NSB, which in this case is mostly the light from stars. The effective coincidence window is about 1.5 ns.

The large telescope mirror is composed of 875 hexagonal facets of 90 cm size, from one flat side to the opposite. Mirror facets are arranged in a parabolic configuration, and the total mirror area is 614 m^2, with a focal length of 36 m. The CT5 camera contains 2048 PMTs. The pixels are hexagons of 42 mm size, equivalent to 0.067° FoV. The total FoV of the CT5 mirror is 3.6°. The integration time for an effective signal is 16 ns.

CT1-4 are sensitive to γ-rays of energies above 100s of GeV [13], while CT5, with a larger mirror dish, can detect fainter radiation, lowering the energy threshold of detectable γ-rays [103].

The array of IACTs can operate in several different modes: (i) **Stereo mode**, when considering only CT1-4. At least two telescopes must be triggered for the event to be recorded. (ii) **Mono mode**, when only CT5 is triggered. (iii) **Hybrid mode**, when all five telescopes are considered. If CT5 is not triggered, then the rest of the telescopes have the same requirement as in stereo mode. The H.E.S.S. observations are conducted in exposure times of 28 minutes, referred to as runs.

5.2 H.E.S.S. data processing

The process of IACT data reduction follows these steps (also introduced in Section 4.7), which is a way to schematise the procedure as following [47]:

1. DL0: calibration of raw DAQ data,
2. DL1: measurement of camera image parameters,
3. DL2: reconstruction of shower parameters,
4. DL3: production of event list and IRFs, and
5. DL4: analysis of scientific results (flux points, spectrum and significance)

There are two main analysis chains of H.E.S.S. data analysis: the H.E.S.S. Analysis Package (HAP) and the Paris Analysis (PA). In this work, we focus on the HAP analysis package. Although HAP enables a complete analysis of detected γ-rays, from raw data to compute flux points and spectra, more advanced tools, such as `Gammapy` [3, 59] are slowly replacing the high-level analysis starting from DL3 products. Therefore, in this work, HAP is used exclusively for low-level data analysis.

5.2.1 DL0: Calibration of raw DAQ

Trigger system
Three thresholds are defined for a signal to be triggered:

1. Number of photoelectrons (p.e.) in a single pixel ($S1$): a pixel is triggered when its signal is above this value, such that electric noise and pedestal are rejected.
2. Number of nearby triggered pixels in the same sector ($S2$): the telescope is triggered when the number of nearby triggered pixels is above this number.
3. Number of triggered telescopes ($S3$): this is defined as the stereoscopic threshold.

For H.E.S.S. I phase, $S1 = 4$ p.e., $S2 = 3$ pixel per sector and $S3 = 2$ telescopes. The choice of trigger threshold directly influences the effective energy threshold and must strike a balance between two key factors: (i) the trigger rate from the NSB should not exceed the detection rate of γ-rays, and (ii) the number of p.e. in the image should be sufficient for a reliable shower reconstruction, typically ~ 100 p.e.

Quality cuts
Quality cuts are applied after the initial triggering. Certain camera pixels may be excluded from an observation due to malfunction or the presence of bright stars in their field of view. The number of deactivated pixels is limited to 10%. Additionally, the global trigger rate must remain above 70% of the average, and the variation in trigger rates among small telescopes should be less than 10%. Weather conditions (such as humidity and temperature) and sky transparency (e.g., cloud coverage) are continuously monitored using a weather station and an infrared LIDAR system.

Instrument calibration

The reconstruction of the signal amplitude in CT1-4 is based on several parameters: the ratio between the low gain (LG) and high gain (HG) channels of the PMTs, the value of the pedestals in the two channels P, the gain in both channels G and the flat-field coefficient FF in each pixel. To calibrate the instrument, each of these parameters is either measured by dedicated runs or directly measured from the data in each observation. The calibration is done after excluding the broken pixels. For a complete explanation of the camera calibration see [7], for CT1-4 updated cameras see [121], and for CT5 see [42] .

The number of photoelectrons in each PMT of the CT1-4 cameras is computed from the analog-to-digital converter (ADC) charge in the two channels as

$$C^{\mathrm{HG}} = \frac{ADC^{\mathrm{HG}} - P^{\mathrm{HG}}}{G^{\mathrm{HG}}} \cdot FF \cdot B^{\mathrm{HG}} \tag{5.1}$$

$$C^{\mathrm{LG}} = \frac{ADC^{\mathrm{LG}} - P^{\mathrm{LG}}}{G^{\mathrm{HG}}} \cdot (\mathrm{HG/LG}) \cdot FF \cdot B^{\mathrm{LG}}, \tag{5.2}$$

where B is the broken pixel flag.

For the updated CT5 camera, the conversion is much simpler, since only one gain channel already provides the charge $\overline{C}$ with the baseline subtracted. The calibrated number of photoelectrons for CT5 is measured as:

$$C = (\overline{C} - P) \cdot FF \cdot B. \tag{5.3}$$

Image cleaning

The NSB, including star, planet, and zodiacal light, is removed after the calibration, by requiring the signal to be above a trigger threshold in several adjacent pixels. This image cleaning can be done in two ways:

- **Tail-cut method**: (i) 4 p.e. for each pixel (same as the pixel trigger condition) and (ii) 7 p.e for the sum of the neighbour signal. Sometimes the thresholds 5 p.e. and 10 p.e. are used [13]. An additional lower intensity threshold is also applied to the pixels computed as three times the width of the pedestal distribution in each run.

  The tail-cuts method provides a simple way for determining whether a pixel is part of a shower image. However, it has limitations: it may fail to remove high-intensity noise pixels and can also crop the images of low-intensity showers.

- **Time-based image cleaning**: To improve image cleaning, timing information can be incorporated. Clustering techniques, such as DBScan, short for Density-Based Spatial Clustering of Applications with Noise, are employed for this purpose. These methods identify clusters based on the time of arrival of signals in the pixels. This approach has been studied by [186] and is already in use by the MAGIC collaboration [18]. Its adaptation and implementation within the H.E.S.S. analysis pipeline are described in detail in [197].

Figure 5.2 shows an example of clustering applied to a CT5 FlashCam image using the DBScan algorithm developed by [63]. This algorithm enables the separation of clusters in an N-dimensional space, without requiring the number of clusters to be specified in advance. Points that do not belong to any cluster are classified as noise. The flexibility in the number of clusters is particularly advantageous for proton-induced events, which can contain multiple distinct structures within the same image. In Figure 5.2, two types of events are displayed: a γ-ray event (top) and a proton event (bottom). The last column in each case shows the identified clusters. Notably, in the proton event, the algorithm is able to distinguish multiple components, including a muon-ring-like structure.

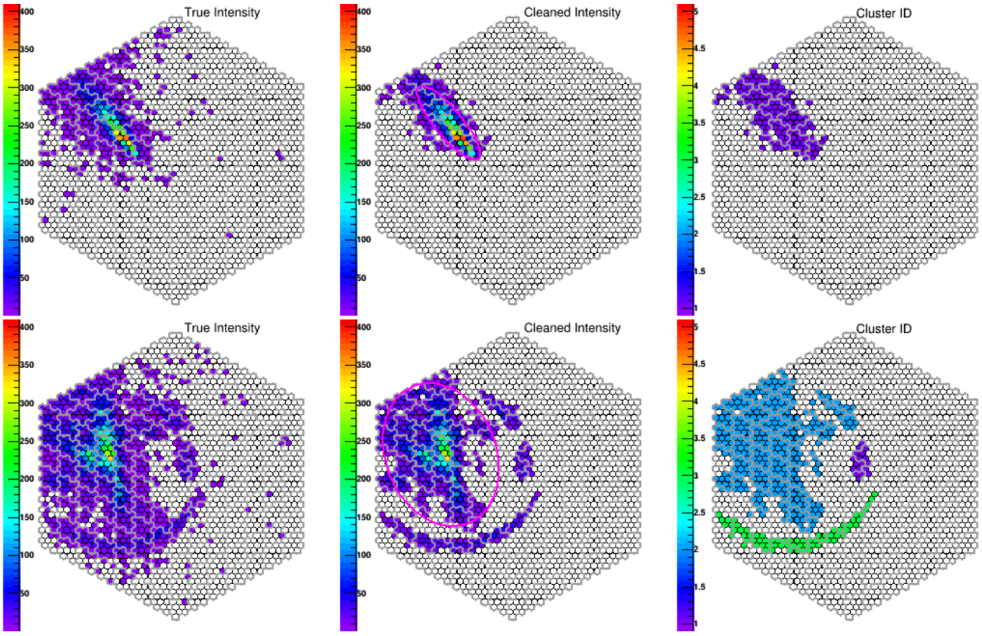

Figure 5.2: Camera image of simulated γ-ray initiated shower (top) and proton initiated shower (bottom). From left to right are the true intensity, the cleaned intensity, and the cluster ID. Figure from [197].

5.2.2 DL1: Image parameters

After image calibration, the parameters of the shower image can be measured, and the events can be identified either as gamma-like or hadron-like.

One way of parameterising the shower image is by determining the geometrical size and moments of the image, known as the Hillas parameters [99]. These parameters were introduced to describe the elliptical shape of the detected Cherenkov images. Figure 5.3 shows a scheme where the Hillas parameters are indicated.

In H.E.S.S., the following parameters for each event image are measured:

- the width: root mean square (RMS) of the signal on the axis perpendicular to the main axis of the ellipse,
- the length: RMS of the signal on the main axis of the ellipse,
- the center of gravity of the image,

- the orientation of the image.
- the offset angle: distance between the expected position of the target and the pointing position of the telescope.

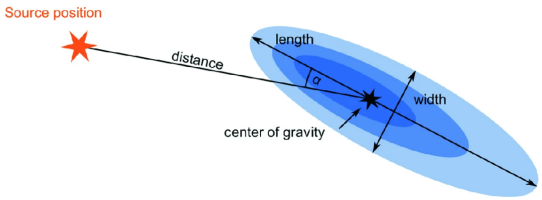

Figure 5.3: Shower image parameters based on Hillas approach. The image of the shower is fitted by an ellipse where the RMS computed along the semi-major and semi-minor axes are the length and width of the shower. The positional weighted average is the center of gravity. Figure from [33].

5.2.3 DL2: Shower parameters

Once the images are properly calibrated and cleaned, event reconstruction can be performed.

Hillas reconstruction

A simple method for reconstructing the shower direction involves using the Hillas parameters in a purely geometrical approach. Figure 5.4 illustrates this reconstruction technique for a stereoscopic observation. The shower direction can be estimated as the intersection point of the major axes. When only a single telescope is used (like, for example, using CT5 in mono mode), the shower direction can still be estimated based on the major axis of the elliptical image. However, mono reconstruction is inherently less precise due to degeneracies in the direction estimation.

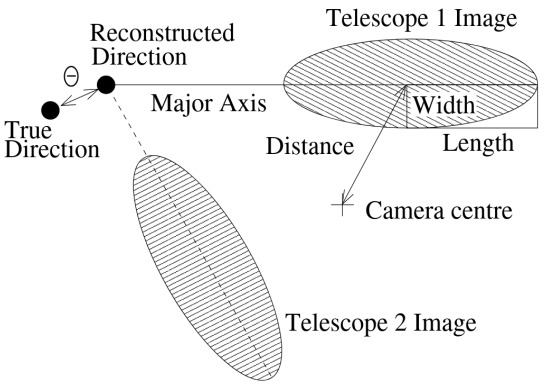

Figure 5.4: Event reconstruction based on Hillas parameters. Figure from [13].

ImPACT reconstruction

The amount of photoelectrons recorded in the image also depends on the primary energy of the initial particle and the impact distance of the shower core. Additionally, the zenith

and azimuth angles of the observation also affect the shower development. The higher the zenith angle (increasing zenith angle towards the ground), the longer is the distance travelled by the shower in the atmosphere, thus it is more affected by the atmospheric conditions. The azimuthal variation is due to the geomagnetic field, which can distort and rotate the shower image by deflection of charged particles.

To account for all these dependencies, a more sophisticated reconstruction method has been developed – the Image Pixel-wise fit for Atmospheric Cherenkov Telescopes (ImPACT) [154]. This algorithm builds a set of templates based on full Monte Carlo (MC) simulations of γ-ray showers and simulations of the telescope optics and instrument electronics. A library of templates is created in a four-dimensional parameter space: 8 zenith angles, 2 azimuth angles, 17 energies, and 25 impact distances. Events are additionally binned in a number of $X_{\max}$, such that in total, over 100,000 image templates are produced.

The data image of an event is fitted, using the results of the Hillas reconstruction as the seed values, to the best template using a maximum likelihood method. The fitting is computationally expensive, so it is only applied after a first round of background rejection. A comparison of the reconstructed energy and angular resolution of the reconstruction using the simple Hillas approach and ImPACT is shown in Figure 5.5.

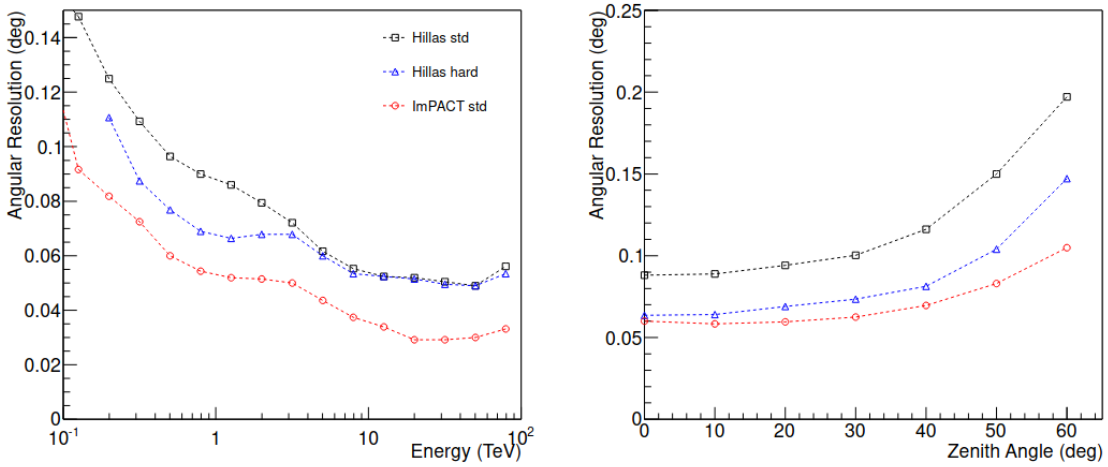

Figure 5.5: Angular resolution (68% containment radius) of different reconstruction methods as a function of the simulated energy at zenith angle 20° (left) and as a function of the zenith angle (right). Hillas std and Hillas hard refer to different image selection and background rejection cuts. Hillas std and ImPACT require the images to have a total intensity above 60 p.e., while Hillas hard requires this value to be 160 p.e. Figure from [154].

5.2.4 DL3: Event selection and IRFs

Gamma-like and hadron-like events are identified at this stage of data reduction. For this, γ-hadron separation methods are employed. Once the list of γ-like events is produced, the instrument response functions (IRFs) are computed. IRFs are essential for estimating the astrophysical fluxes of the sources and for performing the statistical analysis.

γ-hadron separation

One of the earliest methods for reducing hadronic showers involved applying a simple cut on the arrival direction of the showers. This approach was effective for γ/hadron

separation in the case of point sources, with a background rejection factor given by $\kappa = (2\delta\theta/\psi)^2$, where θ is the offset angle, i.e. the angle between the measured direction and the pointing of the telescope, and ψ is the angular diameter of the 'on region' (or 'trigger zone'). An example can be found in [13] where a directional cut was used for hadron suppression. However, this technique becomes ineffective for extended sources, where more advanced separation methods are required.

The separation of γ-ray and hadronic events relies on the intrinsic differences in their shower development. These differences arise from the larger transverse momenta of secondary hadrons, the deeper penetration of hadronic cascades into the atmosphere, and their greater fluctuations. γ-ray-induced showers tend to produce more compact and regular image shapes, while hadronic showers result in more chaotic and diffuse patterns. An illustrative comparison between the shower development of γ-rays and cosmic rays can be found in Figure 4.12 of Section 4.6.1.

In this context, Hillas parameters were naturally adopted for distinguishing between EM and hadronic showers. By applying selection cuts based on these parameters in single-telescope observations, the background rejection was improved by roughly a factor of 10, as reported by [70].

The γ/hadron separation improved with stereoscopic systems of IACTs. Early calculations of the γ-hadron rejection power with stereoscopic systems up to 4 telescopes are provided in Table 2 in [9]. Their calculations showed that the stereoscopic approach can improve the background rejection by an order of magnitude with respect to single telescopes, just by applying orientation and shape cuts, based on Hillas parameters. Another study by [122] proposed a simple 3D model analysis method to reconstruct showers in three dimensions by combining stereoscopic images. They improved the angular resolution of H.E.S.S. at zenith to $0.04^\circ - 0.1^\circ$, and the spectral resolution from $15\% - 20\%$, depending on the reconstruction requirements.

Further improvement in background rejection was achieved with the emergence of multivariate analysis techniques, such as the Random Forest method [36]. [145] demonstrated the applicability of the Boosted Decision Trees (BDT) algorithm, provided by the TMVA package [64], for background suppression in H.E.S.S. data. A schematic representation of a single decision tree can be found in Figure 1 of [145]. To mitigate the statistical instability inherent to individual decision tree, a 'forest' of decision trees is used. In the case of H.E.S.S., the number of trees chosen is 200. The BDT is trained using MC simulations of γ-ray showers and off-data events, taken while the telescopes are pointing towards regions empty of known γ-ray sources.

The training parameters of the BDT method are based on the Hillas parameters. In addition to the length, width, and total intensity of the images, all the additional parameters included in the BDT training are shown in Figure 5.6. This figure shows the distribution for all the training parameters for a set of simulated γ-ray and cosmic-ray events, with zenith angle between $15 - 20^\circ$ and energy range $0.5 - 1.0$ TeV.

The BDT training is performed across multiple energy and zenith angle ranges to optimise performance under varying observational conditions. Ultimately, the BDT combines the multivariate input into a single output parameter, ζ, which represents the likelihood that an event is of γ-ray origin. The distribution of ζ for the same energy and zenith angle band is shown in Figure 5.7, where the separation power of the method between γ-ray and background events can be clearly observed.

The BDT approach is currently the standard γ/hadron separation method implemented in HAP. Based on the trained model, different analysis configurations can be applied depending on the expected spectral characteristics of the source under study. These

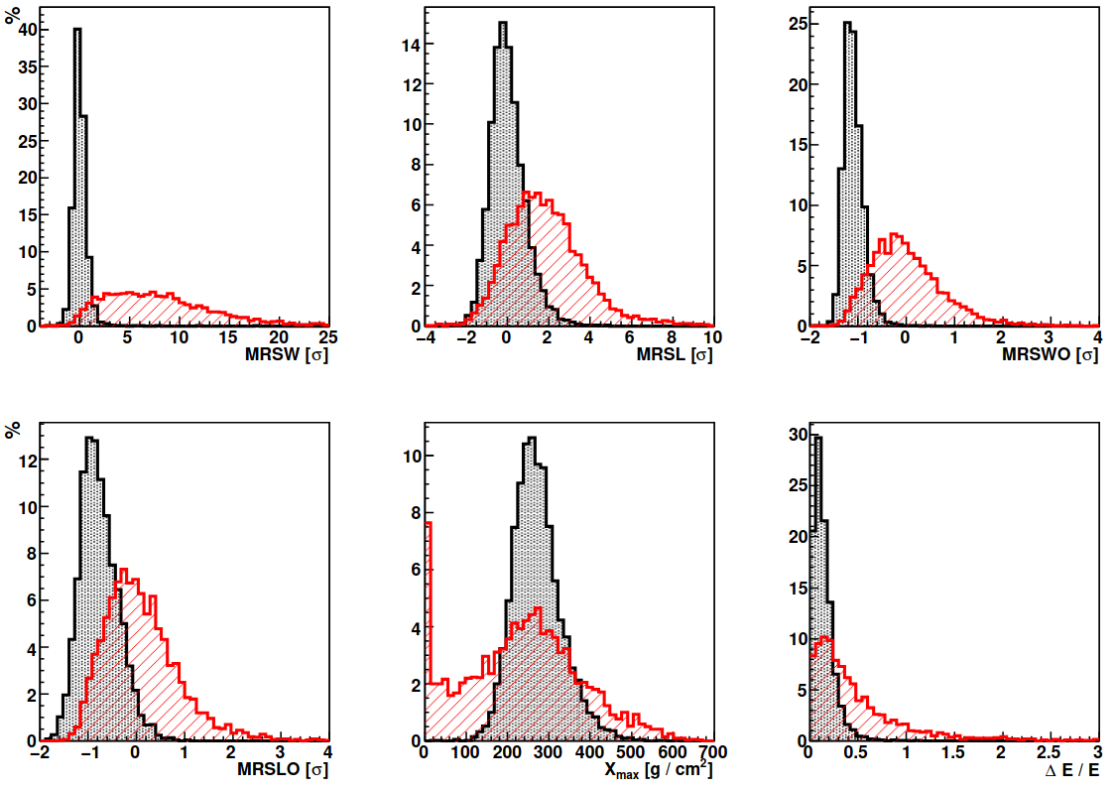

Figure 5.6: Distribution of training variables for γ-rays (black) and CRs (red), with reconstructed energies between 0.5 and 1.0 TeV and zenith angles between 15° and 20°. Figure from [145].

configurations are defined by applying selection cuts on the BDT output parameter, ζ, and on the preselected image intensity threshold of the elliptical shower image. Two configurations are typically used: the "standard" cuts optimized for sources having a Crab-like spectral index of 2.6 and a flux of 10% the Crab flux; and the "hard", designed for fainter sources with harder spectra. The specific values for each configuration are listed in Table 5.1.

Table 5.1: Analysis configuration cuts.

Configuration	Total intensity threshold (p.e.)	ζ threshold
standard	60	0.84
hard	200	0.8

Although the BDT method provides strong background rejection at relatively low energies (below 1 TeV), a significant number of high-energy hadronic showers still survive the cuts. To address this, we introduce a new approach for identifying background events, very effective in the highest energy bins. This method, detailed in Section6.1.2, makes use of muon images captured by the camera of the large H.E.S.S. telescope, CT5.

Instrument response functions

IRFs are necessary for modelling the expected number of γ-ray events produced by a

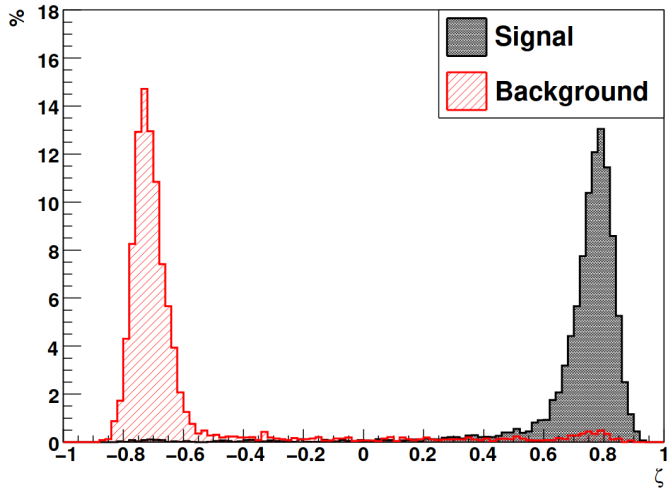

Figure 5.7: Distribution of the output ζ parameter. Results shown for events with zenith angle and energy in the same ranges as in Figure 5.6. Figure from [145].

source as detected by the instrument. Once the list of γ-like events is obtained through the γ/hadron separation, the IRFs are used to convert these detections into an astrophysical flux measurement.

The expected number of detected events for a given instrument, corresponding to a photon emitted from a true position r_{true} with true energy E_{true} at a reconstructed position r with reconstructed energy E at an observation time t_{obs}, can be expressed as:

$$N(r,E)\mathrm{d}r\mathrm{d}E = t_{\text{obs}} \cdot \int_{E_{\text{true}}} \mathrm{d}E_{\text{true}} \int_{r_{\text{true}}} \mathrm{d}r_{\text{true}} R(r,E|r_{\text{true}},E_{\text{true}})\Phi(r_{\text{true}},E_{\text{true}}) + N_{\text{bkg}}(r,E), \tag{5.4}$$

with $R(r,E|r_{\text{true}},E_{\text{true}})$ being the instrument response, $\Phi(r_{\text{true}},E_{\text{true}})$, the model of the astrophysical flux, and $N_{\text{bkg}}(r,E)$ the expected background counts. The instrument response can be expressed as:

$$R(r,E|r_{\text{true}},E_{\text{true}}) = A_{\text{eff}}(r_{\text{true}},E_{\text{true}}) \cdot PSF(r|r_{\text{true}},E_{\text{true}}) \cdot E_{\text{disp}}(E|r_{\text{true}},E_{\text{true}}) \tag{5.5}$$

where we have $A_{\text{eff}}(r_{\text{true}},E_{\text{true}})$ the effective collection area of the detector, $PSF(r|r_{\text{true}},E_{\text{true}})$ the point spread function, and $E_{\text{disp}}(E|r_{\text{true}},E_{\text{true}})$ the energy dispersion. In addition to the background model, these four functions are the IRFs commonly used in γ-ray astrophysics to estimate the signal of the true emission.

These IRFs are produced using simulated MC γ-rays and off-events or simulated hadronic events, and they are generated for different observing conditions (zenith angle, detector optical efficiency) and analysis configurations (reconstruction and selection of the events).

The **effective area** A_{eff} is the area of a perfect detector to collect the same amount of radiation as the actual instrument. A_{eff} depends on parameters like the zenith angle, the photon energy, the offset angle from the pointing position, and the optical efficiency of the telescope.

The **point spread function** $PSF(r|r_{\text{true}},E_{\text{true}})$ gives the spread in reconstructed position on the detector for a point source. Thus, it describes the angular accuracy of the instrument. It also depends on the zenith angle, the photon energy, the offset angle from the pointing position, and the optical efficiency of the telescope.

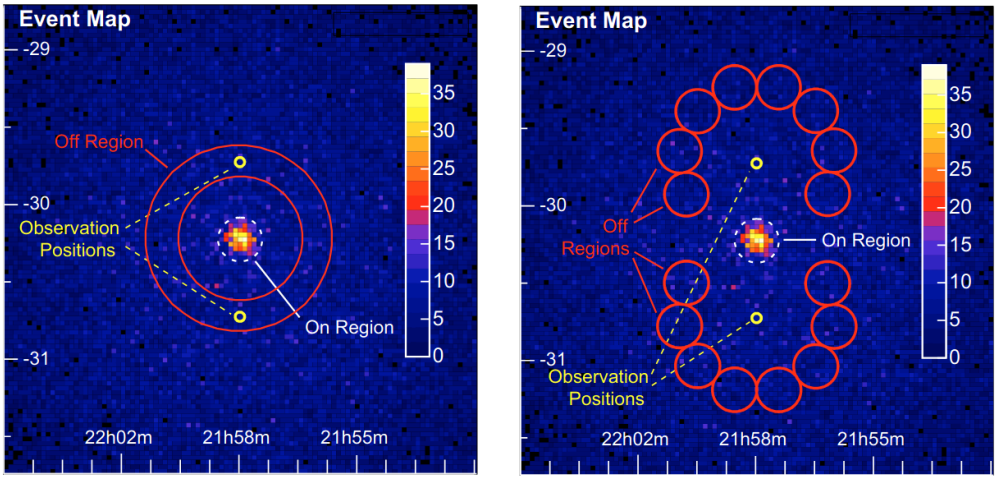

Figure 5.8: Background modelling methods. Ring (left) and reflected regions (right) background models are illustrated schematically on the counts map of 5 hours H.E.S.S. observation of PKS 2155-304. Figure from [25].

The **energy dispersion matrix** E_{disp} represents the probability that a photon with a true energy E_{true} is reconstructed as having energy E.

The **background model** is the expected remaining hadronic events that were misidentified as γ. These events are binned into reconstructed energy and offset angle, and depend on the employed background estimation method.

A more detailed description of the IRFs can be found in [143]. In the following, the different background estimation methods are explained.

Background estimation

To estimate the signal above the noise level in γ-ray observations, the background level must first be determined. In this context, the background consists of hadronic events that are misidentified as γ-rays. Background counting is always carried out after excluding regions associated with known γ-ray sources that are not relevant to the analysis, to avoid contamination from unrelated signal events.

To estimate the background, a model is first derived from off-runs for each operational phase of the instrument. This background model characterises the camera's response to background events as a function of reconstructed energy and spatial coordinates in the camera. A two-dimensional background model assumes radial symmetry in camera coordinates, while a three-dimensional model incorporates both radial and azimuthal dependencies. A comprehensive description of the procedures used to construct 2D and 3D background models is provided in [135].

The simple two-dimensional background model depends solely on the offset angle from the camera centre. In the ring background estimation method, for each pixel in the sky map, a ring at a fixed radius around it is used to estimate the background counts, as shown in the left panel of Figure 5.8. To avoid contamination from known or suspected γ-ray sources within the FoV, exclusion masks are applied to remove these regions from the background estimation. This method is best suited for point-like sources and is primarily used to study source morphology, as it does not account for any energy dependence in the background model.

Another commonly used method to estimate the background rate is the reflected

regions technique. In this approach, the on region, defined as a circular region of a given size, is offset by a certain angle from the telescope's pointing direction for that observation run. The background is then estimated using reflected regions, which are circular regions of the same size as the on region and placed at the same offset angle, but in other directions around the camera's centre. This configuration ensures that the on and reflected regions share similar acceptance conditions. An illustration of this method is shown in the right panel of Figure 5.8. The reflected regions method is used for point-like sources, typically only for spectral analysis, as the counts are integrated over the entire on and reflected regions, thereby discarding the spatial information.

A more advanced method is the Field-of-View (FoV) background model, developed by [135], which is also applied in the analysis of the GC region in this thesis. This approach uses a three-dimensional background model, with two spatial axes and one energy axis, which is compared to the observed data on a run-by-run basis. This is because the number of background counts can vary between runs due to changing observational conditions, such as atmospheric transparency and the optical efficiency of the system. Two parameters are fitted for each run: the normalisation and the tilt of the background spectral shape, the latter being defined as the slope of a power-law function.

5.2.5 DL4: High-level analysis for scientific results

At this stage of data processing, high-level analysis tools such as `Gammapy` can be employed. `Gammapy` takes as input the DL3 event list along with the Instrument Response Functions (IRFs), and is used to compute source fluxes, statistical significance, and other scientific observables.

Binned data

The first step in a `Gammapy` analysis is to convert the event list and IRFs into binned datasets, based on a predefined binning scheme, typically along spatial and energy axes. This is achieved using pixelisation frameworks such as the World Coordinate System (WCS) [38] or HEALPix [85]. The outcome of this step is a set of multidimensional sky maps that serve as the basis for further analysis.

Model fitting

Bright source(s) in the FoV can be modelled to describe their spatial and spectral shapes. The fit of the models is done using maximum likelihood methods, finding the best-fit parameters. The default function minimizer used in `Gammapy` is `iminuit`[55], which also estimates the uncertainty of the fitted parameters.

The spatial morphological model can take various forms: a Dirac delta function for point-like sources, a 2D Gaussian distribution, or a custom template, such as the one used in this work to fit the γ-ray emission from the CMZ.

The point spatial model takes the form:

$$\phi(l, b) = \delta(l - l_0, b - b_0), \tag{5.6}$$

where l, b are the two spatial coordinates, and δ is the Dirac delta function.

The 2D Gaussian source spatial model is defined as:

$$\phi(l, b) = N \exp\left(-\frac{1 - \cos\theta}{2(1 - \cos\sigma)}\right), \tag{5.7}$$

where N is the normalization, θ is the sky separation to the model centre, and σ is the extension of the source model.

The spectral model is usually a power-law function, a power-law function with an exponential cutoff energy, a broken power-law function, or, in some cases, a log-parabola function.

In this work, we use the power law spectral model, expressed as:

$$\phi(E) = \phi_0 \cdot \left(\frac{E}{E_0}\right)^{-\Gamma}, \tag{5.8}$$

where ϕ_0 is the flux normalization, E_0 is the reference energy, and Γ is the spectral index.

And the exponential cutoff power law spectral model, defined by:

$$\phi(E) = \phi_0 \cdot \left(\frac{E}{E_0}\right)^{-\Gamma} \exp\left(-(\lambda E)^{\alpha}\right), \tag{5.9}$$

where $(1/\lambda)^{1/\alpha}$ is the cutoff energy.

More complex spatial and spectral models are available in `Gammapy`, and users also have the flexibility to define custom models tailored to specific analysis needs.

A combined spatial and spectral model is called the sky model in `Gammapy`. A 3D spectro-morphological analysis approach would fit the sky model, giving both the best fit for spatial and spectral models at the same time. This 3D approach has been tested by [135].

Flux points

Flux points as a function of energy are computed based on an assumed spectral model, typically the best-fit model, to evaluate deviations from the modelled spectrum. This is done by dividing the energy range into several bins and fitting the normalisation independently in each bin. If the excess counts in a bin are insufficient for a significant detection, an upper limit is provided instead, based on the chosen confidence level (i.e., the number of sigma used to define the upper bound).

Flux maps can also be computed using the same method, but applied over spatial coordinates, while light curve fluxes are derived by estimating the flux within defined time intervals.

Significance estimation

The significance of the γ-ray data in a sky map is determined via hypothesis testing. Given a source model or excess count as the alternative hypothesis, H_1, and a background-only model as the null hypothesis, H_0, the difference in test statistic is calculated as:

$$TS = -2\log\left(\frac{\mathcal{L}(H_0)}{\mathcal{L}(H_1)}\right) \tag{5.10}$$

where $\mathcal{L}$ is the likelihood of the hypothesis H. The significance σ is calculated as the square root of TS when there is only one degree of freedom.

In astronomy, a 3σ significance is commonly considered as 'evidence', while 5σ can be claimed as a 'discovery' or 'detection'.

Two methods to compute the significance maps are available: by comparing the excess counts to a given model or by comparing the excess counts with the expected background.

Source(s) in the FoV are modelled using both spatial and spectral models. The significance map after removing the fitted relevant source(s) can also be used to asses the quality of the fit. In the ideal case, this residual significance map should follow a Gaussian distribution with a mean of 0 and a standard deviation of 1.

5.3 The SWGO observatory

The Southern Wide-field Gamma-ray Observatory, or SWGO, is expected to provide unprecedented observational capabilities for the most powerful objects and phenomena in the Universe, especially for most of the Galactic plane (see the expected FoV of SWGO, as compared to HAWC located in the Northern hemisphere, in Figure 5.9). The observatory consists of an array of water Cherenkov detectors (WCDs), which can capture the secondary particles in the EAS produced by γ-rays (see Figure 5.10). These secondary particles emit Cherenkov light in the water, detectable by photo-sensors. The registration of the cascade using an array of particle detectors allows a reconstruction of the shower, identifying the direction and energy of the initial γ-ray.

During the Research & Development (R&D) phase, several locations in South America have been considered for the site of SWGO. An important step in the decision was made on August 12th of 2024, when the Atacama Astronomical Park in Chile was announced to be the selected site for SWGO, located in Pampa La Bola, Chile[1]. This park is on an extensive plateau at the top of the Andes, at an altitude of 4,770 m above sea level.

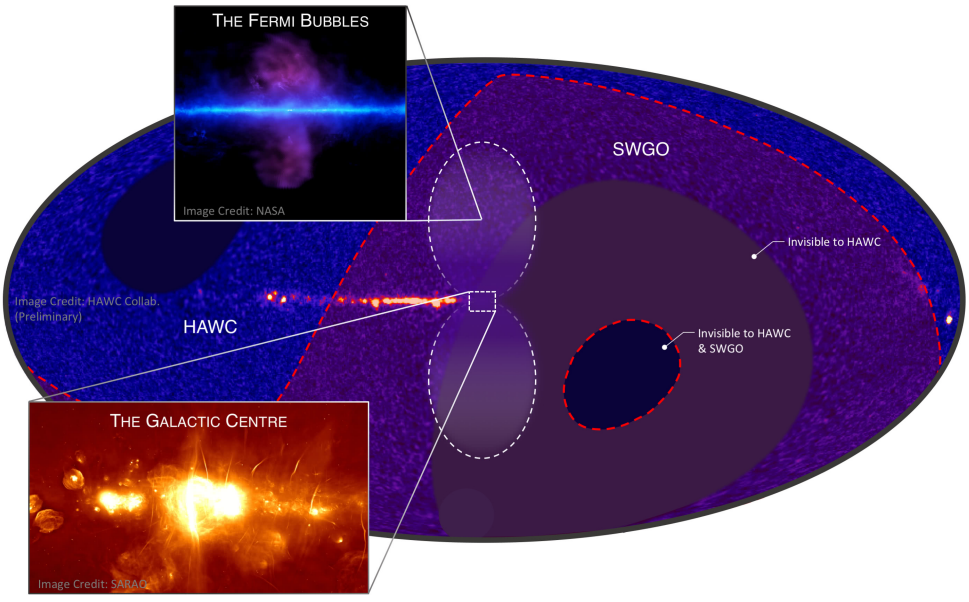

Figure 5.9: Expected FoV of SWGO, in comparison with the FoV of HAWC. Figure from Richard White, MPIK.

[1]See the SWGO site selection press release for more details.

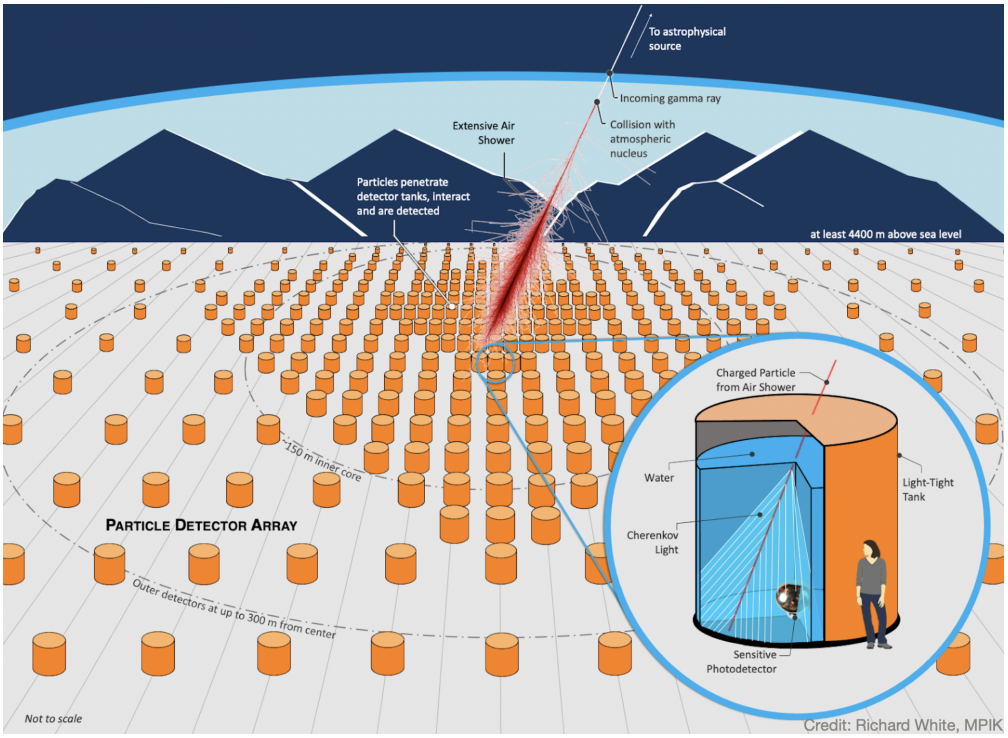

Figure 5.10: The SWGO observatory concept. A detailed view of the WCD unit is shown, along with the example size of the array. Figure from Richard White, MPIK.

5.4 Designs for SWGO

During the R&D phase of SWGO, several different designs have been suggested and tested. In the following, the different options for array layout and tank unit designs are exposed.

5.4.1 Technology options

Several technological options have been explored for the construction of SWGO detectors, considering different possibilities for WCDs, as illustrated in Figure 5.11. The first approach employs individual tank units made from various materials, following a design concept similar to that used by HAWC [2, 16]. Alternative designs consider the deployment of water-filled bladders, using purified water, within either a natural lake or an artificial pond. Although the tank-based solution is considered the more conservative and technically reliable choice, supported by operational experience from HAWC and the Pierre Auger Observatory [158], the lake and pond configurations represent more innovative strategies in the field of ground-based particle detection.

Pond-based WCDs have been implemented in earlier experiments, such as the Milagro Observatory [219] and the WCDA of LHAASO [126], while the natural lake concept was first explored in the 1980s by Kaneko [112]. However, a full-scale detector array based on a natural lake was never constructed, primarily due to challenges posed by high acoustic noise. More recently, renewed interest in the lake concept has led to detailed investigations at MPIK [79, 80]. Following the site selection process for SWGO, the tank-based configuration was ultimately chosen for the initial implementation of the WCD array. Nonetheless, a future extension of the observatory may revisit the natural lake concept for detecting UHE γ-ray showers.

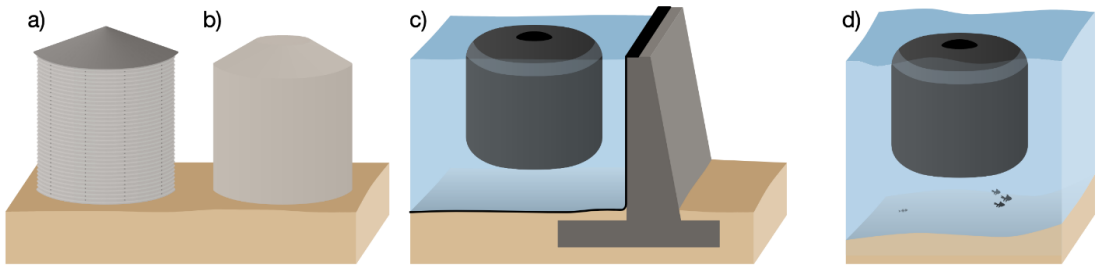

Figure 5.11: Technology options explored for SWGO. Left: corrugated steel (a) and roto-moulded HDPE (b) tanks. Middle: artificial lake or open pond with a floating bladder. Right: natural lake with a floating bladder. Figure from [215].

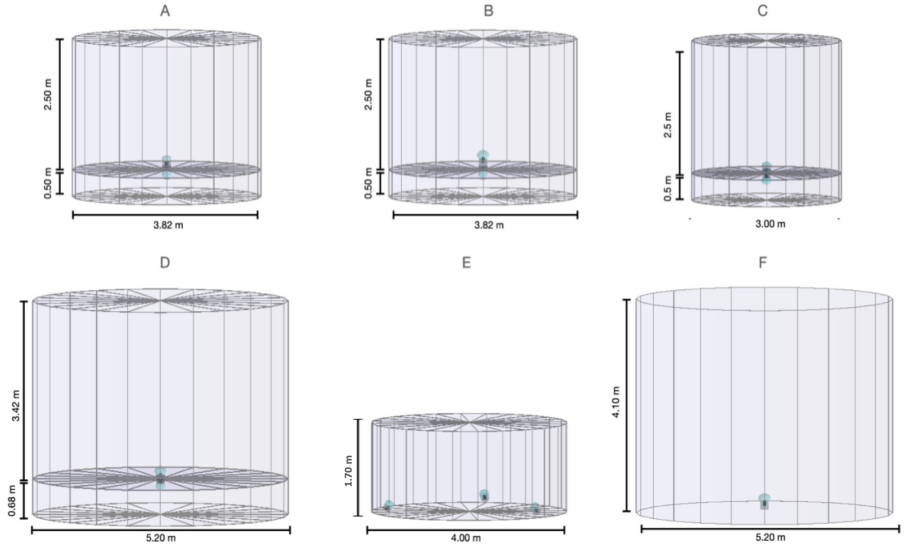

Figure 5.12: Detector unit designs. Figure from the SWGO Collaboration.

5.4.2 Detector unit design

The various water tank designs under consideration for SWGO are presented in Figure 5.12. These designs can be broadly classified into single-layer and double-layer configurations. Tanks A, B, C, and D are double-layer tanks, with the two layers being optically separated. In this configuration, the upper layer is used for particle detection, while the lower layer is dedicated to muon detection, aiding in background rejection. Tanks A and B share the same physical dimensions; however, tank B is equipped with a larger 10-inch PMT, compared to the 8-inch PMT used in tank A.

Designs E and F are single-layer tanks. Tank E incorporates three PMTs instead of a single one and is designed with a shallower water volume than the other options. Tank F is a large single-layer tank, featuring a PMT positioned approximately 4 metres below the water surface, following a design concept similar to that used in the HAWC and LHAASO experiments.

Larger double-layer tanks offer enhanced muon detection efficiency due to the increased depth of the upper volume, which reduces muon punch-through. In contrast, smaller tanks provide improved timing resolution and allow for finer spatial pixelisation. Notably, the three-PMT design of tank E offers a novel approach to γ/hadron separation by identifying asymmetries in the spatial distribution of shower particles.

5.4.3 Array layout

Seven candidate array configurations have been proposed for SWGO, as illustrated in Figure 5.13. Each configuration features a dense core with a high filling factor (FF) of approximately 80%, with the exception of layout 5, which employs a reduced FF of around 40%. These dense cores are surrounded by one or two sparser outer zones. The total radial extent of the arrays ranges from 300 to 1600 metres, with configuration 6 representing the most compact layout and configuration 7 the most extended. The dimensions of layouts 2, 3, and 4 are comparable to those of the LHAASO observatory [93]. All configurations have been designed under the constraint of equal nominal cost.

A dense, compact core enhances the detection efficiency for lower-energy air showers and improves background rejection, particularly through more effective muon identification. In contrast, extended and more sparsely instrumented arrays provide a larger effective area, improving sensitivity to the highest-energy γ-rays. In this context, the proposed configurations have been designed to explore their relative performance.

Layout 1 serves as the reference configuration, consisting of a core with 80% FF and an outer zone with 2% FF. Layout 2 increases the size of the outer zone while reducing the core area. Layout 3 preserves the overall dimensions of layout 2 but organises the outer zone into clusters of seven tanks. Layout 4 introduces a third zone: zone 2 has a 4% FF, while zone 3 is more sparsely populated at 1.25% FF. Layout 5 features a low-density core with only 40% FF. Layout 6 employs an extremely dense core (88% FF) and a very sparse outer region at 1% FF. Finally, layout 7 maximises the overall array footprint by reducing the core and expanding a third zone with a minimal FF of 0.63%.

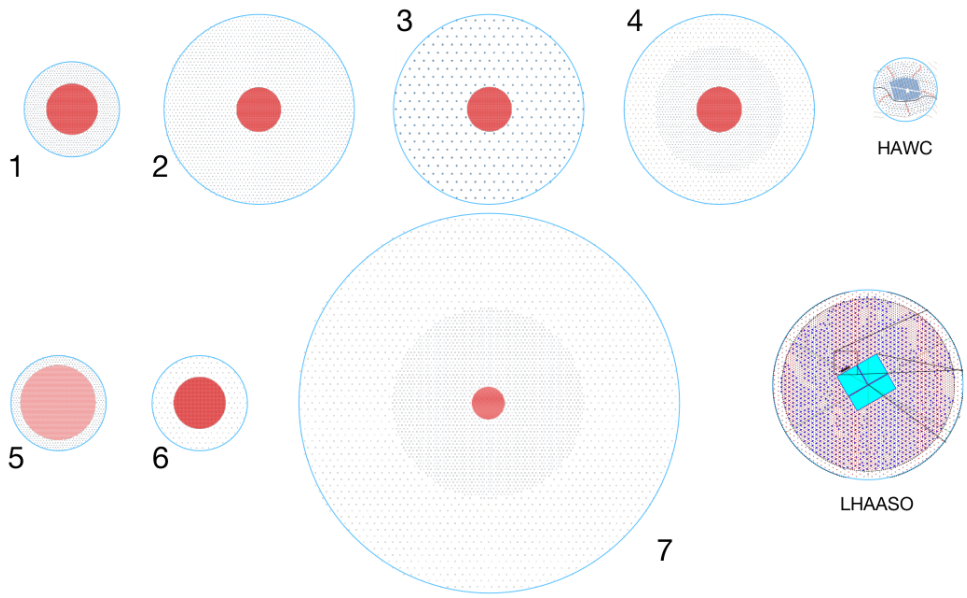

Figure 5.13: Array layouts options proposed for SWGO, compared to HAWC and LHAASO. Each of them was designed under equal nominal cost criteria. Figure from the SWGO Collaboration.

5.4.4 Summary of the configurations

By combining the various detector unit designs with the proposed array layouts, a total of 13 configurations have been considered for performance testing. These configurations are summarised in Table 5.2, which provides details on the filling factor (FF), radial

extent, and number of detector units in each zone.

Config.	Zone 1			Zone 2			Zone 3		
	FF(%)	Radius (m)	Units	FF(%)	Radius (m)	Units	FF(%)	Radius (m)	Units
A1	80	160	5731	5.0	300	858			
B1	80	131	3865	5.0	300	984			
C1	80	137	6829	5.0	300	1542			
D1	80	166	3367	5.0	300	438			
E1	80	150	4639	5.0	300	822			
F1	80	188	4303	5.0	300	378			
A2	80	138	4303	2.5	600	2328			
A3	80	138	4303	2.5	600	2520			
A4	80	140	4429	4.0	400	1518	1.25	600	678
A5	40	234	6109	5.0	300	432			
A6	88	162	6469	1.0	300	168			
A7	80	101	2335	2.5	600	2394	0.63	1200	1842
E4	80	128	3403	4.0	400	1428	1.25	600	624

Table 5.2: Summary of the 13 configurations. Table from the SWGO Collaboraion

5.5 Summary

In this chapter, I provided an overview of the H.E.S.S. telescope array and described the processing steps used to extract scientific results from γ-ray raw data. This analysis procedure can be divided into two parts, according to the software tools employed. The low-level analysis, from raw data to the reconstructed event lists and IRFs, is handled by the HAP software. The high-level analysis, which involves deriving scientific products such as flux points, spectral energy distributions, and significance maps from the event lists and IRFs, is performed using `Gammapy`, a modern open-source tool that is becoming a standard in the VHE γ-ray astronomy community.

The SWGO project has also been reviewed, presenting all candidate designs for the technology, the detector unit, and the array layout. These configurations will be tested for assessing the SWGO performance to observe the GC, and its sensitivity to DM annihilation signal in this region, explained in Section 7.

In the next chapter, an improvement of the background rejection method, ABRIR, integrated into the H.E.S.S. analysis, is explained. Furthermore, its performance is assessed by applying it to a subset of the H.E.S.S. GC observation.

Chapter 6

Background rejection improvements for H.E.S.S.

The use of a new background rejection technique –Algorithm for Background Rejection using Image Residuals (ABRIR) is discussed in this chapter. This algorithm has demonstrated effective performance, reducing background events to less than 30% for energies above 10 TeV when compared to the use of traditional methods alone. The original concept and performance of ABRIR were presented in our publication [151]. Here, I describe an improved implementation of ABRIR within the H.E.S.S. Analysis Package (HAP).

Enhanced sensitivity to the GC region is expected with the application of ABRIR background rejection, as several sources in this region have been shown to emit at energies above tens of TeV. In particular, the CMZ has been reported to emit without a clear energy cutoff, as observed by H.E.S.S. [88] and more recently by HAWC [15], suggesting the possible presence of a PeVatron in the GC region. However, a recent 3D advanced analysis by [216] claims there may be a spectral cutoff, challenging the interpretation of a PeVatron origin.

The application of ABRIR may help distinguish between these two scenarios by better constraining the spectral shape of the CMZ and providing further insights into CR acceleration in the GC. To assess the potential impact of ABRIR, we apply the method to a subset of GC observations and compare the resulting γ-ray spectra of sources with and without ABRIR background rejection. A more detailed investigation of GC γ-ray emission using ABRIR in the full analysis chain will be the focus of future work.

This chapter is organized as follows: Section 6.1 presents an overview of the improved background rejection capabilities achieved with the introduction of the ABRIR algorithm, along with its performance on both γ-ray and background events. Section 6.2 details the application of the ABRIR algorithm to a subset observation of the GC and compares the results with and without ABRIR background rejection. Lastly, Section 6.3 gives a summary of the chapter.

6.1 Gamma/hadron separation improvements for IACTs

In the energy range relevant to ground-based γ-ray observations, CRs greatly outnumber γ-rays. Successfully identifying true γ-ray events among this background is essential for revealing the high-energy Universe.

As discussed in Section 5.2.4, various traditional γ/hadron separation techniques have been applied and demonstrate strong background rejection performance at relatively low energies. However, around 10 TeV, significant number of hadron-induced showers still survive the BDT cuts. The rejection power of these conventional methods at energies above a few tens of TeV typically reaches levels of 10^{-2} to 10^{-3} [25, 145]. In contrast, a more recent study by Olivera-Nieto et al. [150] suggests that using muon-induced

Cherenkov light detected by large telescope mirrors can improve background rejection to levels as low as 10^{-5} for energies above 10 TeV.

This new approach takes advantage of a key difference between hadronic and EM showers – the significantly higher muon content in hadronic cascades. In fact, hadronic showers produce approximately two orders of magnitude more muons than γ-ray induced showers [150]. Moreover, the Cherenkov light produced by these muons can be efficiently detected by the large H.E.S.S. telescope, CT5, as demonstrated in simulations by Olivera-Nieto et al. [150]. A follow-up study, Olivera-Nieto et al. [151], in which I also contributed, further explored this idea by investigating background rejection based on residual light patterns in the shower images.

This section begins with an overview of the original background rejection method introduced in Olivera-Nieto et al. [151], named as the Algorithm for Background Rejection using Image Residuals (ABRIR).It then describes the adaptation of this algorithm within the H.E.S.S. analysis chain (HAP), along with an evaluation of its performance on simulated γ-rays, off-run and real data events.

6.1.1 Cherenkov emission from muons

Muons are produced in hadronic showers and emit Cherenkov light as they propagate through the atmosphere. Due to their suppressed bremsstrahlung cross section compared to electrons, muons experience minimal energy loss, primarily through ionisation, which allows many of them to reach the ground. As they travel in nearly straight lines, they emit Cherenkov light at a constant opening angle, forming a cone around their direction of motion.

The ring shape images produced by ground-level muons on the cameras of IACTs have long been used for calibration purposes. Above approximately 10 GeV, the Cherenkov light emitted by muons becomes largely independent of their energy, due to minimal ionisation losses and saturation effects [75, 209]. The images captured by IACTs are generated from Cherenkov radiation emitted during the final few hundred metres of a muon's path before it passes through or near the telescope's mirror. Because muons produce Cherenkov light of predictable intensity, which is straightforward to simulate, they serve as a reliable calibration source for the optical systems of IACTs.

When muons travel in a straight line through the telescope's primary reflector, they produce a complete ring-shaped image in the camera, as Cherenkov photons are reflected from all azimuthal angles. In principle, any highly energetic charged particle travelling directly toward the telescope could generate a similar ring-shaped pattern. However, hadrons interact more frequently with the atmosphere, and heavier leptons decay too rapidly to reach the ground. Electrons, although long-lived, typically have lower energies and a higher bremsstrahlung cross section, causing them to undergo multiple scattering processes that prevent the formation of clean, ring-shaped images.

Mitchell et al. [134] suggested that a larger number of muon rings produced in EAS could be identified using IACTs. Larger telescope mirrors, in particular, are capable of detecting a higher fraction of these muons, as they can collect Cherenkov photons even at greater impact distances. While this was initially considered a drawback for large IACTs [128], it has been shown that muon images can in fact enhance background rejection at higher energies. This is because hadronic showers produce significantly more muons than electromagnetic cascades, primarily through the decay of charged particles.

As demonstrated by Olivera-Nieto et al. [150], telescopes with mirror diameters of $\geq$ 20m can effectively detect muon-induced Cherenkov light, enabling background rejection levels as low as 10^{-5} at energies above 10TeV. Figure 6.1 illustrates the simulated average

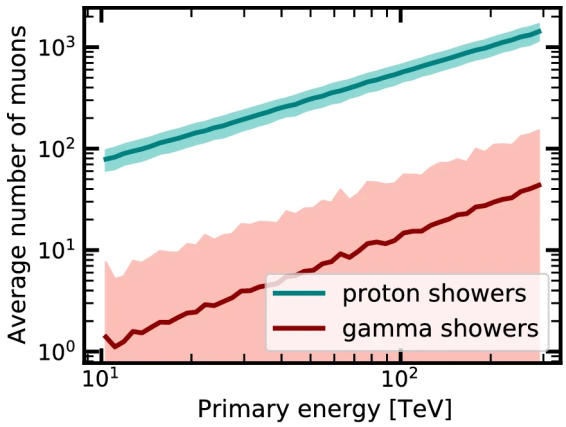

Figure 6.1: Average number of muons produced in proton and γ-ray initiated showers, simulated with CORSIKA. Figure from [150].

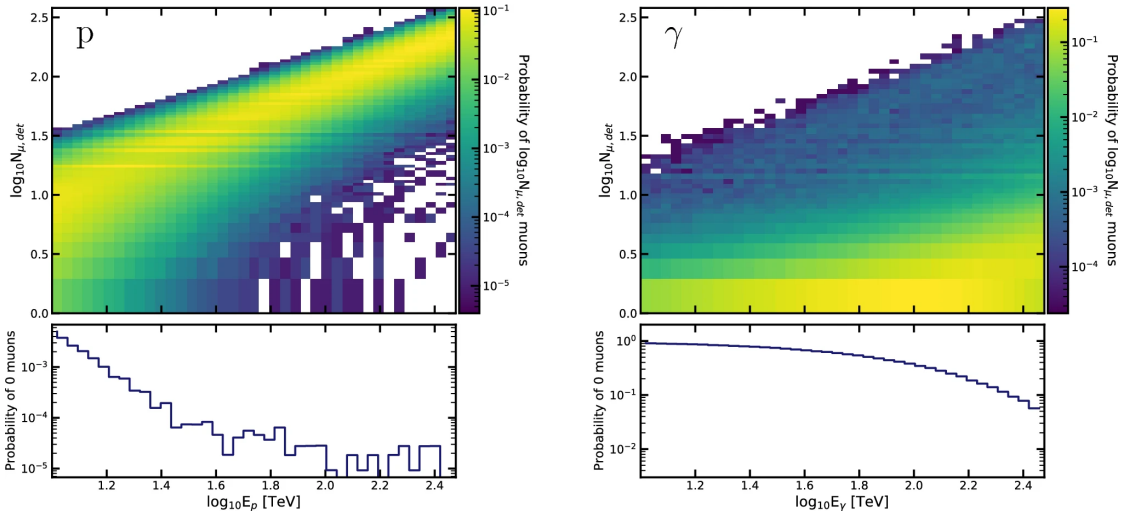

Figure 6.2: Top: Number of detectable muons for proton and γ-ray initiated showers as function of the primary energy. Botom: Probability of detecting zero muon in the showers. Figure from [150].

number of muons in proton- and γ-ray-initiated showers, and Figure 6.2, shows the number of detectable muons per shower. In a follow-up study, Olivera-Nieto et al. [151], we applied the ABRIR background rejection method to H.E.S.S. data and confirmed that, at energies around 20 TeV, the rejection power was improved by a factor of 3–4 (see Section6.1.2).

Identifying muon light in camera images is more challenging than it may seem. The presence of background light, such as the NSB, and the fact that muon images often do not appear as complete rings complicate the task. To distinguish muon and shower signals from the NSB, time-based image cleaning techniques is applied (see Section 5.2.1). Additionally, the appearance of the muon light depends on the impact distance: as the distance increases, only a partial arc of the muon ring is typically visible. Figure 6.3 shows muon ring images for two different energies at four impact distances, demonstrating how only a fraction of the ring is detected at large impact distances. In such cases, the signal can easily be confused with a low-energy shower, even after applying time-based cleaning. To address this, we propose to use the presence of any light in the image that is not associated with the main shower structure, without requiring explicit identification of

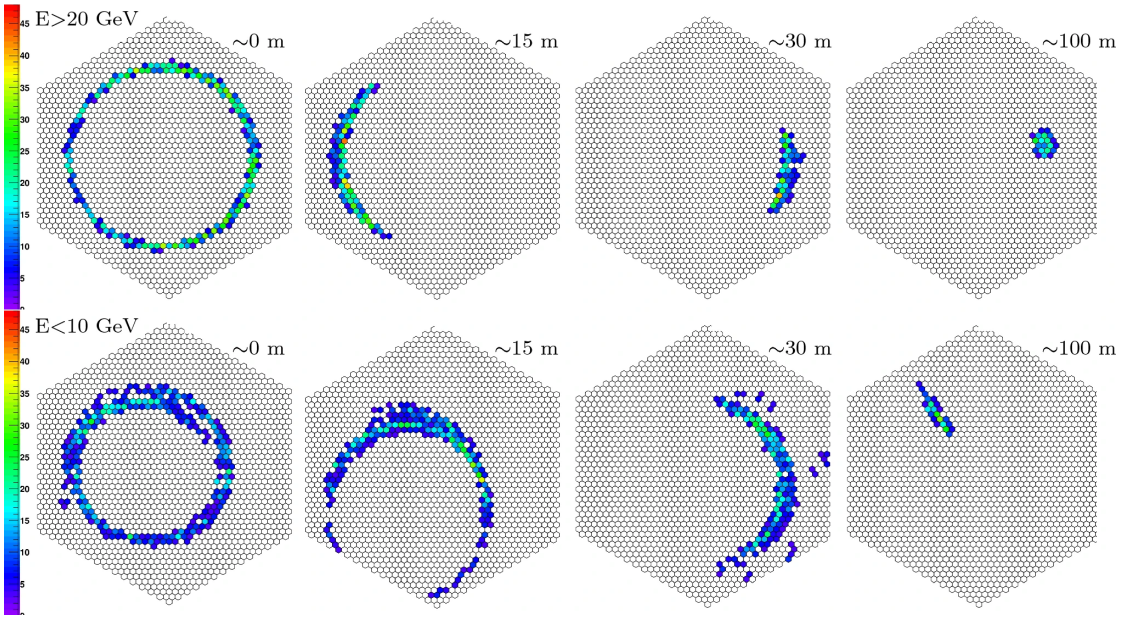

Figure 6.3: Simulated muon images in a 28 m telescope like H.E.S.S. CT5, at two different energies adn different impact distances. Figure from [150].

the muon light itself. This approach simplifies the implementation while still improving the background rejection power.

6.1.2 Algorithm for Background Rejection using Image Residuals - ABRIR

A detailed description of the algorithm can be found in our publication Olivera-Nieto et al. [151]. Here, we provide a summary of the algorithm's logic and its performance. Following that, we describe how the method was adapted and integrated into the HAP analysis framework.

The ABRIR algorithm is designed to identify hadronic events by analysing residual images from the CT5 camera. It compares the observed CT5 image to the expected one, predicted using the best-fit template from the ImPACT reconstruction method. This expected image is determined using the reconstructed energy and direction from the small telescopes, along with the zenith, azimuth, and offset angles of the observation. As such, ABRIR is applied after the standard H.E.S.S. *stereo* reconstruction using ImPACT and an initial γ/hadron separation using BDT tail cuts. The background efficiency after BDT selection is denoted as η_{BDT}, and the total background efficiency when including ABRIR is given by $\eta = \eta_{\mathrm{BDT}} \times \eta_{\mathrm{ABRIR}}$.

The ImPACT template of the expected CT5 image is used to mask the main shower component in the observed CT5 image, allowing residual structures to be examined. For an event to be flagged as a hadronic background, the residual must have more than three pixels. In addition, two conditions must be satisfied: (i) the maximum pixel intensity in the cluster, I_{max}, must exceed 9 p.e., to exclude faint structures, and (ii) the charge-distance parameter, defined as $d_{\mathrm{CH}} = I_{\mathrm{tot}} \cdot d^2$, where I_{tot} is the total intensity of the cluster and d is its distance to the main shower centroid, must be greater than 2 p.e. $\cdot$pixel^2, in order to remove clusters too close to the main shower. These thresholds were chosen to ensure a γ-ray efficiency above 90%.

To assess the performance of the ABRIR algorithm, it is tested on several types of events: simulated γ-rays (generated using CORSIKA [94] and *sim-telarray* [27]),

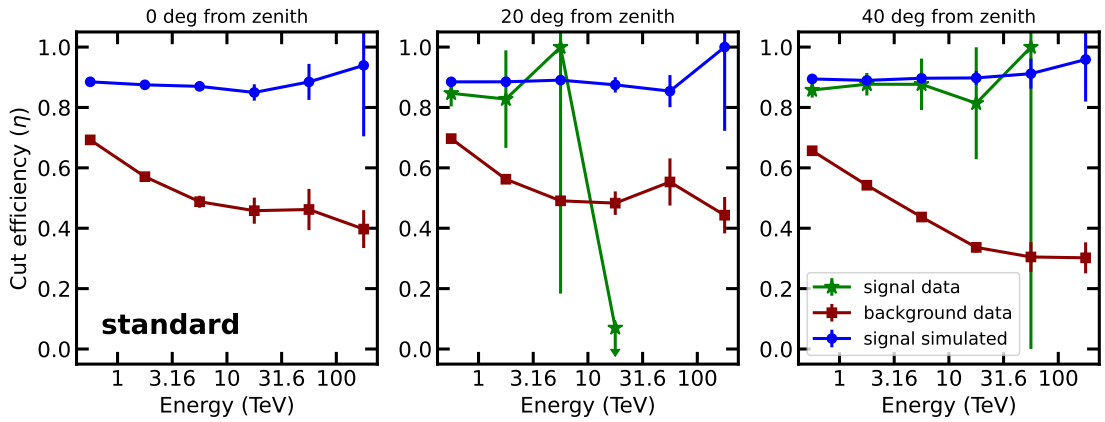

Figure 6.4: Cut efficiency of ABRIR applied after *stereo* H.E.S.S. standard cuts, for signal (green stars), background (red squares), and simulated γ-ray data (blue dots) and at different zenith angles. The signal data are taken within a radius 0.2° of bright γ-ray sources, PKS 2155-304 at 20° zenith range, and the Crab Nebula at 40° range. Figure taken from [151].

background events (off-runs), and real data from the Crab Nebula. The expectation is that most simulated γ-rays will be retained, while background events, recorded from sky regions without known γ-ray sources, will be significantly reduced. Although off-runs may contain some γ-ray contamination from large-scale diffuse emission (EGB) or faint unresolved sources, the flux of cosmic-ray background events is sufficiently high to neglect the γ-ray contribution.

The resulting performance of the ABRIR algorithm is shown in Figure 6.4, where the ABRIR cut efficiency as a function of reconstructed energy for each event type, evaluated across several observation zenith angles, is displayed. The efficiency is defined as the ratio of the number of events after and before applying ABRIR, considering only events that passed the initial BDT cuts. The algorithm significantly reduces the background rate across all energies, with a reduction factor of up to 2.5. Moreover, γ-ray efficiency remains mostly flat across the energy range at around 90%.

A small fraction of γ-ray events is expected to be rejected by the ABRIR algorithm. These cases can be broadly classified into three types: (i) γ-ray induced showers that contain detectable muon light, this can be seen in Figures 6.1 and 6.2; (ii) γ-ray showers involving low-altitude electrons, which can produce light patterns resembling muon features, particularly when occurring close to the telescope dish; and (iii) γ-ray events contaminated by unusually bright night sky background (NSB) light, which can arise from statistical fluctuations in the NSB level in simulations, but also occurs in real observations.

To check the consistency of the results in real data, the ABRIR algorithm was applied to real data from the on-region (inside 0.2°) of the Crab Nebula and PKS 2155-304. As shown in Figure 6.4, the γ-ray efficiency for simulations and real data are consistent, and the rate is almost flat in reconstructed energy. This indicates that most of the rejected γ-ray events are due to the third reason, as the NSB level does not depend on the event energy, unlike the number of detectable muons. Note that the cut efficiency for PKS 2155-304 drops at a few TeV because it is an extragalactic source, and no gamma-rays are expected to arrive from it above this energy due to the absorption on the EBL.

6.1.3 The ABRIR Algorithm in HAP

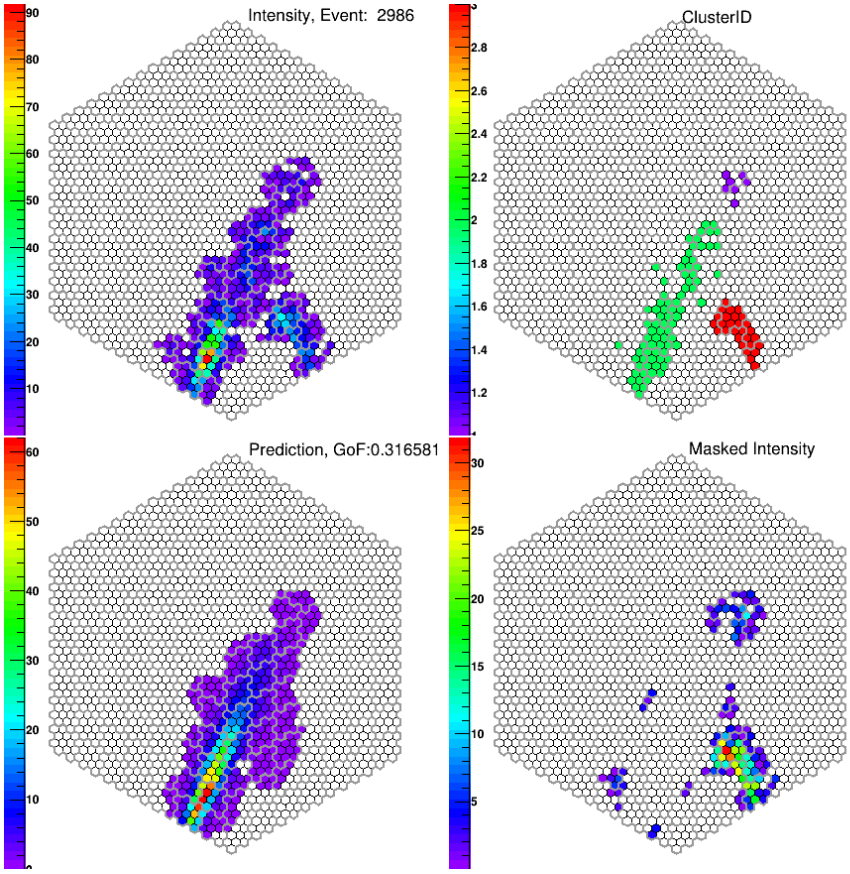

Figure 6.5: Example background data event. Top left is the data image, top right shows the clusters identified by time-based cleaning, bottom left is the ImPACT template image, and bottom right is the masked image.

The ABRIR algorithm is now part of the H.E.S.S. Analysis Package (HAP) software. The original algorithm described in our publication [151] was tested in a `python` environment. The implementation in the HAP software required the translation of the original algorithm into `C` language, as the HAP analysis chain is written in `C`. In HAP, ABRIR extracts additional information from the detected event image taken by the large CT5 telescope following the same logic as in the public version, but with some additional steps. For instance, the time-based cleaning is applied before ABRIR to determine the individual clusters in the camera image, on the one hand, and on the other hand, this image cleaning offers improved NSB cleaning compared to traditional methods.

The algorithm starts by comparing the CT5 template image as obtained by the ImPACT reconstruction and the observed CT5 shower image. When both images exist, which happens when they both pass the total intensity criteria described later, then the residual intensity image is computed, masking the main shower of the template from the data image. ABRIR will then loop over the clusters identified by the time-based image cleaning algorithm to compute the charge-distance for each cluster. If any of the clusters have a charge-distance larger than the threshold equivalent to the one defined in the original algorithm, then the event would be rejected.

Figures 6.5 and 6.6 display the camera image of the example background CR event and the potential γ-ray event observed from the direction of the Crab Nebula, respectively.

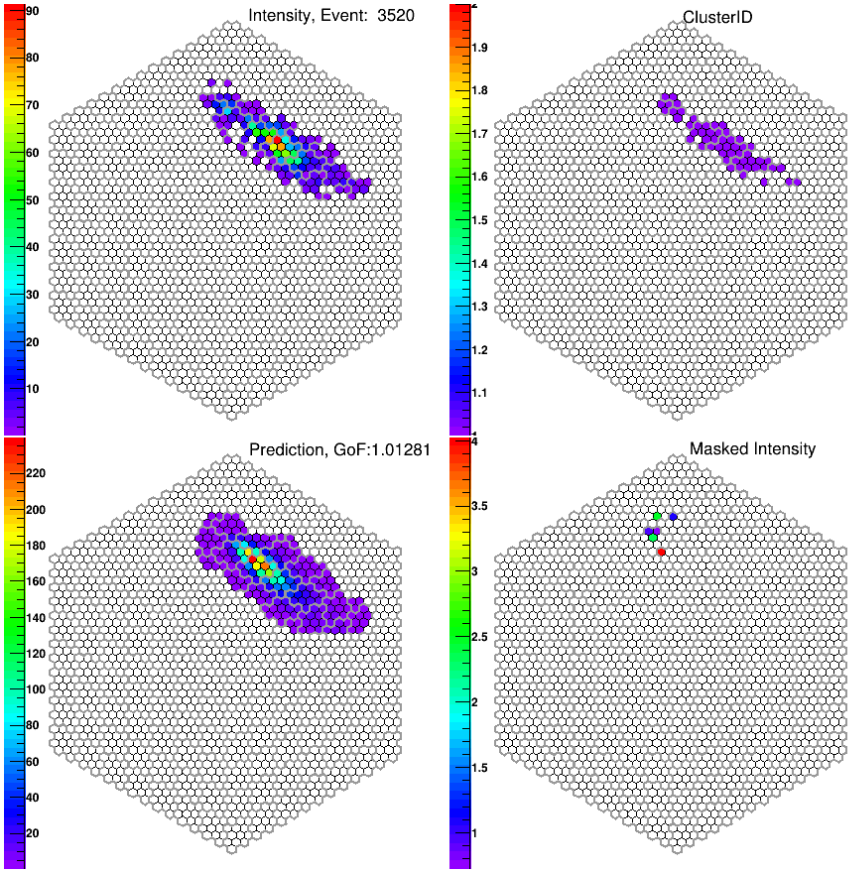

Figure 6.6: Same description as Figure 6.5, for an example γ-ray event.

Both events passed the BDT cut, which means that in a stereo reconstruction of the event with only the small telescopes, these events are considered as γ-rays.

ABRIR event classes

It might happen in some cases that the template CT5 image or the data CT5 image is too faint or non-existent, or in some cases, only one of them exists. To take this into account, before computing the masked residual we set a couple of total intensity thresholds which for the data image is $I^{\mathrm{TH}}_{\mathrm{tot,\,D}} = 60$ p.e. and for the template image is $I^{\mathrm{TH}}_{\mathrm{tot,\,T}} = 10$ p.e. The $I^{\mathrm{TH}}_{\mathrm{tot,\,D}}$ value is chosen according to the standard analysis configuration value, while for the template image, we just need the value to be above zero. We then compare the total intensity of the template images $I_{\mathrm{tot,\,T}}$ and the total intensity of the data image $I_{\mathrm{tot,\,D}}$ to the threshold values.

Four different cases can occur, denoted as different ABRIR event classes:

1. **ABRIR1** ($I_{\mathrm{tot,\,T}} > I^{\mathrm{TH}}_{\mathrm{tot,\,T}}$ and $I_{\mathrm{tot,\,D}} > I^{\mathrm{TH}}_{\mathrm{tot,\,D}}$): Both CT5 template and data exist, therefore we keep these events, and continue with the ABRIR algorithm.

2. **ABRIR2** ($I_{\mathrm{tot,\,T}} < I^{\mathrm{TH}}_{\mathrm{tot,\,T}}$ and $I_{\mathrm{tot,\,D}} > I^{\mathrm{TH}}_{\mathrm{tot,\,D}}$): The CT5 template is zero while the data exists. In this case, the event would be rejected, as the additional cluster is identified in the data, which is most probably of muonic origin.

3. **ABRIR3** ($I_{\mathrm{tot,\,T}} > I^{\mathrm{TH}}_{\mathrm{tot,\,T}}$ and $I_{\mathrm{tot,\,D}} < I^{\mathrm{TH}}_{\mathrm{tot,\,D}}$): The CT5 template exists while data is below threshold. This kind of events is more difficult to understand, but we

reject them as there might be some inconsistency during the reconstruction, or the reconstruction quality is low.

4. **ABRIR4** ($I_{\text{tot, T}} < I^{\text{TH}}_{\text{tot, T}}$ and $I_{\text{tot, D}} < I^{\text{TH}}_{\text{tot, D}}$): Both CT5 template and data are below the thresholds. We keep these events as both prediction and data are non-existent, meaning that we do not expect any contribution from CT5 in this event.

Additionally, two more parameters were considered to assess the quality of the event reconstruction: the ImPACT goodness of fit (GoF) and the reconstructed impact distance of the shower core. Both were evaluated during ABRIR testing and proved to be effective in identifying poorly reconstructed events across all energy ranges.

ImPACT GoF

The ImPACT GoF is computed as the likelihood of the detected image to the fitted template. It is defined as the normalized sum over all pixels of the difference between the log-likelihood of the pixel and the expected value [53]:

$$G = \frac{\sum_{\text{pixel } i} [\ln L(s_i|\mu_i) - \langle \ln L \rangle_{\mu_i}()]}{\sqrt{2 \times \text{NdF}}} \tag{6.1}$$

where s is the observed signal, μ is the model signal, and NdF is the degree of freedom, which corresponds to the number of pixels minus six (the dimensionality of the fitting parameter space including the direction, impact point, X_{max}, and primary energy). The GoF distribution for γ-rays fluctuates around zero and behaves asymptotically like a χ^2, as shown in the distribution in the left panel of Figure 6.7. To avoid the influence of the total intensity of the image on the GoF, we compute a scaled GoF parameter as the GoF divided by the average total intensity over the small telescopes that are participating in that run. We show the dependency of the GoF as a function of the image total intensity in the right panel of Figure 6.7, and the scaled GoF as a function of the total image intensity in the right panel of Figure 6.8. The scaled GoF is less affected by the image intensity, and we can see that most of the γ-rays have a scaled GoF smaller than 1. We compare the scaled GoF of CR background events to γ-ray events in the left panel of Figure 6.8. The scaled GoF of CR events extends to higher values, with much more event counts for scaled GoF $\gtrsim$0.25. A threshold value for the scaled ImPACT GoF equal to one is applied to avoid rejecting significant γ-ray events.

Reconstructed core distance The reconstructed core distance is the impact distance of the shower core to the telescope. For a proper data analysis, we want to avoid showers that are being reconstructed too close to the telescope and those being reconstructed too far from it.

Events with reconstructed impact distances very close to the telescope should be avoided, as they might have worse reconstruction quality. Moreover, showers falling very close to the telescope usually have very intense Cherenkov light that can saturate the camera, and the shower image can be truncated. In contrast, showers falling too far from the telescope are also very faint, leading to poor reconstruction.

Since for simulated γ-rays we know the original core distance, we can compare the reconstructed core distance to the true one, which is shown in Figure 6.9. One can see

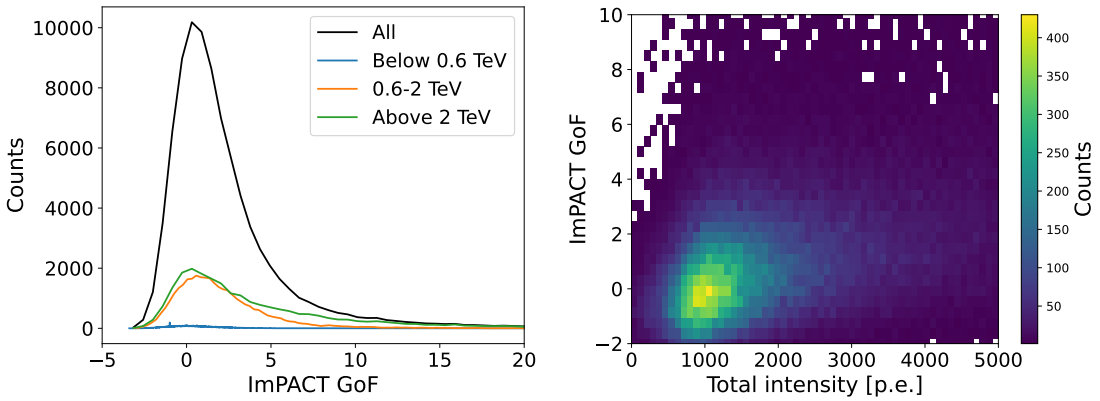

Figure 6.7: Left: ImPACT GoF distribution for simulated γ-rays at different energy ranges at zenith angles around 40°. Right: two-dimensional histogram of ImPACT GoF as a function of the averaged total intensity of shower images over participating small telescopes. The GoF increases with increasing total image intensity.

that for most events, the reconstructed core distance and the true core distance correlate well. Only a small fraction of events with very small core distances and above ∼600 m deviate from the correlation. Therefore, we keep only events with core distances between 1 and 600 m.

As shown, some events are already being rejected at this stage due to inconsistencies between the CT5 template and the recorded image, a large scaled ImPACT GoF (greater than 1), or reconstructed core distances falling outside the safe range (1 – 600 m). At this point, we also evaluate the performance of the ABRIR method using simulated γ-ray events, off-run data, and real observations. The resulting efficiency after applying these selection criteria is presented in Figure 6.10.

The reconstruction quality cuts are now being applied before ABRIR algorithm in the HAP software, right after the reconstruction of the events.

Charge-distance of residual clusters

For those events with data and prediction, i.e. ABRIR event class 1, we mask the pixels in the data image if the same pixel have a predicted intensity above a masking threshold corresponding to 1 p.e. After the masking, ABRIR loops over the remaining clusters to compute their distance to the shower center of gravity in the predicted image d_i and the total intensity $I_\mathrm{tot,i}$. The cluster distance d_i is computed as the sum of pixel-wise distance over residual pixels to the center of gravity of the main shower.

A cluster is only considered if it is comprised of more than three pixels. The charge-distance is then computed as $I_\mathrm{tot,i} \cdot d_\mathrm{i}^2$. The event would be rejected by the algorithm if any of the residual clusters has a charge-distance larger than a threshold value 0.009 p.e. $\cdot$ deg^2 (equivalent to 2 p.e. $\cdot$ pixel^2, units used in [151]).

The distribution of charge-distance is illustrated in Figure 6.11 for γ-ray, off-runs, and data events. We can clearly see that the charge-distance values are well above the cut value. Hence, any residual feature remaining in the masked image will lead to the rejection of this event. For illustration purposes, the charge-distance of non-rejected events is plotted as the bar around 10^{-3} p.e. $\cdot$ deg^2, however, the real value is zero.

The final performance of the ABRIR background rejection method is presented in

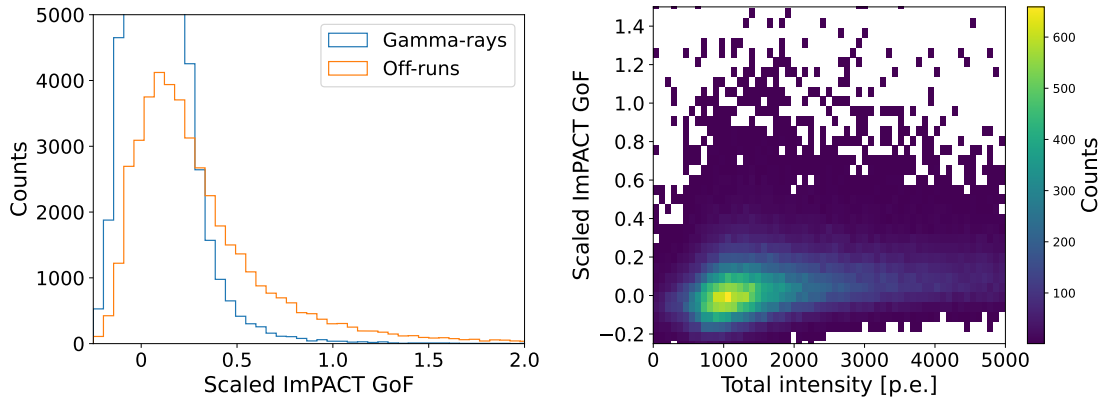

Figure 6.8: Left: scaled ImPACT GoF distribution for simulated γ-ray and off-run event at zenith angles around 40°. Right: two-dimensional histogram of scaled ImPACT GoF for the simulated γ-rays as a function of the averaged total intensity of shower images over participating small telescopes. The distribution of scaled GoF is flatter as a function of the total image intensity, and most of the γ-rays have scaled GoF below 1.

Figure 6.12. Notably, the rejection power for off-run events is even more pronounced than in the previously published results, shown in Figure 6.4.

6.1.4 Summary of improvements with respect to the published version

The improvements of the ABRIR algorithm introduced in the HAP software with respect to the already published version are summarised in the following list.

- First, a time-based cleaning algorithm is used before applying ABRIR to identify the clusters in the image by considering the arrival time information of each pixel (see top right panel of Figures 6.5 and 6.6). This approach not only improves the cleaning of NSB in the shower images but also enables the segmentation of the image into individual clusters of pixels with consistent timing. ABRIR then calculates the charge-distance parameter for each identified cluster and compares it to a threshold of 0.009 p.e.·deg^2. If any cluster exceeds this threshold, the event is flagged as suspicious and is rejected by the algorithm, as it likely contains light from muons.

- Secondly, the ImPACT goodness of fit (GoF) is also exploited to enhance the rejection power of this technique, identifying events with a poor reconstruction quality. We normalize the GoF by the amplitude of the image since the value of the GoF increases with it. The distribution of the scaled goodness of fit for gamma-rays and background events is shown in the left panel of Figure 6.8, for 40° from the zenith. A reasonable value for the scaled ImPACT GoF cut is 1, which also keeps most of the γ-rays.

- In addition, we also consider the reconstructed shower core as a criterion to reject low-quality events. The image of an event can have low brightness either because the primary particle had relatively low energy or because the location of the shower core is far from the telescope. Thus, faint images are sometimes reconstructed as having a very large core distance. A limited core distance can be considered to keep only those events with a reconstructed core less than 600 m, as a loose cut. On

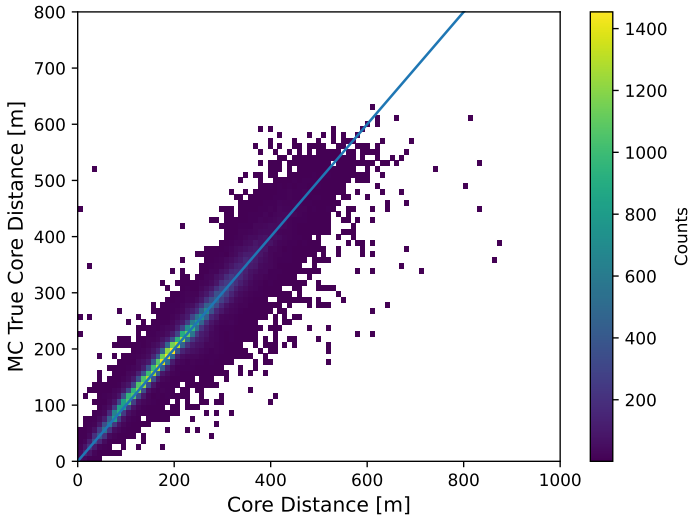

Figure 6.9: 2D histogram of the MC true core distance versus the reconstructed core distance. An identity function is plotted (blue line) on top, for reference. Note that dispersion is observed for showers having very small and very large reconstructed core distances above 600 m.

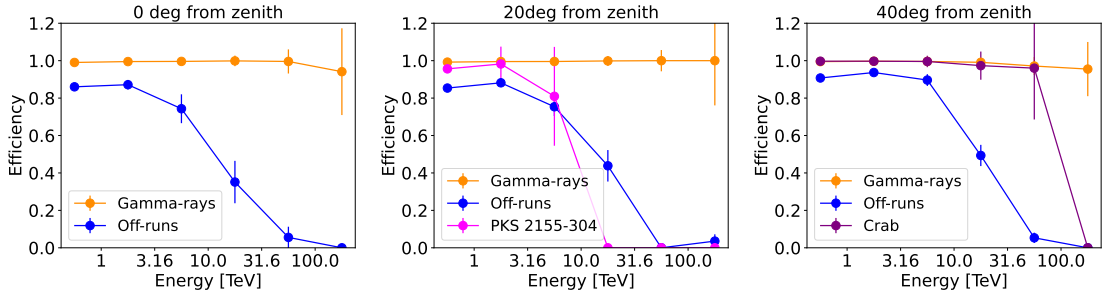

Figure 6.10: Cut efficiency for simulated γ-rays, off-runs, and real data after applying the event selection based on CT5 camera image, scaled ImPACT GoF, and reconstructed core distance cuts.

the other hand, events that fall very close to the telescope can potentially saturate the camera, leading to worse event reconstruction. Thus, we also avoid events with reconstructed core distances below 1 m.

Comparing the ABRIR performance in the HAP chain to the previously published results, a clear improvement in background rejection power is observed for off-run events, particularly at energies above 10 TeV across all zenith angles, where the rejection factor of 3 to 4.5 is observed. At the highest two energy bins, the off-run events were almost reduced to zero. This is because a limited number of observations were available for the testing. The enhancement at energies above 10 TeV is likely due to the introduction of new reconstruction quality cuts and the implementation of time-based cleaning. As shown in Figure 6.10, a significant fraction of off-run events are already being rejected by the cuts on core distance and scaled ImPACT GoF. Applying ABRIR after these cuts further improves background rejection, especially at lower energies.

However, when comparing the off-run efficiency below 10 TeV to the results in Figure6.4 for the events at around 40° zenith angle, a slight reduction in efficiency is observed. The off-run efficiency is now higher by 10 to 30%. This small difference may be attributed to

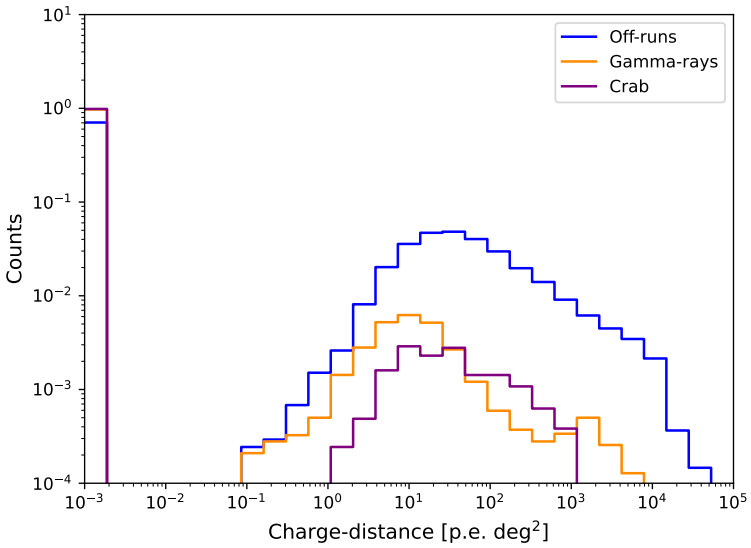

Figure 6.11: ABRIR Charge-distance parameter distribution for simulated γ-rays, off-runs and real data.

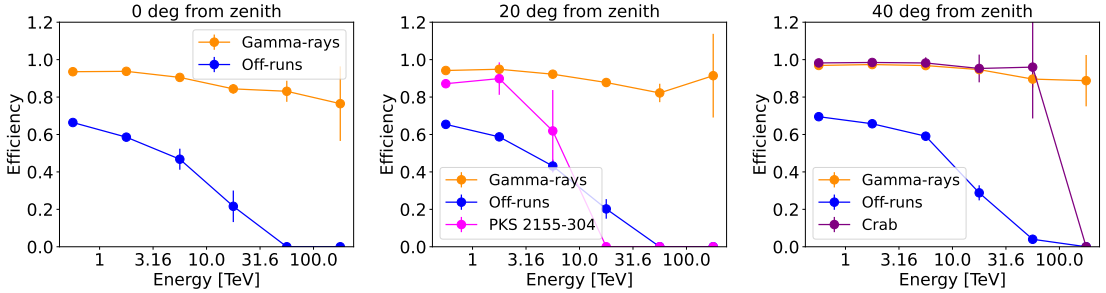

Figure 6.12: ABRIR cut efficiency for simulated γ-rays, off-runs and real data with including the event reconstruction quality cuts.

the time-based cleaning step, which could have removed some residual NSB noise that previously remained in the images.

The following section presents a detailed evaluation of ABRIR performance, applying it to the H.E.S.S. observations of the GC. A comparative analysis is carried out to assess the results with and without the application of ABRIR background rejection.

6.2 Application of ABRIR on Galactic Center data

The GC is a highly complex region, containing several point-like sources and extended diffuse emission from the CMZ and foreground emission from the Galactic disk. In Chapter 2, we reviewed γ-ray observations of the GC conducted by H.E.S.S. [88, 89], which can be mainly separated into the following components: (i) emission from a central source spatially coincident with the SMBH Sgr A*; (ii) the composite supernova remnant G0.9+0.1; (iii) the arc source HESS J1746-285; (iv) diffuse emission associated with molecular gas column density traced by CO, CS, and HCN; (v) large-scale diffuse emission; and (vi) a central Gaussian component.

In this section, a new dataset is used for the analysis of the GC region, which, for the

first time, uses data from CT5 for background rejection using the ABRIR method. The dataset has been processed with time-based image cleaning, which improves the overall image quality and enables the identification of clusters in the images. These clusters serve as input for the ABRIR algorithm to identify and reject CR background events. The analysis is then performed both with and without applying ABRIR, allowing a direct comparison to assess its impact on the analysis results.

In this analysis, we incorporated the gas column density map presented in Chapter 3 as the spatial template model to fit the γ-ray emission from both the CMZ and the Galactic foreground. The main improvements in this gas template include an enhanced separation between CMZ and disk gas components using clustering methods, as well as the inclusion of the atomic hydrogen contribution in the column density estimation. Additionally, a variable X_{CO} factor was applied to convert CO emission into hydrogen column density, which depends on the integrated intensity of each individual line.

6.2.1 Dataset

The dataset selected for testing the ABRIR algorithm must include CT5 observations in the FlashCam era, as the time-based cleaning technique had only been implemented for FlashCam data at the time of testing. The application of this method to data from the older CT5 camera within the HAP chain is currently in progress.

The dataset used in this analysis spans from 8 March 2020 to 1 August 2022, with a total livetime of 104.8 hours. To enable its use for testing, time-based cleaning information was generated, and the corresponding instrument response functions (IRFs) were produced both with and without ABRIR background rejection. This was necessary because the modifications introduced in the HAP software, including time-based image cleaning, additional ImPACT GoF and core distance cuts, and the ABRIR algorithm, affect the instrument's response to γ-ray-like showers. In particular, the increased background rejection rate alters the background distribution, requiring an update of the background model.

This dataset was processed exclusively for the purpose of testing the performance of ABRIR. As such, any spectral or statistical results derived from this analysis should be interpreted with caution.

The events are reconstructed in *stereo* mode, using the small telescopes. It is required that all four small telescopes (CT1–CT4) participate in the observation run. CT5 is also included, but it is used exclusively for background rejection and not for event reconstruction.

Figures 6.13 and 6.14 show the total number of counts and the excess counts, total counts minus background counts, detected from the GC region in the dataset without ABRIR applied (left) and with ABRIR applied (right), respectively. On average, the counts are higher in the dataset without ABRIR, as we would expect since the ABRIR algorithm throws away background events, but also some of the γ-rays (around 10% of them).

The ratio of background counts in the dataset with ABRIR over background counts in the dataset without ABRIR is shown in Figure 6.15. The figure demonstrates that the number of background counts is reduced to around 0.7 times at low energies, up to around 0.2–0.4 at the highest energies. The uncertainty on the ratio is computed under the assumption that the uncertainty in the number of counts follows Poisson statistics, i.e., the square root of the number of counts.

The excess counts with and without ABRIR for the two point-like sources HESS J1745-290 and SNR G0.9+0.1 are illustrated in Figure 6.16 and Figure 6.17. Notice that the

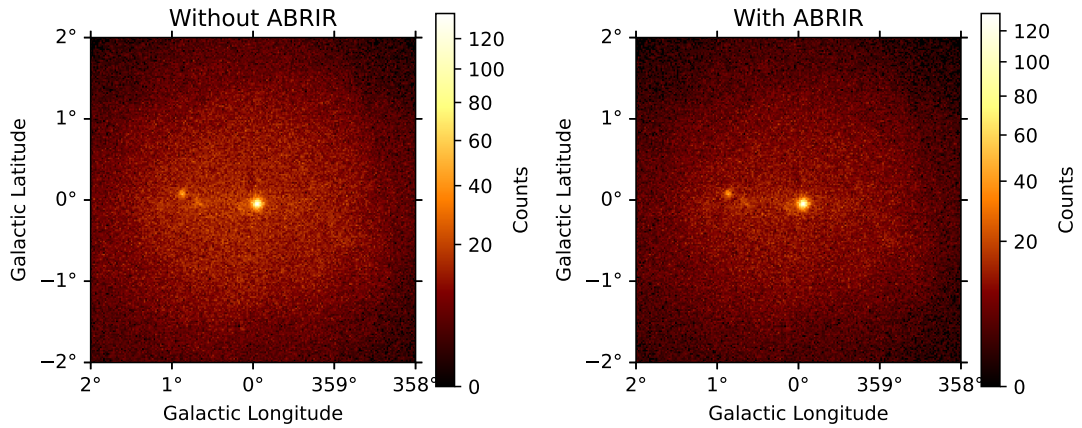

Figure 6.13: Total counts observed from the GC region. Left without applying ABRIR. Right: with applying ABRIR.

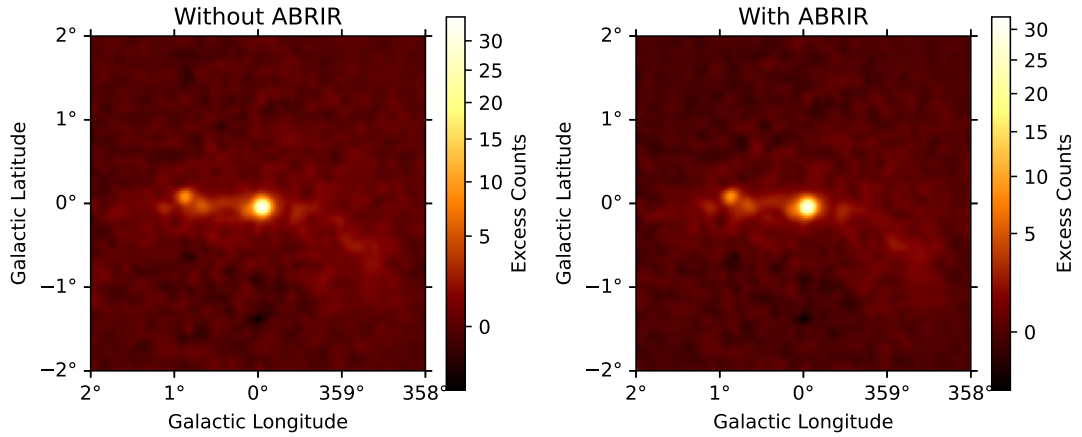

Figure 6.14: Excess counts observed from the GC region. Left: without ABRIR. Right: with ABRIR.

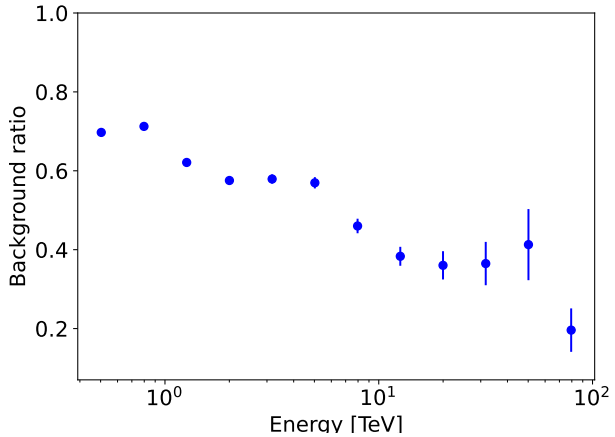

Figure 6.15: Background count ratio with ABRIR over without ABRIR.

excess counts as a function of the reconstructed energy is around 10% lower when ABRIR is applied, which is consistent with expectations shown in the middle panel of Figure 6.12, since the GC has an average zenith angle of around 20 °.

Moreover, the exposure, defined as the effective area multiplied by the livetime is shown in Figure 6.17. This value is computed as the average over the spatial axes in the entire FoV.

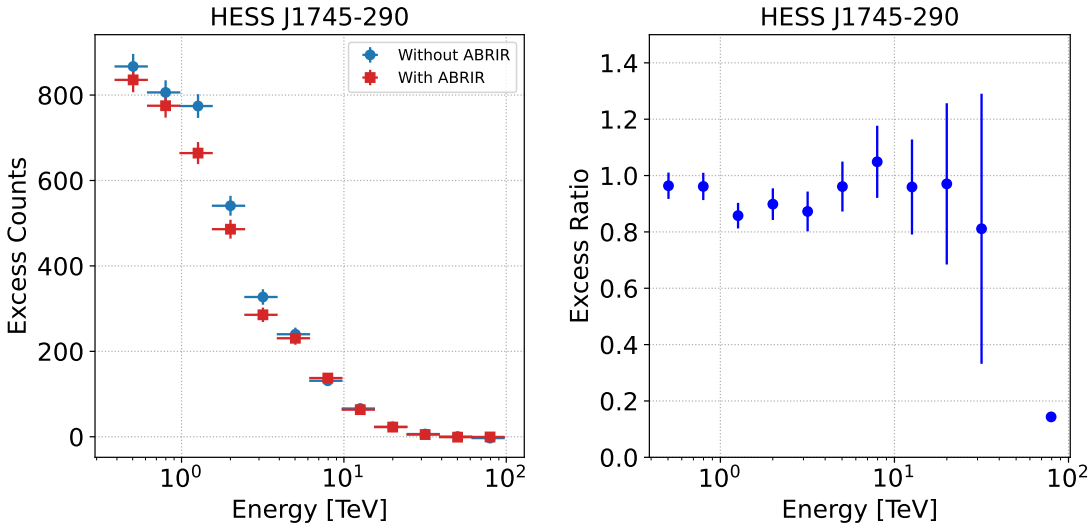

Figure 6.16: Excess counts as a function of reconstructed energy for 0.3° region around HESS J1745-290. Left: excess counts with and without ABRIR. Right: Excess ratio with ABRIR over without ABRIR.

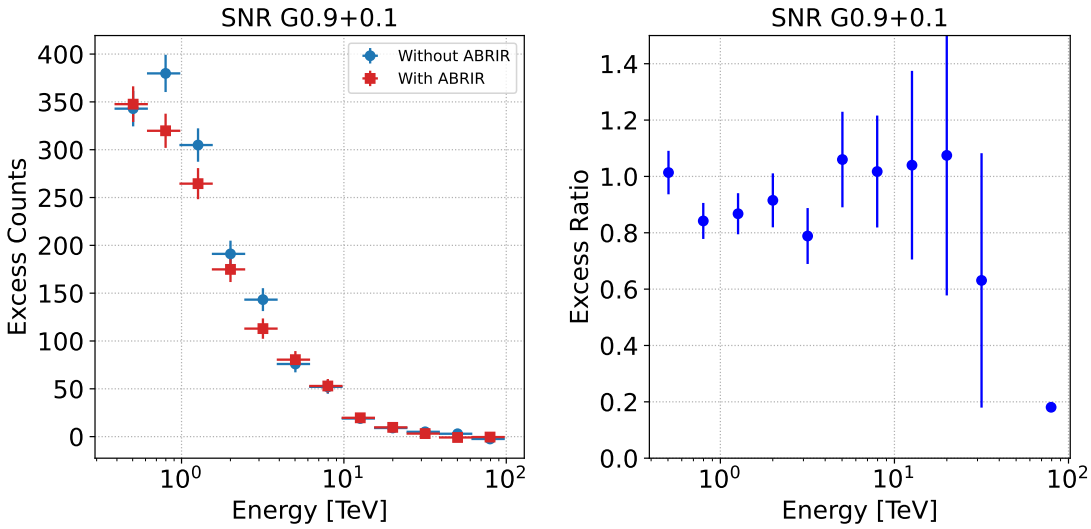

Figure 6.17: Excess counts as a function of reconstructed energy for 0.3° region around SNR G0.9+0.1. Left: excess counts with and without ABRIR. Right: Excess ratio with ABRIR over without ABRIR.

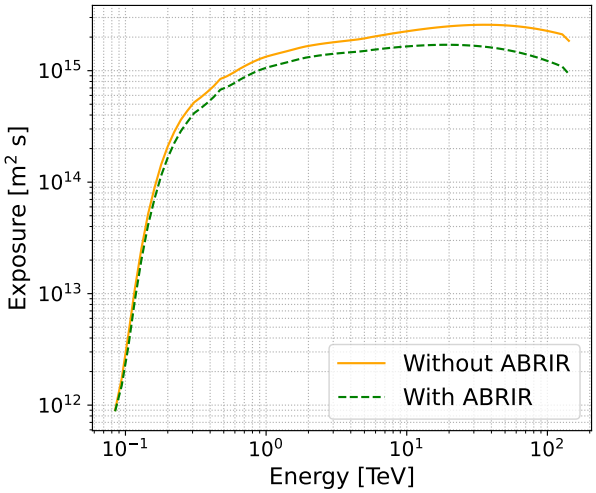

Figure 6.18: Exposure averaged over spatial axes as a function of true energy.

6.2.2 Background model smoothening

An issue that arises after applying ABRIR is that the background model becomes truncated at high energies, above which no events from the off-run dataset remain for constructing the model. To address this, the background model was extrapolated to higher energies, as shown in the right panel of Figure 6.19, using the CR spectral index as a conservative approximation. This correction was applied run-wise, for each pixel in the field of view. The background rate profiles in Figure 6.19 are integrated over the same offset angle for an example run.

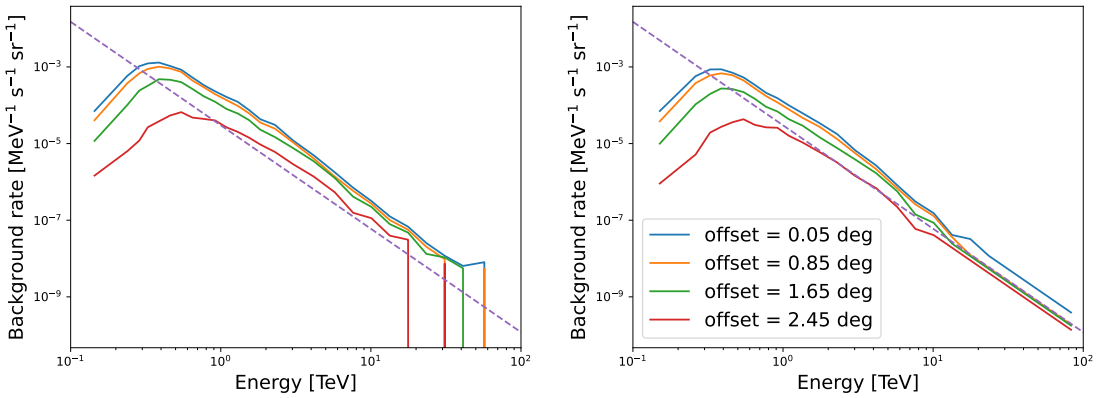

Figure 6.19: Background ratio computed as per energy, unit time, and steradian, before the extrapolation (left) and after the extrapolation (right).

After correcting the background shape for all runs, the data reduction step, converting the event lists and IRFs to binned datasets, is performed in `Gammapy`. For an improved determination of the background level during the binning, a 3D template-based FoV background model [135] is employed, considering the two spatial and one energy dimensions. Moreover, an additional normalization of the background level for each energy bin has been introduced for the spectral model of the background.

6.2.3 Source models

The source components considered in the fitting of the γ-ray emission in the GC region are listed in Table 6.1, where the spatial and spectral models are specified. A brief description of each model is given in the following.

Source name	Spatial model	Spectral model
HESS J1745-290	Point source	Exponential cutoff power law
SNR G0.9+0.1	Point source	Exponential cutoff power law
CMZ gas	Template	Exponential cutoff power law or power law
Foreground gas	Template	Power law
Central Component	Gaussian	Exponential cutoff power law
HESS J1746-285	Point source	Power law

Table 6.1: Summary of sources with their spatial and spectral models.

Central source or HESS J1745-290, which is spatially coincident with the SMBH Sgr A*, is modelled as a point-like source. Its spectral model is an exponential cutoff power law, as its SED was observed to exhibit a turnover at a cutoff energy of approximately 11 TeV [88].

HESS J1747–281, coincident with the composite SNR G0.9+0.1, is the second brightest source in this region after the central source. It has been modelled as a point-like source with an exponential cutoff power law.

CMZ gas emission correlates spatially with the bright diffuse γ-ray ridge observed in the GC region. To model this component, we use our hydrogen column density map, presented in Figure 3.16 of Chapter 3, as a custom spatial template. H. E. S. S. Collaboration [88] fitted its spectrum with a simple power law, as no clear energy cutoff was observed. However, a more recent study by Wong [216] reported that an exponential cutoff power law provides a better statistical fit. In this work, we compare both spectral models to assess which offers a more accurate description of the data.

Foreground gas emission corresponds to a more extended diffuse component, which is modelled using our foreground hydrogen column density map shown in Figure 3.16 of Chapter 3. For this component, a simple power law spectral model is assumed.

Central component is based on the empirical model fitted in H. E. S. S. Collaboration [89]. This component was introduced to account for significant residual emissions in the central region, which remained even after modelling the central source and the CMZ emission. It was also interpreted as having the 1/r CR energy density profile in [88].

In our analysis, we similarly observe that omitting this component results in a strong excess in the residual map. The spatial model is defined as a two-dimensional Gaussian distribution, and the spectral shape is modelled with an exponential cutoff power law.

Arc source or HESS J1746-285 was detected by H.E.S.S. as a faint point-like source located very close to the central source [89]. It is referred to as the arc source due to its spatial coincidence with a prominent filamentary structure observed in radio wavelengths (see Figure 2.9, showing the MeerKAT radio map in Chapter 2). The source is modelled with a power-law spectral shape.

6.2.4 Modelling and results

We fit the sources in two steps. First, the spatial positions of the sources, as well as the spectral index and normalisation of their spectral models, are left free to vary. In the second step, the γ-ray emission is fitted once more, but with the spatial models of each source fixed (i.e., frozen) during the fit.

Also, here, the background has to be included for the fitting, which consists of a FoV background model with the additional normalization per energy bin. This introduces more nuisance parameters to fit the background and account for potential systematics in the spectral shape of the background template.

In the following, results for the fitting with a ECPL spectral model for the CMZ are shown, except for the flux points and spectra of the CMZ, which are shown for both models.

Residual maps

The residual map obtained after fitting all source components is shown in the top panels of Figures 6.20 and 6.21. The residuals are mostly reduced to below 5σ significance. The residual significance distributions, shown in the bottom panels of Figures 6.20 and 6.21, are centered near zero, however, the widths are around 1.2 and 1.3, which are a bit larger than what is expected for a good fit. This is most probably due to the relatively small FoV for the analysis, limited by our gas map. For a proper study of the GC region, a more extended region should be considered, including a larger FoV gas map.

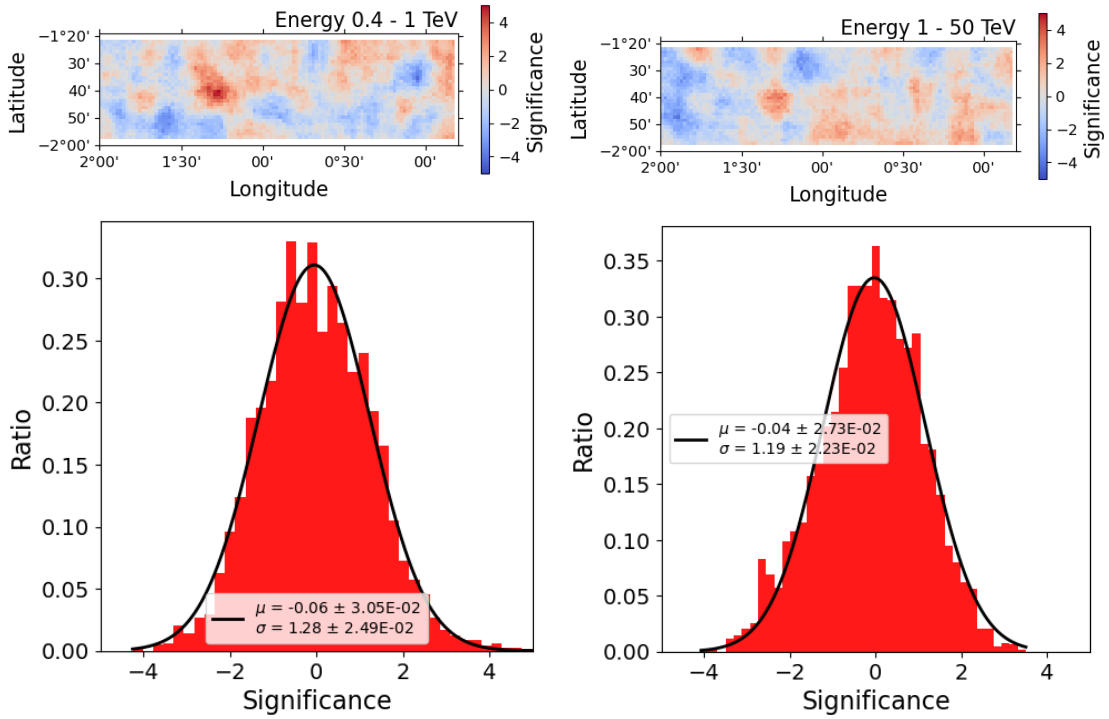

Figure 6.20: Residuals for the analysis without ABRIR. Top: residual maps for two different energy ranges. Bottom: Residual significance profiles for two different energy ranges.

Best fit parameters

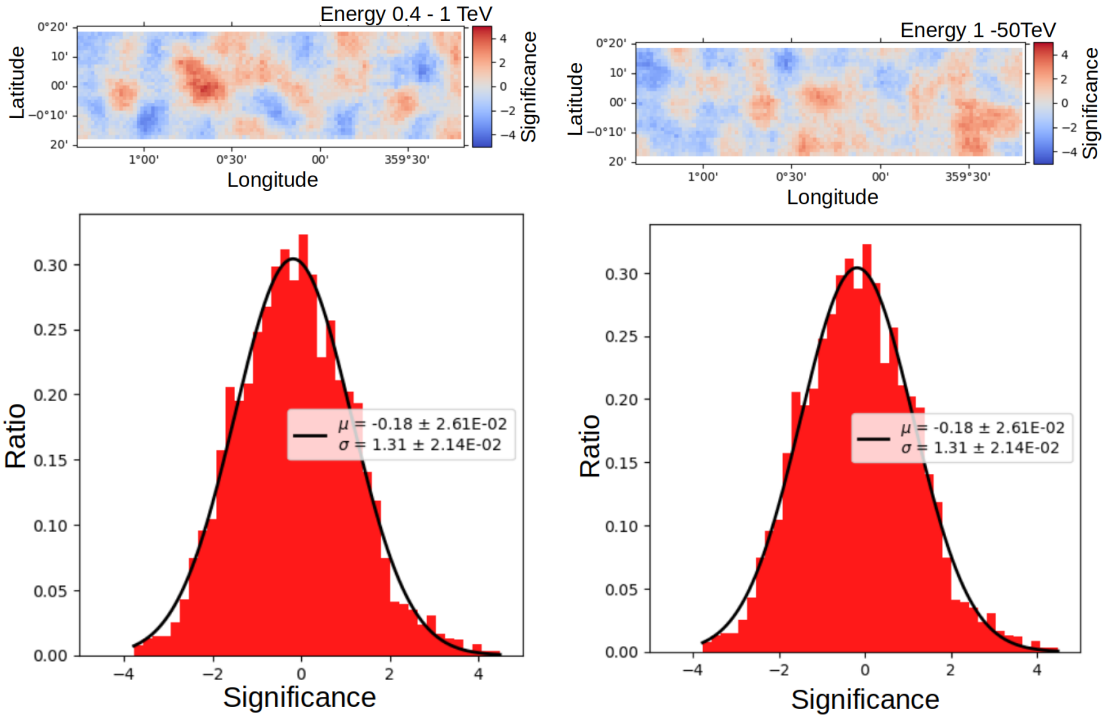

Figure 6.21: Residuals for the analysis with ABRIR. Top: residual maps for two different energy ranges. Bottom: Residual significance profiles for two different energy ranges.

The best-fit parameters obtained from the model fitting, using the spatial and spectral models described above, are listed in Tables 6.2 and 6.3 for without and with the application of ABRIR, respectively. The fitting was performed with `iminuit` [56] within the `Gammapy` framework. For the CMZ emission, results are provided for both a power law (PL) spectral model and an exponential cutoff power law (ECPL) spectral model. The results for the CMZ using the ECPL model are obtained by assuming a sub-exponential cutoff with an α parameter fixed at 0.5. However, due to the limited FoV) in this study, the fit failed to converge. In contrast, the PL model provided a more reasonable fit. As the main objective here is to evaluate the performance of the ABRIR background rejection method, a more sophisticated analysis covering a broader region of the GC is deferred to future work.

Source name	Longitude [°]	Latitude [°]	Index	Flux Normalization [1 / (TeV s cm^2)]	Cutoff energy [TeV]	TS
HESS J1745-290	-0.054	-0.045	2.31 ± 0.08	(18.5 ± 1.7)×10^{-13}	17.18±8.74	166.5
SNR G0.9+0.1	0.870	0.078	2.14 ± 0.13	(6.93 ± 0.62)×10^{-13}	13.55±7.89	514.0
CMZ gas (ECPL)			1.03 ± 0.22	(279.6 ± 82.0)×10^{-13}	0.11±0.10	139.1
CMZ gas (PL)			2.47 ± 0.05	(43.7 ± 4.7) ×10^{-13}		105.4
Foreground gas			2.24 ± 0.06	(16.3 ± 7.4)×10^{-8}		4.23
Central Component			1.50 ± 0.21	(9.22 ± 1.8)×10^{-13}	6.41±1.43	62.18
HESS J1746-285	0.141	-0.108	2.29 ± 0.16	(1.67 ± 0.31)×10^{-13}		56.25

Table 6.2: Model parameters for the different sources for analysis without ABRIR. These results should not be used for physical interpretation, as the dataset and field of view analysed were limited, and further improvements to the analysis methodology are still ongoing.

Source name	Longitude [°]	Latitude [°]	Index	Flux Normalization [1 / (TeV s cm^2)]	Cutoff energy [TeV]	TS
HESS J1745-290	-0.052	-0.045	2.197 ± 0.05	(23.1 ± 1.9)×10^{-13}	11.22±3.44	185.7
SNR G0.9+0.1	0.870	0.078	2.09 ± 0.06	(8.18 ± 0.47)×10^{-13}	13.89±2.81	598.9
CMZ gas (ECPL)			1.33 ± 0.05	(175.2 ± 8.4)×10^{-13}	0.53±0.05	249.3
CMZ gas (PL)			2.48 ± 0.05	(50.6 ± 2.2) ×10^{-13}		127.3
Foreground gas			2.54 ± 0.01	7.20 ± 0.39×10^{-8}		-
Central Component			1.62 ± 0.20	(8.7 ± 1.8)×10^{-13}	9.87±2.32	50.39
HESS J1746-285	0.139	-0.112	2.196 ± 0.12	(2.03 ± 0.31)×10^{-13}		70.87

Table 6.3: Model parameters for the different sources. Parameter values for analysis with ABRIR are presented. These results should not be used for physical interpretation, as the dataset and field of view analysed were limited, and further improvements to the analysis methodology are still ongoing.

Flux points and spectra

I compare the flux points and SEDs obtained with and without the application of ABRIR for each source component, as shown in Figures 6.22, 6.23, 6.24, 6.25, 6.26, 6.27, and 6.28. For the central source and the Arc source, the spectra from previous studies [88, 89] are also included for comparison. The results for the CMZ emission, assuming two different spectral models, are presented in Figures 6.24 and 6.25.

Figure 6.29 illustrates the flux points and the spectrum of each source component, for the analysis without and with ABRIR.

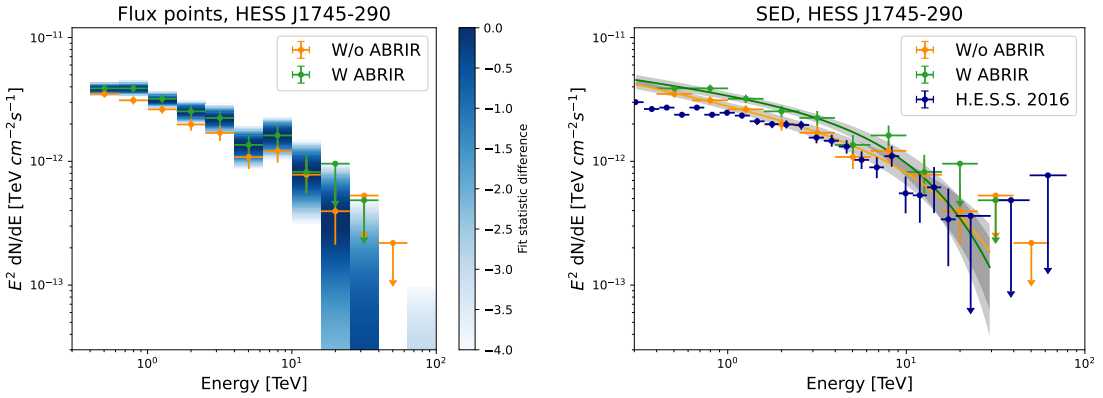

Figure 6.22: Flux points (left) and spectra (right) of the central source coincident with Sgr A*. In each case, the result with and without ABRIR is shown. The shaded areas of the spectra correspond to 1σ confidence interval, and the upper limits are computed using the 95% confidence. Dark blue points are the flux points published by the H.E.S.S. Collaboration [88].

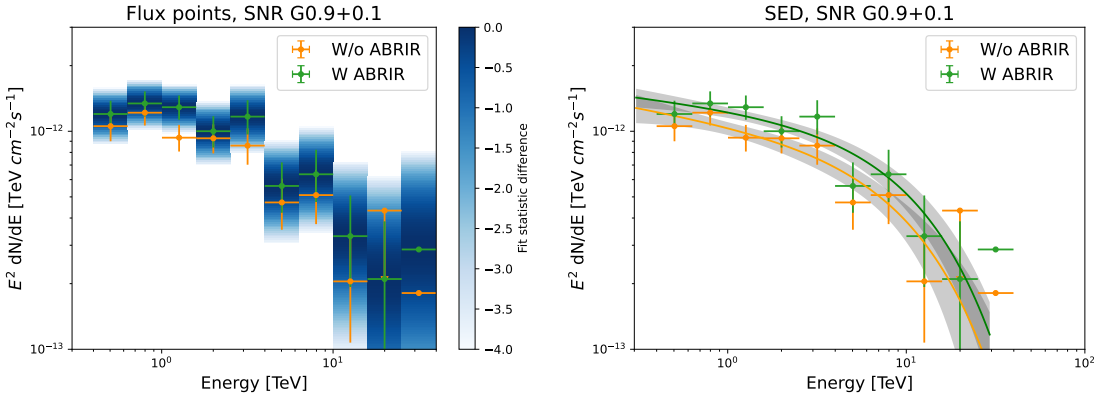

Figure 6.23: Same description as Figure 6.22 for SNR G0.9+0.1.

6.2.5 Discussion

Overall, we observe that the number of background counts is reduced when the ABRIR algorithm is applied. However, approximately 10% of the γ-ray events are also excluded by the algorithm. As a consequence, the excess counts, defined as the difference between total counts and background counts, are slightly lower in the analysis with ABRIR compared to that without it. The exposure is also moderately reduced. Thus, in principle, the estimated γ-ray flux for each source should remain largely consistent with the results obtained without ABRIR.

To verify this expectation, flux points and spectra have been extracted for each of the source components in the GC region. The corresponding γ-ray fluxes and spectral energy distributions (SEDs) are shown in Figures 6.22, 6.23, 6.24, 6.25, 6.26, 6.27, and 6.28. Furthermore, as the ABRIR algorithm successfully reduces the number of background events, a general decrease in flux uncertainties is expected and indeed observed in these figures.

Key observations are summarised in the following list:

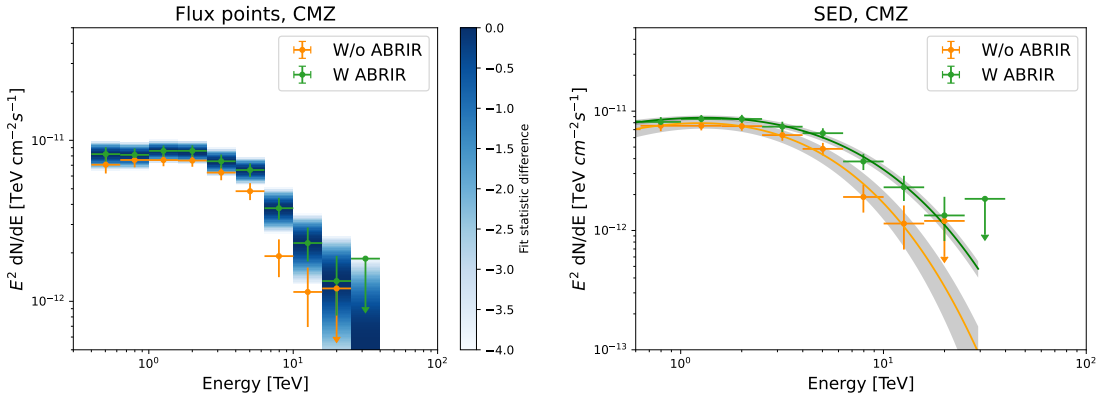

Figure 6.24: Same description as Figure 6.22 for the CMZ, assuming an exponential cutoff power law spectral model.

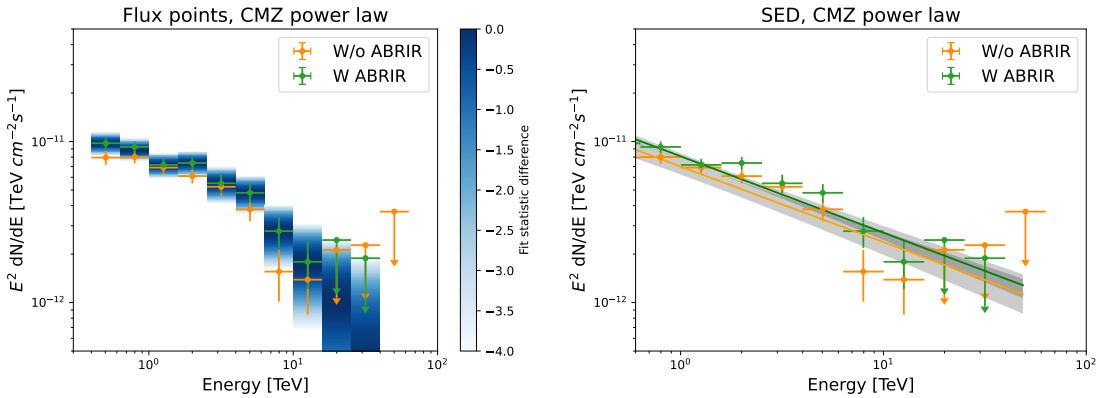

Figure 6.25: Same description as Figure 6.22 for the CMZ, assuming a power law spectral model.

- **Central source or HESS J1745-290**: The fluxes obtained with and without ABRIR are slightly higher than those previously reported by H. E. S. S. Collaboration [88]. Both results are mutually consistent, though the fluxes from the analysis using ABRIR are marginally higher. The spectral shape with ABRIR also exhibits more curvature, characterised by a smaller photon index, higher flux normalisation, and a smaller cutoff energy compared to the result without ABRIR.

- **SNR G0.9+0.1 or HESS J1747–281**: The flux points derived with and without ABRIR are consistent. The analysis using ABRIR yields a slightly flatter photon index and higher flux normalisation.

- **CMZ gas**: At low energy bins, both the SED and flux points are consistent between the analyses with and without ABRIR. However, at higher energies, the fluxes obtained using ABRIR are larger when assuming an ECPL spectral model. In contrast, the results using a simple power-law (PL) model show very little difference between the two analyses. The TS value is higher for the ECPL model than for the PL model, indicating that the ECPL provides a better fit to the data. However, these results should be interpreted with caution. The CMZ region considered in this analysis does not cover the full extent of the CMZ, and contributions from

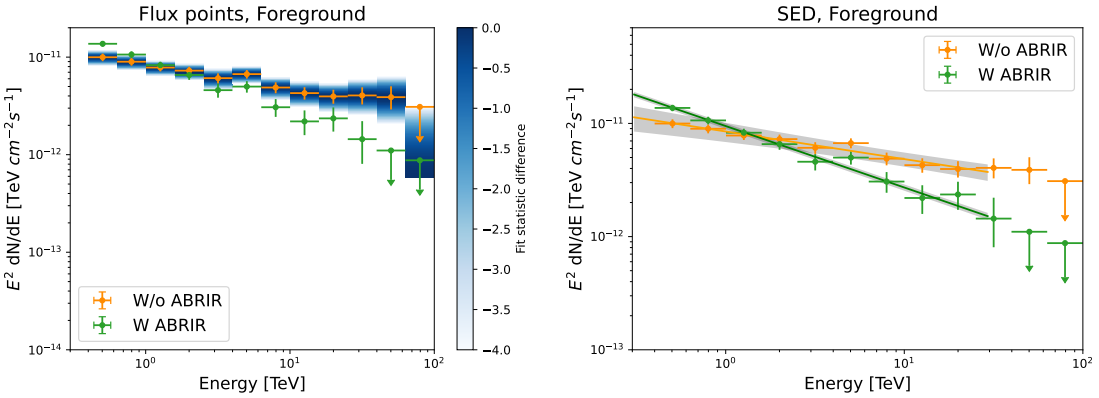

Figure 6.26: Same description as Figure 6.22 for the foreground galactic disk gas component.

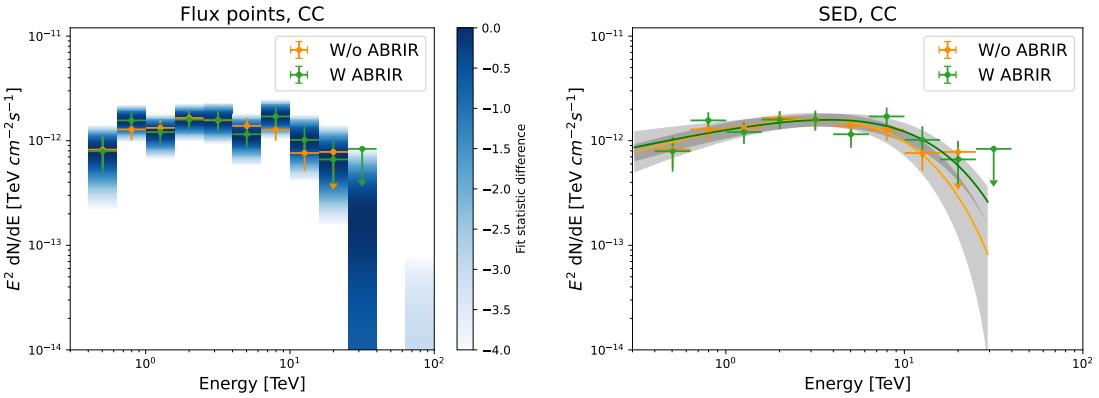

Figure 6.27: Same description as Figure 6.22 for the central component.

emissions outside the selected FoV may affect the accuracy of the measured γ-ray flux. A more comprehensive study should consider a larger spatial region, including the diffuse γ-ray emission from the full CMZ and higher Galactic latitudes, in order to fit the diffuse gamma-ray and CR background.

- **Foreground gas**: The spectrum derived with ABRIR shows a significantly steeper shape compared to that without ABRIR. This discrepancy may result from the suppression of foreground contribution in the fit, as the flux assigned to the CMZ component, particularly at the highest energy bins, increases in the ECPL model when ABRIR is used. Indeed, when the power-law is use for the CMZ spectral model, then the fitted foreground spectra with and without ABRIB are very close.

- **Central component**: The spectrum derived with ABRIR shows a slightly steeper photon index and a lower flux normalisation, with both spectra being highly consistent.

- **Arc source or HESS J1746-285**: This source is detected even in the relatively short dataset of approximately 100 hours. The fluxes and spectra obtained with and without ABRIR are consistent and closely match the previously published results [89].

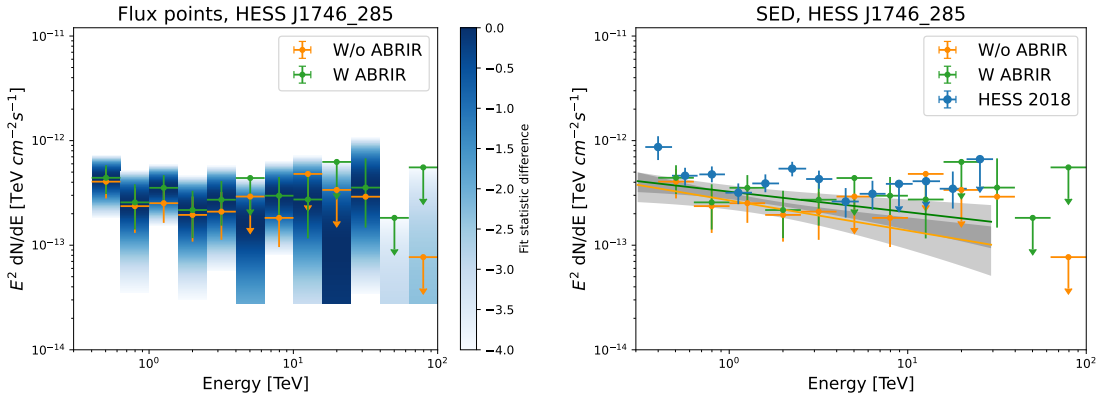

Figure 6.28: Same description as Figure 6.22 for HESS J1746-285. Light blue points are the flux points published by the H.E.S.S. Collaboration [88].

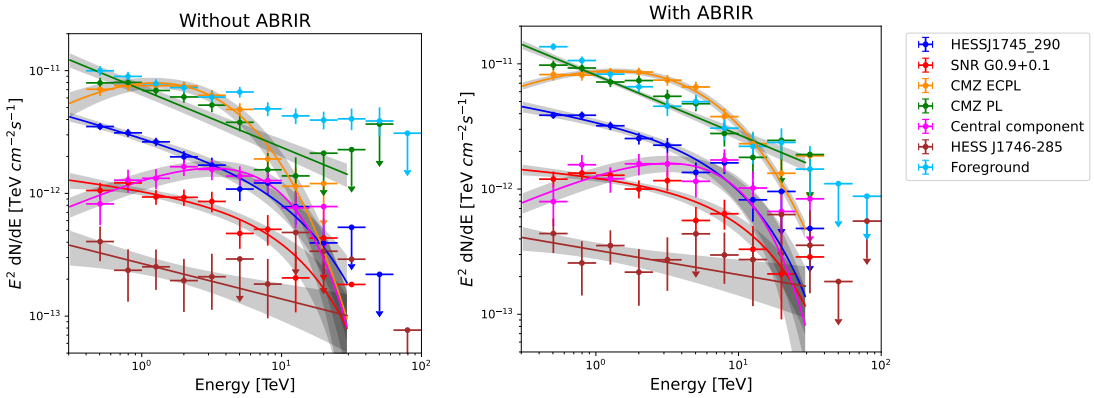

Figure 6.29: Flux points and spectra for all components. Left: without ABRIR. Right: With ABRIR.

A comparison of the source models is presented in Figure 6.29, where the results with and without the application of ABRIR for all components are shown in a single plot. It is more clearly visible in this figure that the uncertainties associated with the SEDs, represented by the 1σ confidence intervals as shaded regions, are generally narrower when ABRIR is applied. Similarly, the uncertainties on the individual flux points are also reduced. These results indicate that ABRIR performs efficiently in reducing the background level of the observations. At the same time, applying ABRIR background rejection leads to consistent flux measurements compared to previous studies, improving the overall significance of the fits and reducing the uncertainties on the fitted spectral parameters.

6.3 Summary

The integration of ABRIR into the HAP analysis chain was presented, along with the introduction of additional selection parameters that further enhanced the algorithm's performance compared to the previously published version.

I then applied ABRIR to the analysis of the GC region and compared the results with

those obtained without employing the ABRIR algorithm. The analysis demonstrated that ABRIR significantly improves the detection significance of sources and reduces uncertainties in the spectral fitting.

These findings support the use of ABRIR for improved background rejection in IACTs equipped with large mirrors. A more complete analysis of the GC region, incorporating the full H.E.S.S. dataset and our newly developed 3D gas distribution for the CMZ (introduced in Chapter 3), is planned. This will be essential for advancing our understanding of particle acceleration processes in this complex region.

The next chapter turns to a different observational technique: water Cherenkov detectors (WCDs). The future WCD observatory SWGO is currently under development, and predictions of its observational performance are essential for guiding design decisions. This chapter will focus on the GC as observed by SWGO and explore the observatory's expected sensitivity to potential dark matter signals.

Chapter 7

The Galactic Centre as seen by SWGO

The GC hosts a variety of astrophysical sources that emit VHE photons across a broad energy range, from MeV to PeV. In addition to its astrophysical richness, the GC is considered a unique target for the search for dark matter (DM) signatures, due to the predicted high DM density concentrated in this region and its proximity to us. Despite its importance, there exists no ground-based instrument in the southern hemisphere sensitive to the highest-energy γ-rays from the GC region.

To address this gap, the new SWGO observatory is being designed. Recent decisions have been made on the configuration of the array and detector unit after exploring many design proposals. In this regard, this work presents an evaluation of the expected performance of SWGO for the observation of γ-ray emission from the GC, along with estimation of its sensitivity to WIMP self-annihilation signals. These simulations have been carried out using the `Gammapy` software package [3, 59], incorporating IRFs that reflect the response of different design configurations for SWGO.

I conducted a comparative study of several candidate array and detector configurations (presented in Section 5.4) that have been proposed and investigated during the SWGO design phase. Two proceedings were published to report the studies using IRFs at different stages of the R&D phase [171, 174]. By examining the performance associated with these configurations, this study contributed to the optimisation of the observatory's final design. My findings show that SWGO will have outstanding sensitivity to thermal relic WIMPs over a wide mass range ($<$1 to $\sim$100 TeV). In doing so, SWGO will strongly complement searches carried out by the future CTAO, particularly in the TeV regime.

Section 7.1 presents the simulation results for GC predictions using the IRFs corresponding to each configuration, including the derived sensitivity curves for SWGO. Additionally, the prospects for DM detection with SWGO are discussed in Section 7.2, considering the Einasto dark matter density profile, following the SWGO benchmarks description. Lastly, Section 7.3 summarises this chapter.

7.1 Prediction for Galactic Center VHE sources as seen by SWGO

This section presents simulations of the GC region, based on source models provided by the CTAO Consortium [50], which are publicly available[1]. These models are constructed using observational data from current instruments like H.E.S.S. and *Fermi*-LAT.

The simulations were performed using `Gammapy` version 1.1 [5, 59]. The expected γ-ray emission was simulated for one year of observation, covering a circular region with a 2.5° radius centered on the GC.

[1] Models are accessible via Zenodo at doi:10.5281/zenodo.10008527.

7.1.1 Source models

For simplicity, the simulation is limited to three point-like sources detected by H.E.S.S.: the central source HESS J1745−290, the composite supernova remnant (SNR) G 0.9+0.1, and HESS J1746−285, commonly referred to as the "arc source" [6, 10, 88, 89]. In addition, the model includes diffuse γ-ray emission associated with the dense molecular gas in the Central Molecular Zone (CMZ), and the diffuse interstellar emission (IEM), assuming the 'IEM-varmin rescaled' model, also provided by [50].

The spatial and spectral models adopted for each of these components are summarised below:

- **Central source or HESS J1745−290**, in spatial coincidence with Sgr A*, is modelled with a point-like source spatial model, and using a exponential cutoff power law for the spectral model, with photon index 2.14, flux normalization 2.5×10^{-12} TeV, and cutoff energy 10.7 TeV.
- **Composite SNR G 0.9+0.1**, simulated also as a point-like source, with a power law spectral shape of photon index 2.4 and flux normalization 8.4×10^{-13} TeV.
- **Arc source HESS J1746−285**, also with a point-like source model, with a power law spectral shape of photon index 2.2 and flux normalization 1.8×10^{-13} TeV.
- **Diffuse emission from the GC ridge or CMZ**, using a template spatial model and a power law spectral model with photon index 2.32 and flux normalization 1.9×10^{-12} TeV.
- **Diffuse IEM background**, using a template spatial model and a power law norm spectral model[2].

7.1.2 Instrument response

To simulate the expected counts from a defined source model using `Gammapy`, it is also necessary to describe how the instrument responds to a given source flux. These characterisations are collectively referred to as instrument response functions (IRFs). Further details on the IRFs used in γ-ray data analysis are provided in Section 5.2.4.

A dedicated set of IRFs has been generated for each of the 13 configurations listed in Table 5.2. These IRFs are binned according to two zenith angle intervals: [0°, 30°] and [30°, 45°], as well as into few reconstructed core location bins depending on the zones of the array layout.

Figure 7.1 illustrates the 68% containment radius of the simulated PSF, the effective exposure, and the energy bias, for three representative configurations. Configuration A1 serves as the reference layout, A7 represents a significantly extended array, and C1 employs the smallest double-layer detector unit size.

7.1.3 Simulation results

For each configuration, 300 simulations of the expected γ-ray observations of the GC region have been produced, for one year of observation time, in order to evaluate the statistical spread. The spatial binning of the simulated datasets is set to 0.1°, a slightly coarse resolution that nonetheless significantly reduces computational costs.

Figures 7.2, 7.3, 7.4, and 7.5 present an example of the predicted γ-ray excess for configuration A1, shown in two energy bins and for each combination of zenith angle

[2]See the model description of power-law norm spectral model in `Gammapy`.

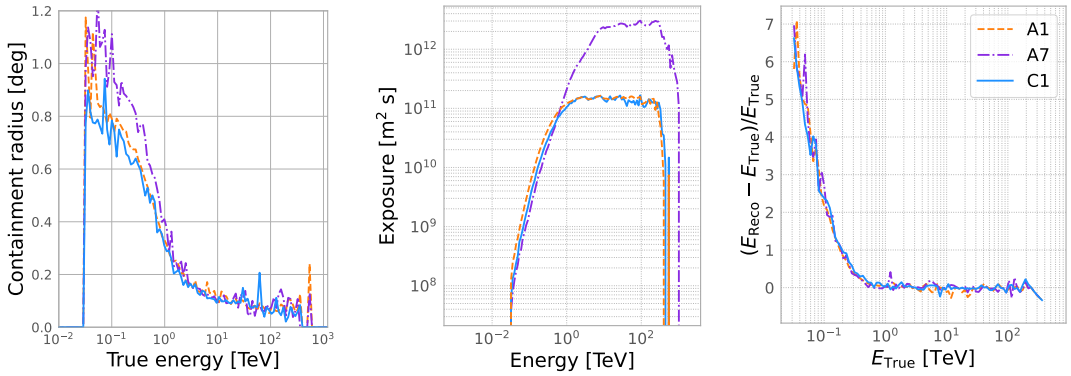

Figure 7.1: Simulated IRFs for candidate SWGO configurations. Left: PSF 68% containment radius. Middle: Effective exposure. Right: Energy bias. Representative configurations A1, A7, and C1 are shown to illustrate the performance for different array and detector sizes.

and core position bins. The influence of different array zones can be clearly observed; in particular, a higher excess is seen in zone 2 for the higher energy bin, indicating that the outer region of the array contributes substantially to the detection of γ-rays at the highest energies.

The corresponding significance map for configuration A1 is shown in Figure 7.6. This map was computed using a correlation radius of 0.15°, integrating over the energy range from 815 GeV to 107 TeV.

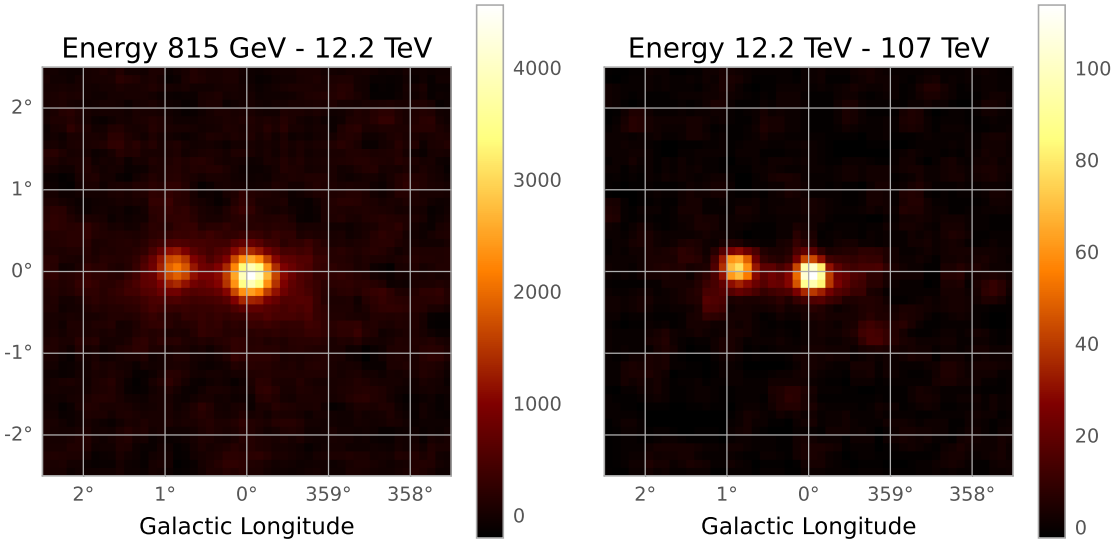

Figure 7.2: Predicted excess map of the GC region using configuration A1 IRFs. Sky map produced for showers reconstructed with core location in zone 1 and zenith angle [0°, 30°]. Correlation radius applied for the smoothing is 0.15°.

To compare the performance of different array layouts and detector unit sizes, I calculated the average significance of the detected sources using hypothesis testing applied to the ensemble of 300 simulations, shown in Figure 7.7. The results indicate that configurations A4, A5, D1, and E1 are among the most effective for detecting the

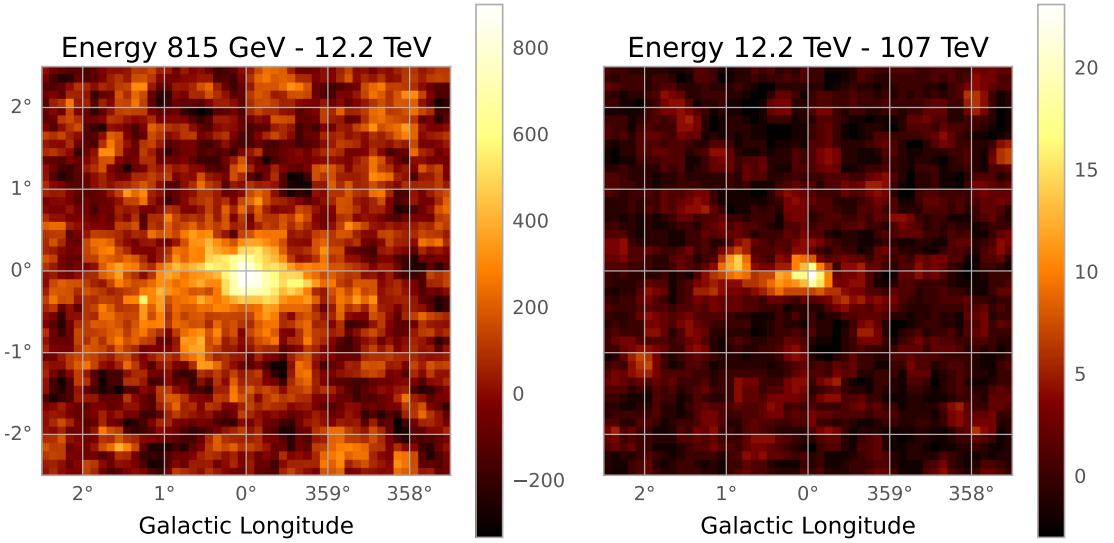

Figure 7.3: Same description as Figure 7.2, for zone 1 and zenith angle [30°, 45°].

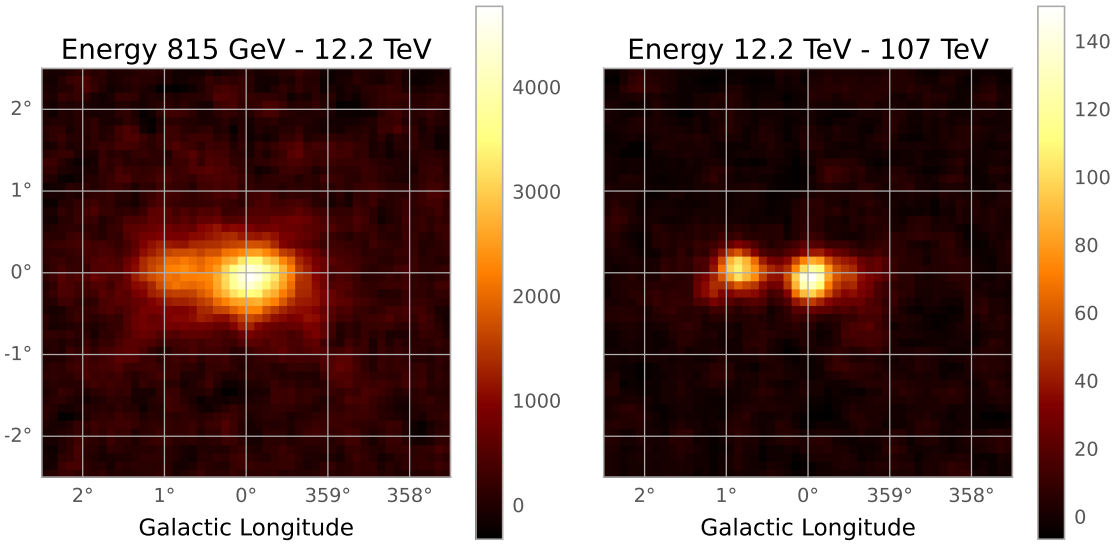

Figure 7.4: Same description as Figure 7.2, for zone 2 and zenith angle [0°, 30°].

central source. However, the performance of configurations A5 and E1 degrades when observing harder-spectrum sources such as the CMZ. This reduction in performance can be attributed to specific design limitations: layout 5 has a relatively small zone 2, resulting in a reduced effective area for capturing high-energy γ-rays. In the case of E1, the shallower tank depth limits the efficiency for detecting secondary particles from high-energy showers.

Conversely, configuration A7 exhibits the opposite trend, it performs less efficiently for softer-spectrum sources like the central source but shows improved sensitivity to harder-spectrum sources such as the CMZ. This behaviour is a result of its smaller zone 1 and substantially larger zones 2 and 3, optimizing the configuration for highest-energy

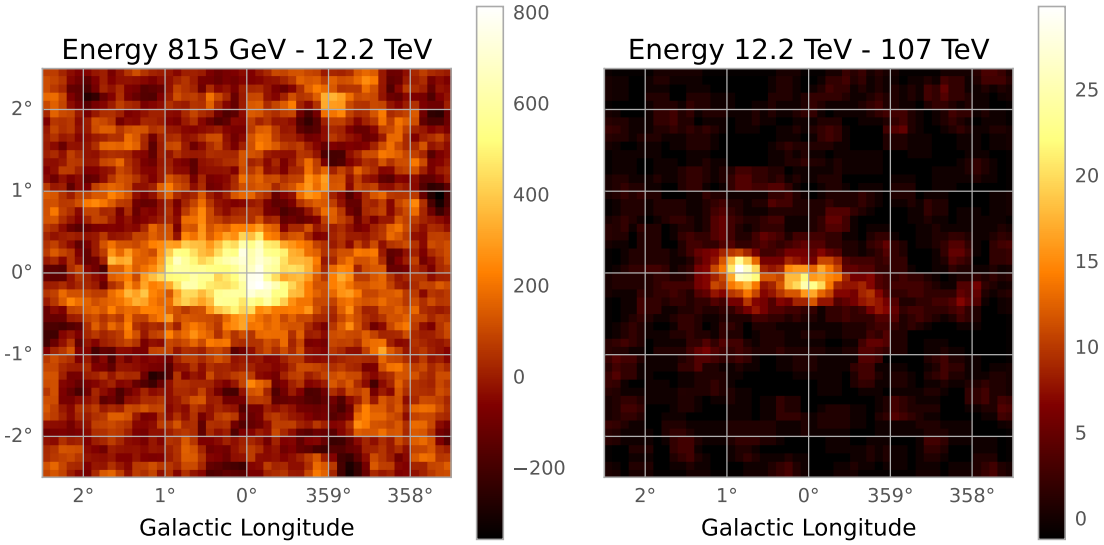

Figure 7.5: Same description as Figure 7.2, for zone 2 and zenith angle [30°, 45°].

γ-ray showers. In contrast, A4 and D1 both exhibit efficient detection for high and low energy showers.

Note that the arc source exhibits very low significance in these simulated datasets. This may be attributed to the limited observation time or the relatively coarse angular resolution used in the simulations. Therefore, it is not included in Figure 7.7.

Following the simulation of the datasets, the source components were fitted using the same spatial and spectral models to evaluate the uncertainties introduced by the inclusion of CR background and IRFs. Due to their relatively high brightness, the fitted spectra for the central source, SNR G0.9+0.1, and the CMZ remain largely consistent across different detector and array design configurations.

As an illustrative example, the spectra of these sources are shown in Figure 7.8 for configuration A4, which is the array layout showing the highest sensitivity in figure 7.7. The differential point-source sensitivity curve for SWGO for the same configuration is also overlaid. All three fitted spectra lie well above the sensitivity threshold, indicating that these components would be robustly detected within less than one year of observation. In particular, SWGO exhibits strong sensitivity at energies above 10 TeV, enabling it to extend the measured spectra of these sources up to several hundred TeV.

It is worth noting that while the simulated models for the SNR and CMZ adopt simple power-law spectra, these components are likely to exhibit spectral breaks at the highest energies. Although such features are not included in the current simulations, SWGO will be well positioned to constrain deviations from a pure power-law shape for these sources in future analyses.

For comparison, the point-source sensitivity curve for CTAO South is also shown in Figure 7.8, corresponding to 50 hours of observation time[3]. The complementarity between SWGO and CTAO, particularly in their energy coverage, can be clearly seen in their

[3]Sensitivity curves adapted from the CTAO official website: https://www.ctao.org/for-scientists/performance/.

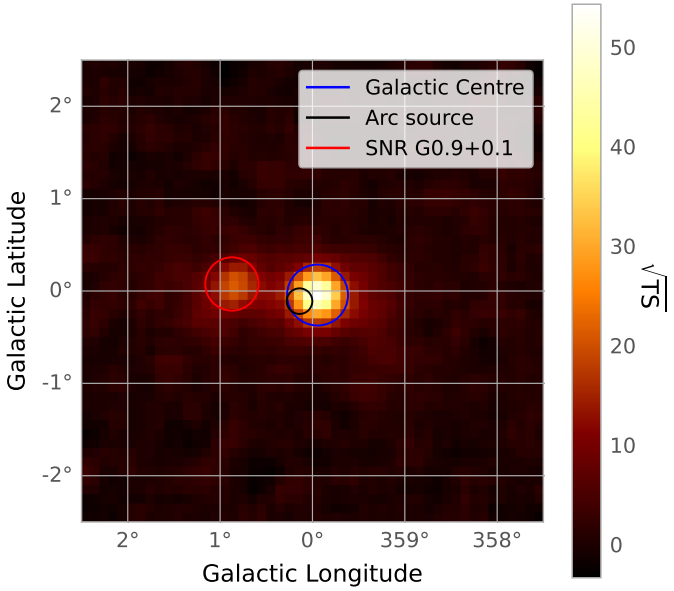

Figure 7.6: Predicted significance map computed using a correlation radius of 0.15° of the GC region for configuration A1. The integrated energy ranges from 815 GeV to 100 TeV, with 1 year of observation time.

sensitivity curves.

7.2 Dark Matter sensitivity

This section describes the study of DM sensitivity of SWGO, assuming that DM is composed of WIMPs. The analysis focuses on the use of the Einasto profile, and considers annihilation into the $b\bar{b}$ and $\tau^+\tau^-$ channels. The simulated observation time is five years, and the spatial region consists of a circular region with a radius of 5° around the GC.

An important remark is that, in traditional analyses of DM signals from the GC region, the Galactic plane is typically masked to suppress contamination from bright astrophysical backgrounds. This approach was adopted, for example, in the previous SWGO sensitivity study by Viana et al. [210], which used simplified "straw man" IRFs. In contrast, the present work does not apply any masking to the Galactic plane. Instead, known astrophysical emission components are incorporated directly into the template-based fitting, enabling a more complete treatment of the GC region. This approach allows for direct access to the densest DM region in the Galaxy, potentially enhancing the sensitivity to a DM signal.

The source models used are identical to those adopted in the previous section for the simulation of the GC region. However, in the fitting procedure, an additional DM component is included. A likelihood analysis is then performed to derive upper limits on the thermal relic cross section, at the 95% confidence level (CL).

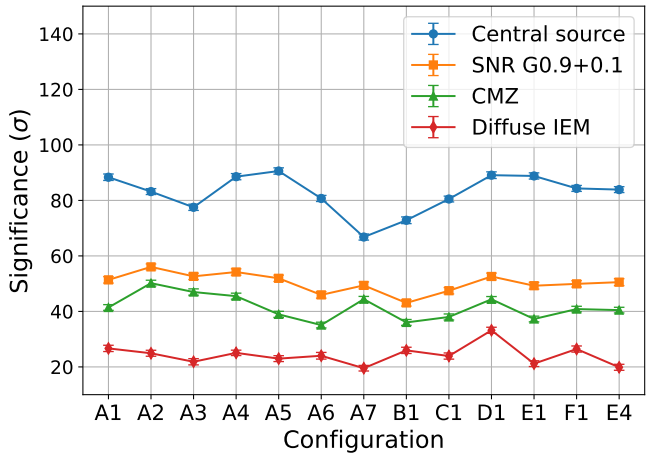

Figure 7.7: Predicted source significance for one year of observation time, as a function of the candidate configurations. Average values over the 300 simulations are shown, with one sigma standard deviation as error bars.

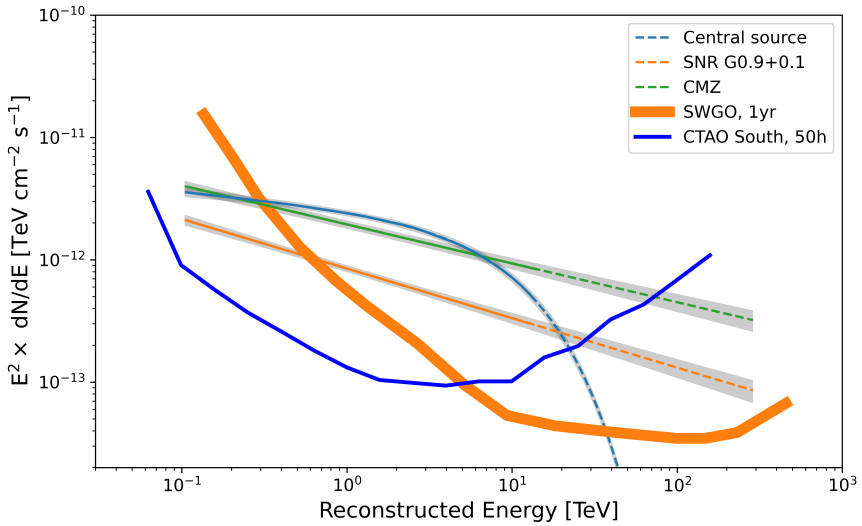

Figure 7.8: The spectra of the central source, SNR G 0.9+0.1 and the CMZ are plotted on top of the SWGO sensitivity curve (thick orange line), which represents the flux of a point-like source reaching 5σ in one year, for a medium-sized detector and a medium-sized array. We also show, as comparison, the sensitivity curve of CTAO South for 50 hours of observation, and note the complementarity of the two future observatories.

7.2.1 Dark matter source model

The DM density profile model is normalised by scaling to a reference density at a specified distance. In this study, we adopt a distance to the Galactic Centre of 8.5 kpc and assume a local DM density of 0.39 GeV cm^{-3}.

The corresponding J-factor map for the Einasto profile is displayed in the left panel of Figure 7.9. The J-factor map serves as the spatial template used in the fitting procedure for the DM component. The associated spectral models depend on the choice of the annihilation channel. The spectra for the channels considered in this work are presented in the right panel of Figure 7.9.

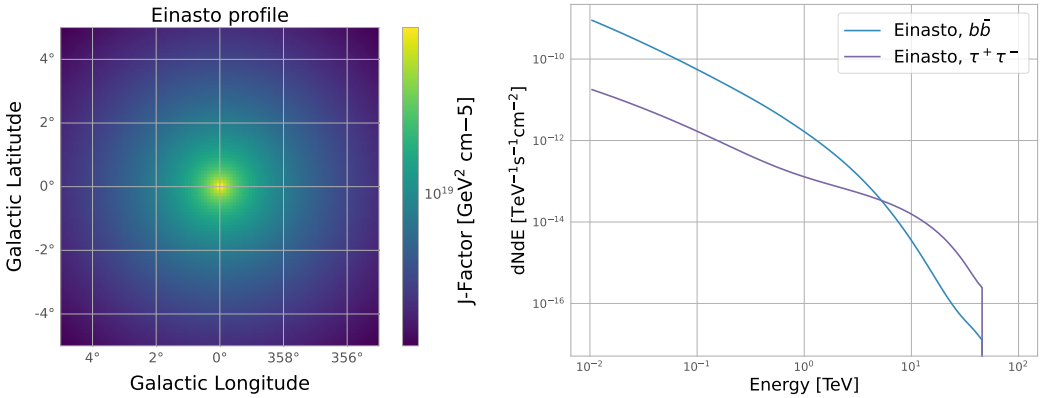

Figure 7.9: Left: J-factor map for the Einasto DM density profile. Right: Spectral models for two annihilation channels, for a DM mass of 50 TeV.

7.2.2 Exclusion limits for the velocity-weighted annihilation cross section

In this study, the DM particle mass is scanned over the range from 100 GeV to 100 TeV, and a total of 100 simulations for each DM mass and annihilation channel are produced. For each mass value, the velocity-averaged annihilation cross section corresponding to the 95% CL upper limit is computed. This is achieved through a 2D joint-likelihood method, comparing the null hypothesis (a background only model) with the alternative hypothesis (including a DM contribution), in different energy and spatial bins.

The expected γ-ray signal was described in Equation 4.33. Assuming that the number of observed events follows a Poisson distribution, the likelihood function is calculated in each bin as a joint-likelihood:

$$\mathcal{L}(M_{\mathrm{DM}}, \langle\sigma v\rangle) = \prod_{ij} \mathcal{L}_{ij}, \tag{7.1}$$

with the single likelihood function being

$$\mathcal{L}_{\mathrm{ij}} = \frac{(B_{\mathrm{ij}} + S_{\mathrm{ij}})^{N_{\mathrm{ij}}} \exp(-B_{\mathrm{ij}} + S_{\mathrm{ij}})}{N_{\mathrm{ij}}!}. \tag{7.2}$$

evaluated in the spatial bin i, energy bin j. B_{ij} is the observe background counts, S_{ij} the expected DM annihilation signal counts, and N_{ij} the total number of counts.

The test statistic is then computed as

$$TS = -\frac{\ln(\mathcal{L}_0(M_{\mathrm{DM}}, \langle\sigma v\rangle))}{\mathcal{L}_{\max}(M_{\mathrm{DM}}, \langle\sigma v\rangle)} \tag{7.3}$$

with $\mathcal{L}_0$ being the null hypothesis, and $\mathcal{L}_{\max}$ the alternative hypothesis with DM. The test statistic is evaluated at the cross section value that maximises the likelihood. The TS follows a χ^2 distribution in the limit of high statistics. Therefore, the 95% CL limit, leaving only one free parameter, corresponds to a TS of 2.71, above which the values of $\langle\sigma v\rangle$ are excluded.

The exclusion limits on the velocity-weighted annihilation cross section at 95% CL is shown in Figures 7.10 and 7.11 for the $b\bar{b}$ and $\tau^+\tau^-$ annihilation channels, respectively. The left panels of each figure show results for different array layouts, while the right panels present the performance of various detector unit designs. Notably, across all configurations,

the derived 95% CL limits fall below the canonical thermal relic annihilation cross section over a wide range of dark matter masses.

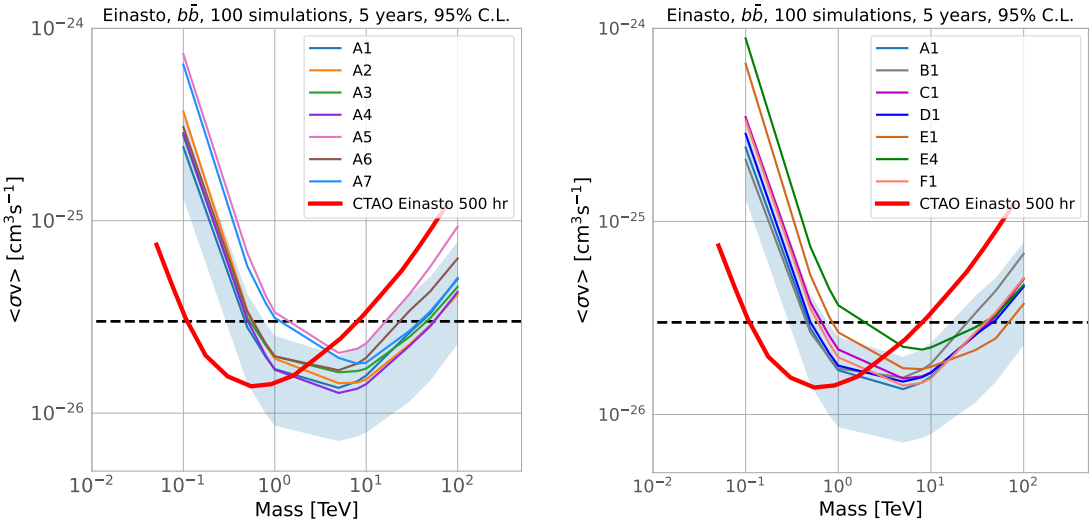

Figure 7.10: Exclusion limits on the velocity-weighted WIMP annihilation cross section at 95% CL, for Einasto profile, and $\mathrm{b\bar{b}}$ channel. The horizontal dashed lines are the thermal relic annihilation cross-section ($\sim 3 \times 10^{-26}\mathrm{cm}^3\mathrm{s}^{-1}$ [24]). Left: results for different array layouts. Right: results for different detector units. The observation time is 5 years. Shaded areas are the 1σ standard deviation band for the A1 configuration. CTAO sensitivity curves are adapted from [210].

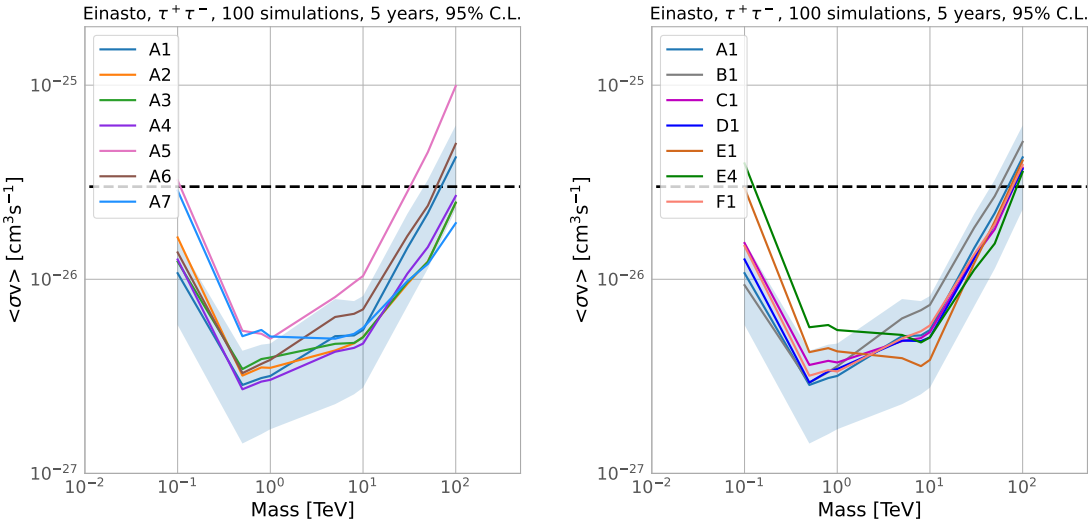

Figure 7.11: Same description as Figure 7.10, for $\tau^+\tau^-$ channel.

For the $b\bar{b}$ channel (see Figure 7.10), configuration A4 offers the best overall performance among the array layouts, while configurations A1 and D1 yield the lowest limits among the detector unit options. A similar trend is observed for the $\tau^+\tau^-$ channel (see Figure 7.11), where configurations A4, A1, and D1 also show the best overall trend.

Smaller array layouts, such as A5 and A6, exhibit reduced sensitivity, particularly at higher DM masses. In the case of A5, the sparser inner array also results in diminished performance at lower DM masses. In contrast, the extremely large array layout A7 shows

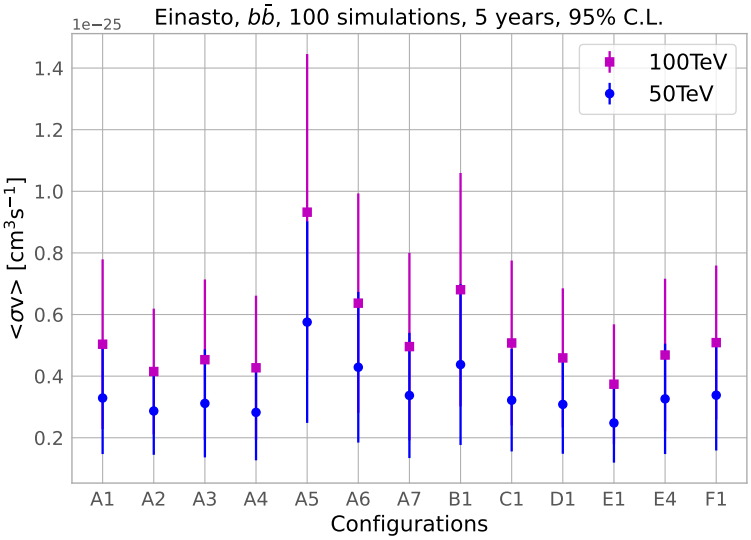

Figure 7.12: Upper exclusion limit on the velocity-weighted cross section for DM annihilation at 50 and 100 TeV DM masses, for the $\mathrm{b\bar{b}}$ annihilation channel.

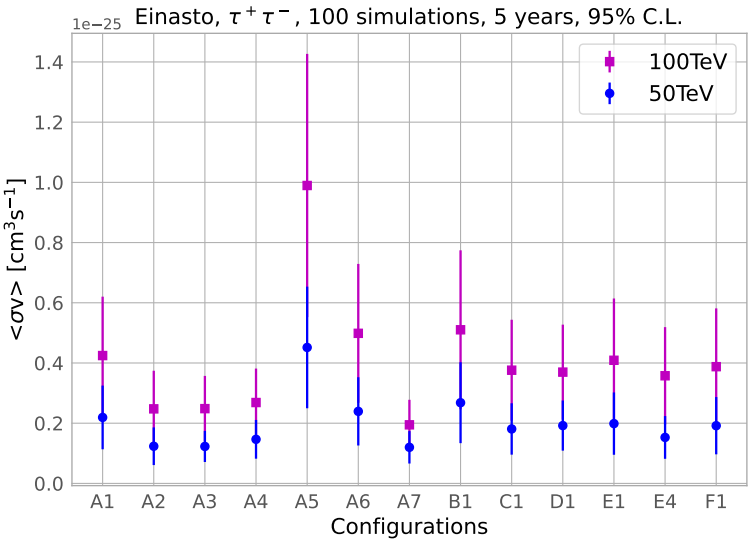

Figure 7.13: Upper exclusion limit on the velocity-weighted cross section for DM annihilation at 50 and 100 TeV DM masses, for the $\tau^+\tau^-$ annihilation channel.

improved sensitivity at high DM masses but is less competitive in the low-mass regime.

Regarding detector unit size, the use of smaller tanks does not appear to significantly impact sensitivity compared to larger tanks. However, the E-tank configuration shows an unexpectedly enhanced performance at high DM masses. This anomaly is likely attributable to issues in the current IRFs, which are not yet final; progress in the production of IRFs remains ongoing.

Focusing on the 50 and 100 TeV DM masses, we show the value of the velocity-weighted cross section limits in Figures 7.12 and 7.13, where we can more clearly see which configurations have optimal sensitivity for DM annihilation signals. One can notice that the lowest values are achieved by configurations A2, A3, A4, which share similar array

sizes; and D1, which can offer sensitivity as good as A2, A3, and A4, simply with a larger detector size (without a larger array layout). A lower limit is also observed for the E-tank, possibly due to the issue explained in the previous paragraph.

These results are similar to the evaluation results of SWGO designs for other sources, such as GRBs and diffuse emission. Therefore, the final design selection consists of a large double-layer tank, with a size similar to D1, and an array layout close to that of layout 1.

7.3 Summary

We investigated the expected γ-ray signal from the GC region as it would be observed by the SWGO observatory, considering all proposed detector unit designs and array layouts, and using the latest IRFs, developed by the SWGO Collaboration. The simulated spectra for the central source, SNR G0.9+0.1, and the GC ridge are shown together with the SWGO sensitivity curve. The results demonstrate that SWGO will be capable of detecting the GC region in less than one year of observation time. Its strong sensitivity at the highest energies, where the spectral shapes of these sources remain uncertain, will allow for improved constraints on their spectral models. Among the various configurations, A4 and D1 exhibit the best performance, as indicated by higher source significance values derived from hypothesis-testing likelihood analysis.

From the DM perspective, we calculated the expected upper limits on the annihilation cross section under the assumption of an Einasto profile and for two annihilation channels. A comparison of the different detector and array configurations shows again that the best sensitivity is achieved using the large-size tank design D and the medium-size array layout 4. These findings have contributed to the evaluation of candidate configurations during the SWGO R&D phase.

Chapter 8

Summary and Outlook

8.1 Summary

This thesis presents a study of the interstellar gas distribution of the Galactic Centre (GC) region, a development of a novel background rejection method for γ-ray analysis, and a prediction of the sensitivity of the future SWGO observatory to both astrophysical γ-ray sources and dark matter annihilation signals. The main findings and conclusions are summarised below:

- A refined estimate of the total hydrogen column density in the central molecular zone (CMZ) was achieved by combining atomic hydrogen (from HI 21 cm emission) and molecular gas tracers (from CO isotopologues: ^{12}CO, ^{13}CO, and C^{18}O). Improved separation between the CMZ and the Galactic disk was performed using spectral line decomposition and clustering techniques based on observation of differences in physical properties between the gas emission in the CMZ and the disk. These are the number of emission lines, the velocity dispersion and the brightness temperature ratio $T_{^{12}\mathrm{CO}}/\ T_{^{13}\mathrm{CO}}$.

- The CO-to-H_2 conversion factor (X_{CO}) was derived for each emission line, assuming the model developed by [82] and taking into account the effects of turbulence following the trend simulated by [28]. This allowed for a more accurate gas mass estimate for both the CMZ and disk gas.

- The separation of CMZ and disk gas components avoided overestimation of gas mass for the CMZ. The total gas mass was estimated at around $(2.3 \pm 0.3) \times 10^7$ $\mathrm{M}_\odot$, with atomic gas accounting for roughly 10%. Without removing the disk component, the mass estimate nearly doubles and the atomic fraction increases to 30%.

- The dust thermal emission was analysed using both single- and two-component modified black-body models. A non-linear relation between dust opacity and gas mass was observed.

- Using the revised gas maps, the cosmic-ray energy density in the CMZ was re-evaluated to be twice higher than the previous values reported in [88]. The CMZ gas was decomposed into 30 molecular cloud structures using clustering algorithms, providing the foundation for a future three-dimensional gas distribution model.

- The implementation of a novel background rejection algorithm –ABRIR– based on image residuals was integrated into the H.E.S.S. analysis chain. Applying ABRIR after traditional background separation significantly improves background suppression, reducing the background events to less than 70% for low energies and less than 10% for high energies, while maintaining high γ-ray efficiency $\sim$90%.

- Analysis of a subset of the H.E.S.S. GC observations with and without ABRIR was presented. The results showed that using ABRIR background rejection led to higher source statistical significance and overall reduced uncertainties in spectral measurements.
- The expected performance of the future Southern Wide-field Gamma-ray Observatory (SWGO) is also examined. Simulations using updated instrument response functions demonstrated that SWGO will be capable of detecting GC γ-ray sources within less than one year of observation, with sensitivity extending up to hundreds of TeV. The predicted spectra of the GC ridge, SNR G0.9+0.1, and the central source all lie well above the SWGO sensitivity curve.
- In addition, the sensitivity of SWGO to DM annihilation signals was studied, assuming WIMP theory, the Einasto density profile, and two DM annihilation channels. Results showed that competitive limits can be achieved across a broad range of WIMP masses and SWGO configurations, especially for large tank designs and medium-sized arrays.

8.2 Outlook: Investigation never ends

While this thesis has addressed several key aspects of the high-energy environment in the GC, it also opens the door to a number of promising directions for future research. Building on the methodologies and datasets developed in this work, the following projects are planned to further refine our understanding of γ-ray emission, cosmic-ray propagation, and the sensitivity of next-generation observatories:

- **3D Gas mass distribution in the CMZ**
  Develop a three-dimensional gas distribution model based on the clustered molecular clouds identified in Chapter 3. γ-ray data from Fermi-LAT and models of CR distribution in the GC will be used for the construction of this 3D model.
- **Full H.E.S.S. dataset analysis with ABRIR**
  Apply the ABRIR background rejection method to the complete H.E.S.S. GC dataset, spanning from the H.E.S.S. I to the FlashCam eras. With the aid of 3D gas model, compute a detailed CR energy density map across the GC, enabling refined study of the CR transport in this region.
- **Updated sensitivity studies for SWGO**
  Conduct refined sensitivity analyses for SWGO using new IRFs generated following the final site and design selection, and after the actual construction of SWGO.

Personal bibliography

Within the framework of this thesis, the following articles were published, to which I made important contributions:

Publications:
In Chapter 3:

- ***Cosmic rays, gas, and dust in the central molecular zone I – X_{CO} factors, cosmic-ray densities, and dust opacities*** [173]
  H. X. Ren, Q. Remy, S. Ravikularaman, M. Bouyahiaoui, F. Conte and J. Djuvsland. Accepted for publication in *Astronomy and Astrophysics.*

In Chapter 6:

- ***A background rejection using image residuals from large telescopes in imaging atmospheric Cherenkov telescope arrays*** [151]
  L. Olivera-Nieto, H. X. Ren, A. M. W. Mitchell, V. Marandon and J. A. Hinton. *European Physical Journal C 82.12*

Conference proceedings:

In Chapter 6:

- ***Algorithm for Background Rejection using Image Residuals*** [171]
  H. X. Ren, L. Olivera-Nieto, A. M. W. Mitchell, V. Marandon and J. A. Hinton. *7th Heidelberg International Symposium on High-Energy Gamma-Ray Astronomy*, July 2022, id.219.

In Chapter 7:

- ***The Galactic Center with a Southern Wide field-of-view Gamma-ray Observatory*** [171]
  H. X. Ren, J. Djuvsland, A. Albert and J. A. Hinton, for the SWGO Collaboration. *38th International Cosmic Ray Conference*, July 2023, Volume 444, id.893.
- ***The Galactic Center as seen by the Southern Wide field-of-view Gamma-ray Observatory*** [174]
  H. X. Ren, J. Djuvsland and J. A. Hinton, for the SWGO Collaboration.*8th Heidelberg International Symposium on High-Energy Gamma-Ray Astronomy*, September 2024.

Articles in preparation:

- ***Cosmic rays, gas, and dust in the central molecular zone II***
  S. Ravikularaman, Q. Remy, H. X. Ren and J. Djuvsland. Aimed for submission to Astronomy and Astrophysics.

Bibliography

[1] Abdalla, H. (2022). Search for Dark Matter Annihilation Signals in the H.E.S.S. Inner Galaxy Survey. *Physical Review Letters*, 129(11):111101.

[2] Abeysekara, A. U. e. a. (2023). The High-Altitude Water Cherenkov (HAWC) observatory in México: The primary detector. *Nuclear Instruments and Methods in Physics Research A*, 1052:168253.

[3] Acero, F. e. a. (2025). Gammapy: Python toolbox for gamma-ray astronomy.

[4] Ackermann, M. e. a. (2014). The Spectrum and Morphology of the Fermi Bubbles. *The Astrophysical Journal*, 793(1):64.

[5] Aguasca-Cabot, A., Donath, A., Feijen, K., et al. (2023). Gammapy: Python toolbox for gamma-ray astronomy.

[6] Aharonian, F., Akhperjanian, A. G., Aye, K. M., et al. (2005). Very high energy gamma rays from the composite SNR G 0.9+0.1. *Astron. & Astrophys.*, 432(2):L25–L29.

[7] Aharonian, F. and et al. (2004). Calibration of cameras of the H.E.S.S. detector. *Astroparticle Physics*, 22(2):109–125.

[8] Aharonian, F. A. (2004a). *Very high energy cosmic gamma radiation : a crucial window on the extreme Universe*.

[9] Aharonian, F. A. and Konopelko, A. K. (1997). Stereo imaging of vhe gamma-ray sources.

[10] Aharonian, F. e. a. (2004b). Very high energy gamma rays from the direction of Sagittarius A*. *Astron. & Astrophys.*, 425:L13–L17.

[11] Aharonian, F. e. a. (2006a). Discovery of very-high-energy γ-rays from the Galactic Centre ridge. *Nature*, 439(7077):695–698.

[12] Aharonian, F. e. a. (2006b). HESS Observations of the Galactic Center Region and Their Possible Dark Matter Interpretation. *Physical Review Letters*, 97(22):221102.

[13] Aharonian, F. e. a. (2006c). Observations of the Crab nebula with HESS. *Astron. & Astrophys.*, 457(3):899–915.

[14] Aharonian, F. e. a. (2022). A deep spectromorphological study of the γ-ray emission surrounding the young massive stellar cluster Westerlund 1. *Astron. & Astrophys.*, 666:A124.

[15] Albert, A. e. a. (2024a). Observation of the Galactic Center PeVatron beyond 100 TeV with HAWC. *The Astrophysical Journal*, 973(1):L34.

[16] Albert, A. e. a. (2024b). Performance of the HAWC Observatory and TeV Gamma-Ray Measurements of the Crab Nebula with Improved Extensive Air Shower Reconstruction Algorithms. *The Astrophysical Journal*, 972(2):144.

[17] Albert, J. and et al. (2006). Observation of Gamma Rays from the Galactic Center with the MAGIC Telescope. *The Astrophysical Journal*, 638(2):L101–L104.

[18] Aliu, E. e. a. (2009). Improving the performance of the single-dish Cherenkov telescope MAGIC through the use of signal timing. *Astroparticle Physics*, 30(6):293–305.

[19] Alves Batista, R. e. a. (2019). Open Questions in Cosmic-Ray Research at Ultrahigh Energies. *Frontiers in Astronomy and Space Sciences*, 6:23.

[20] Athanassoula, E. (1992). Morphology of bar orbits. *Monthly Notices of the Royal Astronomical Society*, 259:328–344.

[21] Bamba, A. and Williams, B. J. (2022). Supernova Remnants: Types and Evolution. In Bambi, C. and Sangangelo, A., editors, *Handbook of X-ray and Gamma-ray Astrophysics*, page 77.

[22] Bania, T. M. (1977). Carbon monoxide in the inner Galaxy. *The Astrophysical Journal*, 216:381–403.

[23] Bartels, R., Krishnamurthy, S., and Weniger, C. (2016). Strong Support for the Millisecond Pulsar Origin of the Galactic Center GeV Excess. *Physical Review Letters*, 116(5):051102.

[24] Beacom, J. F., Bell, N. F., and Mack, G. D. (2007). Upper Bound on the Dark Matter Total Annihilation Cross Section. *Physical Review Letters*, 99(23):231301.

[25] Berge, D., Funk, S., and Hinton, J. (2007). Background modelling in very-high-energy γ-ray astronomy. *Astron. & Astrophys.*, 466(3):1219–1229.

[26] Bergström, L. (2000). Non-baryonic dark matter: observational evidence and detection methods. *Reports on Progress in Physics*, 63(5):793–841.

[27] Bernlöhr, K. (2008). Simulation of imaging atmospheric Cherenkov telescopes with CORSIKA and sim_ telarray. *Astroparticle Physics*, 30(3):149–158.

[28] Bertram, E., Glover, S. C. O., Clark, P. C., Ragan, S. E., and Klessen, R. S. (2016). Synthetic observations of molecular clouds in a galactic centre environment - I. Studying maps of column density and integrated intensity. *Monthly Notices of the Royal Astronomical Society*, 455(4):3763–3778.

[29] Bi, B. e. a. (2022). Performance of the new FlashCam-based camera in the 28m telescope of H.E.S.S. In *37th International Cosmic Ray Conference*, page 743.

[30] Binney, J. and Tremaine, S. (2008). *Galactic Dynamics: Second Edition*.

[31] Blandford, R., Simeon, P., and Yuan, Y. (2014). Cosmic Ray Origins: An Introduction. *Nuclear Physics B Proceedings Supplements*, 256:9–22.

[32] Blumenthal, G. R. and Gould, R. J. (1970). Bremsstrahlung, Synchrotron Radiation, and Compton Scattering of High-Energy Electrons Traversing Dilute Gases. *Reviews of Modern Physics*, 42(2):237–271.

[33] Bose, D., Chitnis, V. R., Majumdar, P., and Acharya, B. S. (2022). Ground-based gamma-ray astronomy: history and development of techniques. *European Physical Journal Special Topics*, 231(1):3–26.

[34] Bradbury, S. (1999). The Very Energetic Radiation Imaging Telescope Array System (VERITAS). In Kieda, D., Salamon, M., and Dingus, B., editors, *26th International Cosmic Ray Conference (ICRC26), Volume 5*, volume 5 of *International Cosmic Ray Conference*, page 280.

[35] Bradford, C. M., Stacey, G. J., Nikola, T., Bolatto, A. D., Jackson, J. M., Savage, M. L., and Davidson, J. A. (2005). Warm Molecular Gas Traced with CO J = 7–>6 in the Galaxy's Central 2 Parsecs: Dynamical Heating of the Circumnuclear Disk. *The Astrophysical Journal*, 623(2):866–876.

[36] Breiman, L. (2001). Random Forests. *Machine Learning*, 45:5–32.

[37] Burkert, A. (1995). The Structure of Dark Matter Halos in Dwarf Galaxies. *The Astrophysical Journal*, 447:L25–L28.

[38] Calabretta, M. R. and Greisen, E. W. (2002). Representations of celestial coordinates in FITS. *Astron. & Astrophys.*, 395:1077–1122.

[39] Cao, Z. e. a. (2019). The Large High Altitude Air Shower Observatory (LHAASO) Science Book (2021 Edition). *arXiv e-prints*, page arXiv:1905.02773.

[40] Cao, Z. e. a. (2021). Ultrahigh-energy photons up to 1.4 petaelectronvolts from 12 γ-ray Galactic sources. *Nature*, 594(7861):33–36.

[41] Cao, Z. e. a. (2023). Measurement of Ultra-High-Energy Diffuse Gamma-Ray Emission of the Galactic Plane from 10 TeV to 1 PeV with LHAASO-KM2A. *Physical Review Letters*, 131(15):151001.

[42] Chalmé-Calvet, R. (2015). *Étalonnage du cinquième télescope de l'expérience H.E.S.S. et observation du Centre Galactique au delà de 30 GeV*. Theses, Université Pierre et Marie Curie - Paris VI.

[43] Chiappini, C. (2001). The Formation and Evolution of the Milky Way. *American Scientist*, 89(6):506.

[44] Ciurlo, A., Paumard, T., Rouan, D., and Clénet, Y. (2016). Hot molecular hydrogen in the central parsec of the Galaxy through near-infrared 3D fitting. *Astron. & Astrophys.*, 594:A113.

[45] Conte, F. (2024). *Gamma-ray emission and absorption in the inner few parsecs of the Galactic Centre*. Dissertation, Heidelberg University.

[46] Contopoulos, G. and Grosbol, P. (1989). Orbits in barred galaxies. *Astronomy and Astrophysics Review*, 1(3-4):261–289.

[47] Contreras, J. L., Satalecka, K., Bernlör, K., Boisson, C., Bregeon, J., Bulgarelli, A., De Cesare, G., de los Reyes, R., Fioretti, V., Kosack, K., Lavalley, C., Lyard, E., Marx, R., Rico, J., Sanguillot, M., Servillat, M., Walter, R., Ward, J. E., and Zoli, A. (2015). Data model issues in the Cherenkov Telescope Array project. In *34th International Cosmic Ray Conference (ICRC2015)*, volume 34 of *International Cosmic Ray Conference*, page 960.

[48] Cortina, J. (2005). Status and First Results of the Magic Telescope. *Astrophysics and Space Science*, 297(1-4):245–255.

[49] Csengeri, T. e. a. (2016). The ATLASGAL survey: distribution of cold dust in the Galactic plane. Combination with Planck data. *Astron. & Astrophys.*, 585:A104.

[50] CTAO Consortium (2023). Prospects for a survey of the Galactic plane with the Cherenkov Telescope Array. *arXiv e-prints*, page arXiv:2310.02828.

[51] Dahmen, G., Huttemeister, S., Wilson, T. L., and Mauersberger, R. (1998). Molecular gas in the Galactic center region. II. Gas mass and N_, = H_2/I_(12)CO conversion based on a C(18)O(J = 1 -> 0) survey. *Astron. & Astrophys.*, 331:959–976.

[52] de Boer, W., Bosse, L., Gebauer, I., Neumann, A., and Biermann, P. L. (2017). Molecular clouds as origin of the Fermi gamma-ray GeV excess. *Physical Review D*, 96(4):043012.

[53] de Naurois, M. and Rolland, L. (2009). A high performance likelihood reconstruction of γ-rays for imaging atmospheric Cherenkov telescopes. *Astroparticle Physics*, 32(5):231–252.

[54] Deason, A. J., Fattahi, A., Frenk, C. S., Grand, R. J. J., Oman, K. A., Garrison-Kimmel, S., Simpson, C. M., and Navarro, J. F. (2020). The edge of the Galaxy. *Monthly Notices of the Royal Astronomical Society*, 496(3):3929–3942.

[55] Dembinski, H. and et al., P. O. (2020). scikit-hep/iminuit.

[56] Dembinski, H. e. a. (2021). iminuit: Jupyter-friendly Python interface for C++ MINUIT2. Astrophysics Source Code Library, record ascl:2108.024.

[57] Di Sciascio, G. (2022). Measurement of Energy Spectrum and Elemental Composition of PeV Cosmic Rays: Open Problems and Prospects. *arXiv e-prints*, page arXiv:2202.11618.

[58] Do, T., Kerzendorf, W., Winsor, N., Støstad, M., Morris, M. R., Lu, J. R., and Ghez, A. M. (2015). Discovery of Low-metallicity Stars in the Central Parsec of the Milky Way. *The Astrophysical Journal*, 809(2):143.

[59] Donath, A. e. a. (2023). Gammapy: A Python package for gamma-ray astronomy. *Astron. & Astrophys.*, 678:A157.

[60] DuVernois, M. A. and Di Sciascio, G. (2022). Detecting Gamma-Rays with Moderate Resolution and Large Field of View: Particle Detector Arrays and Water Cherenkov Technique. In Bambi, C. and Sangangelo, A., editors, *Handbook of X-ray and Gamma-ray Astrophysics*, page 21.

[61] Ekers, R. D., van Gorkom, J. H., Schwarz, U. J., and Goss, W. M. (1983). The radio structure of SGR A. *Astron. & Astrophys.*, 122:143–150.

[62] Essig, R. e. a. (2013). Dark Sectors and New, Light, Weakly-Coupled Particles. *arXiv e-prints*, page arXiv:1311.0029.

[63] Ester, M., Kriegel, H.-P., Sander, J., and Xu, X. (1996). A Density-Based Algorithm for Discovering Clusters in Large Spatial Databases with Noise. In Pfitzner, D. W. and Salmon, J. K., editors, *Second International Conference on Knowledge Discovery and Data Mining (KDD'96). Proceedings of a conference held August 2-4*, pages 226–331.

[64] et al., A. H. (2009). Tmva - toolkit for multivariate data analysis.

[65] et al., A. N. (2015). Revealing the physical properties of molecular gas in orion with a large-scale survey in j = 2-1 lines of 12co, 13co, and c18o. *The Astrophysical Journal Supplement Series*, 216(1):18.

[66] et al., F. P. (2018). Scikit-learn: Machine learning in python.

[67] et al., T. S. (1999). A co(j=2-1) line survey of the galactic center. *Advances in Space Research*, 23(5):985–989. The AGN/Normal Galaxy.

[68] Evans, R. D. and Beiser, A. (1956). The atomic nucleus. *Physics Today*, 9(12):33–34.

[69] Event Horizon Telescope Collaboration (2022). First Sagittarius A* Event Horizon Telescope Results. I. The Shadow of the Supermassive Black Hole in the Center of the Milky Way. *The Astrophysical Journal*, 930(2):L12.

[70] Fegan, D. J. (1997). /hadron separation at tev energies. *Journal of Physics G: Nuclear and Particle Physics*, 23(9):1013.

[71] Ferrière, K. (2012). Interstellar gas within ∼10 pc of Sagittarius A*. *Astron. & Astrophys.*, 540:A50.

[72] Ferrière, K., Gillard, W., and Jean, P. (2007). Spatial distribution of interstellar gas in the innermost 3 kpc of our galaxy. *Astron. & Astrophys.*, 467(2):611–627.

[73] Finkbeiner, D. P., Davis, M., and Schlegel, D. J. (1999). Extrapolation of Galactic Dust Emission at 100 Microns to Cosmic Microwave Background Radiation Frequencies Using FIRAS. *The Astrophysical Journal*, 524(2):867–886.

[74] Gabici, S. (2024). Star clusters as cosmic ray accelerators. In *7th Heidelberg International Symposium on High-Energy Gamma-Ray Astronomy*, page 16.

[75] Gaug, M., Fegan, S., Mitchell, A. M. W., Maccarone, M. C., Mineo, T., and Okumura, A. (2019). Using Muon Rings for the Calibration of the Cherenkov Telescope Array: A Systematic Review of the Method and Its Potential Accuracy. *Astrophysical Journal Supplement*, 243(1):11.

[76] Genzel, R., Eisenhauer, F., and Gillessen, S. (2010). The Galactic Center massive black hole and nuclear star cluster. *Reviews of Modern Physics*, 82(4):3121–3195.

[77] Giavitto, G. e. a. (2015). A major electronics upgrade for the H.E.S.S. Cherenkov telescopes 1-4. In *34th International Cosmic Ray Conference (ICRC2015)*, volume 34 of *International Cosmic Ray Conference*, page 996.

[78] Ginzburg, V. L. and Syrovatskii, S. I. (1964). *The Origin of Cosmic Rays*.

[79] G oksu, H. (2024). *The Southern Wide-field Gamma-ray Observatory: The Lake Approach and the Pulsar Wind Nebula HESS J1825-137* . Dissertation, Friedrich-Alexander-Universität Erlangen-Nürnberg (FAU).

[80] Goksu, H., Hofmann, W., Werner, F., Haist, F., and Hinton, J. (2025). Instrumenting a lake as a wide-field gamma-ray detector. *Nuclear Instruments and Methods in Physics Research A*, 1076:170450.

[81] Gong, M., Ostriker, E. C., and Kim, C.-G. (2018). The X $_{CO}$ Conversion Factor from Galactic Multiphase ISM Simulations. *The Astrophysical Journal*, 858(1):16.

[82] Gong, M., Ostriker, E. C., Kim, C.-G., and Kim, J.-G. (2020). The Environmental Dependence of the X_{CO} Conversion Factor. *The Astrophysical Journal*, 903(2):142.

[83] Goodenough, L. and Hooper, D. (2009). Possible Evidence For Dark Matter Annihilation In The Inner Milky Way From The Fermi Gamma Ray Space Telescope. *arXiv e-prints*, page arXiv:0910.2998.

[84] Goodwin, S. P., Gribbin, J., and Hendry, M. A. (1998). The relative size of the Milky Way. *The Observatory*, 118:201–208.

[85] Górski, K. M., Hivon, E., Banday, A. J., Wandelt, B. D., Hansen, F. K., Reinecke, M., and Bartelmann, M. (2005). HEALPix: A Framework for High-Resolution Discretization and Fast Analysis of Data Distributed on the Sphere. *The Astrophysical Journal*, 622(2):759–771.

[86] GRAVITY Collaboration (2019). A geometric distance measurement to the Galactic center black hole with 0.3% uncertainty. *Astron. & Astrophys.*, 625:L10.

[87] Guesten, R., Genzel, R., Wright, M. C. H., Jaffe, D. T., Stutzki, J., and Harris, A. I. (1987). Aperture Synthesis Observations of the Circumnuclear Ring in the Galactic Center. *The Astrophysical Journal*, 318:124.

[88] H. E. S. S. Collaboration (2016). Acceleration of petaelectronvolt protons in the Galactic Centre. *Nature*, 531(7595):476–479.

[89] H. E. S. S. Collaboration (2018). Characterising the VHE diffuse emission in the central 200 parsecs of our Galaxy with H.E.S.S. *Astron. & Astrophys.*, 612:A9.

[90] Habart, E., Walmsley, M., Verstraete, L., Cazaux, S., Maiolino, R., Cox, P., Boulanger, F., and Pineau des Forêts, G. (2005). Molecular Hydrogen. *Space Science Reviews*, 119(1-4):71–91.

[91] HAWC Collaboration (2013). The HAWC Gamma-Ray Observatory: Observations of Cosmic Rays. *arXiv e-prints*, page arXiv:1310.0072.

[92] Hayashi, K., Okamoto, R., Yamamoto, H., Hayakawa, T., Tachihara, K., and Fukui, Y. (2019). Gas and Dust Properties in the Chamaeleon Molecular Cloud Complex Based on the Optically Thick H I. *The Astrophysical Journal*, 878(2):131.

[93] He, H. and Lhaaso Collaboration (2018). Design of the LHAASO detectors. *Radiation Detection Technology and Methods*, 2(1):7.

[94] Heck, D., Knapp, J., Capdevielle, J. N., Schatz, G., and Thouw, T. (1998). *CORSIKA: a Monte Carlo code to simulate extensive air showers.*

[95] Henshaw, J. D., Barnes, A. T., Battersby, C., Ginsburg, A., Sormani, M. C., and Walker, D. L. (2023). Star Formation in the Central Molecular Zone of the Milky Way. In Inutsuka, S., Aikawa, Y., Muto, T., Tomida, K., and Tamura, M., editors, *Protostars and Planets VII*, volume 534 of *Astronomical Society of the Pacific Conference Series*, page 83.

[96] Hess, V. (2018). On the Observations of the Penetrating Radiation during Seven Balloon Flights. *arXiv e-prints*, page arXiv:1808.02927.

[97] Heywood, I. e. a. (2022). The 1.28 GHz MeerKAT Galactic Center Mosaic. *The Astrophysical Journal*, 925(2):165.

[98] Hillas, A. M. (1984). The Origin of Ultra-High-Energy Cosmic Rays. *Annual Review of Astronomy and Astrophysics*, 22:425–444.

[99] Hillas, A. M. (1985). Cerenkov Light Images of EAS Produced by Primary Gamma Rays and by Nuclei. In Jones, F. C., editor, *19th International Cosmic Ray Conference (ICRC19), Volume 3*, volume 3 of *International Cosmic Ray Conference*, page 445.

[100] Hinton, J. A. and HESS Collaboration (2004). The status of the HESS project. *New Astronomy Reviews*, 48(5-6):331–337.

[101] Hinton, J. A. and Hofmann, W. (2009). Teraelectronvolt Astronomy. *Annual Review of Astronomy and Astrophysics*, 47(1):523–565.

[102] Hofmann, W. and H. E. S. S. Collaboration (2003). Status of the H.E.S.S. Project. In *International Cosmic Ray Conference*, volume 5 of *International Cosmic Ray Conference*, page 2811.

[103] Holler, M., Berge, D., van Eldik, C., Lenain, J. P., Marandon, V., Murach, T., de Naurois, M., Parsons, R. D., Prokoph, H., and Zaborov, D. (2015). Observations of the Crab Nebula with H.E.S.S. Phase II. *arXiv e-prints*, page arXiv:1509.02902.

[104] Hooper, D. and Linden, T. (2011). Origin of the gamma rays from the Galactic Center. *Physical Review D*, 84(12):123005.

[105] Hu, C.-Y., Schruba, A., Sternberg, A., and van Dishoeck, E. F. (2022). Dependence of X $_{CO}$ on Metallicity, Intensity, and Spatial Scale in a Self-regulated Interstellar Medium. *The Astrophysical Journal*, 931(1):28.

[106] Huentemeyer, P., BenZvi, S., Dingus, B., Fleischhack, H., Schoorlemmer, H., and Weisgarber, T. (2019). The Southern Wide-Field Gamma-Ray Observatory (SWGO): A Next-Generation Ground-Based Survey Instrument. In *Bulletin of the American Astronomical Society*, volume 51, page 109.

[107] Hughes, J. P. (1999). The Extraordinarily Rapid Expansion of the X-Ray Remnant of Kepler's Supernova (SN 1604). *The Astrophysical Journal*, 527(1):298–309.

[108] Indriolo, N. e. a. (2015). Herschel Survey of Galactic OH^+, H_2O^+, and H_3O^+: Probing the Molecular Hydrogen Fraction and Cosmic-Ray Ionization Rate. *The Astrophysical Journal*, 800(1):40.

[109] Jones, P. A. e. a. (2012). Spectral imaging of the Central Molecular Zone in multiple 3-mm molecular lines. *Monthly Notices of the Royal Astronomical Society*, 419(4):2961–2986.

[110] Kaluza, T. (2018). On the Unification Problem in Physics. *International Journal of Modern Physics D*, 27(14):1870001.

[111] Kamionkowski, M., Koushiappas, S. M., and Kuhlen, M. (2010). Galactic substructure and dark-matter annihilation in the Milky Way halo. *Physical Review D*, 81(4):043532.

[112] Kaneko, T. e. a. (1983). Acoustic and Vlf-Elf Radio Detections of Super Giant Air Showers. In *International Cosmic Ray Conference*, volume 11 of *International Cosmic Ray Conference*, page 428.

[113] Khlopov, M. Y. (2010). Primordial black holes. *Research in Astronomy and Astrophysics*, 10(6):495–528.

[114] Köhler, M., Ysard, N., and Jones, A. P. (2015). Dust evolution in the transition towards the denser ISM: impact on dust temperature, opacity, and spectral index. *Astron. & Astrophys.*, 579:A15.

[115] Kohno, M. and Sofue, Y. (2024). The CO-to-H_2 conversion factor in the Central Molecular Zone of the Milky Way using CO isotopologues. *Publications of the Astronomical Society of Japan*, 76(4):579–588.

[116] Kosack, K. and et al. (2004). Tev gamma-ray observations of the galactic center. *The Astrophysical Journal*, 608(2):L97.

[117] Krayzel, F. e. a. (2013). Improved sensitivity of H.E.S.S.-II through the fifth telescope focus system. In *33rd International Cosmic Ray Conference (ICRC2013)*, Rio de Janeiro, Brazil. In Proceedings of the 33rd International Cosmic Ray Conference (ICRC2013), Rio de Janeiro (Brazil).

[118] Lau, R. M., Herter, T. L., Morris, M. R., Becklin, E. E., and Adams, J. D. (2013). SOFIA/FORCAST Imaging of the Circumnuclear Ring at the Galactic Center. *The Astrophysical Journal*, 775(1):37.

[119] Le Petit, F., Ruaud, M., Bron, E., Godard, B., Roueff, E., Languignon, D., and Le Bourlot, J. (2016). Physical conditions in the central molecular zone inferred by H_3^+. *Astron. & Astrophys.*, 585:A105.

[120] Lee, S. K., Lisanti, M., Safdi, B. R., Slatyer, T. R., and Xue, W. (2016). Evidence for Unresolved γ -Ray Point Sources in the Inner Galaxy. *Physical Review Letters*, 116(5):051103.

[121] Lefranc, V. (2016). *Recherche de matière noire, observation du centre galactique avec H.E.S.S.et modernisation des caméras de H.E.S.S. I.* Theses, Université Paris Saclay (COmUE).

[122] Lemoine-Goumard, M., Degrange, B., and Tluczykont, M. (2006). Selection and 3d-reconstruction of gamma-ray-induced air showers with a stereoscopic system of atmospheric cherenkov telescopes. *Astroparticle Physics*, 25(3):195–211.

[123] Leroy, A. K. e. a. (2017). Millimeter-wave Line Ratios and Sub-beam Volume Density Distributions. *The Astrophysical Journal*, 835(2):217.

[124] Levin, Y. and Beloborodov, A. M. (2003). Stellar Disk in the Galactic Center: A Remnant of a Dense Accretion Disk? *The Astrophysical Journal*, 590(1):L33–L36.

[125] Lhaaso Collaboration (2021). Peta-electron volt gamma-ray emission from the Crab Nebula. *Science*, 373:425–430.

[126] Ma, X.-H. e. a. (2022). Chapter 1 LHAASO Instruments and Detector technology. *Chinese Physics C*, 46(3):030001.

[127] MAGIC Collaboration (2020). MAGIC observations of the diffuse γ-ray emission in the vicinity of the Galactic center. *Astron. & Astrophys.*, 642:A190.

[128] Maier, G. and Knapp, J. (2007). Cosmic-ray events as background in imaging atmospheric Cherenkov telescopes. *Astroparticle Physics*, 28(1):72–81.

[129] Mayer-Hasselwander, H. A., Bertsch, D. L., Dingus, B. L., Eckart, A., Esposito, J. A., Genzel, R., Hartman, R. C., Hunter, S. D., Kanbach, G., Kniffen, D. A., Lin, Y. C., Michelson, P. F., Muecke, A., von Montigny, C., Mukherjee, R., Nolan, P. L., Pohl, M., Reimer, O., Schneid, E. J., Sreekumar, P., and Thompson, D. J. (1998). High-energy gamma-ray emission from the Galactic Center. *Astron. & Astrophys.*, 335:161–172.

[130] McClure-Griffiths, N. M., Dickey, J. M., Gaensler, B. M., Green, A. J., Green, J. A., and Haverkorn, M. (2012). The Australia Telescope Compact Array H I Survey of the Galactic Center. *Astrophysical Journal Supplement*, 199(1):12.

[131] Meisner, A. M. and Finkbeiner, D. P. (2015). Modeling Thermal Dust Emission with Two Components: Application to the Planck High Frequency Instrument Maps. *The Astrophysical Journal*, 798(2):88.

[132] Merle, A. (2017). keV sterile neutrino Dark Matter. *arXiv e-prints*, page arXiv:1702.08430.

[133] Mills, E. A. C. (2017). The Milky Way's Central Molecular Zone. *arXiv e-prints*, page arXiv:1705.05332.

[134] Mitchell, A. M. W., Dembinski, H. P., and Parsons, R. D. (2019). Potential for measuring the longitudinal and lateral profile of muons in TeV air showers with IACTs. *Astroparticle Physics*, 111:23–34.

[135] Mohrmann, L., Specovius, A., Tiziani, D., Funk, S., Malyshev, D., Nakashima, K., and van Eldik, C. (2019). Validation of open-source science tools and background model construction in γ-ray astronomy. *Astron. & Astrophys.*, 632:A72.

[136] Molinari, S. e. a. (2011). A 100 pc Elliptical and Twisted Ring of Cold and Dense Molecular Clouds Revealed by Herschel Around the Galactic Center. *The Astrophysical Journal*, 735(2):L33.

[137] Molinari, S. e. a. (2016). Hi-GAL, the Herschel infrared Galactic Plane Survey: photometric maps and compact source catalogues. First data release for the inner Milky Way: $+68° \geq l \geq -70°$. *Astron. & Astrophys.*, 591:A149.

[138] Montanari, A. (2022). *Study of the Galactic Center and Search for Dark Matter with the H.E.S.S. Inner Galaxy Survey*. Theses, Université Paris-Saclay.

[139] Montanari, A., Moulin, E., and Malyshev, D. (2021). Search for dark matter annihilation signals from the Galactic Center with the H.E.S.S. Inner Galaxy Survey. *arXiv e-prints*, page arXiv:2108.10302.

[140] Murchikova, E. M., Phinney, E. S., Pancoast, A., and Blandford, R. D. (2019). A cool accretion disk around the Galactic Centre black hole. *Nature*, 570(7759):83–86.

[141] Navarro, J. F., Frenk, C. S., and White, S. D. M. (1997). A Universal Density Profile from Hierarchical Clustering. *The Astrophysical Journal*, 490(2):493–508.

[142] Nigro, C. (2019). *Study of Persistent and Flaring Gamma-Ray Emission from Active Galactic Nuclei with the MAGIC Telescopes and Prospects for Future Open Data Formats in Gamma-Ray Astronomy*. PhD thesis, Humboldt-Universität zu Berlin, Mathematisch-Naturwissenschaftliche Fakultät.

[143] Nigro, C., Hassan, T., and Olivera-Nieto, L. (2021). Evolution of Data Formats in Very-High-Energy Gamma-Ray Astronomy. *Universe*, 7(10):374.

[144] Nilles, H. P. (1984). Supersymmetry, supergravity and particle physics. *Physics Reports*, 110(1-2):1–162.

[145] Ohm, S., van Eldik, C., and Egberts, K. (2009). γ/hadron separation in very-high-energy γ-ray astronomy using a multivariate analysis method. *Astroparticle Physics*, 31(5):383–391.

[146] Oka, T., Geballe, T. R., Goto, M., Usuda, T., Benjamin, McCall, J., and Indriolo, N. (2019). The Central 300 pc of the Galaxy Probed by Infrared Spectra of H_3^+ and CO. I. Predominance of Warm and Diffuse Gas and High H_2 Ionization Rate. *The Astrophysical Journal*, 883(1):54.

[147] Oka, T., Hasegawa, T., Hayashi, M., Handa, T., and Sakamoto, S. (1998). CO (J = 2–1) Line Observations of the Galactic Center Molecular Cloud Complex. II. Dynamical Structure and Physical Conditions. *The Astrophysical Journal*, 493(2):730–761.

[148] Oka, T., Nagai, M., Kamegai, K., and Tanaka, K. (2011). A New Look at the Galactic Circumnuclear Disk. *The Astrophysical Journal*, 732(2):120.

[149] Okamoto, R., Yamamoto, H., Tachihara, K., Hayakawa, T., Hayashi, K., and Fukui, Y. (2017). H I, CO, and Dust in the Perseus Cloud. *The Astrophysical Journal*, 838(2):132.

[150] Olivera-Nieto, L., Mitchell, A. M. W., Bernlöhr, K., and Hinton, J. A. (2021). Muons as a tool for background rejection in imaging atmospheric Cherenkov telescope arrays. *European Physical Journal C*, 81(12):1101.

[151] Olivera-Nieto, L., Ren, H. X., Mitchell, A. M. W., Marandon, V., and Hinton, J. A. (2022). Background rejection using image residuals from large telescopes in imaging atmospheric Cherenkov telescope arrays. *European Physical Journal C*, 82(12):1118.

[152] Omont, A. (2007). Molecules in galaxies. *Reports on Progress in Physics*, 70(7):1099.

[153] Paré, D., Butterfield, N. O., Chuss, D. T., Guerra, J. A., Iuliano, J. I., Karpovich, K., Morris, M. R., and Wollack, E. J. (2024). SOFIA/HAWC+ Far-infrared Polarimetric Large-area CMZ Exploration Survey. III. Full Survey Data Set. *The Astrophysical Journal*, 969(2):150.

[154] Parsons, R. D. and Hinton, J. A. (2014). A Monte Carlo template based analysis for air-Cherenkov arrays. *Astroparticle Physics*, 56:26–34.

[155] Peñaloza, C. H., Clark, P. C., Glover, S. C. O., Shetty, R., and Klessen, R. S. (2016). Using co line ratios to trace the physical properties of molecular clouds. *Monthly Notices of the Royal Astronomical Society*, 465(2):2277–2285.

[156] Peron, G., Morlino, G., Gabici, S., Amato, E., Purushothaman, A., and Brusa, M. (2024). On the Correlation between Young Massive Star Clusters and Gamma-Ray Unassociated Sources. *The Astrophysical Journal*, 972(2):L22.

[157] Petry, D. e. a. (1996). Detection of VHE γ-rays from MKN 421 with the HEGRA Cherenkov Telescopes. *Astron. & Astrophys.*, 311:L13–L16.

[158] Pierre Auger Collaboration (2008). The surface detector system of the Pierre Auger Observatory. *Nuclear Instruments and Methods in Physics Research A*, 586(3):409–420.

[159] Planck Collaboration (2014a). Planck 2013 results. XI. All-sky model of thermal dust emission. *Astron. & Astrophys.*, 571:A11.

[160] Planck Collaboration (2014b). Planck 2013 results. XIII. Galactic CO emission. *Astron. & Astrophys.*, 571:A13.

[161] Planck Collaboration (2020). Planck 2018 results. VI. Cosmological parameters. *Astron. & Astrophys.*, 641:A6.

[162] Planck Collaboration and Fermi Collaboration (2015). Planck intermediate results. XXVIII. Interstellar gas and dust in the Chamaeleon clouds as seen by Fermi LAT and Planck. *Astron. & Astrophys.*, 582:A31.

[163] Ponti, G., Hofmann, F., Churazov, E., Morris, M. R., Haberl, F., Nandra, K., Terrier, R., Clavel, M., and Goldwurm, A. (2019). An X-ray chimney extending hundreds of parsecs above and below the Galactic Centre. *Nature*, 567(7748):347–350.

[164] Predehl, P. e. a. (2020). Detection of large-scale X-ray bubbles in the Milky Way halo. *Nature*, 588(7837):227–231.

[165] Punch, M. e. a. (1992). Detection of TeV photons from the active galaxy Markarian 421. *Nature*, 358(6386):477–478.

[166] Ramana-Murthy, P. V., Wolfendale, A. W., and Watson, A. (1994). Gamma-Ray Astronomy - ED.2. *The Observatory*, 114:36.

[167] Ravikularaman, S. (2024). *Les interactions de rayons cosmiques dans le centre galactique*. PhD thesis, Université Paris Cité. Thèse de doctorat dirigée par Gabici, Stefano et Goldwurm, Andrea Physique Université Paris Cité 2024.

[168] Reach, W. T. e. a. (1995). Far-Infrared Spectral Observations of the Galaxy by COBE. *The Astrophysical Journal*, 451:188.

[169] Remy, Q. (2016). *Traceurs de gaz et de poussières du milieu interstellaire local*. Theses, Université Sorbonne Paris Cité.

[170] Remy, Q., Grenier, I. A., Marshall, D. J., and Casandjian, J. M. (2017). Cosmic rays, gas and dust in nearby anticentre clouds. I. CO-to-H_2 conversion factors and dust opacities. *Astron. & Astrophys.*, 601:A78.

[171] Ren, H. X., e. a. (2024). Galactic Centre with a Southern Wide Field-of-view Gamma-ray Observatory. In *38th International Cosmic Ray Conference*, page 893.

[172] Ren, H. X. and Olivera-Nieto, L. and Mitchell, A. M. W. and Marandon, V. and Hinton, J. A. (2022). Algorithm for Background Rejection using Image Residuals. volume submitted.

[173] Ren, H. X., Remy, Q., Ravikularaman, S., Bouyahiaoui, M., Conte, F., and Djuvsland, J. (2025). Cosmic rays, gas and dust in the central molecular zone i – x_{CO} factors, cosmic-ray densities and dust opacities.

[174] Ren, H. X. e. a. (2025). The Galactic Center as seen by the Southern Wide field-of-view Gamma-ray Observatory. In *Memorie della Societa Astronomica Italiana*, volume submitted.

[175] Rinchiuso, L., Moulin, E., Viana, A., Van Eldik, C., and Veh, J. (2017). Dark matter gamma-ray line searches toward the Galactic Center halo with H.E.S.S. I. *arXiv e-prints*, page arXiv:1708.08358.

[176] Roman-Duval, J., Heyer, M., Brunt, C. M., Clark, P., Klessen, R., and Shetty, R. (2016). Distribution and Mass of Diffuse and Dense CO Gas in the Milky Way. *The Astrophysical Journal*, 818(2):144.

[177] Roy, A., Martin, P. G., Polychroni, D., Bontemps, S., Abergel, A., André, P., Arzoumanian, D., Di Francesco, J., Hill, T., Konyves, V., Nguyen-Luong, Q., Pezzuto, S., Schneider, N., Testi, L., and White, G. (2013). Changes of Dust Opacity with Density in the Orion A Molecular Cloud. *The Astrophysical Journal*, 763(1):55.

[178] Rubin, V. C. (1983). Dark matter in spiral galaxies. *Scientific American*, 248:96–106.

[179] Sawada, T., Hasegawa, T., Handa, T., and Cohen, R. J. (2004). A molecular face-on view of the Galactic Centre region. *Monthly Notices of the Royal Astronomical Society*, 349(4):1167–1178.

[180] Schödel, R., Eckart, A., Alexander, T., Merritt, D., Genzel, R., Sternberg, A., Meyer, L., Kul, F., Moultaka, J., Ott, T., and Straubmeier, C. (2007). The structure of the nuclear stellar cluster of the Milky Way. *Astron. & Astrophys.*, 469(1):125–146.

[181] Schödel, R., Merritt, D., and Eckart, A. (2009). The nuclear star cluster of the Milky Way: proper motions and mass. *Astron. & Astrophys.*, 502(1):91–111.

[182] Schödel, R., Ott, T., Genzel, R., Eckart, A., Mouawad, N., and Alexander, T. (2003). Stellar Dynamics in the Central Arcsecond of Our Galaxy. *The Astrophysical Journal*, 596(2):1015–1034.

[183] Schoenfelder, V. e. a. (1993). Instrument Description and Performance of the Imaging Gamma-Ray Telescope COMPTEL aboard the Compton Gamma-Ray Observatory. *Astrophysical Journal Supplement*, 86:657.

[184] Schuller, F. e. a. (2021). The SEDIGISM survey: First Data Release and overview of the Galactic structure. *Monthly Notices of the Royal Astronomical Society*, 500(3):3064–3082.

[185] Shaffer, T. M., Pratt, E. C., and Grimm, J. (2017). Utilizing the power of cerenkov light with nanotechnology. *Nature Nanotechnology*, 12(106-117).

[186] Shayduk, M. and Consortium, C. (2013). Optimized Next-neighbour Image Cleaning Method for Cherenkov Telescopes. In *International Cosmic Ray Conference*, volume 33 of *International Cosmic Ray Conference*, page 3000.

[187] Shen, J. and Zheng, X.-W. (2020). The bar and spiral arms in the Milky Way: structure and kinematics. *Research in Astronomy and Astrophysics*, 20(10):159.

[188] Shirley, Y. L. (2015). The Critical Density and the Effective Excitation Density of Commonly Observed Molecular Dense Gas Tracers. *Publications of the Astronomical Society of the Pacific*, 127(949):299.

[189] Shull, J. M. (2022). Observing interstellar molecular hydrogen. *Physics Today*, 75(12):12–12.

[190] Smith, A. J. (2010). A Survey of Fermi Catalog Sources using data from the Milagro Gamma-Ray Observatory. *arXiv e-prints*, page arXiv:1001.3695.

[191] Sofue, Y. (2017). Optical thickness, spin temperature and correction factor for the density of Galactic H I gas. *Monthly Notices of the Royal Astronomical Society*, 468(4):4030–4038.

[192] Sofue, Y. (2022). Three-dimensional structure of the central molecular zone. *Monthly Notices of the Royal Astronomical Society*, 516(1):907–923.

[193] Solanki, S., Ressler, S. M., Murchikova, L., Stone, J. M., and Morris, M. R. (2023). The Inner 2 pc of Sagittarius A*: Simulations of the Circumnuclear Disk and Multiphase Gas Accretion in the Galactic Center. *The Astrophysical Journal*, 953(1):22.

[194] Solomon, P. M. and Wickramasinghe, N. C. (1969). Molecular and Solid Hydrogen in Dense Interstellar Clouds. *The Astrophysical Journal*, 158:449.

[195] Springel, V., White, S. D. M., Frenk, C. S., Navarro, J. F., Jenkins, A., Vogelsberger, M., Wang, J., Ludlow, A., and Helmi, A. (2008). Prospects for detecting supersymmetric dark matter in the Galactic halo. *Nature*, 456(7218):73–76.

[196] Stecker, F. W. (1975). On the Origin of Cosmic Rays. In *International Cosmic Ray Conference*, volume 1 of *International Cosmic Ray Conference*, page 70.

[197] Steinmassl, S. F. (2023). *Probing particle acceleration in stellar binary systems using gamma-ray observations*. Dissertation, Heidelberg University.

[198] Su, M., Slatyer, T. R., and Finkbeiner, D. P. (2010). Giant gamma-ray bubbles from fermi-lat: Active galactic nucleus activity or bipolar galactic wind? *The Astrophysical Journal*, 724(2):1044.

[199] Su, M., Slatyer, T. R., and Finkbeiner, D. P. (2010). Giant Gamma-ray Bubbles from Fermi-LAT: Active Galactic Nucleus Activity or Bipolar Galactic Wind? *The Astrophysical Journal*, 724(2):1044–1082.

[200] Tanimori, T. (1998a). Detection of TeV Gamma Rays from SN1006. In Koyama, K., Kitamoto, S., and Itoh, M., editors, *The Hot Universe*, volume 188 of *IAU Symposium*, page 121.

[201] Tanimori, T. e. a. (1998b). Detection of Gamma Rays of up to 50 TeV from the Crab Nebula. *The Astrophysical Journal*, 492(1):L33–L36.

[202] Tibaldo, L., Gaggero, D., and Martin, P. (2021). Gamma Rays as Probes of Cosmic-Ray Propagation and Interactions in Galaxies. *Universe*, 7(5):141.

[203] Tokuyama, S., Oka, T., Takekawa, S., Iwata, Y., Tsujimoto, S., Yamada, M., Furusawa, M., and Nomura, M. (2019). High-resolution CO images of the Galactic central molecular zone. *Publications of the Astronomical Society of Japan*, 71:S19.

[204] Tomsick, J. and COSI Collaboration (2022). The Compton Spectrometer and Imager Project for MeV Astronomy. In *37th International Cosmic Ray Conference*, page 652.

[205] Tricco, T. S., Price, D. J., and Laibe, G. (2017). Is the dust-to-gas ratio constant in molecular clouds? *Monthly Notices of the Royal Astronomical Society*, 471(1):L52–L56.

[206] Tsuboi, M., Handa, T., and Ukita, N. (1999). Dense Molecular Clouds in the Galactic Center Region. I. Observations and Data. *Astrophysical Journal Supplement*, 120(1):1–39.

[207] Tsuboi, M., Kitamura, Y., Uehara, K., Miyawaki, R., Tsutsumi, T., Miyazaki, A., and Miyoshi, M. (2017). ALMA View of the Galactic Center Minispiral: Ionized Gas Flows around Sagittarius A*. *The Astrophysical Journal*, 842(2):94.

[208] Tsuchiya, K. e. a. (2004). Detection of sub-tev gamma rays from the galactic center direction by cangaroo-ii. *The Astrophysical Journal*, 606(2):L115.

[209] Vacanti, G., Fleury, P., Jiang, Y., Paré, E., Rovero, A. C., Sarazin, X., Urban, M., and Weekes, T. C. (1994). Muon ring images with an atmospheric Čerenkov telescope. *Astroparticle Physics*, 2(1):1–11.

[210] Viana, A., Schoorlemmer, H., Albert, A., de Souza, V., Harding, J. P., and Hinton, J. (2019). Searching for dark matter in the Galactic halo with a wide field of view TeV gamma-ray observatory in the Southern Hemisphere. *JCAP*, 2019(12):061.

[211] Völk, H. J. and Bernlöhr, K. (2009). Imaging very high energy gamma-ray telescopes. *Experimental Astronomy*, 25(1-3):173–191.

[212] Wagner, R. M. (2006). *Measurement of very high energy gamma-ray emission from four blazars using the MAGIC telescope and a comparative blazar study*. PhD thesis, Max-Planck-Institute for Physics, Munich.

[213] Wakelam, V. e. a. (2017). H_2 formation on interstellar dust grains: The viewpoints of theory, experiments, models and observations. *Molecular Astrophysics*, 9:1–36.

[214] Weekes, T. C. e. a. (1989). Observation of TeV Gamma Rays from the Crab Nebula Using the Atmospheric Cerenkov Imaging Technique. *The Astrophysical Journal*, 342:379.

[215] Werner, F. and Nellen, L. (2021). Technological options for the Southern Wide-field Gamma-ray Observatory (SWGO) and current design status. In *Proceedings of 37th International Cosmic Ray Conference — PoS(ICRC2021)*, volume 395, page 714.

[216] Wong, Y. W. (2023). *Diffuse Gamma-Ray Emission from the Galactic Centre with H.E.S.S.* Dissertation, Friedrich-Alexander-Universität Erlangen-Nürnberg (FAU).

[217] Yan, Q.-Z., Walsh, A. J., Dawson, J. R., Macquart, J. P., Blackwell, R., Burton, M. G., Rowell, G. P., Zhang, B., Xu, Y., Tang, Z.-H., and Hancock, P. J. (2017). Towards a three-dimensional distribution of the molecular clouds in the Galactic Centre. *Monthly Notices of the Royal Astronomical Society*, 471(3):2523–2536.

[218] Yelda, S., Ghez, A. M., Lu, J. R., Do, T., Meyer, L., Morris, M. R., and Matthews, K. (2014). Properties of the Remnant Clockwise Disk of Young Stars in the Galactic Center. *The Astrophysical Journal*, 783(2):131.

[219] Yodh, G. B. (1997). The MILAGRO Gamma Ray Observatory. *Nuclear Physics B Proceedings Supplements*, 52(3):264–268.

[220] Ysard, N., Koehler, M., Jimenez-Serra, I., Jones, A. P., and Verstraete, L. (2019). From grains to pebbles: the influence of size distribution and chemical composition on dust emission properties. *Astron. & Astrophys.*, 631:A88.

[221] Zhao, J.-H., Morris, M. R., Goss, W. M., and An, T. (2009). Dynamics of Ionized Gas at the Galactic Center: Very Large Array Observations of the Three-dimensional Velocity Field and Location of the Ionized Streams in Sagittarius A West. *The Astrophysical Journal*, 699(1):186–214.

[222] Zwicky, F. (1937). On the Masses of Nebulae and of Clusters of Nebulae. *The Astrophysical Journal*, 86:217.

List of Figures

List of Tables

Acknowledgements

I would like to express my heartfelt gratitude to my supervisor, Prof. Dr. Jim Hinton, for giving me the opportunity to work in this excellent research group in the Max Planck Institute for Nuclear Physics. Thank you for selecting me as your PhD student and for offering me such a fascinating topic. For being so supportive always, and for giving me all those inspiring ideas. We were very optimistic and ambitious, at te beginning, aiming to study many aspects of the Galactic Centre. Although the scope of the thesis eventually shifted, I remain enthusiastic about continuing in this field and pursuing our original goals.

My deepest thanks go to Dr. Julia Djuvsland, for always being there to listen, for guiding me in the field of dark matter studies, something completely new to me and for our many enriching discussions. Thank you for your patience in proof-reading my thesis, publications, and proceedings, and for your nice suggestions at every step.

I am very grateful to Prof. Dr. Simon Glover for being part of my thesis committee and for his support in inviting expert Professors in the field of the Galactic Centre to our MPIK meeting. I also thank you sincerely for agreeing to referee this thesis.

Special thanks to Dr. Teresa Marrodan Undagoitia and Prof. Dr. Tilman Plehn for kindly agreeing to be part of my examination committee.

I am deeply thankful to Dr. Quentin Remy for introducing me to the field of gas and dust observations, and for guiding me in using `Gammapy`. Thank you also for proof-reading parts of my thesis and for your continuous support.

I also want to thank Dr. Sruthiranjani Ravikularaman, Dr. Makarim Bouyahiaoui, and Dr. Francesco Conte for the collaborative work, stimulating discussions, and all the help throughout.

I would like thank Dr. Richard Tuffs for your valuable advice and insights into gas and dust emissions in the Galactic Centre.

A big thank to Dr. Brian Reville for patiently explaining all the theoretical questions I had, and for your advice and inspiring ideas.

I am also very grateful to Dr. Vincent Marandon for helping me understand the HAP framework, and to Lars Mohrmann for your continuous technical support.

My thanks extend to all colleagues in the group for creating such a supportive and enjoyable environment. Many thanks to Dr. Laura Olivera-Nieto for the guidance you gave me from the day I started my PhD, for all the support, and for proof-reading parts of my thesis. Thank you, Dr. Hazal Goksu, for proof-reading through a chapter of my thesis and for always inviting me to join fun social activities, including dancing and kickboxing! Special thanks to Dr. Davide Depaoli and Isabella Sofia for the wonderful lunch breaks! Thanks also to Dr. Mischa Breuhaus, for being my first German friend. Many thanks to Dr. Felix Werner for proof-reading the abstract and helping me with the German version of it. Sincere thanks to Ruth Crespo for helping me settle in Heidelberg and for guiding me through visa applications for my work trips.

Outside work, I would like to thank my friends. A warm hug to Jing Li, for your companionship, trust, and for always enjoying my cooking whenever I asked you to come by. Thanks also to my friends Xiaoling Zhou, Dr. Jieshuang Wang, Dr. Zhiqiu Huang, Dr. Yufung Wong, Dini Li, and Kefei Zou for the many unforgettable moments we shared,

in heidelberg and ouside. To my best friend Ibtisam Saban, thank you for years of joy, for your unwavering support, and for always being there for me, even across distances. My heartfelt thanks to Dr. Qing Zhang for your encouraging spirit, for always making me feel better after we talk, and for all the movies we've enjoyed together, both online and in person. To my friends in Namibia, thank you for making my time there such a joyful and unforgettable experience.

I am very grateful to Jianci Tan for your companionship in the second half of my PhD, with your beautiful music and dancing. Thank you also for the advice that drastically changed the way I am thinking and acting.

My greatest thanks go to Chao Chen, my fiancé, for being the cornerstone of my life. Thank you for your endless patience, your quiet strength and belief in me, for all the things you've done without ever seeking credit, and for supporting me unconditionally, both personally and professionally. Thank you for the being by my side in the final days before submission and for helping me fixing those disturbing LaTeX errors.

Finally, I want to thank my parents for their unconditional support, for giving me the freedom to explore and pursue everything I set my heart on, and for preparing the most comforting meals whenever I came home. And to my brothers and my grandaunt, thank you, because without you, I wouldn't become who I am.